Repository Istituzionale dei Prodotti della Ricerca del Politecnico di Bari

Using nonlinear optimization to understand coherent structures in turbulence and transition

This is a PhD Thesis

Original Citation:
Using nonlinear optimization to understand coherent structures in turbulence and transition / Farano, Mirko. - (2018). [10.60576/poliba/iris/farano-mirko_phd2018]

Availability:
This version is available at http://hdl.handle.net/11589/120403 since: 2018-01-19

Published version
Politecnico di Bari
DOI:10.60576/poliba/iris/farano-mirko_phd2018

Terms of use:
Altro tipo di accesso

(Article begins on next page)

20 April 2024

Politecnico
di Bari

Department of Mechanics, Mathematics and Management
MECHANICAL AND MANAGEMENT ENGINEERING
Ph.D. Program
SSD: ING-IND/06–FLUID DYNAMICS
SSD: ING-IND/08–FLUID MACHINERY

Final Dissertation

Using nonlinear optimization to understand coherent structures in turbulence and transition

---

by
Mirko Farano

Supervisors:

Prof. Pietro De Palma

Prof. Stefania Cherubini

Prof. Jean-Christophe Robinet

Coordinator of Ph.D Program:
Prof. Giuseppe Pompeo Demelio.

Course n°30, 01/11/2014-31/10/2017

Politecnico
di Bari

Department of Mechanics, Mathematics and Management
MECHANICAL AND MANAGEMENT ENGINEERING
Ph.D. Program
SSD: ING-IND/06–FLUID DYNAMICS
SSD: ING-IND/08–FLUID MACHINERY
Final Dissertation

Using nonlinear optimization to understand coherent structures in turbulence and transition

---

by
Mirko Farano

Referees:

Prof. Carlo Cossu

Prof. Colm-cille P. Caulfield

Supervisors:

Prof. Pietro De Palma

Prof. Stefania Cherubini

Prof. Jean-Christophe Robinet

Coordinator of Ph.D Program:
Prof. Giuseppe Pompeo Demelio

Course n°30, 01/11/2014-31/10/2017

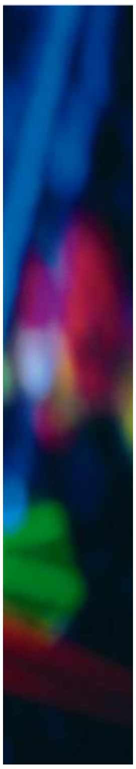

2017-ENAM-00XX

École doctorale n° 432 : Sciences des Métiers de l'ingénieur

Doctorat ParisTech

THÈSE

pour obtenir le grade de docteur délivré par

l'École Nationale Supérieure d'Arts et Métiers

Spécialité “ Mécanique des fluides ”

présentée et soutenue publiquement par

Mirko FARANO

01/12/2017

Using nonlinear optimization to understand coherent structures in turbulence and transition

Directeurs de thèse : **Pr. Jean-Christophe ROBINET, Pr. Pietro DE PALMA**
Co-encadrement de la thèse : **Pr. Stefania CHERUBINI**

Jury

Mme Laurette S. TUCKERMAN, Directeur de Recherche, PMMH-ESPCI, Paris	Président du jury
M. Carlo COSSU, Directeur de Recherche, LHEEA, Nantes	Rapporteur
M. Colm-cille P. CAULFIELD, Professeur, DAMTP, University of Cambridge	Rapporteur
M. Yohann DUGUET, Chargé de recherche, LIMSI-CNRS, Orsay	Examinateur
M. Tobias M. SCHNEIDER, Professeur, ECSP-EPFL, Lausanne	Examinateur
M. Jean-Christophe ROBINET, Professeur, DynFLuid, Arts et Métiers ParisTech	Directeur
M. Pietro DE PALMA, Professeur, DMMM, Politecnico di Bari	Directeur
Mme Stefania CHERUBINI, Professeur, DMMM, Politecnico di Bari	Co-directeur

THÈSE

Arts et Métiers ParisTech - ENSAM
Laboratoire DynFluid

"I realized that from now on a large part of my life would be spent finding and correcting my own mistakes"

Maurice Wilkes, 1949

Acknowledgements

First of all I would like to express my sincere gratitudes to Professor Jean-Christophe Robinet who has been my supervisor since the beginning of my study and whose long and fruitful discussions have provided me many helpful suggestions, important advices and constant encouragement during the course of this work. Special thanks are due to Professor Pietro De Palma, who followed my thesis work closely during my periods in Italy and not only, giving me many valuable suggestions and constructive advices. Sincere gratitude is due to Professor Tobias Schneider, for accepting me to spend last year, and my near future in his laboratory, showing intense academic interest in my studies, as well as providing valuable suggestions and support that improved the quality of this thesis.

A special thanks is due to Professor Stefania Cherubini, who would deserve another manuscript only for acknowledgements. At many stages in the course of this research project I benefited from her advice, particularly so when exploring new ideas. Her positive outlook and confidence in my research inspired me and gave me confidence. Her careful editing contributed enormously to the production of this thesis. I have been extremely lucky to have her as supervisor who cared so much about my work and myself.

I would like to express my gratitude to the referees of this thesis, Professor Carlo Cossu and Professor Colm-cille Caulfield, who accepted to revise my manuscript.

Yohann Duguet is gratefully acknowledged for several discussions and suggestions given to me since my first workshop in Paris.

I would like to thank all the members of the three laboratory in which I had the chance to spend my PhD. A particular thanks goes to my friends at Dynfluid, to which I'm mostly attached, and all friends I met in Paris: Andrea, Chloé, Damien, Edoardo, Jean-Christophe, Francesco, Deianira, Flavia and Elena.

Among them, many many thanks to Luca, Elio, and my colleague for many years now, Alessandro, with which I have shared a lot of scientific and especially unforgettable less scientific moments. They are amazing persons and our friendships will last forever.

Many thanks to my colleagues in Bari, Dario, Davide, Gioacchino, Mario, Onofrio, and to my friends, Gianni, Barbara, Antonio, Marialuisa, Gerry and Ettore.

Last, but not least, I'd like to thank all the fantastic people I met in Lausanne, Alessia, Ayshe, Emilio, Florian, Francesco, Giacomo, Gioele, Iryna, Sajjad, Simon, Steven, Professor François Gallaire and my flatmate Emilie.

Most of all I am grateful to my parents and my brother Vincenzo, who always encouraged me to concentrate on my studies and supported me in any of my choices.

Finally, I would like to express my heartiest thanks to Michela for having supported me during the course of this work. Despite the thousands of miles that have divided us, she has always been able to make me feel her love. Without her help and encouragement, this study would not have been the same. Many thanks also to her family for being me close in those three years.

The list of people to acknowledge is still long and the risk of forgetting people proportionally increases with it.

Thanks to all of you for being part of this adventure!

Contents

I General contents 1
I.1 Overview 1
I.2 Subcritical transition to turbulence 3
I.3 Bursts and large scale motion in turbulent shear flow 6
I.4 Dynamical systems and transition to turbulence 9
II Subcritical transition scenarios via linear and nonlinear localized optimal perturbations in plane Poiseuille flow 11
II.1 Introduction 11
II.2 Problem formulation 12
II.2.1 The optimization problem 13
II.3 Results 13
II.3.1 Optimal perturbations 14
II.3.1.1 Nonlinear 1-norm optimization 14
II.3.1.2 Linear p-norm optimization 19
II.3.2 Transition mechanisms 22
II.3.2.1 Short target time analysis 23
II.3.2.2 Long target time analysis 29
II.4 Conclusions 33
II.5 Appendix 34
III Hairpin-like optimal perturbations in plane Poiseuille flow 37
III.1 Introduction 37
III.2 Problem formulation 37
III.3 Results 38
III.4 Conclusions 47
IV Optimal bursts in turbulent channel flow 49
IV.1 Introduction 49
IV.2 Problem formulation 50
IV.3 Results 51
IV.3.1 Optimal perturbations 51
IV.3.1.1 Optimal perturbations at the inner time scale 53
IV.3.1.2 Optimal perturbations at the outer time scale 53
IV.3.1.3 Probability density function analysis 55
IV.3.1.4 Topology analysis 56
IV.3.1.5 Spectra analysis 58

IV.3.2 Time evolution of the outer optimal perturbation 62
IV.3.2.1 Production and dissipation analysis 62
IV.3.2.2 Analysis of the flow structures 64
IV.4 Conclusion 67
IV.5 Appendix 69
V Nonlinear large-scale optimal structures in turbulent channel flow 73
V.1 Introduction 73
V.2 Numerical methods 74
V.2.1 Nonlinear optimization 74
V.3 Results 75
V.3.1 Nonlinear optimal structures 75
V.4 Conclusions 85
VI How hairpin structures emerge from exact solutions of shear flows 87
VI.1 Introduction 87
VI.2 Problem formulation 88
VI.3 Results 89
VI.4 Conclusion 94
VII CHELA: Computing HEteroclinic connections using a Lagrange multiplier Algorithm 97
VII.1 Introduction 97
VII.2 Problem formulation 98
VII.3 Results 101
VII.4 Conclusions and outlooks 103
VIII Overall conclusions 111
VIII.1 Conclusions 111
VIII.2 Perspectives 113

References 117

List of Figures

II.1 (a) Optimal energy gain curve versus target time obtained with linear (red line) and nonlinear $1-norm$ optimization with initial energy $E_0 = 10^{-7}$ (green line) and $E_0 = 2.5 \times 10^{-7}$ (blue line). (b) Optimal energy at target time versus initial energy for $T_{opt} = 20$. The different shapes of the symbols indicate different types of optimal solutions resulting from the optimisation at the chosen T_{opt} and E_0: triangles for linear optimals, circles for weakly non linear and squares for highly nonlinear optimals. 14

II.2 Different families of optimal perturbations on the plane T_{opt} and E_0 for p=1. In the top frame, the symbols indicate the different types of optimal solutions resulting from the optimisation at the chosen T_{opt} and E_0: triangles for linear optimals; circles for weakly nonlinear; squares for highly nonlinear optimals; and diamonds for hairpin-like optimals. The solid lines indicate the energy thresholds for shape modification. In the bottom frames, the linear, weakly nonlinear, highly nonlinear, and hairpin-like optimal solutions (from left to right) are represented using iso-surfaces of the Q-criterion, coloured in yellow/green for positive/negative values of the streamwise vorticity, respectively. The optimal solutions shown are the ones represented by full symbols in the top frame. The dashed line represents the transition thresholds for the nonlinear optimals given in table II.2. 15

II.3 Shape of the nonlinear 1-norm optimal perturbation (WNLOP solution) for (a) $T_{opt} = 10$, $E_0 = 1,25 \times 10^{-6}$ and (b) $T_{opt} = 20$, $E_0 = 6.5 \times 10^{-7}$. Isosurfaces of the Q-criterion at $t = 0$, $Q = 0.000195$ (a), $Q = 0.00011$ (c) and (b,d) at $t = T_{opt}$ ($Q = 0.011$ (b), $Q = 0.003$ (d)). The isosurfaces are colored by contours of streamwise vorticity. 17

II.4 Nonlinear 1-norm optimal perturbation (HNLOP solution) for (a,b) $T_{opt} = 20$ and $E_0 = 7,5 \times 10^{-7}$; (c,d) $T_{opt} = 30$ and $E_0 = 2.5 \times 10^{-7}$. Isosurfaces of the Q-criterion (colored) and of the streamwise velocity disturbance (light grey for positive and black for negative values) at (a) t=0 ($Q = 0.005$, $u = \pm 0.07$), (b) t=20 ($Q = 0.2$, $u = \pm 0.2$), (c) t=0 ($Q = 0.002$, $u = \pm 0.04$), and (d) t=30 ($Q = 0.1$, $u = \pm 0.15$). The Q-criterion surfaces are colored by contours of the streamwise vorticity. 18

II.5 (a) Energy gain and (b) p-norm gain as a function of p for $T_{opt} = 10$. Each symbol (x) represents an optimization. 19

II.6 50-norm linear optimal perturbation for $T_{opt} = 10$. Isosurfaces of Q-criterion ($Q = 0.01$) at (a) $t = 0$ and (b) $t = 10$. The isosurfaces (a) are colored by contours of the streamwise vorticity. 20

II.7 Evolution in time of the energy and 50-norm gain for the linear 50-norm optimal perturbation with three different optimization time. 21

II.8 50-norm linear optimal perturbation for $T_{opt} = 20$ and (a) $L_x = 2\pi$, and (b) $L_x = 4\pi$, at $t = 0$. Isosurfaces of Q-criterion ($Q = 0.01$). 22

II.9 Time evolution of the rms of the velocity (left) and vorticity (right) components for the WNLOP with $E_0 = 1.25 \times 10^{-6}$ (top frames) and $E_0 = 1 \times 10^{-6}$ (middle frames), and of the 50-norm LOP with $E_0 = 10^{-6}$ (bottom frames), computed for $T_{opt} = 10$. 24

II.10 Snapshots of the time evolution of the weakly nonlinear optimal perturbation found for $E_0 = 1.25 \times 10^{-6}$. Isosurface of Q-criterion ($Q = 0.5$, grey), and of the streamwise velocity disturbance ($u = \pm 0.1$, green for negative and yellow for positive). 26

II.11 Snapshots of the time evolution of the weakly nonlinear optimal perturbation computed for $E_0 = 1.25 \times 10^{-6}$, $T_{opt} = 10$. Isolines of streamwise velocity disturbance (red positive, black negative), and contours of spanwise vorticity (white positive, black negative) on a $z = 2$ plane. 26

II.12 Time evolution of the Fourier streamwise and spanwise wavenumbers for the two optimals computed at $T_{opt} = 10$ with initial energy $E_0 = 1.25 \times 10^{-6}$; a nonlinear 1-norm (a) and a linear 50-norm optimal (b). 27

II.13 Evolution of linear 50-norm optimal perturbation for $T_{opt} = 10$ and $E_0 = 10^{-6}$. (a,b,c,d,e,f) Isosurface of Q-criterion ($Q = 0.07$, grey), and of streamwise velocity disturbance ($u = -0.9$, green and $u = 0.15$, yellow). 28

II.14 Evolution of linear 50-norm optimal perturbation computed for $T_{opt} = 10$ and $E_0 = 10^{-6}$. Isolines of streamwise velocity disturbance (red positive, black negative), and contours of spanwise vorticity (white positive, black negative) on a $z = 1.6$ plane. 29

II.15 Time evolution of the rms of the velocity (left) and vorticity (right) components for the 50-norm LOP (top frames) and the HNLOP (bottom frames) with $E_0 = 2.5 \times 10^{-7}$, computed for $T_{opt} = 30$. 30

II.16 Snapshots of the time evolution of the highly nonlinear optimal perturbation computed for $T_{opt} = 30$ and $E_0 = 2.5 \times 10^{-7}$. Isosurface of Q-criterion ($Q = 0.01 Q_{max}$) colored by streamwise vorticity, and isosurfaces of streamwise velocity disturbance ($u = \pm 0.5 u_{max}$, black negative and white positive). 31

II.17 Snapshots of the time evolution of the HNLOP computed for $E_0 = 2.5 \times 10^{-7}$, $T_{opt} = 30$. Isolines of streamwise velocity disturbance (red positive, black negative), and contours of spanwise vorticity (white positive, black negative) on a $z = 2$ plane. 31

II.18 Time evolution of the Fourier streamwise and spanwise wavenumbers for the two optimals computed at $T_{opt} = 30$ with initial energy $E_0 = 2.5 \times 10^{-7}$; a nonlinear 1-norm (a) and a linear 50-norm optimal (b). 32

II.19 Energy gain (green dashed line) ϵ (blue dash-dotted line) and r (red solid line) plotted against iteration for (left) the Hairpin-like OP, $T_{opt} = 16$ at $E_0 = 2 \times 10^6$ and (right) the HNLOP $T_{opt} = 30$ at $E_0 = 2.5 \times 10^7$ 36

III.1 Log-Log plot indicating the scaling law for the initial energy (squares), the transition threshold (circles) (a), and the energy gain (b) for the short-time nonlinear optimal perturbation at the nonlinearity threshold. 38

III.2 Isosurfaces of the Q-criterion colored by the stream wise vorticity value for the nonlinear optimal perturbation obtained for $Re = 4000$, $T_{opt} = 10$, and $E_0 = 2 \times 10^{-6}$: (a) $t = 0$, $Q = 0.01$ ($Q_{max} = 0.086$) and (b) $t = 10$, $Q = 0.2$ ($Q_{max} = 3.88$). 40

III.3 Isosurfaces of the three velocity components (light grey for positive and black for negative values, $u, v, w = \pm 0.01$) of the nonlinear optimal perturbation for $T_{opt} = 10$: (top frames) $E_0 = 2 \times 10^{-6}$, $Re = 4000$; and (bottom frames) $E_0 = 1 \times 10^{-5}$, $Re = 2000$. 41

III.4 Time evolution of the energy gain, velocity (left) and vorticity (right) rms values for the nonlinear optimal perturbation with $Re = 4000$, $E_0 = 2 \times 10^{-6}$, and $T_{opt} = 10$ 41

III.5 Time evolution of the nonlinear optimal perturbation for $Re = 4000$, $T_{opt} = 10$, and $E_0 = 2 \times 10^{-6}$: Isosurface of Q-criterion ((a-e) $Q = 0.02$; (f) $Q = 0.1$, green) and streamwise velocity disturbance ($u = -0.03$, black). $Q_{max} = 0.086, 1.03, 1.99, 7.5, 21.5, 35.4$ for figures (a) to (f), respectively. . . 42

III.6 Velocity profile along the principal axis of the TED extracted at two different times from the DNS (black) and the linearized DNS (red), initialized by the nonlinear optimal at $(Re, E_0) = (4000, 2 \times 10^{-6})$. The insets show the Q-criterion surfaces (left: $Q = 0.2$ and $Q_{max} = 1.03$; right: $Q = 0.3$ and $Q_{max} = 3.9$; green) and the principal axis (red lines) at two different times. The dot indicates the CVS. 43

III.7 Contours of the logarithm of the probability density function of the wall-normal and streamwise velocity disturbance in a $u - v$ plane ($w = 0$) for $0 \leq y \leq 1$, extracted at $t = 0, 1, 6, 10$ from a DNS initialized with the nonlinear optimal with $T_{opt} = 10$ and $E_0 = 2 \times 10^{-6}$. The values of the logarithm of the PDF have been normalized with respect to the total number of points of the computational domain. 44

III.8 Wall-normal and streamwise components of the velocity vector disturbance along the principal axis of the TED for the nonlinear optimal with $E_0 = 2 \times 10^{-6}$: (a) $t = 0$, (b) $t = 14$. Isosurface of the Q-criterion ((a) $Q = 0.01$ and $Q_{max} = 0.086$, (b) $Q = 4$ and $Q_{max} = 12.05$) 45

III.9 Streamwise velocity (solid lines) and vorticity magnitude (dashed lines) profiles at $t = 10$ along a wall-normal line passing through the hairpin head computed by the DNS (a) and by the linearized DNS (b), initialized with the nonlinear optimal for $E_0 = 2 \times 10^{-6}$. Circles indicate inflection points. 45

III.10 Time evolution of the nonlinear optimal perturbation obtained for $T_{opt} = 10$ and $E_0 = 2 \times 10^{-6}$ on the plane $z = 2$. Isosurfaces of the Q-criterion ($Q = 0.1$, green), isolines of the streamwise velocity disturbance (red positive, black negative), and contours of the wall-normal velocity disturbance (white positive, black negative). $Q_{max} = 0.61, 3.88, 21.52$ for figures (a) to (c), respectively. 46

III.11 Time evolution of the nonlinear optimal perturbation obtained for $T_{opt} = 10$ and $E_0 = 2 \times 10^{-6}$ on the plane $z = 2$ obtained by a linearized DNS. Isosurfaces of the Q-criterion ($Q = 0.1$, green), isolines of the streamwise velocity disturbance (red positive, black negative), and contours of the wall-normal velocity disturbance (white positive, black negative). $Q_{max} = 0.79, 0.25, 0.05$ for figures (a) to (c), respectively. 46

IV.1 Shape of the optimal perturbation for $T^+_{in} = 80$ and $E_0 = 10^{-2}$ at (a) $t^+ = 0$ and (b) $t^+ = T^+_{in}$: isosurface of negative streamwise velocity (green, (a) $\tilde{u} = -0.025$, (b) $\tilde{u} = -0.18$) and Q-criterion ((a) $Q = 10^{-6}$, (b) (a) $Q = 2 \times 10^{-6}$) coloured by the value of the streamwise vorticity (positive blue, negative red). 52

IV.2 Shape of the optimal perturbation for $T^+_{out} = 305$ and $E_0 = 10^{-2}$ at (a) $t^+ = 0$ and (b) $t^+ = T^+_{out}$: isosurface of negative streamwise velocity (green, (a) $\tilde{u} = -0.016$, (b) $\tilde{u} = -0.3$) and Q-criterion ((a) $Q = 0.045$, (b) (a) $Q = 0.15$) coloured by the value of the streamwise vorticity (positive blue, negative red). 52

IV.3 Shape of the optimal perturbation for $T^+_{out} = 305$ and $E_0 = 10^{-2}$ at $t^+ = T^+_{out}$: isosurface of negative streamwise velocity (green) (a,b); isosurface of Q-criterion coloured by contours of streamwise vorticity (positive blue, negative red) (b). The isosurface values are the same as in figure IV.2 (b). Small solid circles indicate small hairpin vortices, big dashed circles indicate big hairpin vortices. 54

IV.4 Outer optimal perturbation obtained for $T^+_{out} = 305$ and $E_0 = 10^{-2}$: isosurfaces of the Q-criterion (green) and isocontours of streamwise velocity (blue negative, red positive) on the planes $z^+ = 860$ and $z^+ = 320$. The isosurfaces values are the same as in figure IV.2 (b). 54

IV.5 Logarithm of the PDF of the streamwise and wall normal velocity for the outer optimal structures at $t = T_{out}$ (left) and for the fully turbulent flow (right) at different constant y^+-planes: $y^+ = 10$, $y^+ = 50$, $y^+ = 100$, from top to bottom. 57

IV.6 Sketch of the flow topologies associated with different regions of the $Q - R$ plane, Q and R being the second and third invariant of the velocity gradient tensor, and $D = (27/4)R^2 + Q^3$ (Blackburn et al., 1996). 58

IV.7 Logarithm of the PDF of the nondimensional second (Q^*) and third (R^*) invariant of the velocity gradient tensor, for the outer optimal structures at $t = T_{out}$ (left) and for the fully turbulent flow (right) at different constant $y^+-plane$ (from top to bottom: $y^+ = 10, 50, 100$). Notice that $Q^* = Q/Q_w$ and $R^* = R/Q_w^{3/2}$, Q_w being the second invariant of the antisymmetric part of the tensor A, averaged on each y^+- constant plane. 59

IV.8 Logarithm of the premultiplied power spectrum versus the wall normal distance y^+ for the DNS (shaded contours), inner optimal solution (blue isolines) and outer optimal solution (black isolines) at target time. The symbols X and O indicate the maximum value for the inner and outer peak, respectively. The green dotted line joining the inner and outer energy peak provides the scaling laws $y^+ = c(k^+_{x,z})^{-1}$, with slopes (a) $c = 0.0921$, (b) $c = 0.4608$, (c) $c = 0.6970$, (d) $c = 0.1028$, (e) $c = 0.1439$, (f) $c = 0.1287$. . 61

IV.9 (a) Time evolution of the energy E (red), production P_V (blue), Reynolds stress production $P_{\tau V}$ (cyan), and dissipation D_V (green). (b) Trajectories in the plane $D_V - P_V$ of the production P_V, Reynolds stress production $P_{\tau V}$, and total production $P_{TotV} = P_V + P_{\tau V}$. The time interval between symbols is equal to $\Delta t^+ = 24.5$. 62

IV.10(a) Time evolution of the net local energy production, given by the difference between the production and dissipation at each y^+ (shaded contours), and of the wall-normal energy flux (isolines for $\Phi^+ = 1, 2, 3, 4$, from the outermost to the innermost contour) for the outer optimal structure. (b) Net local energy production (red dashed line) and wall-normal flux (black solid line) versus y^+, extracted at $t^+ = 2T^+_{out}$, showing a production peak in the inner zone ($y^+ \approx 20$), whereas the outer region is characterized by a weak dissipation. 63

IV.11Snapshots of the time evolution of the outer optimal structures: isosurfaces of Q-criterion coloured by the wall normal distance y^+. 66

IV.12(Left) Sketch of the main steps of the dynamics of the outer optimal perturbation based on the snapshots (right) extracted at (a) $t^+ = 49$, (b) $t^+ = 123$, (c) $t^+ = 147.5$, (d) $t^+ = 294$, (e) $t^+ = 172, 196.5$, (f) $t^+ = 221$. Isosurfaces of negative streamwise velocity (green) and Q-criterion coloured by the values of streamwise vorticity (blue for positive, red for negative). . 67

IV.13Left frame: mean velocity profile U^+ versus the wall-normal coordinate y^+ (blue thick lines) obtained by the present DNS (solid) compared with the results of Kim et al. (1987) (dashed). The black thin lines are the linear (solid) and logarithmic (dashed) profiles. Right frame: root mean square of $\tilde{u}$ (red), $\tilde{v}$ (blue), $\tilde{w}$ (green), and Reynolds shear stress $\overline{\tilde{u}\tilde{v}}$ (black) normalized by the wall shear velocity, versus y^+ obtained by the present DNS (solid) compared with the results of Kim et al. (1987) (dashed). . . . 70

IV.14Left frame: streamwise (red), wall-normal (blue) and spanwise (green) components of the divergence of the Reynolds stress tensor τ versus y^+ obtained by the present DNS. Right frame: energy of $\nabla \cdot [\tilde{\mathbf{u}}\tilde{\mathbf{u}}]$ (where $[\bullet]$ denotes the spatial average in the $y = const$ planes) for the outer (red line) and inner (green line) optimal perturbations versus time; the dashed line indicates the energy of $\nabla \cdot \tau$. 70

V.1 Instantaneous isosurfaces of the second invariant of the velocity gradient tensor, Q-criterion ($Q/Q_{max} = 0.025$), coloured by the streamwise velocity: left, C180; right, C590 76

V.2 Streamwise-averaged perturbation of the mean flow for C180 (left) and C590 (right), on a $y-z$ plane scaled in outer units (bottom) and a close-up where the lengths are scaled in inner units (top). Blue (red) contours indicate negative (positive) values of the streamwise velocity perturbations. 76

V.3 Shape of the optimal perturbations at $t=T$: isosurfaces of negative streamwise velocity perturbation ($\tilde{u}/\tilde{u}_{max}=0.45$, green) and of the second invariant of the velocity gradient tensor, Q-criterion ($Q/Q_{max}=0.025$, grey). C180, $E_0=10^{-2}$ (left) and C590, $E_0=7.5\times10^{-4}$ (right). 77

V.4 Contours of the logarithm of the premultiplied energy density spectra in the $k_x^+-y^+$ plane for the optimal solutions at target time (shaded contours) and the DNS (solid lines) for C180 (left) and C590 (right). The symbols X indicate the peak values of the optimal spectra. The gray zones for C180 indicate the cut off values of y^+ and k_x^+ corresponding to the half height and streamwise length of the channel. 79

V.5 Contours of the logarithm of the premultiplied energy density spectra in the $k_z^+-y^+$ plane for the optimal solutions at target time (shaded contours) and the DNS (solid lines) for C180 (left) and C590 (right). The symbols X indicate the peak values of the optimal spectra. The gray zones for C180 indicate the cut off values of y^+ and k_z^+ corresponding to the half height and spanwise length of the channel. 80

V.6 Isosurfaces of the two-point cross-correlation coefficient R_{11} for the DNS (left) and the optimal perturbation at target time (right) for C180. Red (blue) surfaces represent positive (negative) values. The green circles represent the reference points y_r, with values $y_r=10,50,100$ (top to bottom). 82

V.7 Isosurfaces of the two-point cross-correlation coefficient R_{11} for the DNS (left) and the optimal perturbation at target time (right) for C590. Red (blue) surfaces represent positive (negative) values. The green circles represent the reference points y_r, with values $y_r=10,50,100,180$ (top to bottom). 83

V.8 Time evolution of the net local energy production, given by the difference between the production and dissipation at each y^+ for the optimal disturbance for C180 (left) and C590 (right). Continuous and dashed lines represent respectively positive and negative values. The gray zones for C180 indicate the cut off values of y^+ corresponding to the half size of the channel. 85

V.9 Lift-up production term averaged in the streamwise direction (shaded contours) and streamwise instantaneous velocity component (solid contours) in a z^+-y^+ plane for the optimal perturbations in C180 (left) and C590 (right). The gray zones for C180 indicate the cut off values of y^+ corresponding to the half size of the channel. 85

VI.1 (a) Travelling wave $\mathbf{u}_{TW}$ and (b) associated optimal perturbation $\mathbf{u}'(0)$ lying at $t = 0$ in an energy shell $E_0 = 10^{-6}$ around TW2 providing a maximum energy amplifications at $T_{opt} = 10$. (c-d) Full velocity field $\mathbf{u}_{TW}+\mathbf{u}'(t)$ obtained by evolving the initial optimal perturbation on top of TW2: snapshots at $t = 5$, and $t = T_{opt} = 10$, respectively, both showing a train of hairpin vortices. (a,c,d) Isosurfaces of the Q criterion (yellow) of the full velocity field and of the positive streamwise velocity perturbation with respect to the laminar flow (violet). Isolines: streamwise velocity perturbation with respect to the laminar flow (orange for negative, violet for positive). (b) Isosurfaces of positive (red) and negative (blue) streamwise velocity perturbation $\mathbf{u}'(0)$. Isolines: streamwise velocity perturbation $\mathbf{u}'(0)$ (red for positive, blue for negative). 90

VI.2 Evolution in time of the energy of three optimal perturbations (solid lines) with initial energy $E_0 = 10^{-6}$ (blue) 10^{-7} (green) 10^{-8} (red). Dashed lines represent the energy obtained for the same initial perturbations with the unstable directions of TW2 projected out. Inset: square root of the energy gain versus time. The black line is the energy gain obtained by a linear optimization. The dots indicate the times at which the flow fields in figure VI.1 (c) VI.3 (b,d) (from blue to red) have been extracted, which corresponds to the energy level $\approx 2.3 \times 10^{-4}$, at which the hairpin vortices are observed. 91

VI.3 Optimal perturbations $\mathbf{u}'(0)$ lying at $t = 0$ in an energy shell (a) $E_0 = 10^{-7}$, (c) $E_0 = 10^{-8}$ around TW2 providing the maximum energy amplification at $T_{opt} = 10$ (red, blue surfaces for positive, negative streamwise velocity perturbation, as well as for the isolines). Full velocity field $\mathbf{u}_{TW} + \mathbf{u}(t)$ obtained by evolving the two initial optimal perturbations on top of TW2: snapshots are extracted at $t = 18$ (b) and $t = 26.5$ (d), respectively, corresponding to the green and red dots in figure VI.2. Both snapshots show a train of hairpin vortices provided by the yellow surfaces representing the Q criterion of the full velocity field, whereas the isocontours represent the deviation from the laminar profile of the streamwise instantaneous velocity (violet for positive, orange for negative). 92

VI.4 (a) Sketch illustrating the transient growth of a vector given by the sum of two time-decaying non-orthogonal eigenvectors, s_1 and s_2. While the amplitude of the two components of the vector along these eigendirections decreases in time (from top to bottom), the module of the resulting vector is transiently amplified (compare blue circle with red one). (b) Overlap matrix with entries given by the scalar product between the eigenvectors of the NS equations linearised around TW2, $\widehat{\mathbf{u}}_i, \widehat{\mathbf{u}}_j$. The darker the entry, the larger the overlap, with values between 0 and 1. For mutually orthogonal eigenvectors (as would be the case for a normal matrix) the scalar product would be non zero only on the matrix diagonal. 93

VI.5 Sketch of the trajectory of the optimal perturbation initially lying on the neighbourhood of the ECS on a projection of the phase space given by the projection of the perturbation on the unstable direction u_1, and the stable ones s_1, s_2. The red line shows a trajectory associated to a rapid energy amplification (measured as the square of the distance from the ECS) in the stable subspace (yellow plane) with respect to the more classical scenario where the slower amplification follows the unstable one (blue line). The red and blue solid lines represent the trajectory in the full 3D space u_1, s_1, s_2, whereas the red dashed line is the projection of the trajectory in the 2D space s_1, s_2. 93

VII.1 Schematic sketch describing the algorithm for computing heteroclinic connections using nonlinear optimization method based on Lagrange multipliers. The sketch shows how the initial condition, and the related trajectory towards the final ECS, changes after updating the optimization time T_{opt} (dashed lines). The algorithm stops when the integration time is sufficiently large to allow the flow field to be sufficiently close to the final stage (solid line). 99

VII.2 Left: Plots of distances of the velocity field $\mathbf{u}(t)$ to the target equilibrium $\mathbf{u}_{ECS_{in}}$ along the computed heteroclinic connections versus time. The dashed line represents the highest residual value for the heteroclinic connections computed in Halcrow et al. (2009). Right: Projection of the orbits onto the energy input rate, I, and the dissipation rate, D, normalized by their value in laminar flow. 102

VII.3 Streamwise averaged velocity field (with the laminar flow subtracted) at $t = 0$, $t = 43$, $t = 100$, $t = 157$, $t = 214$, $t = T_{opt}$, respectively (from top left to bottom right) of the computed heteroclinic connection from $EQ4$ to $EQ3$. Shaded contours represent the streamwise velocity (blue negative, red positive). The quiver plot shows the wall normal and spanwise component. Scales are set to the maximum (minimum) value of the quantities of the initial ECS. 103

VII.4 Streamwise averaged velocity field (with the laminar flow subtracted) at $t = 0$, $t = 26$, $t = 82$, $t = 123$, $t = 164$, $t = T_{opt}$, respectively (from top left to bottom right) of the computed heteroclinic connection from $EQ4$ to $EQ9$. Shaded contours represent the streamwise velocity (blue negative, red positive). The quiver plot shows the wall normal and spanwise component. Scales are set to the maximum (minimum) value of the quantities of the initial ECS. 104

VII.5 Streamwise averaged velocity field (with the laminar flow subtracted) at $t = 0$, $t = 26$, $t = 78$, $t = 130$, $t = 183$, $t = T_{opt}$, respectively (from top left to bottom right) of the computed heteroclinic connection from $EQ9$ to $EQ3$. Shaded contours represent the streamwise velocity (blue negative, red positive). The quiver plot shows the wall normal and spanwise component. Scales are set to the maximum (minimum) value of the quantities of the initial ECS. 105

VII.6 Streamwise averaged velocity field (with the laminar flow subtracted) at $t = 0$, $t = 60$, $t = 90$, $t = 120$, $t = 200$, $t = T_{opt}$, respectively (from top left to bottom right) of the computed heteroclinic connection from $EQ9$ to $EQ1$. Shaded contours represent the streamwise velocity (blue negative, red positive). The quiver plot shows the wall normal and spanwise component. Scales are set to the maximum (minimum) value of the quantities of the initial ECS. 106

VII.7 Streamwise averaged velocity field (with the laminar flow subtracted) at $t = 0$, $t = 9$, $t = 48$, $t = 87$, $t = 127$, $t = T_{opt}$, respectively (from top left to bottom right) of the computed heteroclinic connection from $EQ10$ to $EQ1$. Shaded contours represent the streamwise velocity (blue negative, red positive). The quiver plot shows the wall normal and spanwise component. Scales are set to the maximum (minimum) value of the quantities of the initial ECS. 107

VII.8 Streamwise averaged velocity field (with the laminar flow subtracted) at $t = 0$, $t = 50$, $t = 80$, $t = 110$, $t = 150$, $t = T_{opt}$, respectively (from top left to bottom right) of the computed heteroclinic connection from $EQ11$ to $EQ1$. Shaded contours represent the streamwise velocity (blue negative, red positive). The quiver plot show the wall normal and spanwise component. Scales are set to the maximum (minimum) value of the quantities of the initial ECS. 108

VII.9 A state-space projection of the computed heteroclinic connections at $Re = 400$. Symbols and colours are the same as in figure VII.2. 109

List of Tables

II.1 Maximum absolute values of the disturbance velocity and vorticity components for the optimal perturbations obtained by linear 50-norm and nonlinear 1-norm optimizations with $T_{opt} = 20$ and $E_0 = 5 \times 10^{-7}$ (left columns), and with $E_0 = 7.5 \times 10^{-7}$ (right columns). 22
II.2 Values of the transition energy thresholds associated with the optimal perturbations computed at the indicated target time. 25

IV.1 Wave length and corresponding wall normal position of the peaks of the premultiplied energy density spectrum shown in figure IV.8. 60

V.1 Simulation parameters for the two cases considered in the present work. . . 74
V.2 Wavelength and corresponding wall-normal position of the peaks of the premultiplied energy density spectra shown in figure V.4. 78

VII.1 Computed heteroclinic connections for $Re = 400$ and corresponding symmetry subspace. The dimension of the unstable manifold of the starting equilibrium (ECS_{out}) is $d(W^u)$, while $d(W^u_S)$ is the dimension of the intersection of the unstable manifold with the symmetry invariant subspace reported here for the initial and final equilibrium (ECS_{in}). 101

Chapter I

General contents

I.1 Overview

This thesis aims at unravelling the main mechanisms involved in transitional and turbulent flows. The central idea is to use nonlinear optimization technique to investigate the role of coherent structures usually observed in such conditions and give an explanation of their origin and role.

We start considering a linearly stable laminar flow. Such a flow is characterized by very ordered motion of particles, with no eddies nor swirls of fluids (Reynolds, 1883). Within this limit, we apply the optimization framework to identify among all initial disturbances of a given energy the most amplified coherent perturbations (highly correlated in time and space) able to trigger transition to turbulence (Cherubini et al., 2015, 2010b; Duguet et al., 2013; Monokrousos et al., 2010; Rabin et al., 2012). In principle, small perturbation theory (i.e. linear stability analysis) predicts stability of the laminar profile under a critical Reynolds number; in practice, transition is observed already at values of the Reynolds number even below the critical one. This is typically observed in subcritical flows where all the eigenmodes are damped: energy amplification is only observed for those disturbances characterized by strong transient growth. From a mathematical point of view, transient growth is associated with non-normality of the linearised Navier-Stokes equations (Butler and Farrell, 1992). In particular, non-normal growth arises from the constructive interference of damped eigenmodes which are nearly antiparallel, and typically results in the creation of streamwise elongated flow structures, called streaks. On the contrary, in a nonlinear framework, the optimal mechanisms triggering turbulence are different: localized and wavy optimal perturbations are found, which are more efficient in terms of energy growth than their linear counterpart. Thus, the aim is to identify initial, localized coherent structures which most easily bring the flow on the verge of turbulent transition. Within the nonlinear framework, among all the optimal perturbations, *"minimal seeds"* are of particular importance as they are characterized by the minimum distance from the laminar state (Pringle and Kerswell, 2010). Those optimal disturbances give a measure of how nonlinearly stable the laminar state is through the value of the minimal energy to initiate transition. In the present work, several optimal, linear and nonlinear localized initial conditions are computed and compared for the laminar plane Poiseuille flow in the subcritical regime.

Once turbulence is well established, shear flows are characterized by the chaotic dynamics of fluctuations around a statistically steady mean flow. Most of the effort in the last decades has aimed at studying the turbulent regime by analysing the flow statistics, which are well characterized by simple and robust laws (Pope, 2001). However, in addition to these chaotic dynamics, turbulent flows also appear to be populated by coherent structures, i.e. fluid motions highly correlated over both space and time, with wavelengths and lifetimes obtained by statistical analysis. These coherent structures carry a large part of the flow momentum, and it is still an open question how they influence mean and global quantities. In order to study the dynamics of coherent structures, we use a fully 3D nonlinear optimization to maximize the energy of perturbations of the turbulent mean flow. The results of this optimization allow us to unravel the presence of optimally growing coherent structures in a turbulent channel flow and understand the main mechanism in terms of energy exchange and production.

An extension of the nonlinear dynamical system theory is applied to further investigate transitional and turbulent flows governed by the Navier-Stokes equations. (Eckhardt et al., 2007a) Time evolution of the state vector is represented by a sequence of points in an appropriate state space, each representing the state variables at a given time. In this framework, transition to turbulence, and turbulence itself, is viewed as a path in phase space that approaches invariant solutions, i.e. fixed points, travelling waves, periodic orbit and chaotic attractors, and spends a substantial fraction of its time in their neighbourhood. Each of the invariant solutions has stable and unstable manifolds, and their intersections contain connecting orbits for the state of the system to follow as it visits these building blocks, associated with coherent structures (Kawahara et al., 2012). Hence, stable and unstable manifolds of the above simple invariant solutions could represent turbulent dynamics, whereas the simple solutions themselves would represent coherent structures embedded in a turbulent state. Such connections are called homoclinic and heteroclinic connections. To study the behaviour of the perturbations in the vicinity of those invariant solutions we use modal stability analysis and transient growth theory (the so called non-modal analysis). The latter is once again based on the already mentioned nonlinear optimization algorithm. We consider the dynamics in the vicinity of one equilibrium to investigate the importance of its stable and unstable manifold. In particular we aim at investigating whether, as currently supposed, the unstable manifold has a main role during the time evolution of perturbations escaping from exact coherent states while following a turbulent trajectory in the chaotic saddle [1]. In fact, as discussed in Gibson et al. (2008), the turbulent dynamics consists as a series of transitions between saddle states which compose the chaotic saddle, the low number of unstable modes for each of these states resulting in an intrinsic low-dimensionality observed in turbulence (Waleffe, 2002). The results presented in this thesis provide a new perspective on the problem, considering the evolution of a superposition of stable modes rather than just the most unstable ones of the considered exact coherent state and revealing how the non-orthogonality of these modes can lead to short-time energy growth overcoming the one evolving in the unstable subspace. In the same framework, nonlinear optimization algorithm is used to compute heteroclinic connections among invariant states.

The present work is thus divided in three main parts: i) transition to turbulence; ii) turbulent dynamics; iii) dynamical system analysis. Each of the three parts is composed of two chapters containing the problem formulation and results, respectively. In the following three subsections, the state of the art and the motivations of the this work are given for each of these three topics.

---

[1] A *chaotic saddle* is an invariant compact set $\mathbf{C}$ that is neither attracting nor repelling and contains a chaotic trajectory which is dense in $\mathbf{C}$.

I.2 Subcritical transition to turbulence

Transition to turbulence in shear flows is a longstanding problem that has been challenging generations of researchers since the early experiments of Reynolds (1883). It is now clear that, even for simple shear flows, transition cannot be linked only to a linear instability arising at a well-defined critical value of the Reynolds number, Re_c (unconditional instability). For instance, pipe and plane Couette flows have an infinite value of Re_c but can experience transition for sufficiently high values of the Reynolds number, $Re > Re_g$ (Avila et al., 2011; Bottin and Chaté, 1998). For other shear flows, such as plane Poiseuille and boundary-layer flows, even if a finite value of Re_c does exist, transition is often subcritical, being observed at $Re_g < Re < Re_c$ when the laminar base flow is perturbed with a sufficiently high amplitude (see Patel and Head (1969), Schlichting and Gersten (2000)). In these conditions the stability of the flow is conditional, namely it depends on the shape and intensity of perturbations brought to the base flow. The determination of the minimum-energy perturbation capable of leading the flow to transition is a crucial issue for understanding subcritical transition and indeed is a difficult task (Cossu, 2005). In fact, shear flows can be very sensitive to small modifications of the initial perturbations, as proven in the experiment by Darbyshire and Mullin (1995), in which the authors observed that the same perturbation (within the accuracy of the experimental resolution) may lead to very different outcomes in terms of transition to turbulence.

With the aim of determining transition thresholds, in the last decades there has been a large interest in perturbations transiently amplifying due to the non-normality of the Navier–Stokes operator. These small-amplitude initial perturbations can reach in a finite time large amplitudes, sufficient to trigger nonlinear effects leading the flow to transition (Landahl, 1980; Trefethen et al., 1993). The search for these transiently growing perturbations led to the concept of "optimal perturbations" experiencing the largest amplification over a finite time horizon. For plane channel flow, Butler and Farrell (1992) found that, in a linear framework, the maximum energy amplification over time can be obtained by a pair of streamwise-invariant vortices generating in a finite time a pair of streamwise-invariant streaks (Farrell, 1988). However, these streamwise-invariant structures are different from perturbations that are usually observed in real flows during transition. In fact, in real flow configurations, disturbances are mostly due to localized imperfections of the wall surface (for pipes and channels), or to freestream turbulence and acoustic waves (in the case of boundary-layer flows). As a result, transition to turbulence is often observed in localized spots or puffs (Perry et al., 1981; Singer, 1996; Wygnanski and Champagne, 1973; Wygnanski et al., 1976) which spread in space and merge, leading the flow to sustained turbulence. The early phases of development of turbulent spots or puffs triggered by localized perturbations (Perry et al., 1981; Singer, 1996), localized pulses or jets of finite amplitude have been used to explain the intrinsic mechanisms of subcritical transition to turbulence in pipe flow (Hof et al., 2005; Mellibovsky and Meseguer, 2007), and in plane

Couette flow (Dauchot and Daviaud, 1995). The formation of turbulent spots from localized perturbations for $Re_g < Re < Re_c$ has been investigated in channel and boundary layer flows (Henningson et al., 1993; Levin and Henningson, 2007). However, in these studies the chosen initial perturbations have simple shapes such as pulses, jets (Singer and Joslin, 1994), localized pairs of alternated vortices (Levin and Henningson, 2007) or rings (Suponitsky et al., 2005). Those perturbations could not guarantee a large energy growth as optimal perturbations; thus, they need very large initial amplitudes to achieve transition, largely outgrowing the transition thresholds sought for the considered flows. Thus, in order to accurately evaluate such energy thresholds for more realistic, localized perturbations, an energy optimisation encouraging the localization of perturbations would be more appropriate (Cherubini et al., 2010b; Monokrousos et al., 2010).

Recently, constrained optimisations of the p-norm of the disturbance energy have been used by Foures et al. (2013), with the aim of promoting localization of the optimal perturbation. Using higher-order norms as objective functions allows one to reduce the spatial extent of the optimal perturbation (Foures et al., 2013), revealing the existence of possible "hotspots" in the flow. This technique can be very useful for designing experimental set-ups, in which perturbations can be injected only locally, as well as control devices, in which a "minimal-energy" actuation is desired. Increasing the order of the energy norm in the objective function, the resulting optimal disturbance becomes more and more localized even for simple shear flows such as plane Poiseuille flow; whereas, for these parallel shear flows, a linear optimisation of the L_2-norm of the perturbation velocity vector always leads to spatially extended structures such as streamwise-invariant streaks. For plane Poiseuille flow, linear p-norm optimizations performed by Foures et al. (2013) in a two-dimensional framework have provided two types of localized optimal disturbances: one localized at the center of the channel and the other one at the wall, capable to extract energy from the base flow in two different ways. However, how p-norms behave in a three-dimensional flow configuration, in the presence of a strong transient non-local mechanism such as the lift-up effect (Landahl, 1980) was not yet been investigated. In particular, it was still not been established whether those localized linear optimals are indeed efficient in inducing subcritical transition, in terms of both time to transition and initial energy.

Recent studies have shown that, for simple shear flows, transition thresholds can be accurately determined by using energy optimisations including nonlinear effects (Cherubini et al., 2015; Duguet et al., 2010, 2013; Rabin et al., 2012). By this approach, the optimization procedure naturally leads to large-amplitude localized disturbances capable of producing a large energy growth due to nonlinear local effects. Nonlinear optimizations have been performed for pipe (Pringle et al., 2012; Pringle and Kerswell, 2010), boundary layer (Cherubini et al., 2015, 2010a, 2011b) and Couette (Cherubini et al., 2013; Duguet et al., 2013; Monokrousos et al., 2011; Rabin et al., 2012) flows. These authors optimize a functional linked to the turbulent dynamics, namely the perturbation kinetic energy (see Pringle and Kerswell (2010), Pringle et al. (2012), Rabin et al. (2012), Cherubini and De Palma (2013)) or the time-averaged dissipation (see Monokrousos et al. (2011) and Duguet et al. (2013)), including nonlinear terms into the optimization and thus following the evolution of the perturbation until transition is initiated. Optimizing for long times, and bisecting the initial energy, one can find the perturbation of minimal energy which brings the flow on the verge of transition (Cherubini et al., 2015; Duguet et al., 2013; Rabin et al., 2012). In fact, the amplification of such nonlinear optimal disturbances largely outgrows that of the linear optimals (Cherubini et al., 2011b; Pringle et al., 2012), leading to transition for lower values of the initial energy. However, it is still not clear how this large energy growth is linked to the shape and/or to the higher amplitude of the nonlinear perturbations. When comparing a linear (non-localized) and a nonlinear (localized) optimal perturbation having the same initial energy, not only the shape of the two optimals differs, but also their relative amplitudes, since the localization property of the latter induces larger velocity values for the same energy. A more appropriate comparison should make use of localized linear optimal perturbations, such as those obtained by a linear p-norm optimization (Foures et al., 2012).

In order to analyse and compare the structures and transition scenarios of localized disturbance, linear and nonlinear optimal perturbations in plane Poiseuille flow at subcritical values of the Reynolds number have been computed, and the results are shown in chapter II. The comparison of the different outcomes, in terms of energy growth and consequent transition, between the linear p-norm and the nonlinear energy optimization, allows us to analyze: i) the effects of nonlinearity in the localization of perturbations; ii) the relative importance of the shape and amplitude of different initial perturbations for inducing transition.

From this study it has been possible to recognise different kind of coherent structures involved in the transitional process. Their generation, instability, and sustainment mechanisms have been useful to explain many details of the dynamics of such flows. Tuning optimization parameters, two main kind of coherent structures have been identified, such as streaky structures and hairpin vortices, which have been observed experimentally and numerically in channel flows, pipe flows, and boundary-layer flows (Adrian, 2007; Matsubara and Alfredsson, 2001; Singer, 1996; Townsend, 1980; Wu and Moin, 2009a).

Streaky structures are observed at different scales in transitional and turbulent shear flows (Brandt et al., 2004; Hwang and Cossu, 2010b) and their origin seems now to be well understood. As conjectured by Landahl (1980) some decades ago, elongated near-wall zones of low or high momentum are created by a mechanism of transient growth of the perturbations known as lift-up effect. This mechanism is based on the transport of the mean shear by rolls of streamwise vorticity. The shape of these optimal perturbations corresponds well to the coherent structures found in transitional and turbulent flows in a low-to-moderate disturbance environment (Matsubara and Alfredsson, 2001). Thus, streaky structures can be explained as the projection of flow disturbances onto the linear optimal flow structure (Luchini, 2000).

Also the formation mechanism of hairpin vortices has been extensively studied. Wu and Moin (2009a) have analyzed the generation of hairpin structures from Λ shaped vortex structures induced in a boundary layer by the receptivity process from large amplitude free stream turbulence; Acarlar and Smith (1987) and Henningson et al. (1993) have studied the formation of hairpin vortices by localized disturbances in boundary-layer and channel flows, respectively. Suponitsky et al. (2005) have studied a simple model of interaction between a localized vortical disturbance and a uniform unbounded shear flow, showing that a small-amplitude initial disturbance always evolves into a streaky structure, whereas a large-amplitude one evolves into a hairpin vortex under some conditions. Furthermore, it is well established that hairpin vortices may appear as the consequence of the secondary instability and break-up of elongated streaks (Schmid and Henningson, 2012). These and many other studies indicate that, unlike streaky structures, hairpin vortices are generated through nonlinear interactions (Eitel-Amor et al., 2015). The fact that they naturally arise in many transitional and turbulent shear flows, as the consequence of the instability of streaks or induced by other causes (such as roughness elements or flow injection at wall) suggests the existence of a strong energy growth mechanism triggered by nonlinearity. Whether the hairpin vortex might be recognized as an optimal flow structure in a nonlinear energy growth process is the question we address in the chapter III. With this purpose, we perform nonlinear optimisations in a simple parallel shear flow such as the plane Poiseuille flow. As mentioned before, nonlinear optimisations in parallel shear flows have been already performed by Cherubini and De Palma (2013); Monokrousos et al. (2011); Pringle et al. (2012); Pringle and Kerswell (2010); Rabin et al. (2012) for pipe and Couette flow. In both cases the nonlinear optimal perturbations were found to induce strongly bent streaks, but hairpin vortices were never observed. However, in those works optimisations were performed for rather long target times, for which the lift-up mechanism dominates the dynamics, whereas Karp and Cohen (2014) provide the description of a nonlinear mechanism generating hairpin vortices acting on a time scale which is one order of magnitude smaller. In order to focus our optimisation analysis on the generation of the hairpin structure, we have chosen small target times ($\mathcal{O}(10\ h/U)$, h and U being the reference length and velocity, respectively) and finite amplitude initial perturbations to rapidly trigger nonlinear effects. In particular, the chosen time scale is typical of the Orr mechanism, much smaller than the typical scale of the lift-up one.

I.3 Bursts and large scale motion in turbulent shear flow

Turbulence is a widespread complex phenomenon influencing the behavior of a large variety of natural and engineering systems. Flow in a channel (Sano and Tamai, 2016), ocean mixing (Moum et al., 2013), and the explosion of a rotating massive star (Mösta et al., 2015) are three examples of very different phenomena characterized by turbulent dynamics involving chaotic fluctuations of the physical properties and sharing the same basic properties. The atmosphere itself, up to a hundred meters from the Earth's surface, is characterized by a turbulent, chaotic motion, whose deep knowledge and accurate modeling may have tremendous implications for improving meteorological and climatological predictions (Marusic et al., 2010). Yet, achieving a thorough comprehension of the dynamics of wall-bounded turbulent flow remains a formidable challenge since turbulence appears in a variety of different states and patterns competing with the ordered laminar state (Barkley et al., 2015; Barkley and Tuckerman, 2007; Tuckerman et al., 2014).

To determine low-order models for the onset of this chaotic motion from a laminar regime, recent studies have turned their attention to the dynamics of large scale structures, neglecting the random small scale motion: two main examples are the direct percolation model recently provided by Lemoult et al. (2016) and Chantry et al. (2017), and the front propagation scenario by Barkley et al. (2015), explaining the coexistence of turbulent patterns competing with the laminar state in the transitional regime.

Even when the flow reaches a fully developed turbulent regime, it remains characterized by small-scale chaotic fluctuations as well as *coherent structures*, i.e. fluid motions highly correlated over both space and time (Panton, 2001), with characteristic wavelengths and lifetimes. From a dynamical point of view, this coherent motion carries a much larger momentum than the chaotic motion at small scales; thus, a careful characterization of such structures bears an enormous potential for modeling and controlling the self-sustained turbulence dynamics.

The first evidence of coherent motion in turbulent flows dates back to the sixties, when Kline et al. (1967) ran a series of experiments in a boundary-layer flow, observing "*surprisingly well-organized spatially and temporally dependent motions*" in the form of streaks. These streaks populate the region close to the wall, the buffer layer representing the *inner region*, with an average spanwise spacing $\lambda_z^+ \approx 100$ (where the superscript $^+$ indicates variables expressed in inner units, non-dimensionalized by the viscous length scale $\delta_\nu = \nu/u_\tau$, ν being the kinematic viscosity and $u_\tau = \sqrt{\dfrac{\tau_w}{\rho}}$ the friction velocity, where τ_w is the shear stress given at the boundary.

Such streaky structures are continuously regenerated in a cycle based on the *lift-up* mechanism that does not depend on the outer flow, making them a robust, long-living feature of the inner layer (Hamilton et al., 1995; Jiménez and Pinelli, 1999; Waleffe, 1997). Concerning this regeneration cycle, a strong consensus has been achieved in the last years about the self-sustained process proposed by Hamilton et al. (1995) and Waleffe (1997). Based on modal and non-modal instability analysis, these authors conjectured a cyclic process composed of the following three steps: i) streamwise streak originate from weak streamwise vortices, due to the inherently non-modal *lift-up* process; ii) saturating nonlinearly, they become prone to secondary instability; iii) the consequent streaks oscillations recreate streamwise vorticity by nonlinear interactions, leading back to the first step. Such a self-sustained process can explain the robustness of oscillating streaky structures observed in transitional and turbulent flows. The extension of this theory led to the discovery of self-sustained exact coherent structures (Faisst and Eckhardt, 2003; Hof et al., 2004; Waleffe, 1998), which are steady, periodic or chaotic states of the phase space with few unstable directions, that populate the chaotic saddle representing wall turbulence at low Reynolds numbers (Faisst and Eckhardt, 2003; Hof et al., 2004; Waleffe, 1998).

Moreover, it has been also observed (Adrian, 2007; Tomkins and Adrian, 2003) that large-scale coherent structures populate the *outer region* of wall-bounded turbulent flows, with average spanwise length $\lambda_z \approx \mathcal{O}(h)$ (h being the outer length scale, for instance the half height of a channel flow or the boundary-layer thickness of the flow over a flat plate). These large-scale structures have the form of packets of hairpin vortices (Adrian, 2007) or large-scale oscillating streaks (Tomkins and Adrian, 2003). Hwang and Cossu (2010b) have recently shown that large-scale streaky structures remain self-sustained even when small-scale motion is artificially damped. This numerical observation has been supported by the results of a linear transient growth analysis of perturbations of a mean turbulent velocity profile, showing that large-scale streamwise streaks can be amplified by a *coherent lift-up* effect, without the need of smaller scale structures to sustain this growth (Cossu et al., 2009; Hwang and Cossu, 2010a; Pujals et al., 2009).

Chapter IV and V aim at investigating whether large-scale streaks can be optimally-growing in a nonlinear framework for a turbulent channel flow. Towards this aim, a fully 3D nonlinear optimization is used to maximize the energy of perturbations of the turbulent mean flow. The results of this nonlinear optimization allow us to show the presence of an optimally growing oscillating streaky motion at the outer scale in a turbulent channel flow at $Re_\tau = 590$. These optimal flow structures will be compared to those at $Re_\tau = 180$, in order to investigate the reason why the coherent structures observed in Direct Numerical Simulations (DNS) and experiments change their typical scale and shape when increasing Re_τ.

These results suggest a scenario based on self-sustained cycles acting at different spatial scales from the inner to the outer scale. Nevertheless, this is only a part of the complex dynamics of wall turbulence, in which inner and outer scale structures are found to influence each other, as recently shown by Hwang et al. (2016a), who observed a close interaction between large-scale coherent structures and near-wall small-scale streaks. In fact, the coexistence of separate cycles at different scales does not explain the spatial and temporal intermittency of large-scale velocity fluctuations and their possible interaction with inner-scale structures (Hwang et al., 2016a; Jiménez, 1999), neither the existence of the high-energy *bursting* events, inherently short-lived and intermittent (Jiménez et al., 2005), recurrently observed in wall-bounded turbulent flows.

Bursting events are dynamically very important since they carry about 80% of the Reynolds stress production (Panton, 2001), accounting for a large part of the energy transported through the flow. To characterize these vigorous events, quadrant analysis of time series data have been used, showing a sequence of Q2 ($u < 0$, $v > 0$) events called *ejections* (i.e., slow fluid carried up by a positive wall-normal motion), suddenly followed by rather longer Q4 ($u > 0$, $v < 0$) events known as *sweeps* (high-speed fluid pushed down towards the wall) (Bogard and Tiederman, 1986). Very recently, using a filtered and over-damped large-eddy simulation (LES), Hwang and Bengana (2016) observed the occurrence of bursting event for isolated attached eddies of different size, the related spanwise length scale ranging between $\lambda_z^+ \approx 100$ and $\lambda_z \approx 1.5h$. Therefore, these energy oscillations are inherently present in the coherent motion of a fully turbulent flow even when small-scale fluctuations are damped out.

However, despite the robustness of bursts and their main features are now well recognized, their origin is still not clear. Some authors have linked them to the secondary instability of streaks; others, to the appearance of *hairpin-shaped* vortical structures (Moin and Kim, 1985), which can regenerate into packets populating the outer region of the flow (Robinson, 1991), in the same way as streaks populate the buffer layer. Recently, Jiménez has investigated by a linear analysis the role of the Orr mechanism in the bursting phenomenon (Jiménez, 2013, 2015), showing that large-scale modes of the wall-normal velocity in a turbulent minimal channel are well described by transient Orr bursts only at short times (order $0.15h/u_\tau$), whereas at longer times nonlinearity becomes relevant.

Chapter IV aims also at providing a thorough view of energetic structures in wall-bounded turbulent flow, explaining the recurrence of bursting events as an interaction between streaky and vortical structures at different scales. The final goal is to investigate whether the formation of transient coherent structures inducing bursting events in a wall-bounded turbulent flow is governed by an energy maximization process on a suitable time scale. Being bursts short-lived and highly energetic, we use a transient growth approach in a nonlinear framework in order to unravel which kind of flow structures are able to trigger rapid events with a strong energy growth in a canonic wall-bounded turbulent flow such as the channel flow. In the same way as a linear transient growth analysis on a mean turbulent profile could explain the linear growth of streaky structures in turbulent flows

(Butler and Farrell, 1993; Pujals et al., 2009), a nonlinear approach is a suitable way for studying the energetic transient events characterized by ejections and sweeps. With respect to the recent linear analysis provided by Jiménez (2013, 2015), we take into account nonlinear interactions since the time horizon of the optimization analysis is larger than the linear time interval limit indicated by Jiménez (2015).

I.4 Dynamical systems and transition to turbulence

In contrast with traditional claiming that turbulence should be studied by statistical tools (Kim et al., 1987), a new perspective has been considered, assuming that turbulence could be described as deterministic chaos in the framework of dynamical systems theory (Eckhardt et al., 2008, 2007b; Kerswell, 2005), even if there is a wide gap between the classical low-dimensional chaotic systems theory and the very high degree-of-freedom dynamics of turbulent flows. In this context, the understanding of transitional and turbulent flows has been boosted by the discovery of the first nonlinear equilibrium and periodic solutions of the full Navier-Stokes equation (Gibson et al., 2009; Nagata, 1990). With the improvement of the computational resources, it has been possible to compute an increasing number of these nonlinear unstable invariant solutions in several flow systems (Kawahara et al., 2012). It has turned out that they are significant for a theoretical description of not only transition to turbulence but also fully turbulent flow (Hwang et al., 2016b; Park and Graham, 2015; Rawat et al., 2015, 2016; Sasaki et al., 2016; Yasuda et al., 2014).
Apply dynamical systems theory to fluid flow simulations means to consider the state space of the system as the space of all velocity fields that fulfil the boundary conditions and the incompressibility condition.
In this framework the turbulent region of state space is populated by numerous invariant solutions, immersed in a web of homoclinic and heteroclinic connections (Halcrow et al., 2009; Hof and Budanur, 2017; Toh and Itano, 2003; van Veen and Kawahara, 2011). A turbulent trajectory in the state space performs a walk through this forest, where it transiently approaches an invariant solution, and stays in its neighbourhood for some time before being pushed away along an unstable direction, then approaching another solution (Kawahara et al., 2012). Thus, organized structures appear when a turbulent state approaches such invariant solutions. Of those structures captured by fully nonlinear non-trivial exact coherent states, most of them are composed of streamwise vortices and streaks (Gibson et al., 2009), and are related to the self-sustained process (Waleffe, 1997). However, another relevant coherent structure often observed in transitional and turbulent flows, namely the hairpin-vortex structure, has not yet been directly related to exact coherent states in the form of nonlinear fixed points or periodic orbits. Moreover to those structures a precise place in this dynamical system view of turbulence has not been given yet.
This may indicate that these recurrent vortices do not constitute an element of the self-sustained mechanism and that they might be linked to the passage from one equilibrium state to the other. Many numerical and experimental studies report strong energetic events, i.e. bursts (Adrian, 2007; Farano et al., 2017) associated with the onset of hairpin vortices. This observation leads to the idea that hairpin structures might be linked to a state space trajectory leaving an exact coherent state in a direction of strong energetic

growth, which could be the unstable eigendirection, as previously described as a usual scenario of trajectories that leave a state and approach another invariant state. According to this idea, hairpin-vortices should have been found following unstable directions of some invariant solutions. But once again, no evidence of this has been provided.

Starting from the idea that the flow cannot spend an infinite time close to an invariant solutions, so that unstable directions might not be relevant (exponential growth), an alternative direction in the stable manifold providing a large energy growth at short time due to the non-normality of the Navier-Stokes operator (Farrell, 1988) could give an answer to this problem. This possibility has not been investigated yet, leaving as an open question the representation of hairpin vortices in the dynamical systems framework. In chapter VI we try to investigate whether this is the case or not.

This is not the only possible scenario. The overall picture of the dynamical-system description of turbulence is based on the idea that paths connecting invariant solutions provide the route for the system to wander from one state to another. The dynamics may shadow heteroclinic connections between exact coherent states (Halcrow et al., 2009; Kawahara et al., 2012). Thus with the dynamical systems picture of turbulence in mind, it is important to study such connections. Computationally, this remains a hard task.

Halcrow et al. (2009) have computed heteroclinic connections in plane Couette flow, and in the same system, even a homoclinic tangle has been explicitly calculated by van Veen and Kawahara (2011). Traces of the presence of possible heteroclinic and homoclinic connections have been shown by Toh and Itano (2003) in plane Poiseuille flow, by Kreilos et al. (2013) in the asymptotic suction boundary layer and recently by Hof and Budanur (2017) in the pipe flow (Duguet et al., 2008a,b). Nevertheless, a robust method for computing those objects for the fluid dynamics equations has never been given. For this purpose, an efficient method for computing heteroclinic connection is proposed in chapter VII (also suitable for applications on general infinite dimension dynamical system) based on nonlinear optimization methods (Cherubini et al., 2010a; Monokrousos et al., 2011; Pringle and Kerswell, 2010). The method is applied to the study of plane Couette flow to have a direct comparison with previous results of Halcrow et al. (2009), discovering new connections that were not found by existing algorithms. Moreover the choice of this particular flow case is also motivated by the fact that a larger number of invariant solutions exist and are easily accessible (Gibson, 2014).

Chapter II

Subcritical transition scenarios via linear and nonlinear localized optimal perturbations in plane Poiseuille flow

Contents

II.1 Introduction **11**
II.2 Problem formulation **12**
  II.2.1 The optimization problem 13
II.3 Results **13**
  II.3.1 Optimal perturbations 14
  II.3.2 Transition mechanisms 22
II.4 Conclusions **33**
II.5 Appendix **34**

II.1 Introduction

Subcritical transition in plane Poiseuille flow is investigated by means of a Lagrange-multiplier direct-adjoint optimization procedure with the aim of finding localized three-dimensional perturbations optimally growing in a given time interval (target time). Space localization of these optimal perturbations (OPs) is achieved by choosing as objective function either a p-norm (with $p \gg 1$) of the perturbation energy density in a linear framework; or the classical (1-norm) perturbation energy, including nonlinear effects. Notice that the 1-norm of the energy density corresponds to the 2-norm of the velocity field, whereas the ∞-norm of the energy, corresponds to the maximum value of the local energy. In this chapter we aim at analyzing the structure of linear and nonlinear localized OPs for Poiseuille flow, and compare their transition thresholds and scenarios. The nonlinear optimization approach provides three types of solutions: a weakly nonlinear, a hairpin-like and a highly nonlinear optimal perturbation, depending on the value of the initial energy and the target time. The former shows localization only in the wall-normal direction, whereas the latter appears much more localized and breaks the spanwise symmetry found at lower target times. Both solutions show spanwise inclined vortices and large values of the streamwise component of velocity already at the initial time. On the other hand, p-norm optimal perturbations, although being strongly localized in space, keep a shape similar to linear 1-norm optimal perturbations, showing streamwise-aligned vortices characterized by low values of the streamwise velocity component. When used for initializing direct numerical simulations, in most of the cases nonlinear OPs provide the most efficient route to transition in terms of time to transition and initial energy, even when they are less localized in space than the p-norm OP. The p-norm OP follows a transition path similar to the oblique transition scenario, with slightly oscillating streaks which saturate and eventually experience secondary instability. On the other hand, the nonlinear OP rapidly forms large-amplitude bent streaks and skips the phases of streak saturation, providing a contemporary growth of all of the velocity components due to strong nonlinear coupling.

II.2 Problem formulation

We consider the incompressible flow driven by a constant pressure gradient between two plates, known as the plane Poiseuille flow. Nondimensional variables are chosen such that half the distance between the plates is $h = 1$ and the centerline velocity of the laminar flow is $U_c = 1$. The dynamics of such a flow is governed by the Navier–Stokes (NS) equations:

$$\frac{\partial U_i}{\partial x_i} = 0, \tag{II.1}$$

$$\frac{\partial U_k}{\partial t} + \frac{\partial (U_k U_j)}{\partial x_j} + \frac{\partial P}{\partial x_k} - \frac{1}{Re}\frac{\partial^2 U_k}{\partial x_j^2} = 0, \tag{II.2}$$

where t is the time, Re is the Reynolds number, P is the pressure, $\mathbf{U}$ is the velocity vector having components U, V, W, $\mathbf{x}$ is the position vector in space having components x, y, z: x for the streamwise direction, y for the wall-normal direction, and z for the spanwise direction. With the aforementioned normalization, the laminar-flow solution is given by the following parabolic profile:

$$\overline{U} = y(2-y); \quad \overline{V} = 0; \quad \overline{W} = 0. \tag{II.3}$$

This velocity profile is considered as the base flow, $(\overline{U}_i, \overline{P})$, onto which finite amplitude perturbations, (u_i, p), are superposed. The evolution of these perturbations is governed by the Navier-Stokes equations written in perturbative formulation, which are solved imposing Dirichlet boundary conditions for the three velocity components at the y-constant boundaries, whereas periodicity of the perturbation is prescribed in the spanwise and streamwise directions. All computations have been performed at $Re = 4000$. If not specified, the streamwise and wall-normal dimensions of the domain are equal to 2π and 2, respectively, whereas the spanwise domain length is equal to π. Notice that, for validation purposes, we have chosen the same Reynolds number and the same streamwise and wall-normal domain dimensions employed by Foures et al. (2013) in a two-dimensional framework. The chosen domain is discretized using a $300 \times 100 \times 120$ grid points using a staggered grid and the Navier–Stokes equations are solved by a fractional-step method with second-order accuracy in space and time (Verzicco and Orlandi (1996)).

II.2.1 The optimization problem

The optimization procedure employed in the present analysis aims at computing the velocity perturbation at $t = 0$ providing the maximum value of the objective function at a given target time, T_{opt}. The chosen objective function is the ratio between the p-norm of the energy density, E_p, measured at target time T_{opt}, and the initial energy $E(0)$, where:

$$E_p(t) = \left(\frac{1}{V} \int_V (e\,(t))^p \, dV \right)^{1/p} = \left(\frac{1}{V} \int_V \left(\frac{1}{2} u_i u_i\,(t) \right)^p dV \right)^{1/p} \tag{II.4}$$

is the p-norm of the energy density and

$$E(0) = \frac{1}{V} \int_V \frac{1}{2} u_i u_i\,(0)\, dV \tag{II.5}$$

is the initial energy.

For $p = 1$, the classical definition of the energy density (often called 1-norm in this chapter) is recovered. As discussed by Foures et al. (2013), increasing the value of p, the optimal perturbation will be more and more localized in a limited region of the domain with a higher energy density. It is worth noting that a similar localization effect has been recovered in previous works based on a nonlinear optimization procedure, using the 1-norm of the energy density as objective function Cherubini et al. (2011b); Monokrousos et al. (2011); Pringle et al. (2012).

The optimization problem is subject to partial differential constraints (Pinnau and Ulbrich, 2008), namely the perturbative NS equations. For nonlinear optimization, the initial value of the energy density is imposed ($E(0) = E_0$). This choice is motivated by the possibility of comparing the results with the 1-norm optimization having the same initial energy. In order to optimize the chosen objective function subject to these constraints, a *Lagrange multiplier technique* is used (see Zuccher et al. (2004)). The method consists of adding these constraints to the objective function via scalar product with the Lagrange multipliers (or adjoint variables) $(u_i^\dagger, p^\dagger, \lambda)$, yielding an *augmented functional* provided in the appendix II.5. This functional is then derived with respect to the direct and adjoint variables, leading to the adjoint equations, as well as the compatibility conditions, which are responsible for the localization of the optimal perturbation when the p-norm of the energy density is used as objective function (see the discussion in II.5). These equations are solved by using an iterative procedure based on the successive integration of the direct and adjoint equations, coupled with a *gradient-based methods* as discussed in more detail in II.5. Convergence is attained when the variation of the objective function between two successive iterations is smaller than a chosen threshold, chosen equal to $\epsilon = 10^{-5}$.

II.3 Results

The linear and nonlinear optimization procedures described above have been employed to study subcritical transition in plane Poiseuille flow at $Re = 4000$. Linear and nonlinear optimal perturbations with $p = 1$ will be presented in subsection II.3.1.1. Then, in subsection II.3.1.2, the value of p will be increased, and the linear p-norm optimal perturbations will be discussed and compared with the previous ones.

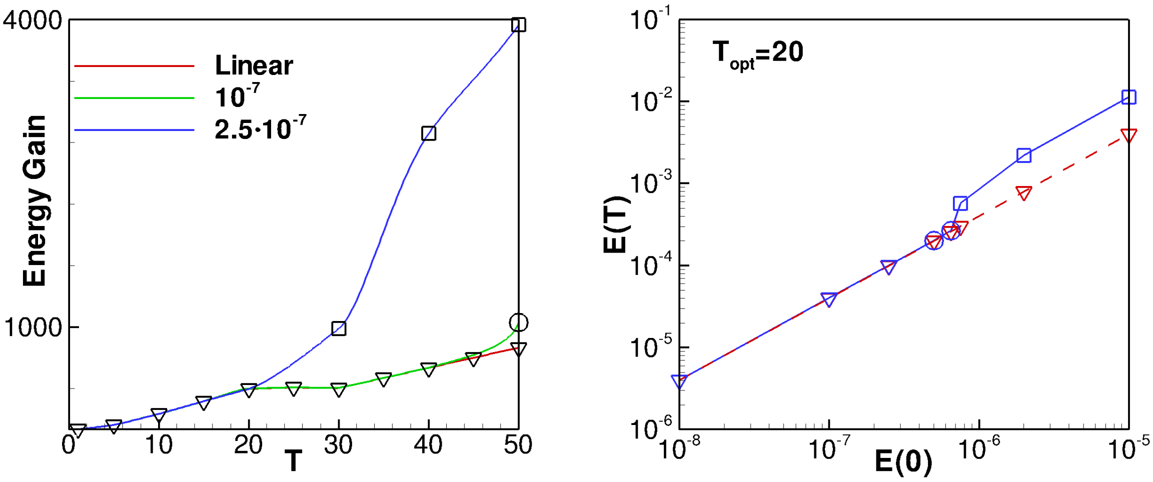

Figure II.1: (a) Optimal energy gain curve versus target time obtained with linear (red line) and nonlinear $1-norm$ optimization with initial energy $E_0 = 10^{-7}$ (green line) and $E_0 = 2.5 \times 10^{-7}$ (blue line). (b) Optimal energy at target time versus initial energy for $T_{opt} = 20$. The different shapes of the symbols indicate different types of optimal solutions resulting from the optimisation at the chosen T_{opt} and E_0: triangles for linear optimals, circles for weakly non linear and squares for highly nonlinear optimals.

To allow a meaningful comparison between linear and nonlinear results, the work will focus on rather small target times, $T_{opt} < 50$. However, as discussed in section II.3.1.1, the results at the considered target times appear representative of the dynamics that can be found at larger times.

II.3.1 Optimal perturbations

II.3.1.1 Nonlinear 1-norm optimization

Nonlinear optimisations have been performed for several initial energies in the range $[10^{-8}, 10^{-5}]$, and for several different target times, $T_{opt} = 10, 15, 16, 18, 20, 30, 40, 50$ (for the largest ones, the value of the initial energy has been limited to 10^{-6} in order to avoid transition at the target time, allowing convergence of the optimization algorithm). Figure II.1 (a) provides the optimal energy gain computed for several target times by means of linear (red line) and nonlinear (green and blue lines) 1-norm optimizations using two different values of the initial energy. The three curves demonstrate the strong increase of the energy gain due to nonlinear effects, for sufficiently large target times and initial energies. The strong effect of the initial energy on the resulting energy gain can be also observed in Figure II.1 (b), providing the energy at target time versus the initial energy obtained with a nonlinear optimisazion for $T_{opt} = 20$. The chosen values of T_{opt} and E_0 strongly influence also the shape of the resulting optimal perturbations; in particular by changing T_{opt} and E_0, we have found four families of optimal perturbations, which are represented by different symbols in figures II.1 (a-b) as well as in figure II.2. The different shapes of the four types of optimal perturbations are shown in the bottom subframes of figure II.2 for comparison purposes, using the iso-surfaces of the Q-criterion (

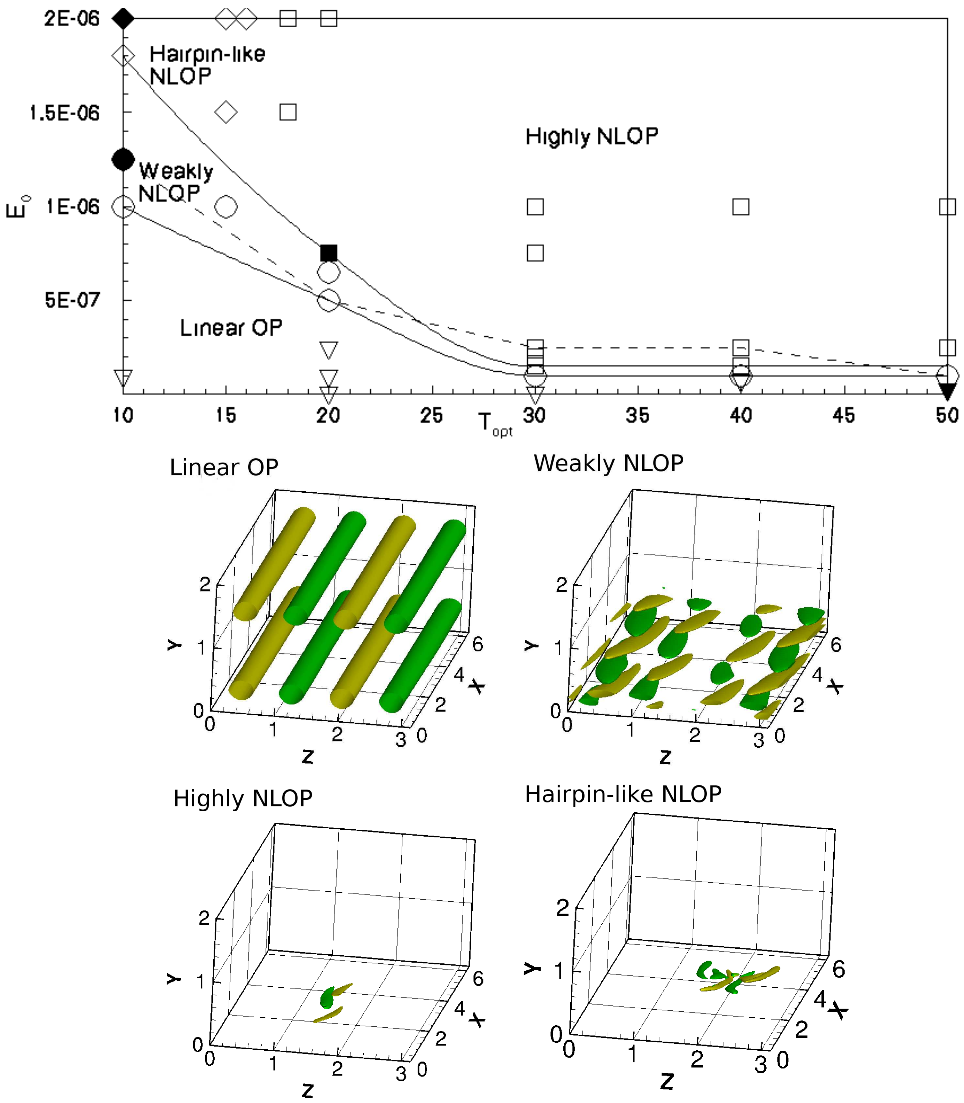

Figure II.2: Different families of optimal perturbations on the plane T_{opt} and E_0 for p=1. In the top frame, the symbols indicate the different types of optimal solutions resulting from the optimisation at the chosen T_{opt} and E_0: triangles for linear optimals; circles for weakly nonlinear; squares for highly nonlinear optimals; and diamonds for hairpin-like optimals. The solid lines indicate the energy thresholds for shape modification. In the bottom frames, the linear, weakly nonlinear, highly nonlinear, and hairpin-like optimal solutions (from left to right) are represented using iso-surfaces of the Q-criterion, coloured in yellow/green for positive/negative values of the streamwise vorticity, respectively. The optimal solutions shown are the ones represented by full symbols in the top frame. The dashed line represents the transition thresholds for the nonlinear optimals given in table II.2.

$Q = \frac{1}{2}(||\Omega||^2 - ||S||^2)$, Ω and S being the vorticity tensor and the rate-of-strain tensor, respectively, according to Hunt et al. (1988)). The first one (first subframe from the left, represented by triangles in the top frame) corresponds to the *linear* optimal perturbations (LOP), which is also obtained by nonlinear optimisations for sufficiently small values of $E(0)$. The second type, shown in the second subframe and represented by circles in the top frame of figure II.2, is labeled *weakly nonlinear* optimal perturbation (WNLOP), and it is found for increasing values of $E(0)$. This optimal solution shows a localization only in the wall-normal direction. Increasing the initial energy for $T_{opt} \geq 18$ we have found optimal solutions of the third family, the *highly nonlinear* optimal perturbations (HNLOP), shown in the third subframe and represented by squares in the top frame of figure II.2. These solutions are localized in the three spatial directions and do not present any symmetry. Finally, for large values of $E(0)$ and very small target times ($T_{opt} < 18$), we obtain *hairpin-like nonlinear* optimal solutions (see also Farano et al. (2015), chapter III), shown in the fourth subframe and represented by diamonds in the top frame of figure II.2, so called because they are able to generate hairpin vortices at the target time. The latter type of nonlinear optimal perturbation is associated with very large values of the initial energies, much larger than the transition threshold energy characterizing the other types of perturbations. In the following we will analyze in detail the weakly and highly nonlinear optimal perturbations, whereas for further details about the hairpin-like optimal solution the reader is referred to Farano et al. (2015) (chapter III). Moreover, figure II.2 provides in solid lines the approximate threshold energy values for which the shape of the perturbation changes from one family to the other. As one can observe in figure II.2, these energy thresholds vary strongly for a small target time, and converge towards a constant values for $T_{opt} \geq 30$. This result has motivated our choice to limit T_{opt} to a maximum value of 50. For comparison purposes, we have represented by the dashed line the threshold energy at which the computed nonlinear optimal perturbations are able to lead the flow to transition (see also the values in table II.2 and the related comments in subsection II.3.2). One can observe that, at the transition threshold, the OP are either of weakly nonlinear or highly nonlinear type, depending on the target time, so that the transition threshold does not correspond to any of the shape-associated thresholds represented by the solid lines. Remarkably, linear OP are not found to induce transition for the initial energy at which they are obtained by the optimisation, even when noise is added to the initial perturbation field (see the discussion in subsection II.3.2).

The weakly nonlinear optimal solution is shown at initial time in figure II.3 (a), for $T_{opt} = 10$, $E_0 = 1.25 \times 10^{-6}$, and in figure II.3 (c) for $T_{opt} = 20$, $E_0 = 6.5 \times 10^{-7}$. Such a solution shows a space localization in the wall-normal direction with respect to a linear optimal perturbation which instead occupies both the walls of the channel. One can observe that both initial optimal solutions shown in figures II.3 (a) and (c), as well as their evolution at target times (figures II.3 (b) and (d)) are localized on one of the two walls. Moreover, their shape is quite different from the linear optimal perturbations found by Butler and Farrell (1992), which are characterized by streamwise-aligned vortices. In fact, weakly nonlinear optimal solutions are characterized by alternated vortices inclined with respect to the streamwise direction, which lay on the flanks of a region of negative streamwise velocity disturbance. The vortices are inclined with respect to the mean flow, both in the wall-normal and in the spanwise direction. The upstream tilting with respect to the wall-normal direction is linked to the Orr mechanism (Orr, 1907) already

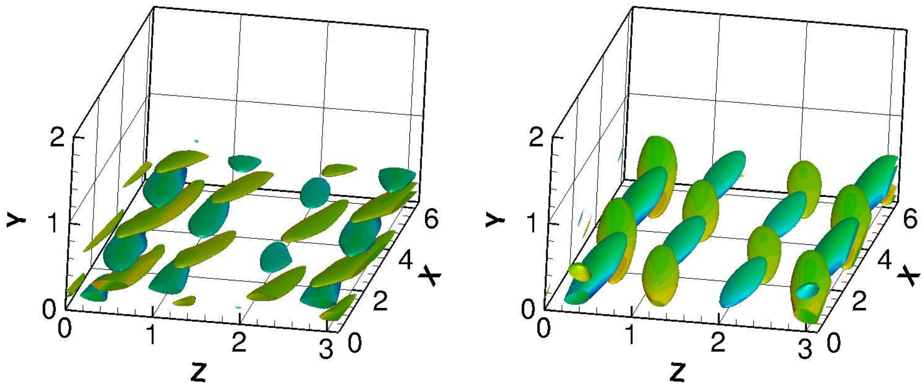

(a) t=0 (b) t=10

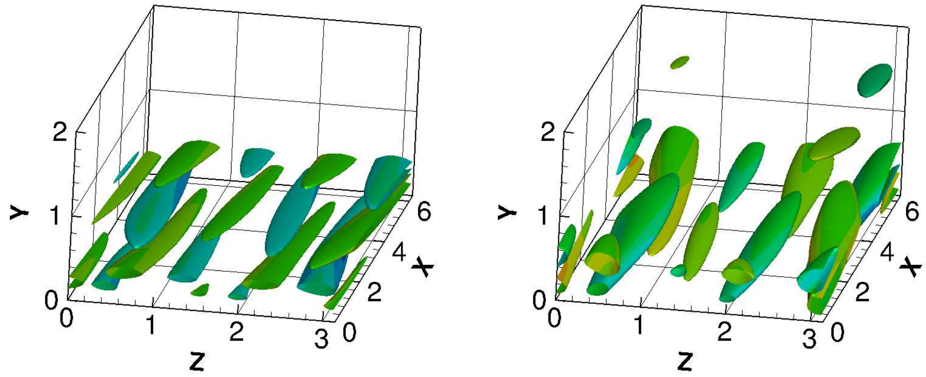

(c) t=0 (d) t=10

Figure II.3: Shape of the nonlinear 1-norm optimal perturbation (WNLOP solution) for (a) $T_{opt} = 10$, $E_0 = 1,25 \times 10^{-6}$ and (b) $T_{opt} = 20$, $E_0 = 6.5 \times 10^{-7}$. Isosurfaces of the Q-criterion at $t = 0$, $Q = 0.000195$ (a), $Q = 0.00011$ (c) and (b,d) at $t = T_{opt}$ ($Q = 0.011$ (b), $Q = 0.003$ (d)). The isosurfaces are colored by contours of streamwise vorticity.

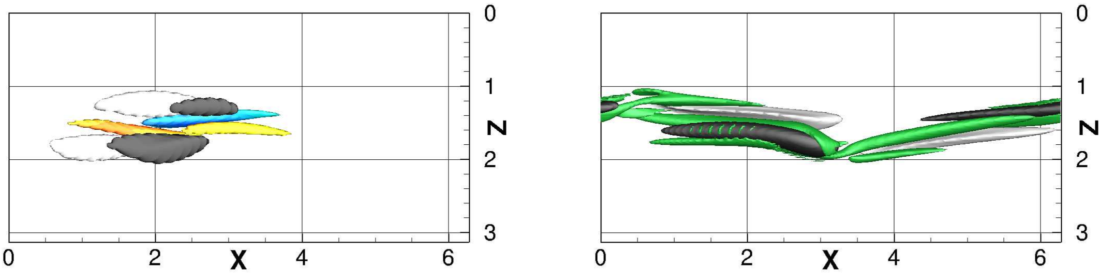

(a) t=0 (b) t=20

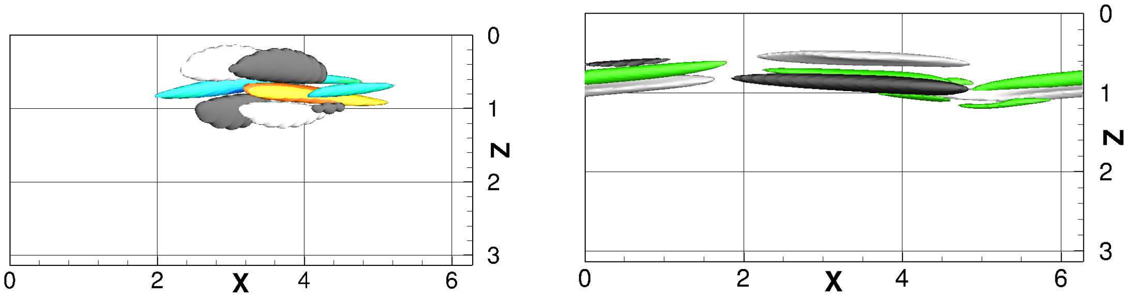

(c) t=0 (d) t=30

Figure II.4: Nonlinear 1-norm optimal perturbation (HNLOP solution) for (a,b) $T_{opt} = 20$ and $E_0 = 7,5 \times 10^{-7}$; (c,d) $T_{opt} = 30$ and $E_0 = 2.5 \times 10^{-7}$. Isosurfaces of the Q-criterion (colored) and of the streamwise velocity disturbance (light grey for positive and black for negative values) at (a) t=0 ($Q = 0.005$, $u = \pm 0.07$), (b) t=20 ($Q = 0.2$, $u = \pm 0.2$), (c) t=0 ($Q = 0.002$, $u = \pm 0.04$), and (d) t=30 ($Q = 0.1$, $u = \pm 0.15$). The Q-criterion surfaces are colored by contours of the streamwise vorticity.

observed in the linear case, whereas the spanwise tilting is not found in the linear case. However, the spanwise inclination of the initial vortices is a common feature of nonlinear optimal perturbations in shear flows, such as the ones found in the Blasius boundary-layer (Cherubini et al., 2011b), the Couette (Cherubini and De Palma, 2013), and the asymptotic suction boundary layer flow (Cherubini et al., 2015). One can also notice in figure II.3 that, increasing the target time, the vortices elongate in the streamwise direction, without loosing their spanwise inclination. Thus, this first type of nonlinear optimal structure appears to break the wall-normal symmetry of the base flow, providing the first effects of localization induced by nonlinearity.

As shown in figure II.2, increasing the target time as well as E_0, the HNLOP is obtained. Figure II.4 demonstrates that this optimal perturbation does not present any symmetry; it is characterized by localized staggered-inclined vortices on the flanks of packets of large streamwise velocity perturbation. Such a structure recalls the sinuous localized oscillation of streaks, as well as the nonlinear optimal solution also found for a Couette flow by Cherubini and De Palma (2013); Cherubini et al. (2013); Duguet et al. (2013); Monokrousos et al. (2011); Rabin et al. (2012). This solution is quite different from the weakly nonlinear one, mostly for its strong spatial localization in the streamwise and spanwise directions. In fact, all of the velocity components decrease of two orders of magnitude in the x and z directions going from the perturbation towards the boundaries of the computational domain. Further increasing the initial energy and/or the target

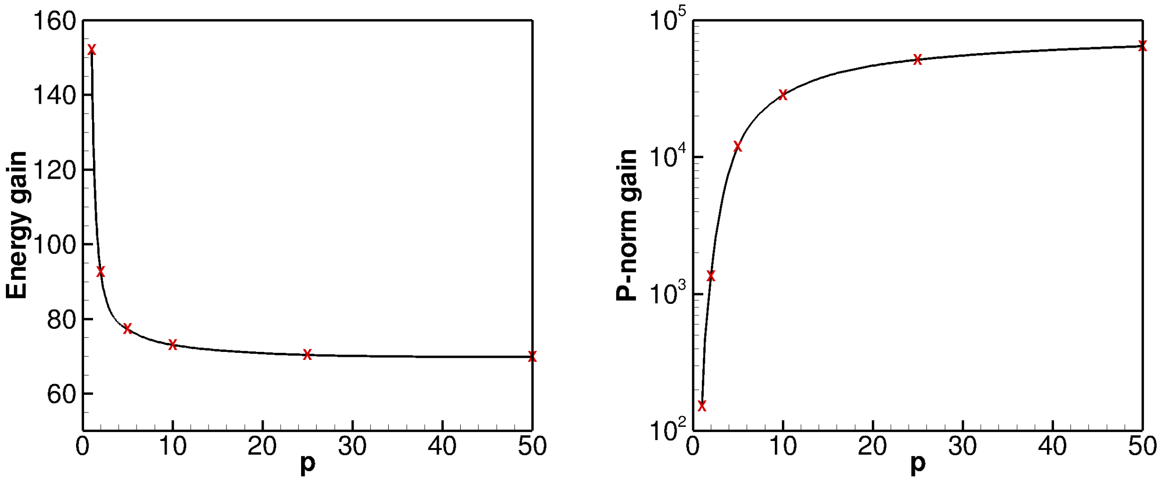

(a) Energy gain (b) P-norm gain

Figure II.5: (a) Energy gain and (b) p-norm gain as a function of p for $T_{opt} = 10$. Each symbol (x) represents an optimization.

time, the optimal perturbation maintains a similar basic structure, as one can observe in figure II.4 (c,d) for $T_{opt} = 30$. It is noteworthy that the same localized structure is found for a larger domain length, although it can be replicated several times in the spanwise or in the streamwise direction, for large initial energies.

II.3.1.2 Linear p-norm optimization

In the previous section we have discussed the progressive localization of the optimal perturbations when increasing the target time and the initial energy, for a nonlinear optimization of the energy gain. In this section we aim at investigating the effect of increasing the energy norm order, p, on the shape and amplitude of the optimal disturbance. We will discuss analogies and differences between the nonlinear 1-norm optimals and the linear p-norm optimal perturbations in order to uncover the basic mechanisms of energy amplification in linear and nonlinear framework, for three-dimensional Poiseuille flow.

Figure II.5 provides the distribution of the energy gain and of the p-norm gain ($E_p(T_{opt})/E_0$) versus the value of p, for $T_{opt} = 10$. When p is increased, the energy gain decreases (left frame), since it is not the objective function of the optimization process. On the other hand, the p-norm gain increases with p (right frame), saturating for large values of the norm order. A similar behavior has been found also for larger target times, the p-norm gain converging toward a constant value for $p \to 50$. Thus, the largest value of p used here, $p = 50$, can be considered representative for maximizing the p-norm gain (as also concluded by Foures et al. (2013) for the two-dimensional case).

In a two-dimensional framework, p-norm optimizations have been found very sensitive to the initialization of the optimisation procedure. By changing the initial guess, Foures et al. (2013) found two different p-norm optimal solutions: one was localized at the center of the channel whereas the other was localized along one of the walls. Thus, following Foures et al. (2013), we have used random noise perturbation localized in several

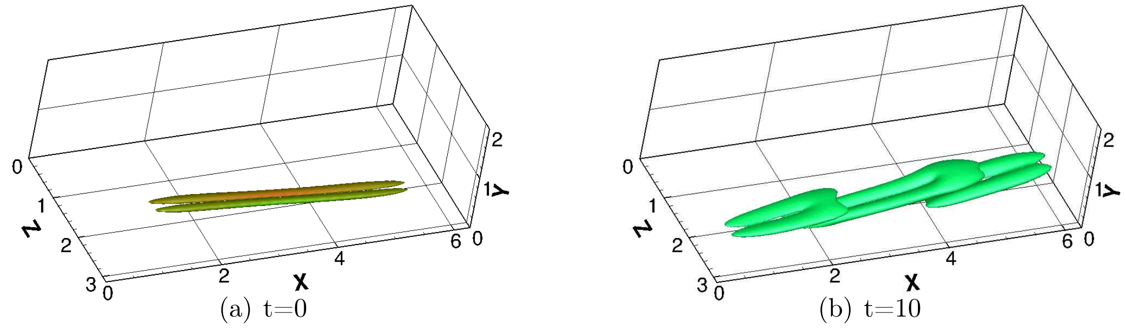

(a) t=0 (b) t=10

Figure II.6: 50-norm linear optimal perturbation for $T_{opt} = 10$. Isosurfaces of Q-criterion ($Q = 0.01$) at (a) $t = 0$ and (b) $t = 10$. The isosurfaces (a) are colored by contours of the streamwise vorticity.

zones of the domain to initialize the computations. In particular, the localization of the initial guess has been obtained by multiplying a perturbation field of white noise by the function $f(x_i) = (x_i - x_i^+)^2(x - x_i^-)^2 \exp((x_i - x_i^c)^2/\sigma)$ where $x_i^{+,-}$ indicate the maximum/minimum value of the selected spatial coordinate, x_i^c is the point at which we choose to localize the perturbation, and σ is its chosen length. This procedure has been validated by performing optimisations in a two-dimensional framework, reproducing exactly the two types of p-norm optimals found by Foures et al. (2013). However, for three-dimensional perturbations, we have found only one type of solution, independent of the initialization of the optimization process. This optimal solution is also very robust with respect to changes of the parameter p. In fact, the same localized solution is found already for $p = 2$, the only difference with respect to the one found for $p = 50$ being the values of the velocity components. In all cases, the shape of the disturbance slightly varies as long as $p \geq 2$. This is probably due to the existence, in three space dimensions, of the lift-up mechanism, which is a very powerful mechanism dominating the perturbation growth.

The optimal 50-norm perturbation obtained for $T_{opt} = 10$ is shown in figure II.6. It is characterized by a pair of vorticity tubes, highly localized at one wall and tilted upstream. These vorticity tubes do not show any inclination in the spanwise direction, unlike the highly nonlinear optimal solution; however, both solutions are characterized by very thin vortices tilted upstream. At target time, after tilting, the vortices connect each other, creating a “tooth” structure that resembles a “linear” precursor of a hairpin vortex. However, since nonlinearity is necessary to sustain hairpin structures, at larger times this “tooth” structure relaxes towards a pair of streamwise vortices inducing streamwise streaks, as it will be shown in the next section.

Increasing the target time, we obtain a larger energy gain, as one can observe in figure II.7, providing the time evolution of the energy gain (a) and of the p-norm gain (b) for three different target times obtained using the linearized Navier-Stokes equations (compare with the values shown in figure II.1 for the 1-norm linear and nonlinear case). Moreover, as shown in figure II.8, for an increase of the target time the localized perturbation increases its streamwise length. This is due to the fact that the only energy growth mechanisms in a linear framework are the Orr and the lift-up effects: for the former to reach the maximum energy growth at a larger time, the structure must be longer to complete the

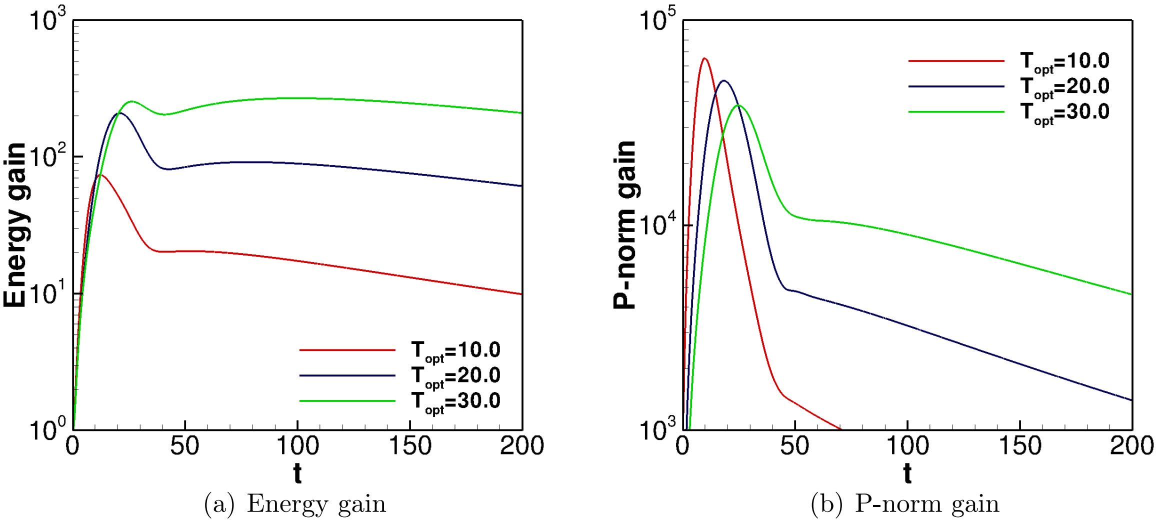

(a) Energy gain (b) P-norm gain

Figure II.7: Evolution in time of the energy and 50-norm gain for the linear 50-norm optimal perturbation with three different optimization time.

tilting in a longer time (compare figure II.8 (a) with figure II.6 (a)). This elongation of the perturbation is linked to a decrease of the optimal p-norm gain, shown in figure II.7 (b), as well as to an increase of the energy gain (due to the formation of larger-amplitude streaks). This indicates that the p-norm optimization is well adapted to compute localized optimal disturbances only for sufficiently small values of the target time, at least in the case of shear flows for which the lift-up effect is strong. Concerning the influence of the domain length, optimizations performed for $T_{opt} = 20$ using a double streamwise domain length (see figure II.8 (b)) further confirm that the elongation of the structures is not due to interactions of the vortices with their own tail. We can conclude that the basic shape of this p-norm optimal structure is almost independent of both the target time and the length of the domain, except for the increase of its streamwise length with the target time. Thus, as it could be anticipated, the p-norm optimals do not show similarities with the nonlinear ones, except for their strong localization, since the absence of nonlinear terms in the optimization loop inhibits nonlinear typical features such as the spanwise inclinations of the vortices. These differences are reflected also in the relative amplitudes of the velocity components. Tables II.1 provides the maximum absolute values of the three velocity components for the 50-norm linear and the 1-norm nonlinear perturbations for $T_{opt} = 20$, $E_0 = 5 \times 10^{-7}$ (left columns) and $E_0 = 7.5 \times 10^{-7}$ (right columns). Remember that the linear optimal solutions are simply scaled by E_0 for comparison purpose, since the linear optimization procedure is independent of the value of the initial energy. The WNLOPs (second column) show values of v and w one order of magnitude lower than the ones obtained in the case of the p-norm LOP computed for the same target time. Although surprising, these lower values can be easily explained by noticing that the p-norm linear optimal is much more localized than the weakly nonlinear ones. For the HNLOP, the maximum amplitudes tend to increase (right column), due to the stronger localization of the flow structures. However, one can notice that the relative amplitudes of the velocity components are different: in the linear p-norm case v and w have similar

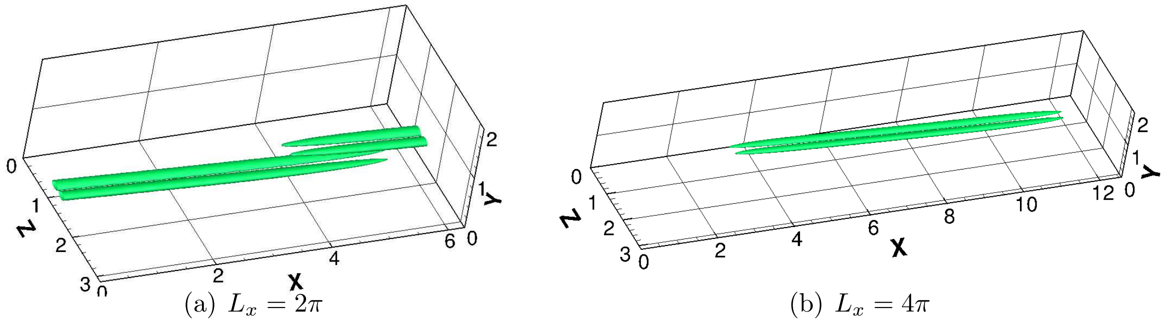

(a) $L_x = 2\pi$ (b) $L_x = 4\pi$

Figure II.8: 50-norm linear optimal perturbation for $T_{opt} = 20$ and (a) $L_x = 2\pi$, and (b) $L_x = 4\pi$, at $t = 0$. Isosurfaces of Q-criterion ($Q = 0.01$).

	LOP, $p = 50$	*WNLOP*, $p = 1$	*LOP*, $p = 50$	*HNLOP*, $p = 1$
E_0	5×10^{-7}	5×10^{-7}	7.5×10^{-7}	7.5×10^{-7}
u	5.0×10^{-3}	1.4×10^{-3}	6.1×10^{-3}	1.0×10^{-2}
v	1.4×10^{-2}	1.7×10^{-3}	1.7×10^{-2}	7.0×10^{-3}
w	1.1×10^{-2}	4.6×10^{-3}	1.3×10^{-2}	1.5×10^{-2}

Table II.1: Maximum absolute values of the disturbance velocity and vorticity components for the optimal perturbations obtained by linear 50-norm and nonlinear 1-norm optimizations with $T_{opt} = 20$ and $E_0 = 5 \times 10^{-7}$ (left columns), and with $E_0 = 7.5 \times 10^{-7}$ (right columns).

values, being both larger than u, whereas for the 1-norm nonlinear optimal $u \approx w$, v being the smallest component. In fact, for linear optimals the streamwise component is always smaller than the other two components, since the initial disturbance is basically composed by streamwise vortices, characterized by the v and w velocity components. On the other hand, nonlinear optimizations always provide large values of the streamwise component, inducing defects in the streamwise base flow velocity profile (see Cherubini et al. (2011b) for the case of the boundary-layer and Cherubini and De Palma (2013) for the Couette flow). The influence of such differences on the transition scenarios initiated by these different rapidly growing perturbations will be analyzed in the next section.

II.3.2 Transition mechanisms

We have performed several Direct Numerical Simulations (DNSs) initialized with the optimal disturbances described in the previous section with several initial energies. In particular, the nonlinear optimal perturbations preserve the initial energy for which they have been computed, whereas the linear optimal perturbations have been rescaled with suitable values of $E(0)$. The initial energy values have been bisected in order to determine the minimum perturbation energy necessary to achieve transition to turbulence (where the rms curves obtained for different energy levels have been compared in order to detect transition to turbulence). These transition thresholds are provided in table II.2 for the nonlinear and linear p-norm optimal perturbations. For linear 1-norm optimal perturbations, which are streamwise-independent, it is customary to add a small-amplitude noise field to the initial optimal perturbation for breaking its streamwise invariance and allow the flow to reach turbulence (Kreiss et al., 1994; Reddy et al., 1998). Even though this noise field is not necessary for triggering transition when initializing with the streamwise-dependent p-norm optimal disturbances (or the nonlinear ones), the transition thresholds might still be sensitive to the presence of additional random disturbances (Cossu et al., 2011). Thus, we have performed further DNSs in presence of a noise field of initial energy equal to 1% and 2% of E_0, verifying that the transition thresholds provided in table II.2 are marginally affected by the presence of the noise. One can see that, except for the lowest target time, $T_{opt} = 10$, the nonlinear optimal perturbations are able to induce transition at a lower energy than the p-norm ones. In particular, for $T_{opt} \leq 20$, the nonlinear solutions found at the threshold energy are of the family of weakly nonlinear optimal solutions, whereas highly nonlinear optimals are found at threshold for $T_{opt} \geq 30$. Thus, in some cases even the weakly nonlinear optimal solutions are more efficient then p-norm ones, despite their weaker localization. This confirms that, not the localization, but rather the peculiar shape of the perturbation selected by nonlinear mechanisms is crucial to efficiently induce transition.

In the following, we will discuss and compare the route to transition of linear $p-$norm and nonlinear $1-$norm perturbations at the threshold energy, first in the case of short target times ($T_{opt} \leq 20$, discussed in subsection II.3.2.1) and then for longer target times ($T_{opt} > 20$, subsection II.3.2.2). For characterizing and comparing the transition scenarios we have computed the *rms* value of the components of velocity and vorticity during the time evolution of the perturbations, the rms value of the generic variable f being defined as $f^2_{rms} = \frac{1}{V}\int_V (f-F)^2 dV$, where F is the value of the variable for the base flow. Moreover, Fourier transforms in x and z of the perturbation field have been performed on a $y-constant$ plane, in order to track the development of different modes characterized by streamwise and spanwise wavenumbers $n\alpha$ and $m\beta$, with $\alpha = 2\pi/L_x$ and $\beta = 2\pi/L_z$. In the following, the different modes will be indicated by the pair (n, m) (see Schmid and Henningson (2012)).

II.3.2.1 Short target time analysis

In this section the transition scenarios induced by 1-norm WNLOPs and p-norm LOPs computed for $T_{opt} \leq 20$ are analyzed and compared. Figure II.9 shows the *rms* values of the velocity and vorticity components for the WNLOPs obtained with $T_{opt} = 10$, $E_0 = 1.25 \times 10^{-6}$ (a-b) and $E_0 = 1.0 \times 10^{-6}$ (c-d), as well as for the 50-norm LOP with $E_0 = 1.0 \times 10^{-6}$ (e-f). For the WNLOP, all of the velocity components initially grow due to the Orr-mechanism for $t < 10$. When the perturbation reaches a positive inclination with respect to the base flow, a modified lift-up effect (Cherubini et al., 2011b) begins to induce the growth of the streamwise velocity component, while the amplitude of the v and w components drops (see figure II.9 (a) for $10 < t < 25$). Concerning the vorticity, figure II.9 (b) shows that after a small initial reduction of the streamwise component due to the initial tilting of the counter-rotating vortices ($t < 5$), all of the vorticity components start to grow up to $t \approx 20$. The spanwise and wall-normal components grow due to the velocity gradients induced by the formation of positive and negative streaks. Whereas, concerning the streamwise vorticity, its growth is not linked to the formation of the streaks, but

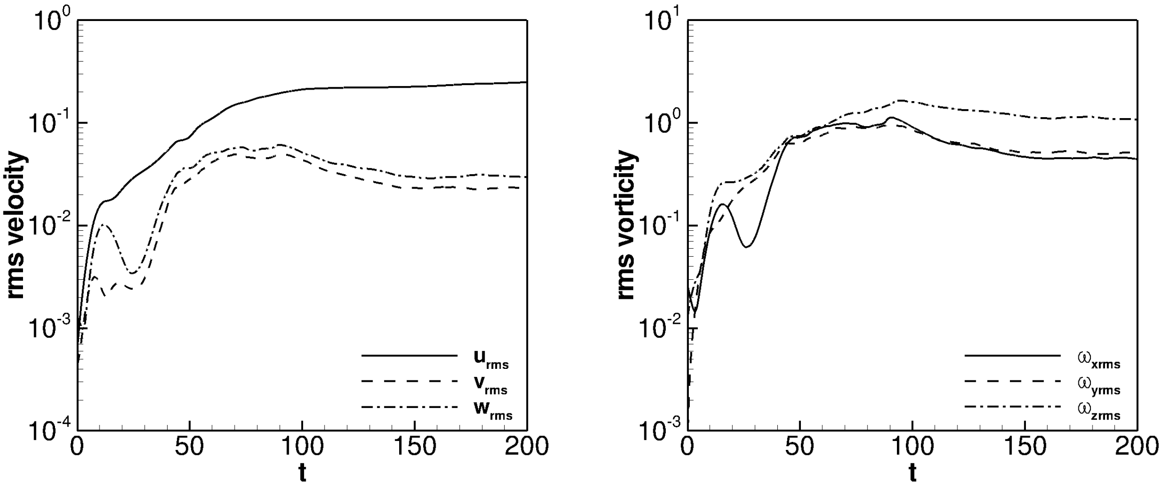

(a) WNLOP, $E_0 = 1.25 \times 10^{-6}$ (b) WNLOP, $E_0 = 1.25 \times 10^{-6}$

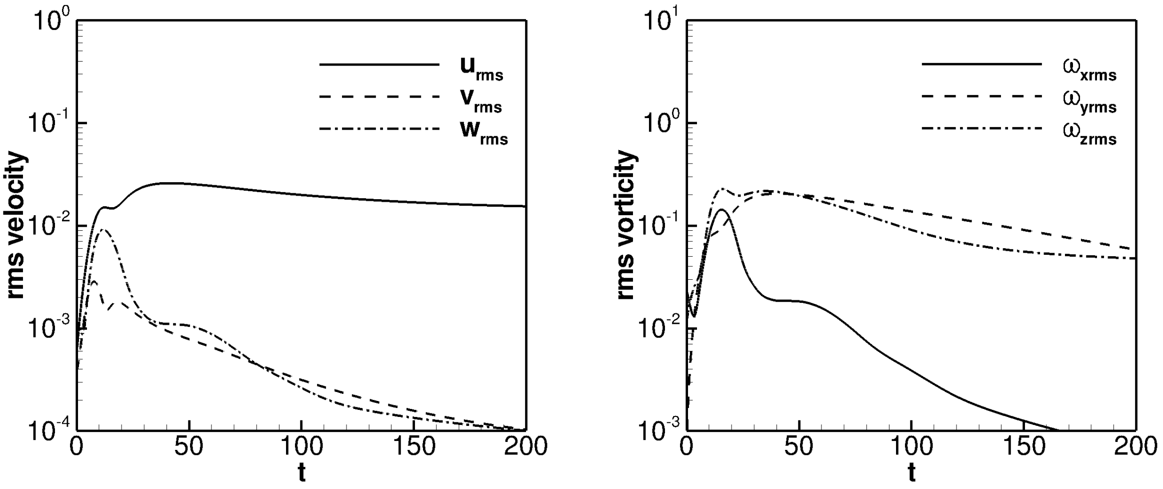

(c) WNLOP, $E_0 = 1 \times 10^{-6}$ (d) WNLOP, $E_0 = 1 \times 10^{-6}$

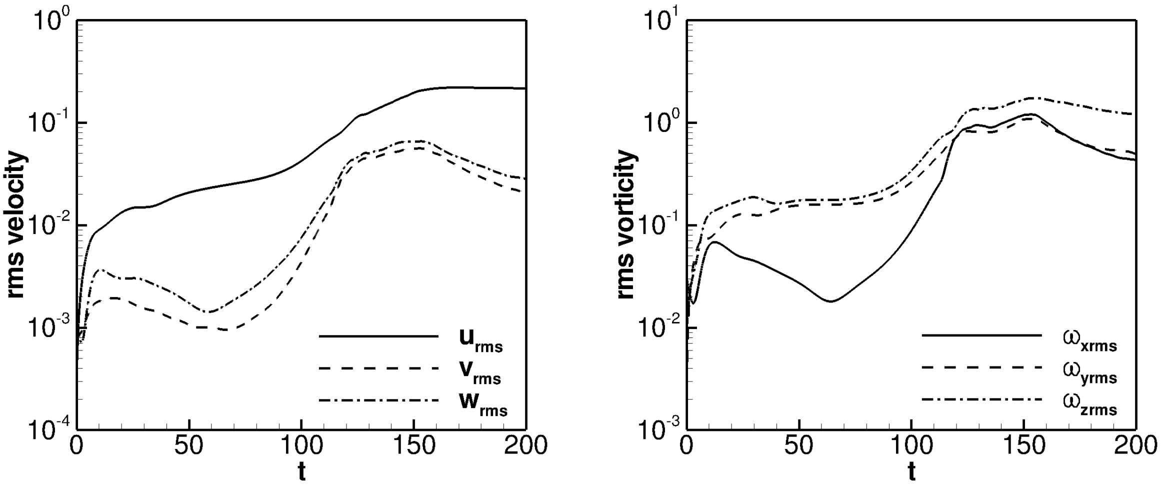

(e) 50-norm LOP, $E_0 = 1 \times 10^{-6}$ (f) 50-norm LOP, $E_0 = 1 \times 10^{-6}$

Figure II.9: Time evolution of the rms of the velocity (left) and vorticity (right) components for the WNLOP with $E_0 = 1.25 \times 10^{-6}$ (top frames) and $E_0 = 1 \times 10^{-6}$ (middle frames), and of the 50-norm LOP with $E_0 = 10^{-6}$ (bottom frames), computed for $T_{opt} = 10$.

Target time	NLOP, 1-norm	LOP, 50-norm
10	$\approx 1.25 \times 10^{-6}$	$\approx 1 \times 10^{-6}$
20	$\approx 5 \times 10^{-7}$	$\approx 6.5 \times 10^{-7}$
30	$\approx 2.5 \times 10^{-7}$	$\approx 6.5 \times 10^{-7}$
40	$\approx 2.5 \times 10^{-7}$	$\approx 2 \times 10^{-6}$
50	$\approx 1 \times 10^{-7}$	$\gg 1 \times 10^{-5}$

Table II.2: Values of the transition energy thresholds associated with the optimal perturbations computed at the indicated target time.

rather to their modulation (Cherubini and De Palma, 2013). In particular, looking at the vorticity transport equation, for the streamwise component of the vorticity one has:

$$\frac{D\omega_x}{Dt} = \frac{\partial u}{\partial x}\omega_x + \frac{\partial u}{\partial y}\omega_y + \frac{\partial u}{\partial z}\omega_z + \frac{1}{Re}\nabla^2\omega_x. \tag{II.6}$$

At $t = 0$, the wall-normal component of the vorticity is very small (see figure II.9 (b)) so the growth of ω_x is mostly driven by the streamwise and spanwise modulation of the streamwise velocity component. Thus, in order to allow the growth of the streamwise vorticity already at short time and rapidly trigger a self-sustained process (see Waleffe (1997)), this nonlinear optimal is characterized by a finite-amplitude streamwise velocity component modulated in x and z. Moreover, the initial vortices are not streamwise-aligned, but they present a spanwise inclination, namely a spanwise vorticity component, at initial time. However, these mechanisms of initial growth of the streamwise velocity and vorticity are not sufficient to induce transition to turbulence, until the third element of the self-sustained process, namely the secondary instability of the streaks, is activated (Brandt et al., 2000). This happens at $t \approx 25$, when the spanwise and wall-normal components of the velocity start to grow again in time, finally inducing transition to turbulence (at $t \approx 50$). If the saturated streaks are not large enough for triggering secondary instability, the flow relaminarizes after the first transient growth phases. This is clearly shown in Figure II.9 (c) and (d), providing the velocity and vorticity rms values for the nonlinear optimal at lower initial energy, $E_0 = 10^{-6}$. These rms curves show that a perturbation having a similar shape but lower amplitude experiences a very similar evolution up to $t \approx 20$, but secondary instability is not triggered and the flow relaminarizes.

Snapshots of the time evolution of the weakly nonlinear optimal perturbation leading to turbulence are shown in figure II.10, providing the isosurfaces of the Q criterion and of the streamwise velocity disturbance. One can observe the formation of oscillating streaks at $t = 25$, their growth and saturation at $t = 31$ and $t = 37$, followed by the development of strong vortical structures due to streak secondary instability at $t = 43$ and $t = 49$. The streak instability is of inflectional type (Schmid and Henningson, 2012), due to the deformation of the velocity profile in the spanwise and wall-normal direction induced by the large-amplitude negative streaks. This instability increases the spanwise and wall-normal components of the vorticity, leading to the formation of arch vortices connecting the initial neighboring vortex structures, finally forming a sequence of *hairpin* vortices. This mechanism can be better observed in figures II.11, where the streaks (solid lines) and the spanwise vorticity (contours) are shown in a longitudinal (z-constant) plane. The

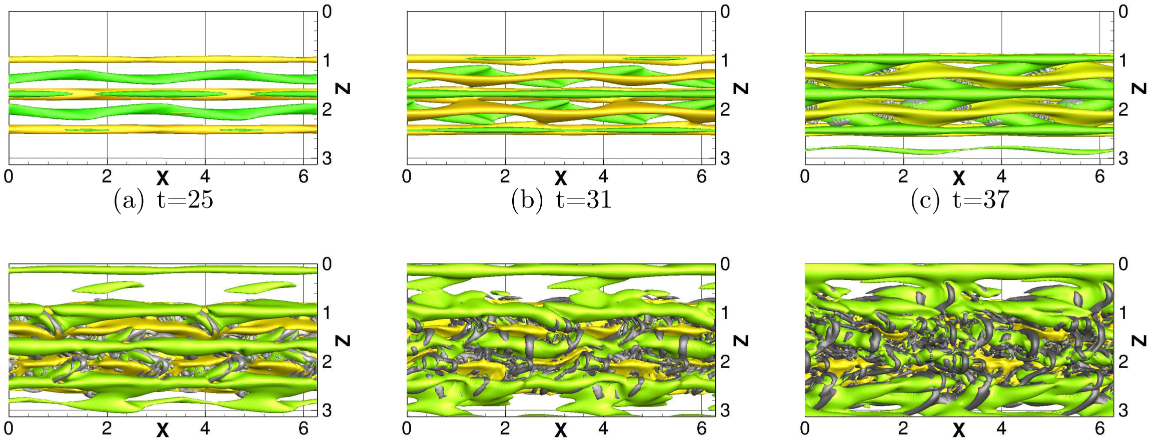

(a) t=25 (b) t=31 (c) t=37

(d) t=43 (e) t=46 (f) t=49

Figure II.10: Snapshots of the time evolution of the weakly nonlinear optimal perturbation found for $E_0 = 1.25 \times 10^{-6}$. Isosurface of Q-criterion ($Q = 0.5$, grey), and of the streamwise velocity disturbance ($u = \pm 0.1$, green for negative and yellow for positive).

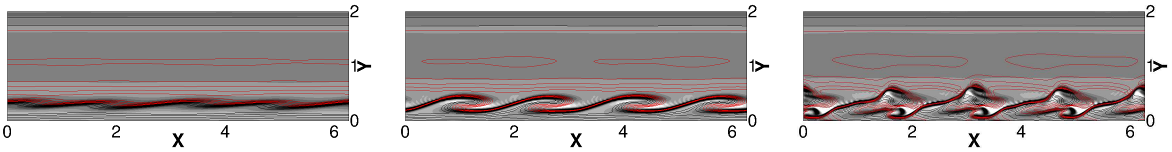

(a) t=29 (b) t=37 (c) t=41

Figure II.11: Snapshots of the time evolution of the weakly nonlinear optimal perturbation computed for $E_0 = 1.25 \times 10^{-6}$, $T_{opt} = 10$. Isolines of streamwise velocity disturbance (red positive, black negative), and contours of spanwise vorticity (white positive, black negative) on a $z = 2$ plane.

creation of these large-amplitude spanwise vortices provides, through nonlinear coupling, the last element for the activation of the Waleffe self-sustaining process, eventually leading the flow to a chaotic state. We can observe three main differences with respect to the classical scenario of secondary instability of streamwise streaks (Brandt et al., 2000): i) due to the Orr mechanism, all of the velocity components initially grow; ii) due to the initial modulation of the streamwise component of velocity, the streamwise vorticity increases too; iii) due to the initial spanwise inclination of the streamwise vortices, the streaks are already modulated in the streamwise direction before secondary instability is triggered. Indeed, this transition scenario appears more similar to the one induced by oblique waves, which have been found to trigger transition at lower energies than streamwise vortices in shear flows (Duguet et al., 2010; Reddy et al., 1998). In this scenario, initial perturbations modulated in x and z are able to create, by nonlinear coupling, streamwise streaks that experience secondary instability. For analyzing this type of transition scenario, Reddy et al. (1998) fed the flow by a pair of oblique waves with wavenumber $(1, \pm 1)$. These waves develop by generating streamwise vortices having wavenumber $(0, 2)$, which, while decreasing in amplitude, generate streaks that saturate

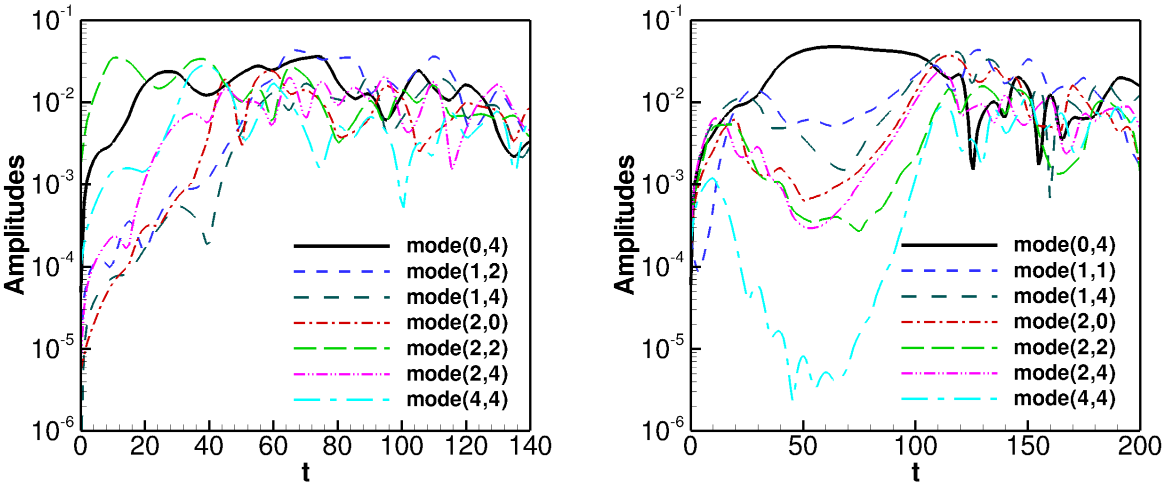

(a) Weakly nonlinear optimal

(b) Linear 50-norm optimal

Figure II.12: Time evolution of the Fourier streamwise and spanwise wavenumbers for the two optimals computed at $T_{opt} = 10$ with initial energy $E_0 = 1.25 \times 10^{-6}$; a nonlinear 1-norm (a) and a linear 50-norm optimal (b).

and experience secondary instability, inducing at later times the growth of $(2,2)$ and $(1,1)$ modes. In order to verify whether the mechanism of transition of the WNLOP shares some features with the oblique transition scenario, we analyze the evolution in time of the most amplified Fourier modes for the WNLOP, provided in figure II.12 (a). One can observe that the oblique mode $(2,2)$ is indeed the mode of largest amplitude at $t = 0$, indicating that the initial optimal perturbation has a modal composition similar to an oblique wave. At early times, a large growth of the streaky $(0,4)$ mode is also observed. However, these streaks do not experience a saturation phase, but they quickly break down. Moreover, many other modes grow at early times, included the initial oblique mode $(2,2)$ which does not decrease in amplitude before transition. This simultaneous, rapid growth of several modes is due to the fact that, due to the presence of nonlinear terms in the optimization procedure, this optimal perturbation has already in its initial structure the basic elements to trigger the three mechanisms of the Waleffe self sustained cycle: i) streamwise vorticity to create the streaks; ii) spanwise inclination to modulate them; iii) sufficiently high amplitudes to induce nonlinear coupling.

This transition scenario for the WNLOP at $T_{opt} = 10$ is now compared with the one induced by a p-norm LOP computed at the same target time, initialized with $E_0 = 10^{-6}$. Comparing figures II.9 (a) and (e), one can observe that for the 50-norm case the rms-values saturate later in time (for $t > 150$ instead of $t > 75$), meaning that its evolution towards transition needs more time than the previous case. The initial growth of the velocity components due to the Orr mechanism occurs on the same time scale, but the decrease and following increase of the wall-normal and spanwise velocity components are much slower than in the nonlinear case (although the optimals have been computed for the same target time). Notice also that the streamwise vorticity increases only at early times, and then decreases reaching values quite smaller than the initial one. This is clearly due to the fact that the modulation in x of the streamwise velocity component is present

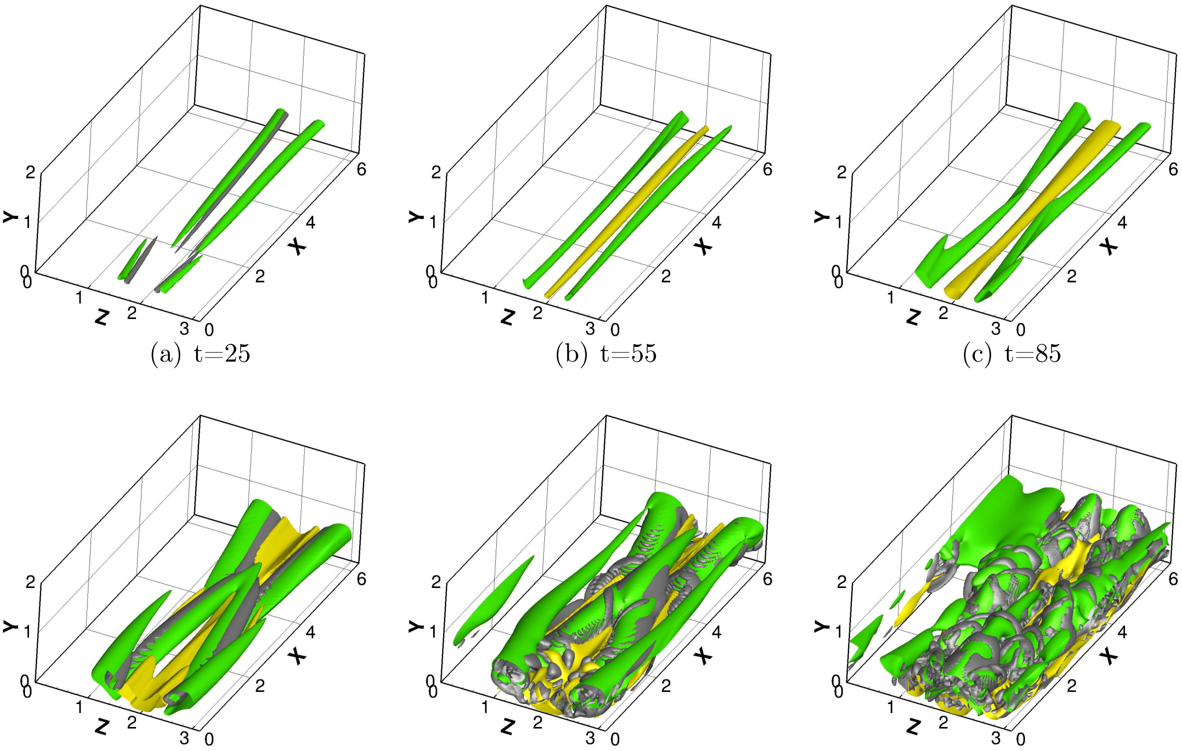

(a) t=25 (b) t=55 (c) t=85

(d) t=105 (e) t=115 (f) t=120

Figure II.13: Evolution of linear 50-norm optimal perturbation for $T_{opt} = 10$ and $E_0 = 10^{-6}$. (a,b,c,d,e,f) Isosurface of Q-criterion ($Q = 0.07$, grey), and of streamwise velocity disturbance ($u = -0.9$, green and $u = 0.15$, yellow).

only at short times and fades away when streamwise streaks are created, not sustaining the growth of ω_x.

Figure II.13 provides snapshots of the evolution of streaks (yellow and green) and vortices (gray) showing the creation of bent streaks and their secondary instability. The streamwise modulation of the streaks is much weaker than in the nonlinear case (compare with figure II.10), and the streaks remain almost streamwise-aligned up to $t \approx 80$, whereas in the weakly nonlinear case strong modulations are observed already in the very early phases of transition. Strong modulations of the streaks can be observed only at $t \approx 100$, leading to the formation of Λ-shaped structures that generate a population of hairpin vortices. Similarly to what has been shown before, the secondary instability of the streaks is due to the formation of the inflection points, as one can observe in the z-constant sections in figure II.14. However, in the nonlinear case, these inflection points occur with a different wavelength and at different times with respect to the linear case, as one can verify by comparing figure II.14 with figure II.11. The wavelengths of these structures have been analyzed by performing a Fourier analysis, provided in figure II.12 (b). The figure shows that the oblique mode $(2, 2)$ is again the mode of largest amplitude at $t = 0$, even if at early times the difference among the amplitudes of the different Fourier modes is small. Moreover, the development of the modes strongly resembles that of the oblique transition scenario: except in the early phases in which the Orr mechanism is active, the growth of the streaks is associated with a strong decrease of the oblique modes (see the

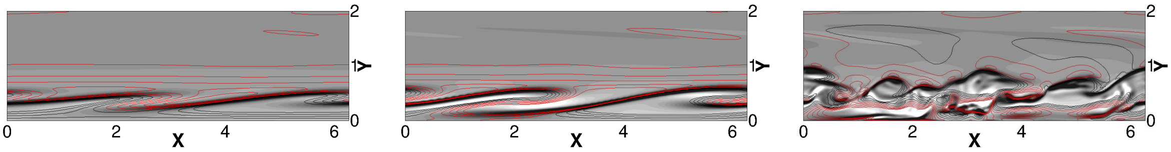

(a) t=100 (b) t=110 (c) t=120

Figure II.14: Evolution of linear 50-norm optimal perturbation computed for $T_{opt} = 10$ and $E_0 = 10^{-6}$. Isolines of streamwise velocity disturbance (red positive, black negative), and contours of spanwise vorticity (white positive, black negative) on a $z = 1.6$ plane.

evolution of the $(4, 4)$, $(2, 2)$ and $(1, 1)$ modes in figure II.12 (b)). One can also observe the long phase of saturation of the streaks represented by the long plateau of the $(0, 4)$ mode. Finally, after the saturation of the streaks a new growth of the oblique modes is observed due to the secondary instability of the streaks. In particular, the streak instability is characterized mostly by modes of streamwise wavenumber 2 instead of 4, observed for the fundamental oblique scenario (Schmid and Henningson, 2012) and for the weakly nonlinear optimal perturbation evolution. In fact, comparing figure II.11 with figure II.14, one can observe that the Kelvin-Helmholtz instability has a double streamwise wavelength in the latter case. Thus, in the 50-norm case the secondary instability is more likely triggered by the subharmonic varicose mode instead of the fundamental one, as for the fundamental oblique wave scenario. Except the initial modal composition, this scenario appears more similar to the oblique scenario, being based on the generation of streamwise streaks by modulated initial perturbations, and their successive saturation and breakdown. This is due to the fact that a linear optimization can rely only on linear mechanisms to grow in time, such as the Orr and the lift-up ones, thus it has to create streaks to induce transition. On the other hand, a nonlinear optimization can couple these mechanisms by nonlinear effects to directly induce a growth of all of the modes at the same time.

Similar transition scenarios are observed for optimal perturbations computed for $T_{opt} = 20$, the only difference being that the weakly nonlinear optimal experiences transition for an initial energy slightly lower than the 50-norm linear optimal (see table II.2). Thus, comparing the route to transition of the WNLOP with the 50-norm LOP for $T_{opt} \leq 20$ can lead to two main conclusions: i) the transition route of the 50-norm optimal is similar to the subharmonic oblique transition scenario already known in the literature, whereas the WNLOP reaches transition by inducing a simultaneous growth of many different modes; ii) in terms of initial energy, the 50-norm optimal perturbation is more efficient than the weakly nonlinear one only at very short target time ($T_{opt} = 10$), whereas it is always less efficient in terms of transition time.

II.3.2.2 Long target time analysis

For $T_{opt} = 30$, the highly nonlinear optimal is the lowest-energy solution able to lead to transition. Figure II.15 shows the rms values of velocity and vorticity versus time for the 50-norm (top) and highly nonlinear (bottom) optimal perturbations computed with $E_0 = 2.5 \times 10^{-7}$ for $T_{opt} = 30$. The former perturbation creates streaks that saturate and then decay, since they are not accompanied by the increase of the other velocity

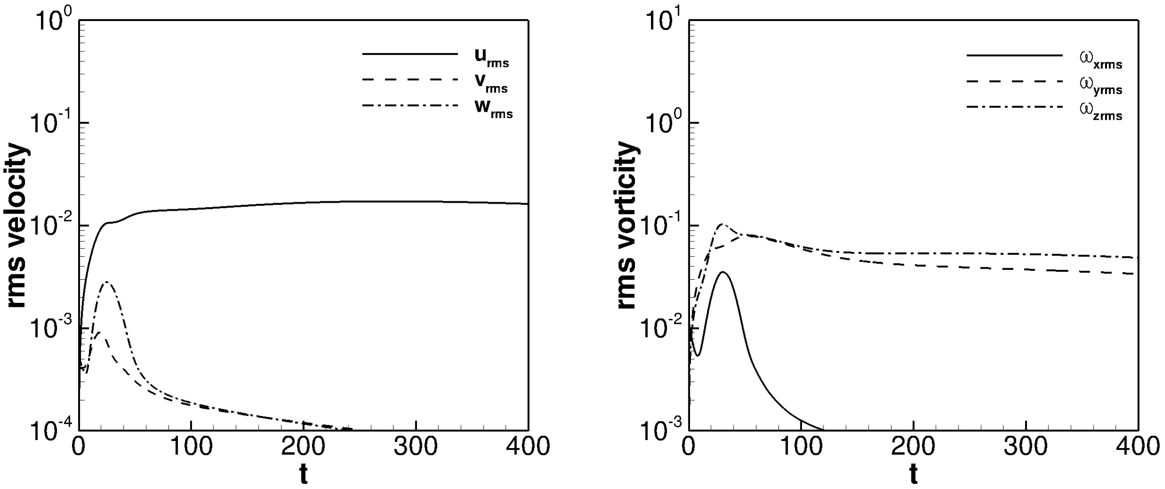

(a) 50-norm LOP (b) 50-norm LOP

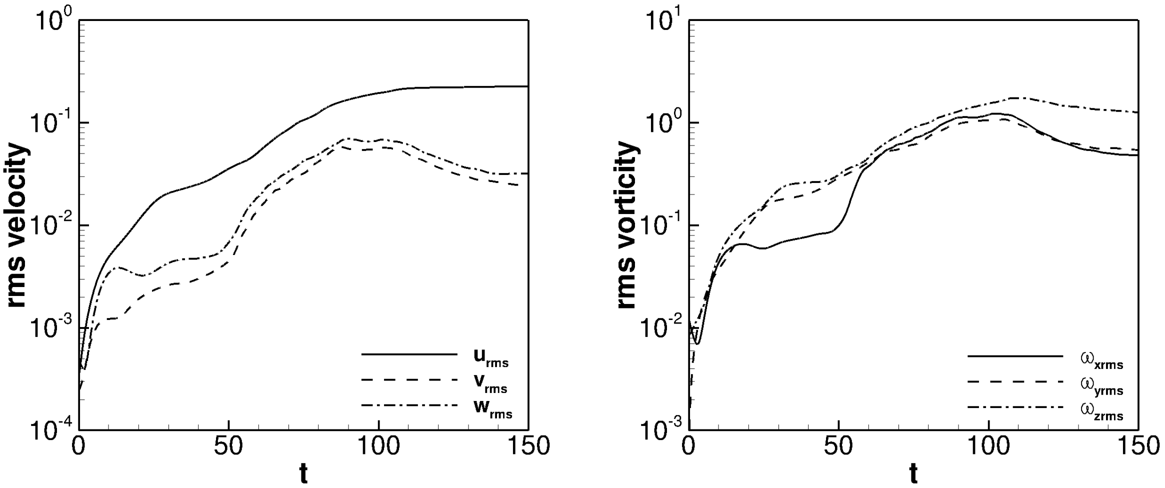

(c) HNLOP (d) HNLOP

Figure II.15: Time evolution of the rms of the velocity (left) and vorticity (right) components for the 50-norm LOP (top frames) and the HNLOP (bottom frames) with $E_0 = 2.5 \times 10^{-7}$, computed for $T_{opt} = 30$.

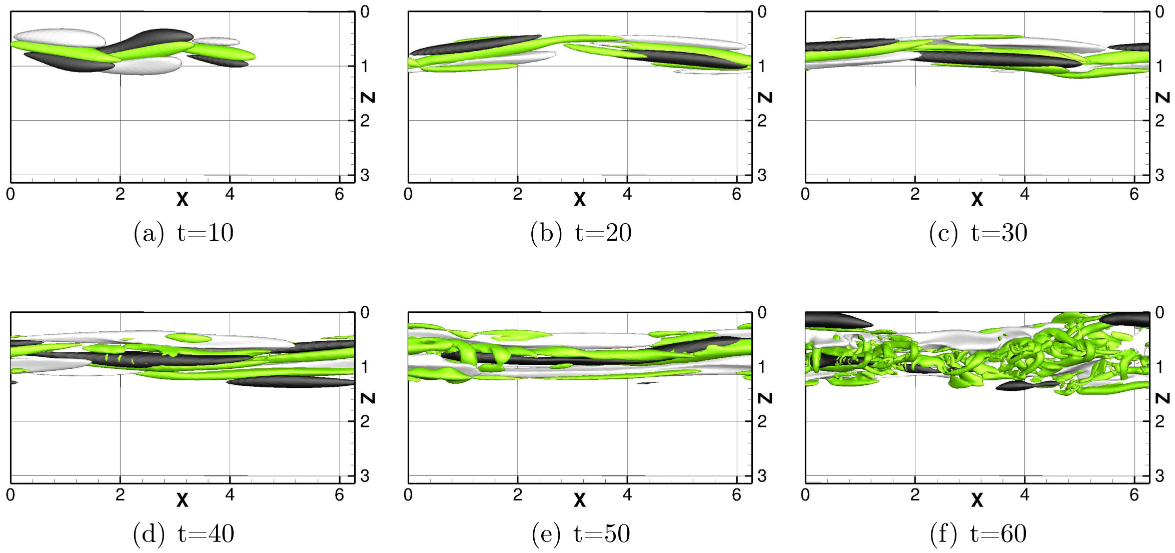

(a) t=10 (b) t=20 (c) t=30

(d) t=40 (e) t=50 (f) t=60

Figure II.16: Snapshots of the time evolution of the highly nonlinear optimal perturbation computed for $T_{opt} = 30$ and $E_0 = 2.5 \times 10^{-7}$. Isosurface of Q-criterion ($Q = 0.01Q_{max}$) colored by streamwise vorticity, and isosurfaces of streamwise velocity disturbance ($u = \pm 0.5u_{max}$, black negative and white positive).

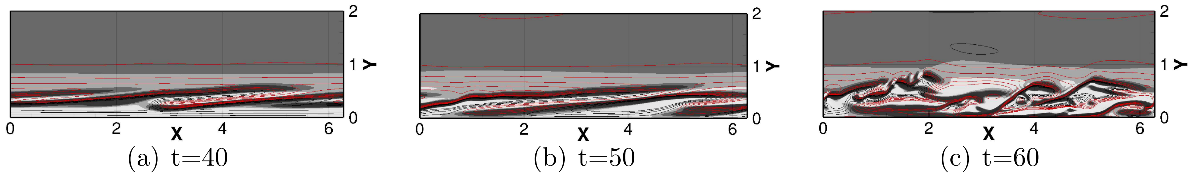

(a) t=40 (b) t=50 (c) t=60

Figure II.17: Snapshots of the time evolution of the HNLOP computed for $E_0 = 2.5\times10^{-7}$, $T_{opt} = 30$. Isolines of streamwise velocity disturbance (red positive, black negative), and contours of spanwise vorticity (white positive, black negative) on a $z = 2$ plane.

components (except for the first slight increase due to the Orr mechanism). This is due to the fact that, for $T_{opt} > 20$, the lift-up dominates the energy growth mechanisms in a linear framework, thus the perturbation is optimized with respect to a linear mechanism that cannot self-sustain in the absence of other source of growth for the v and w components. On the other hand, in the highly nonlinear optimal case shown in figure II.15 (bottom), although a slight decrease of the v component is observed after the Orr mechanism, these components are found to grow together with the streamwise component. Moreover, similarly to what has been observed in figure II.9 for a lower T_{opt} and a larger E_0, the streamwise component does not need to saturate to induce the v and w increase, since the three components of velocity are nonlinearly coupled. One can also observe that, although a lower initial energy is imposed with respect to the WNLOP case, transition is reached very quickly, since the highly nonlinear optimal found for these values of the energy and target time exploits all of the nonlinear effects to rapidly induce transition.

Snapshots of the evolution towards transition for the HNLOP computed with $T_{opt} = 30$ and $E_0 = 2.5\times10^{-7}$ are shown in figure II.16. After tilting downstream exploiting the Orr

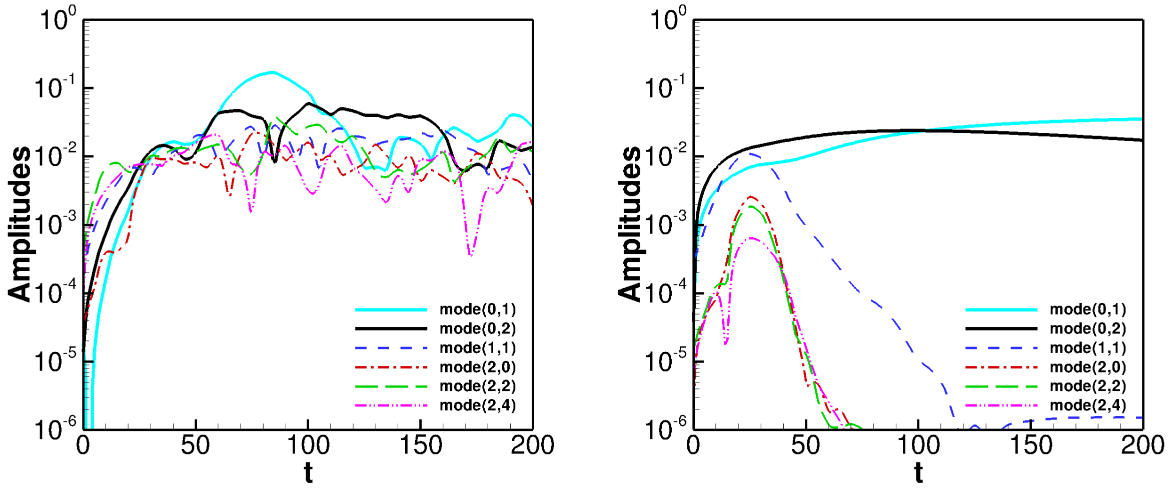

(a) Highly nonlinear optimal (b) Linear 50-norm optimal

Figure II.18: Time evolution of the Fourier streamwise and spanwise wavenumbers for the two optimals computed at $T_{opt} = 30$ with initial energy $E_0 = 2.5 \times 10^{-7}$; a nonlinear 1-norm (a) and a linear 50-norm optimal (b).

mechanism (first frame for $t = 10$), the inclined vortices begin to transport the base-flow momentum, creating localized and modulated zones of high and low streamwise perturbation (black and white isosurface of streamwise velocity disturbance). These positive and negative zones are initially alternated in x and z, and the initial vortices are localized in space. As time increases, the vortices are stretched in the streamwise directions by the mean flow (compare the second and third frame for $t = 20$ and $t = 30$); as a consequence, at $t = 40$ the nonsymmetric vortices begin to merge on top of the negative streamwise velocity disturbance, creating *cane*-like vortical structures. At the same time, the regions of positive and negative streamwise velocity begin to merge, inducing at $t = 50$ the creation of elongated bent streaks. In particular, two high-speed bent streaks can be observed on the side of a central low-speed streak; in the zone of interaction of the low- and the high-speed streaks ($x \approx 1$ in figure II.16 (e)), strong vorticity is created due to the presence of strong inflection points. This local instability then produces smaller-scale vortical structures leading the flow to turbulence (sixth frame for $t = 60$). The evolution of spanwise vorticity (isocontours) and streamwise velocity (isolines) perturbation is shown in a $z - const$ plane in figure II.17. One can observe the complex alternated pattern given by the low- and high-speed streaks, and the strong vorticity created in localized regions of the flow, leading to turbulence already at $t = 60$ (compare with figure II.14, in which a chaotic behaviour is observed only at $t = 120$). It is also noteworthy that the dynamics of the HNLOP is similar to the one found for nonlinear optimal disturbances in Couette flow (Cherubini and De Palma, 2013; Duguet et al., 2013), indicating that in parallel shear flows this nonlinear optimal transition scenario has a general relevance.

The Fourier transform of the velocity signal extracted each five time units, provided in figure II.18 (a), shows that all of the Fourier modes grow at the same time, with similar slopes and amplitudes. Moreover, no saturation phase is observed for the streaky modes, $(0, 1)$ and $(0, 2)$. Thus, the HNLOP is able to induce a very rapid simultaneous growth of all of the modes; this growth is even more rapid than the one found for the WNLOP, which could rely on weaker nonlinear effects. On the other hand, the 50-norm linear optimal computed for the same target time and normalized with the same initial energy only induces the growth of the streaky modes, $(0, 1)$ and $(0, 2)$, which very rapidly increase their energy, as shown in figure II.18 (b). However, while the streaks slowly saturate in time, the other modes rapidly decay, since nonlinear effects are not exploited enough to sustain a regeneration cycle.

In conclusion, p-norm linear and 1-norm nonlinear optimal disturbances appear to be characterized by important differences in their route to transition. Both perturbations rely only on linear energy growth mechanisms in their initial evolution phases; however, nonlinear optimal perturbations are able to exploit all of the energy growth mechanisms occurring over different timescales, allowing a simultaneous growth of different interacting modes which successfully lead the flow to transition.

II.4 Conclusions

Localized optimal perturbations (OPs) for plane Poiseuille flow have been computed using two optimization approaches based on the Lagrange multipliers formulation: a linear optimization, using the p-norm (with $p = 50$) of the energy perturbation as objective function, and a nonlinear optimization, considering the 1-norm energy perturbation as objective function. These OPs maximize the objective function at a given target time T_{opt} and for a given initial energy E_0 in the case of the nonlinear procedure. The shape of the p-norm linear OP is rather robust. In fact, for considered target times and initial energies, it is characterized by a pair of localized vortices aligned with the streamwise direction and mirror-symmetric with respect to the spanwise direction. A weaker localization in the streamwise direction is recovered for large target times, the streamwise vortices elongating in the streamwise direction, whereas the spanwise length of the disturbance remains unchanged. On the other hand, the use of the nonlinear approach allows one to unravel the rich structure of optimal perturbations which change strongly depending on target time and initial energy. In fact, for low values of T_{opt} ($T_{opt} < 20$) and intermediate values of E_0, a *weakly nonlinear optimal* perturbation has been found, composed by alternated vortices inclined with respect to the streamwise direction, with large values of the streamwise velocity disturbance. This OP localizes at one of the two walls, thus breaking the wall-normal symmetry of the linear OPs. For larger target time ($T_{opt} \geq 20$), a *highly nonlinear optimal* perturbation is found for sufficiently high values of E_0, which breaks also the spanwise symmetry. In this case, the disturbance strongly localizes in all spatial directions, being composed of spanwise inclined vortices along patches of large-amplitude streamwise velocity, very similar to the nonlinear OP found for Couette flow by Cherubini and De Palma (2013). Finally, for very short target times and high values of the initial energy, a *hairpin-like nonlinear optimal* perturbation is obtained (not analyzed in the present chapter). Thus, although both linear and nonlinear optimizations provide localized OPs, the shape and characteristics of linear p-norm and nonlinear OPs are rather different: i) p-norm optimal vortices are streamwise-aligned, whereas nonlinear ones are inclined; ii) p-norm OPs loose their streamwise localization when the target time is increased, whereas the nonlinear OPs become more and more localized; iii) for sufficiently high initial energies, the relative amplitudes of the velocity components differ, the streamwise component being the smallest for the linear p-norm OP, the wall-normal component, instead, for the nonlinear OP.

Concerning the route to transition, the p-norm OP follows a transition path similar to the oblique transition scenario, with slightly oscillating streaks, created by a modulated initial perturbation, which saturate and then experience a secondary instability. The weakly nonlinear OP has an initial modal composition resembling an oblique wave. However, it can induce a faster transition by generating bent large amplitude streaks instead of streamwise aligned ones, skipping the phase of saturation typical of the oblique scenario. On the other hand, for the highly nonlinear OPs, all of the velocity components grow together, due to important nonlinear effects leading to transition very efficiently. As expected, in most of the cases the nonlinear optimals induce transition to turbulence for lower energies (about one third for $T_{opt} = 30$) and in a shorter time than the p-norm ones. Decreasing the initial energy of a factor three can be very important in industrial applications or for actuators controlling the flow. Moreover, nonlinear optimal disturbances computed for a very long target time can provide the minimal-energy threshold for transition, allowing one to determining the amplitude thresholds for conditional stability in subcritical transition. Thus, an open and interesting question might be the physical meaning and benefits of p-norm OPs computed in a nonlinear framework. Using both nonlinearity and higher-order norms to localize the initial perturbation could provide interesting results.

In the next chapter we will discuss in details the $hairpin-like$ nonlinear optimal solution obtained for short target times and high value of initial energies. A new prospective of the route to turbulence in high energy disturbance environment is then proposed.

II.5 Appendix

The *augmented functional* for the optimisation reads:

$$\begin{aligned}\mathfrak{L}\left(u_k, p, u_k^\dagger, p^\dagger, u_k(T), u_k(0), \lambda\right) &= \frac{E_p(T_{opt})}{E(0)} \\ -\int_0^{T_{opt}}\int_V u_i^\dagger \left(\frac{\partial u_i}{\partial t} + \frac{\partial (u_i U_j)}{\partial x_j} + \frac{\partial (U_i u_j)}{\partial x_j} + \frac{\partial p}{\partial x_i} - \frac{1}{Re}\frac{\partial^2 u_i}{\partial x_j^2} + \frac{\partial (u_i u_j)}{\partial x_j}\right) dtdV& \\ -\int_0^{T_{opt}}\int_V p^\dagger \frac{\partial u_i}{\partial x_i} dtdV - \lambda\left(\frac{E_0}{E(0)} - 1\right)&. \qquad \text{(II.7)}\end{aligned}$$

Therefore, looking for the extrema of $\mathfrak{L}$ with respect to every independent variable, we get the equations that close the optimization problem:

$$
\begin{aligned}
\frac{\partial \mathfrak{L}}{\partial \lambda} &= \frac{E_0}{E(0)} - 1 = 0 && \text{(II.8)}\\
\frac{\partial \mathfrak{L}}{\partial u_k^\dagger} &= \frac{\partial u_k}{\partial t} + \frac{\partial (u_k U_j)}{\partial x_j} + \frac{\partial (U_k u_j)}{\partial x_j} + \frac{\partial p}{\partial x_k} - \frac{1}{Re}\frac{\partial^2 u_k}{\partial x_j^2} + \frac{\partial (u_k u_j)}{\partial x_j} = 0 && \text{(II.9)}\\
\frac{\partial \mathfrak{L}}{\partial p^\dagger} &= \frac{\partial u_i}{\partial x_i} = 0 && \text{(II.10)}\\
\frac{\partial \mathfrak{L}}{\partial p} &= \frac{\partial u_i^\dagger}{\partial x_i} = 0 && \text{(II.11)}\\
\frac{\partial \mathfrak{L}}{\partial u_k} &= \frac{\partial u_k^\dagger}{\partial t} + \frac{\partial (u_k^\dagger U_j)}{\partial x_j} - u_i^\dagger \frac{\partial U_i}{\partial x_k} + \frac{\partial p^\dagger}{\partial x_k} + \frac{1}{Re}\frac{\partial^2 u_k^\dagger}{\partial x_j^2} + \\
&+ \underbrace{\frac{\partial (u_k^\dagger u_j)}{\partial x_j} - u_i^\dagger \frac{\partial u_i}{\partial x_k}}_{direct-adjoint\, coupling\, terms} = 0 && \text{(II.12)}\\
\frac{\partial \mathfrak{L}}{\partial u_k(T)} &= \frac{\left(\frac{1}{V}\int_V \left(\frac{1}{2}u_i(T)u_i(T)\right)^p dV\right)^{\left(\frac{1}{p}-1\right)} \left(\frac{1}{2}u_i(T)u_i(T)\right)^{(p-1)} u_k(T)}{E(0)} + \\
&- u_k^\dagger(T) = 0 && \text{(II.13)}\\
\frac{\partial \mathfrak{L}}{\partial u_k(0)} &= -\frac{E_p(T) - \lambda E_0}{E(0)^2} u_k(0) + u_k^\dagger(0) = 0 && \text{(II.14)}
\end{aligned}
$$

Equations (II.8), (II.9) and (II.10) represent the constraints of the optimization problem. Equations (II.11) and (II.12) are the perturbative adjoint Navier–Stokes equations, obtained after integration by parts of equations (II.7) and successive derivation with respect to the direct variables. Imposing the boundary conditions on the direct variables, the following boundary conditions are obtained for the adjoint variables: $u_i^\dagger = 0$ and $p^\dagger = 0$ at y-constant boundaries; periodic boundary conditions at the other boundaries. Equation (II.13) represents the compatibility conditions between the direct and the adjoint problem at $t = T_{opt}$, whereas equation (II.14) is the gradient that we aim at nullifying. Notice that equation (II.13) is responsible for the localization of the optimal perturbation when the p-norm of the energy density is used as the objective function. As described by Foures et al. (2013), initializing the optimization process with a random noise localized in a given region of the flow, step (II.13) of the procedure will localize the perturbation more and more during the optimization process. Thus, the algorithm wouldn't have any possibility of exploring other regions of the solution space, providing the local optimal solution for that particular initialization.

These equations are solved by using an iterative procedure. The optimization cycle starts providing an initial guess for the optimal perturbation $u_i(0)$; then, the Navier–Stokes equations (II.9), (II.10) (direct problem) are solved forward in time up to the target time. Then, the adjoint variables are computed by using the compatibility condition (II.13) at ($t = T_{opt}$), and the adjoint equations (II.11), (II.12) are solved backward in time up to $t = 0$. To switch back to direct variables, and close the optimization loop, we use the *gradient-based methods* proposed by Foures et al. (2013). At each direct-adjoint iteration, the objective function is evaluated in order to assess if its variation between

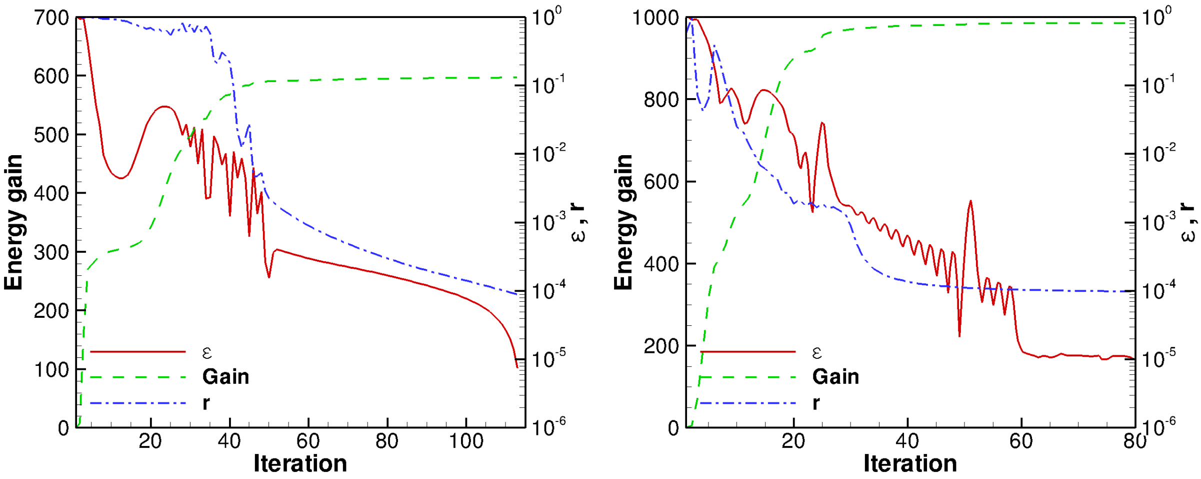

(a) (b)

Figure II.19: Energy gain (green dashed line) ϵ (blue dash-dotted line) and r (red solid line) plotted against iteration for (left) the Hairpin-like OP, $T_{opt} = 16$ at $E_0 = 2 \times 10^6$ and (right) the HNLOP $T_{opt} = 30$ at $E_0 = 2.5 \times 10^7$

two successive iterations, ϵ, is smaller than a chosen threshold. In this case, the cycle is stopped. To keep the computational cost affordable, a threshold value equal to $\epsilon = 10^{-5}$ has been chosen. Concerning the convergence of the algorithm, figure II.19 shows: i) the residual ϵ, ii) the energy gain, iii) the normalised residual $r = \frac{\|\nabla \mathfrak{L}^{\perp}\|_2^2}{\|\nabla \mathfrak{L}\|_2^2}$ (being $\nabla \mathfrak{L}^{\perp}$ the ortogonal component of the gradient of the Lagrangian functional with respect to the initial velocity field), versus the iterations, for two different nonlinear optimizations providing the hairpin-like OP (left) and the HNLOP (right), respectively. As one can see, in both cases the energy reaches an (almost) constant value, and the value of ϵ is not seen to oscillate at the end of the iteration process. Concerning the normalised residual r, for both optimization it reaches a value of $O(10^{-4})$, with a decreasing smooth tendency in the first case, and an asymptotic value for the second, indicating convergence of the algorithm. It is noteworthy that the same procedure is used for a linear or nonlinear optimization, the only difference being that the nonlinear terms in equation (II.9) are set to zero in the linear case. This implies the cancellation of the direct-adjoint coupling terms in equation (II.12). The absence of these terms makes the procedure much faster, since for evaluating these coupling terms the direct variables need to be stored at each time step of the direct problem integration in order to be available for the integration of the adjoint equations backward in time.

Chapter III

Hairpin-like optimal perturbations in plane Poiseuille flow

Contents

III.1 Introduction 37

III.2 Problem formulation 37

III.3 Results 38

III.4 Conclusions 47

III.1 Introduction

In this chapter it is shown that hairpin vortex structures can be the outcome of a nonlinear optimal growth process, in a similar way as streaky structures can be linked to a linear optimal one. To this purpose, nonlinear optimisations based on a Lagrange multiplier technique coupled with a direct-adjoint iterative procedure are performed in a plane Poiseuille flow at subcritical values of the Reynolds number, aiming at quickly triggering nonlinear effects. Choosing a suitable time scale for such an optimization process, it is found that the initial optimal perturbation is composed of sweeps and ejections resulting in a hairpin vortex structure at target time. These alternating sweeps and ejections create the potential for an inflection instability occurring in a localized region away from the wall, generating the head of the primary and secondary hairpin structures, quickly inducing transition to turbulent flow. This result could explain why the final stage of transition to turbulence and turbulent shear flows are characterized by a high density of hairpin structures.

III.2 Problem formulation

The Navier–Stokes (NS) equations are solved to compute the flow between two parallel plates, choosing the nondimensional variables so that half the distance between the plates is $h = 1$ and the centerline velocity of the laminar flow is $U_c = 1$. Dirichlet boundary

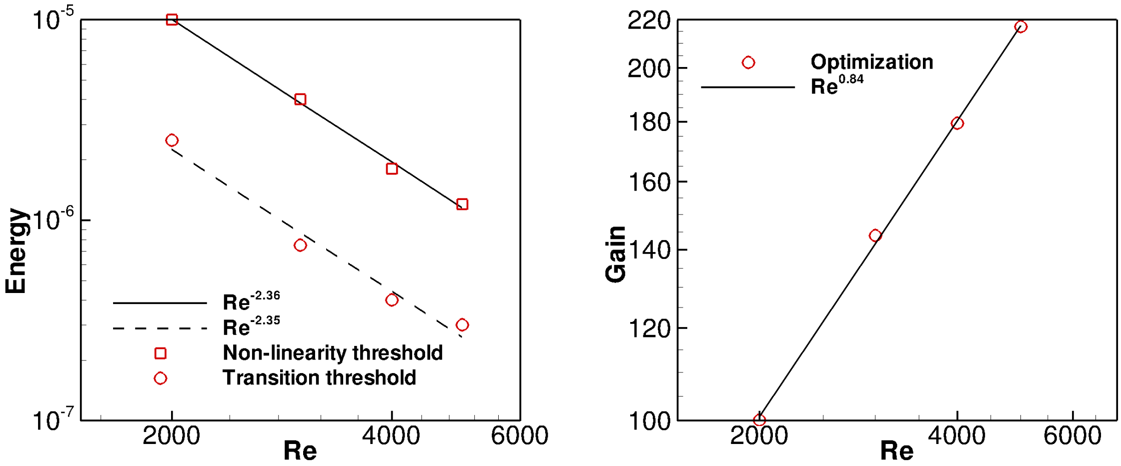

(a) Nonlinearity and transition thresholds

(b) Energy gain

Figure III.1: Log-Log plot indicating the scaling law for the initial energy (squares), the transition threshold (circles) (a), and the energy gain (b) for the short-time nonlinear optimal perturbation at the nonlinearity threshold.

conditions for the three velocity components are imposed at the upper and lower walls of the computational box; whereas periodicity is prescribed in the streamwise and spanwise directions (denoted x and z, respectively, whereas y denotes the wall-normal direction). The streamwise, wall-normal, and spanwise dimensions of the computional domain are 2π, 2, and π, respectively. The NS equations are solved by a fractional-step method with second-order accuracy in space and time (Verzicco and Orlandi (1996)), using a staggered grid with $300 \times 100 \times 120$ points, determined by a grid refinement study.
The optimisation procedure aims at computing the velocity perturbation $\mathbf{u} = (u, v, w)^T$ at $t = 0$ providing the maximum value of a chosen objective function at a given target time, T_{opt}. The objective function is the ratio between the energy density at T_{opt} and the initial (given) one ($E(0) = E_0$), the energy density being defined as:

$$E(t) = \frac{1}{2V} \int_V (u^2 + v^2 + w^2)\,(t)\, dV. \tag{III.1}$$

where V is the volume of the computational domain.

The optimisation problem is subject to partial differential constraints, namely the nonlinear NS equations in a perturbative form. The constrained optimisation is performed by a Lagrange multiplier technique coupled with a direct-adjoint iterative looping procedure using a gradient-based method. For further details about the optimisation algorithm the reader is referred to Cherubini et al. (2010a, 2011b) and appendix II.5.

III.3 Results

We perform nonlinear optimisations of finite-amplitude three-dimensional perturbations for the plane Poiseuille flow focusing on subcritical values of the Reynolds number, namely,

$Re = 2000, 3000, 4000, 5000$. In order to find optimal perturbations rapidly triggering coherent structures generated by nonlinear effects, we focus on the time scale of the Orr mechanism, preventing the dominant effect of the lift-up mechanism which acts on a larger time scale. Butler and Farrell (1992) found that the lift-up time scale for the Poiseuille flow at $Re = 5000$ is about equal to 380. On the other hand, performing several linear two-dimensional optimisations, we have found that the transient energy growth due to the Orr mechanism peaks at $t \approx 10$ for all of the considered Reynolds numbers. Thus, $T_{opt} = 10$ has been chosen for the following nonlinear three-dimensional optimisations. Moreover, using this short target time, we need a sufficiently large initial energy density in order to trigger nonlinear mechanisms. As discussed in the previous chapter, several nonlinear optimisations have been performed increasing the value of E_0 until, quite suddenly, the initial optimal perturbation localizes in space and the energy gain increases with respect to a linear optimization. The increment of the energy gain with respect to the linear case is between 10% and 30% for the values of the Reynolds number considered here. The value of E_0 has been successively bisected in order to determine with an accuracy of two digits the *nonlinearity threshold*, i.e. the initial energy at which the nonlinear optimal localizes and the energy gain increases by more than 10% with respect to the linear value. The values of this energy threshold are shown in Figure III.1 (a) for all considered values of Re; they appear well fitted by the scaling law $E_{0th} \propto Re^{-2.36}$. The corresponding energy gain at target time obtained by nonlinear optimization is provided in figure III.1 (b). For all considered Reynolds numbers, the energy gain increases by two order of magnitude in only 10 time units, increasing with Re following a law $Re^{0.84}$.

It is noteworthy that the value of the nonlinearity threshold is greater than the minimal energy capable of inducing transition, as one would anticipate. For example, we have performed optimizations and bisections for $T_{opt} = 50$ and $Re = 4000$ finding a transition energy threshold of about 1×10^{-7} (see table II.2) which is one order of magnitude lower than the energy corresponding to the nonlinearity threshold. On the other hand, the energy at the *nonlinearity threshold* is not very high since we have verified that the linear optimal perturbation rescaled with E_{0th} does not lead to transition. In order to indicate the distance of the nonlinearity threshold from the laminar-turbulent boundary for each optimal perturbation, figure III.1 (a) also provides the rescaled energy level necessary for placing each optimal perturbation (computed at the nonlinearity threshold) on the laminar-turbulent boundary. Notice that the scaling law for the transition threshold ($E(0) \propto Re^{-2.35}$, corresponding about to a $Re^{-1.2}$ scaling on the amplitude) is not far from the value provided by the experimental analysis of Cohen et al. (2009), who found a scaling law on the threshold amplitude leading to transition of $A \propto Re^{-3/2}$ using wall-normal flow injection for inducing hairpin vortices.

Figure III.2 (a) shows the nonlinear optimal perturbation obtained for $(Re, E_0) = (4000, 2\times 10^{-6})$, composed at $t = 0$ of several thin tubes of counter-rotating vorticity alternated in the spanwise direction and fully localized in space. The vortices are characterized by a large streamwise vorticity component and are tilted against the base flow, confirming the presence of linear energy growth mechanisms such as the Orr (Orr, 1907) and the lift-up (Landahl, 1980) mechanisms. However, this optimal solution is strongly different from the linear ones computed for the same flow due to: i) its strong localization; ii) its smaller wavelength in the spanwise direction; iii) the presence of an inclination of the vortical structures with respect to the streamwise direction. In particular, figure III.2 (a) shows

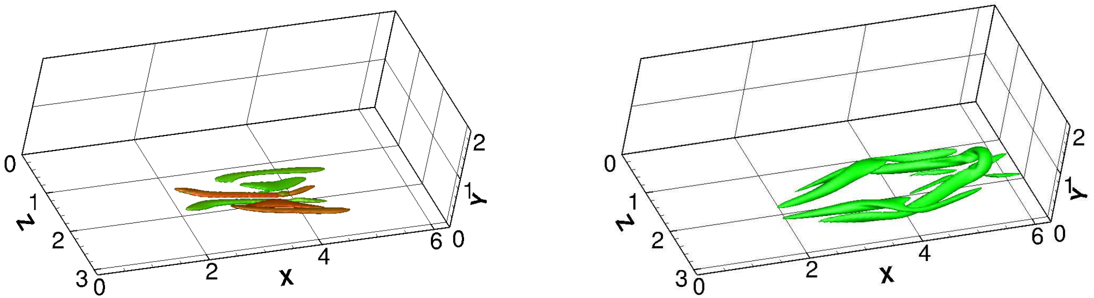

(a) t=0 (b) t=10

Figure III.2: Isosurfaces of the Q-criterion colored by the stream wise vorticity value for the nonlinear optimal perturbation obtained for $Re = 4000$, $T_{opt} = 10$, and $E_0 = 2 \times 10^{-6}$: (a) $t = 0$, $Q = 0.01$ ($Q_{max} = 0.086$) and (b) $t = 10$, $Q = 0.2$ ($Q_{max} = 3.88$).

three pairs of vortices, all of them having different streamwise inclination and length, characterized by a streamwise vorticity of alternating sign. One can observe that the two inner pairs of vortices at the center of the structure are very close to each other. When such a structure evolves in time, a strong interaction of the vortices occurs immediately after the tilting in the streamwise direction. Therefore, a “hot spot” is created, leading to the formation of the hairpin vortex at target time $t = T_{opt} = 10$, as shown in figure III.2 (b). It is also noteworthy that, unlike other parallel shear flows, such as Couette flow (Cherubini and De Palma, 2013), this nonlinear optimal structure is characterized by a symmetry with respect to a $z - const$ plane, which is maintained when the initial energy E_0 is increased. We have verified in the previous chapter that the optimal perturbation is characterized by this symmetry only for small target times ($T_{opt} \leq 16$); for target times typical of the lift-up mechanism, the optimal perturbation strongly resembles the one found in Couette flow (Cherubini and De Palma, 2013). Figure III.3 (a) clearly shows the symmetry of the streamwise and wall-normal velocity components, whereas the spanwise component is antisymmetric with respect to a $z-$constant axis, recalling the structure of varicose perturbations (Schmid and Henningson, 2012). Moreover, it is worth noting that the streamwise and wall-normal components of the velocity clearly show a Λ structure oriented against the flow. This structure, once tilted by the Orr mechanism, becomes a precursor of the hairpin vortex. Very similar structures are found for different Reynolds numbers, as shown in figures III.3 (d-f) for $Re = 2000$, although the latter perturbations are characterized by larger amplitudes (see the scaling in figure III.1).

Direct numerical simulation (DNS) has been employed to study the time evolution of the initial optimal perturbation into a hairpin vortex and its subsequent transition to turbulence. The nonlinear optimal perturbation computed for $Re = 4000$ with $E_0 = 2 \times 10^{-6}$, has been used to initialize the computation. The results are shown in figure III.4 providing the rms values of velocity (left) and vorticity (right) versus time. It appears that all of the velocity and vorticity components grow together until reaching transition in a relatively short time (at $t \approx 50$). It is noteworthy that in other transition scenarios, such as oblique and streaks instability (see Schmid and Henningson (2012)), the streamwise velocity experiences a much larger growth than the other components at short times. Snapshots of the time evolution of the vorticity (green) and of the negative streamwise velocity (black) are provided in figure III.5. The initial vortex tubes are alternated in z

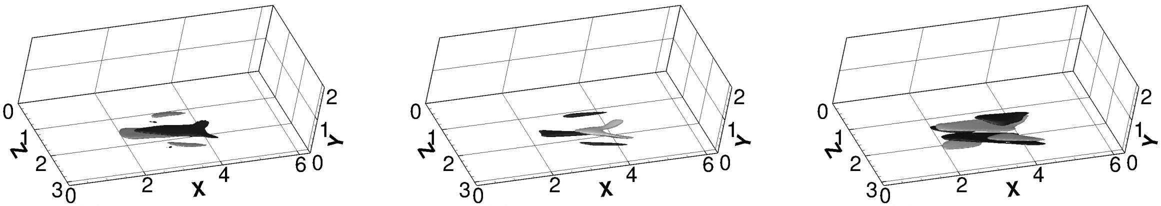

(a) u, $Re = 4000$ (b) v, $Re = 4000$ (c) w, $Re = 4000$

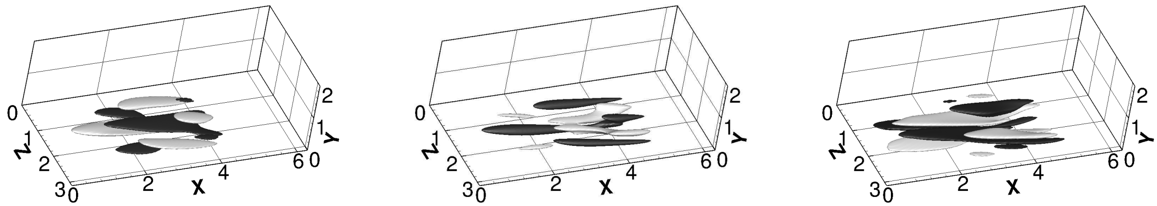

(d) u, $Re = 2000$ (e) v, $Re = 2000$ (f) w, $Re = 2000$

Figure III.3: Isosurfaces of the three velocity components (light grey for positive and black for negative values, $u, v, w = \pm 0.01$) of the nonlinear optimal perturbation for $T_{opt} = 10$: (top frames) $E_0 = 2 \times 10^{-6}$, $Re = 4000$; and (bottom frames) $E_0 = 1 \times 10^{-5}$, $Re = 2000$.

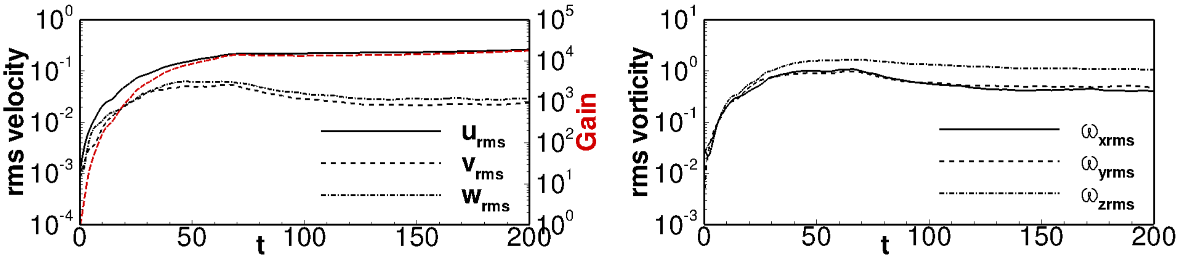

Figure III.4: Time evolution of the energy gain, velocity (left) and vorticity (right) rms values for the nonlinear optimal perturbation with $Re = 4000$, $E_0 = 2 \times 10^{-6}$, and $T_{opt} = 10$

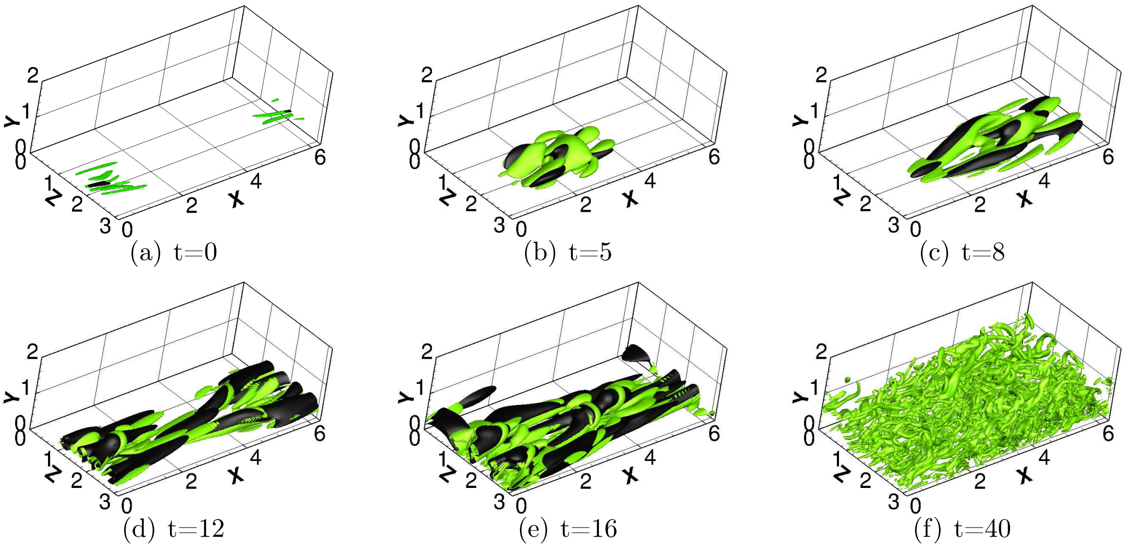

(a) t=0 (b) t=5 (c) t=8

(d) t=12 (e) t=16 (f) t=40

Figure III.5: Time evolution of the nonlinear optimal perturbation for $Re = 4000$, $T_{opt} = 10$, and $E_0 = 2 \times 10^{-6}$: Isosurface of Q-criterion ((a-e) $Q = 0.02$; (f) $Q = 0.1$, green) and streamwise velocity disturbance ($u = -0.03$, black). $Q_{max} = 0.086, 1.03, 1.99, 7.5, 21.5, 35.4$ for figures (a) to (f), respectively.

and have opposite inclination with respect to the streamwise direction (see figure III.5 (a)), so that the downstream tilting due to the Orr mechanism induces already at $t = 4$ the merging of two of these vortices in a tube of spanwise vorticity resembling a hairpin head (see frames (b)-(c)). Patches of positive and negative streamwise velocity can be observed in the flow; for $t \leq T_{opt}$ they appear rather localized in the streamwise direction (frame (c)) and they elongate in the streamwise direction, creating bent streaks only at times larger than the target time (frames (d-e)). It appears that the hairpin head is originated by a strong localized streamwise velocity defect (Adrian, 2007), which is rather large already at $t = 0$ (see the rms values in figure III.1). This defect further increases its amplitude due to the Orr mechanism and to a *modified lift-up* mechanism (see Cherubini et al. (2011b)) driven by the initial vortex tubes, until inducing local inflection points in the instantaneous velocity profile. The dynamics of the nonlinear optimal perturbation shares some important features with the dynamics of the finite-amplitude perturbations analyzed by Suponitsky et al. (2005). In particular, those authors observed the formation of a single hairpin vortex by initial Gaussian vortices of maximum vorticity magnitude $\boldsymbol{\omega}_{max} > 1$ and streamwise characteristic length $L < 5$. Such constraints are satisfied by the nonlinear optimal perturbations obtained here which is characterized by $\boldsymbol{\omega}_{max} \approx 1.8$ and $L \approx 2.5$. Thus, to better analyze the dynamics of the nonlinear optimal perturbation, we have studied the evolution of the main vortical structures in time following the approach of Suponitsky et al. (2005). Let us define the center of the vortical structure (CVS), whose coordinates are defined by the following equation:

$$X_i = \frac{\int_V \mid \boldsymbol{\omega} \mid^2 x_i dV}{\int_V \mid \boldsymbol{\omega} \mid^2 dV}, \tag{III.2}$$

where $\mid \boldsymbol{\omega} \mid$ is the magnitude of the vorticity vector, the denominator is the enstrophy integral, and the index $i = 1, 2, 3$ represents Cartesian components. To identify the spatial

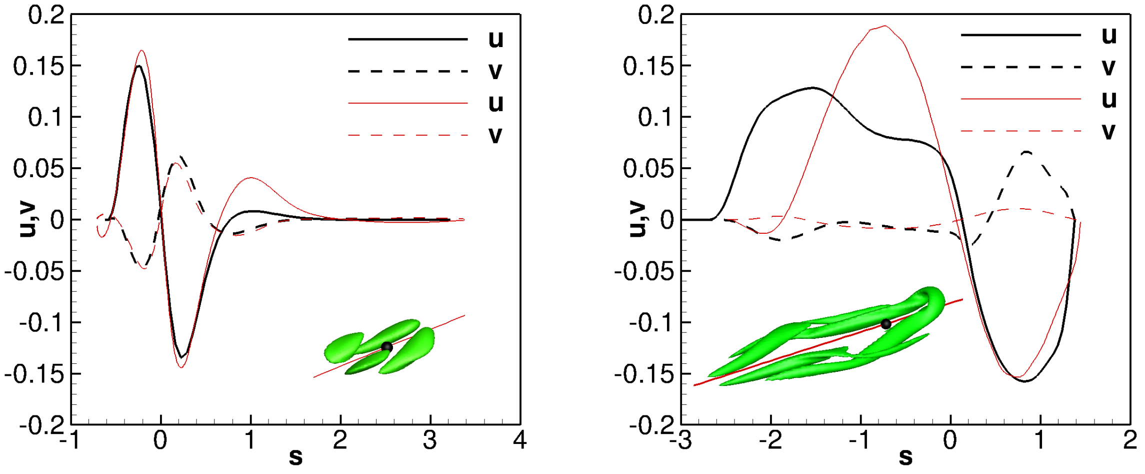

(a) t=5

(b) t=10

Figure III.6: Velocity profile along the principal axis of the TED extracted at two different times from the DNS (black) and the linearized DNS (red), initialized by the nonlinear optimal at $(Re, E_0) = (4000, 2 \times 10^{-6})$. The insets show the Q-criterion surfaces (left: $Q = 0.2$ and $Q_{max} = 1.03$; right: $Q = 0.3$ and $Q_{max} = 3.9$; green) and the principal axis (red lines) at two different times. The dot indicates the CVS.

orientation of the vortical structure centered at X_i, we employ the tensor of enstrophy distribution (TED), defined as follows:

$$T_{ij} = \int_V \mid \boldsymbol{\omega} \mid^2 (x_i - X_i)(x_j - X_j) dV. \tag{III.3}$$

Since T_{ij} is a symmetric tensor, all its eigenvalues are real. The eigenvector associated with the largest eigenvalue identifies the direction of the *principal axis* of the vortex, along which the vortex has the largest extension (Suponitsky et al., 2005). The insets in figures III.6 (a) and (b) show by red lines the principal axis of the vortical structures (represented in green by the Q criterion surfaces) extracted from the DNS at $t = 5$ and $t = 10$, respectively. Being the flow structures mainly aligned with the principal axis, we evaluate along this axis the distribution of the streamwise and wall-normal velocity components. The black lines in figures III.6 (a) and (b) show such distributions versus the abscissa s along the principal axis ($s = 0$ at the CVS) at two different times. At $t = 5$ (figure III.6 (a)) we can observe that the velocity components u and v mostly have opposite sign and are equal to zero for $s = 0$. This behaviour recalls a fundamental feature of eddy motion in wall turbulence, namely, fluctuations have higher probability of spending time in the second (Q2) and fourth (Q4) quadrants of the $u - v$ plane (Adrian, 2007), inducing two kind of events: i) *ejections*, characterized by negative streamwise fluctuations lifted away from the wall by positive wall-normal fluctuations; ii) *sweeps*, characterized by positive streamwise fluctuations being transported toward the wall. To confirm such a similarity, we have computed the spatial probability density function (PDF) of the perturbation velocity components at different times. Figure III.7 shows the PDF values (in a logarithmic scale) of the streamwise and wall-normal components of the velocity

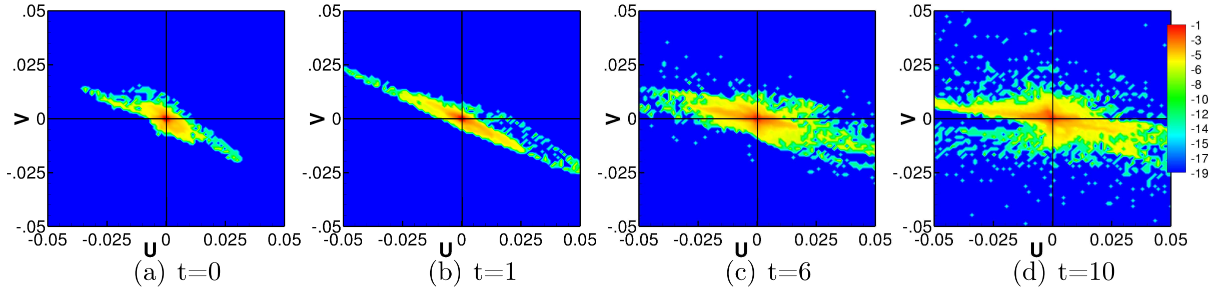

(a) t=0 (b) t=1 (c) t=6 (d) t=10

Figure III.7: Contours of the logarithm of the probability density function of the wall-normal and streamwise velocity disturbance in a $u - v$ plane ($w = 0$) for $0 \leq y \leq 1$, extracted at $t = 0, 1, 6, 10$ from a DNS initialized with the nonlinear optimal with $T_{opt} = 10$ and $E_0 = 2 \times 10^{-6}$. The values of the logarithm of the PDF have been normalized with respect to the total number of points of the computational domain.

perturbation, confirming the presence of ejections and sweeps already at $t = 0$ and up to the time of formation of the hairpin vortex. For instance, in Figure III.6 (a) a sweep is observed upstream of the CVS ($s < 0$) followed by a strong ejection and a weak sweep downstream of the CVS ($s > 0$). At $t \approx 10$, the hairpin head is formed downstream of the CVS ($s > 0$), in correspondence with an ejection, as shown in figure III.6 (b). This is not surprising since, as found in wall turbulence for a channel flow, the eddy associated to an ejection has a hairpin vortex shape (Adrian, 2007). Comparing figure III.6 (a) and (b), one can observe that when the hairpin head is formed, the zone of ejection increases its intensity, while the sweep region enlarges in the streamwise direction, reducing its intensity. When the evolution of the same initial perturbation is computed by a DNS based on the solution of the linearized NS equations, the velocity distribution for $t > 5$ is characterized by increasing values of u and much lower values of v, as provided by the red thin lines in figure III.6. Therefore, in the linearized case, streaks with larger intensity will be formed due to the lift-up effect but they will not be associated with wall-normal velocities of opposite signs, rapidly damping the ejection event that is responsible for the lifting of the hairpin head, thus preventing the creation of the hairpin structure. Figure III.8 shows that the alternation of strong sweeps and ejections found at $t = 0$ is maintained at larger times, thus representing the basic element for the rapid hairpin formation. Moreover, in figure III.8 (b) one can observe that the hairpin head is placed right in the zone of interaction of the stronger ejection with the stronger sweep, indicating that the formation of the spanwise vortex connecting the initial quasi-streamwise vortices might be a consequence of an inflectional instability taking place in this interaction zone. This observation is in agreement with the minimal flow-element model proposed by Cohen et al. (2014), in which a wavy spanwise vortex sheet was necessary to provide the inflection points for creating hairpin vortices from streamwise counter-rotating vortex pairs. Figure III.9 (a) and (b) provide the instantaneous velocity and vorticity profiles at $t = 10$, computed solving the nonlinear and the linearized NS equations, respectively, extracted along a vertical axis passing through the hairpin head obtained in the nonlinear case. In figure III.9 (a) one can observe an inflection point, located at the ordinate corresponding to the peak of vorticity coinciding with the hairpin head (at $y \approx 0.7$), in the outer zone of the velocity profile; whereas, in the near-wall region, at $y \approx 0.15$, one can observe the

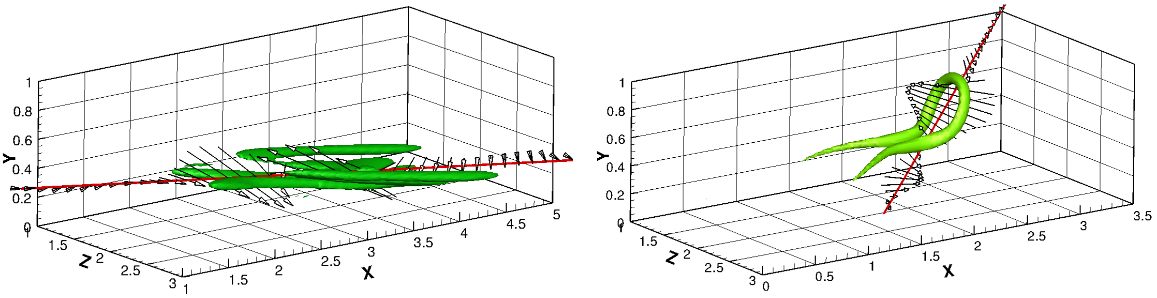

(a) t=0 (b) t=14

Figure III.8: Wall-normal and streamwise components of the velocity vector disturbance along the principal axis of the TED for the nonlinear optimal with $E_0 = 2 \times 10^{-6}$: (a) $t = 0$, (b) $t = 14$. Isosurface of the Q-criterion ((a) $Q = 0.01$ and $Q_{max} = 0.086$, (b) $Q = 4$ and $Q_{max} = 12.05$)

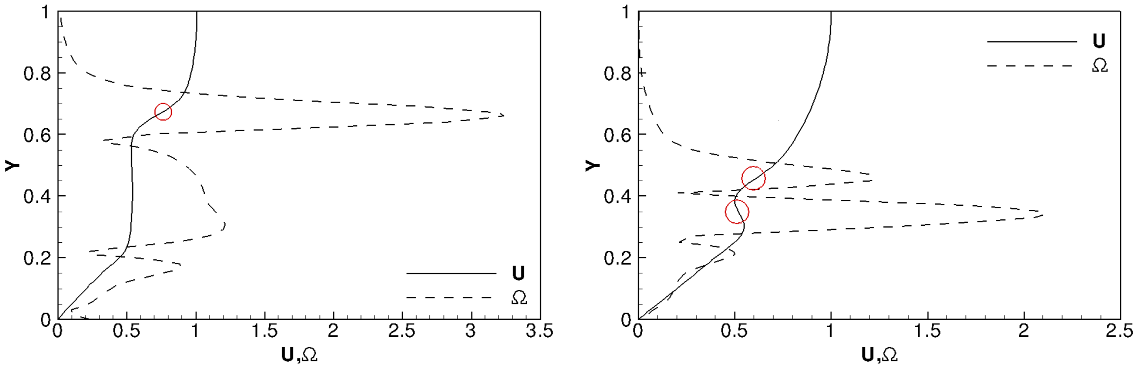

(a) t=10 nonlinear DNS (b) t=10 linearized DNS

Figure III.9: Streamwise velocity (solid lines) and vorticity magnitude (dashed lines) profiles at $t = 10$ along a wall-normal line passing through the hairpin head computed by the DNS (a) and by the linearized DNS (b), initialized with the nonlinear optimal for $E_0 = 2 \times 10^{-6}$. Circles indicate inflection points.

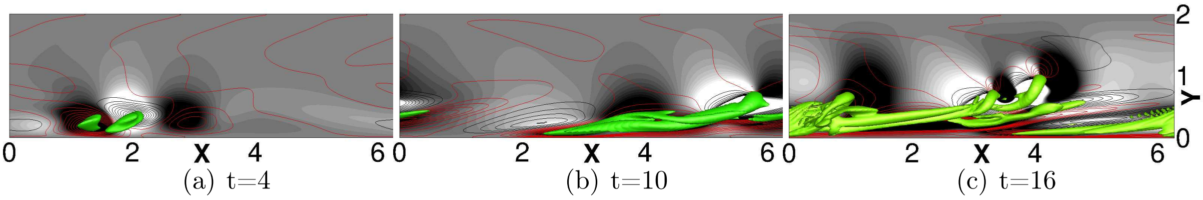

(a) t=4 (b) t=10 (c) t=16

Figure III.10: Time evolution of the nonlinear optimal perturbation obtained for $T_{opt} = 10$ and $E_0 = 2 \times 10^{-6}$ on the plane $z = 2$. Isosurfaces of the Q-criterion ($Q = 0.1$, green), isolines of the streamwise velocity disturbance (red positive, black negative), and contours of the wall-normal velocity disturbance (white positive, black negative). $Q_{max} = 0.61, 3.88, 21.52$ for figures (a) to (c), respectively.

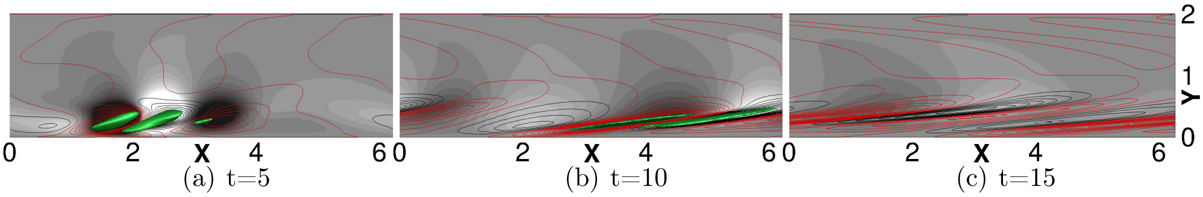

(a) t=5 (b) t=10 (c) t=15

Figure III.11: Time evolution of the nonlinear optimal perturbation obtained for $T_{opt} = 10$ and $E_0 = 2 \times 10^{-6}$ on the plane $z = 2$ obtained by a linearized DNS. Isosurfaces of the Q-criterion ($Q = 0.1$, green), isolines of the streamwise velocity disturbance (red positive, black negative), and contours of the wall-normal velocity disturbance (white positive, black negative). $Q_{max} = 0.79, 0.25, 0.05$ for figures (a) to (c), respectively.

deformation of the velocity profile induced by the formation of a negative streak. The inflection point is observed in the linearized case as well (figure III.9 (b)), but it is placed closer to the wall ($y \approx 0.4$), consistent with a shear layer instability induced by a streak. In the nonlinear case, the vorticity peak moves in time towards the center of the channel, reaching an amplitude one order of magnitude larger than that of the linearized case. When the head of the hairpin is pushed by the wall-normal perturbation toward the center of the channel, it is advected by the base flow at a higher velocity with respect to the part near the wall, stretching the whole vortical structure in the streamwise direction. Then, due to conservation of circulation, stretching provides a further growth of the vorticity, sustaining the hairpin vortex and allowing secondary hairpin structures to be created (Adrian, 2007). The time evolution of the hairpin structure is visualized in figure III.10, providing DNS snapshots showing isosurfaces of the Q-criterion (green), isolines of the streamwise velocity disturbance (red positive and black negative), and isocontours of the wall-normal velocity (white positive and black negative). One can notice the alternation of patches of u and v with different signs, spread all over the domain, and their effect on the lifting and stretching of the hairpin structure. Nonlinear effects are crucial to sustain the alternation of the u and v perturbation components as well as the vortical structures. This can be clearly inferred by comparing figure III.10 with figure III.11, showing the time evolution of the nonlinear optimal perturbation obtained by a linearized DNS.

III.4 Conclusions

Nonlinear optimal perturbations having shape of hairpin vortices at target time have been computed for the plane Poiseuille flow, using small target times and finite initial energies. The corresponding initial optimal perturbations are localized in space and composed of spanwise-alternated thin vorticity tubes inclined with respect to the streamwise direction and placed around regions of large streamwise and wall-normal perturbations of opposite sign resembling localized sweeps and ejections. The streamwise alternation of sweeps and ejections induces strong streamwise velocity defects which generate an inflectional point in the velocity profile. Inflectional instability thus create a spanwise vorticity tube that is lifted and stretched, generating the hairpin head. Transition is triggered suddenly and occurs in a very localized region, inducing the formation of a hairpin structure already at target time ($t = 10$). The initial flow structure able to create a hairpin vortex in a very short time ($t \approx 10$), rapidly leading the flow to turbulence, may be considered as a hairpin precursor, characterized by alternated sweeps and ejections of amplitude varying with Re^{-1}. It appears that, when nonlinear effects are neglected, the wall-normal velocity component is not maintained in time, while the streamwise components largely increase due to the lift-up mechanism, hampering the creation of the hairpin vortex and the subsequent fast transition to turbulence.

Thus, we have shown that, for the plane Poiseuille flow, a suitable combination of localized sweeps and ejections is capable of maximizing the energy growth in a short time interval generating a hairpin structure and transition towards turbulence. This nonlinear optimal growth mechanism could be the reason why the final stages of transition to turbulence and turbulent shear flows are characterized by a high density of hairpin structures. Future work will aim at extending these findings to different shear flows, as well as to noisy or turbulent environments.

This result confirms the fact that hairpin vortices are strong energetic and short-time living structures, at least in transition channel flow. Nevertheless, those structures are also observed in fully turbulent flows and are usually associated to the presence of bursting events. An extension of this analysis to turbulent channel flow might unravel important features of these recurrent events and gives more informations about the structures populating such shear flows. Are burst events really associated to the presence of hairpin vortices? Which kind of coherent structures populating turbulent shear flows are relevant in the dynamics? The next two chapters will try to answer to those questions.

Chapter IV

Optimal bursts in turbulent channel flow

Contents

IV.1 Introduction **49**
IV.2 Problem formulation **50**
IV.3 Results **51**
    IV.3.1 Optimal perturbations 51
    IV.3.2 Time evolution of the outer optimal perturbation 62
IV.4 Conclusion **67**
IV.5 Appendix **69**

IV.1 Introduction

Bursts are recurrent, transient, highly energetic events characterized by localized variations of velocity and vorticity in turbulent wall-bounded flows. In this chapter, a nonlinear energy optimization strategy is employed to investigate whether the origin of such bursting events in a turbulent channel flow can be related to the presence of high-amplitude coherent structures. The results show that bursting events correspond to optimal-energy flow structures embedded in the fully-turbulent flow. In particular, optimal structures inducing energy peaks at short time are initially composed of highly oscillating vortices and streaks near the wall. At moderate friction Reynolds numbers, through the bursts, energy is exchanged between the streaks and packets of hairpin vortices of different sizes reaching the outer scale. Such an optimal flow configuration reproduces well the spatial spectra as well as the probability density function typical of turbulent flows, recovering the mechanism of direct-inverse energy cascade. These results represent an important step towards understanding the dynamics of turbulence at moderate Reynolds numbers and paves the way to new nonlinear techniques to manipulate and control the self-sustained turbulence dynamics.

IV.2 Problem formulation

We consider a turbulent channel flow at friction Reynolds number $Re_\tau = u_\tau h/\nu = 180$; u_τ, h, and ν being the friction velocity, the half-height of the channel, and the kinematic viscosity, respectively. Since two scalings of the variables are employed, variables expressed in inner units (normalized using u_τ and viscous length scale, $\delta_\nu = \nu/u_\tau$) are indicated with the superscript $^+$, whereas variables without any superscript are scaled in outer units (normalized using the centerline velocity U_c and h).

Incompressible flow is computed by solving the Navier–Stokes equations (NS) in a box having streamwise, wall-normal, and spanwise dimensions equal to $l_x = 4\pi$, $l_y = 2$, $l_z = 2\pi$, respectively. No-slip boundary conditions for the three velocity components are imposed at the walls, whereas periodicity is prescribed in the streamwise and spanwise directions. The nonlinear evolution of perturbations to the mean turbulent velocity profile is computed by solving the following system of equations ($\widetilde{NS}$):

$$\begin{aligned} \frac{\partial \tilde{\mathbf{u}}}{\partial t} &= -\tilde{\mathbf{u}} \cdot \nabla \tilde{\mathbf{u}} - \tilde{\mathbf{u}} \cdot \nabla \mathbf{U} - \mathbf{U} \cdot \nabla \tilde{\mathbf{u}} - \nabla \tilde{\mathrm{p}} + \frac{1}{Re} \nabla^2 \tilde{\mathbf{u}} + \nabla \cdot \tau, \\ \nabla \cdot \tilde{\mathbf{u}} &= 0, \end{aligned} \tag{IV.1}$$

where $\widetilde{\mathbf{u}} = (\widetilde{u}, \widetilde{v}, \widetilde{w})^T$ and $\tilde{\mathrm{p}}$ represent the velocity and pressure perturbations, respectively, which are composed of a coherent and a fluctuating part; $\mathbf{U}$ is the mean turbulent flow velocity profile; τ is the Reynolds stress tensor forcing the mean turbulent velocity profile (see equation (IV.9) in the Appendix IV.5); and $Re = U_c h/\nu$. The Reynolds stress tensor is computed a-priori by Direct Numerical Simulation (DNS) of the fully turbulent flow. Details of the derivation of equations (IV.1) are provided in the Appendix.

Using equations (IV.1), we look for perturbations capable of inducing a peak of kinetic energy in a finite time T. Thus, we maximize the kinetic energy growth at time T, $G(T) = E(T)/E(0)$, where

$$E(t) = \{\tilde{\mathbf{u}}(t), \tilde{\mathbf{u}}(t)\} = \int_V \left(\widetilde{u}^2 + \widetilde{v}^2 + \widetilde{w}^2\right)(t) dV, \tag{IV.2}$$

and V is the volume of the computational domain. The energy gain $G(T)$ is maximized using a Lagrange multiplier approach, the initial energy E_0, equations (IV.1), and the incompressibility condition is imposed as constraints using the Lagrange multipliers or adjoint variables $(\widetilde{\mathbf{u}}^\dagger, \mathrm{p}^\dagger, \lambda)$, as follows:

$$\mathfrak{L} = \frac{E(T)}{E(0)} - \int_0^T \left\{\widetilde{\mathbf{u}}^\dagger, \widetilde{NS}\right\} dt - \int_0^T \left\{\widetilde{p}^\dagger, (\nabla \cdot \widetilde{\mathbf{u}})\right\} dt - \lambda \left(\frac{E(0)}{E_0} - 1\right). \tag{IV.3}$$

Deriving the functional $\mathfrak{L}$ with respect to the variables $\widetilde{\mathbf{u}}, \widetilde{p}$, one obtains the following adjoint equations:

$$\begin{aligned} \frac{\partial \widetilde{\mathbf{u}}^\dagger}{\partial t} &= \widetilde{\mathbf{u}}^\dagger \cdot (\nabla \mathbf{U})^T - \mathbf{U} \cdot \nabla \widetilde{\mathbf{u}}^\dagger - \nabla \mathrm{p}^\dagger - \frac{1}{Re} \nabla^2 \widetilde{\mathbf{u}}^\dagger + \widetilde{\mathbf{u}}^\dagger \cdot (\nabla \widetilde{\mathbf{u}})^T - \widetilde{\mathbf{u}} \cdot \nabla \widetilde{\mathbf{u}}^\dagger, \\ \nabla \cdot \widetilde{\mathbf{u}}^\dagger &= 0, \end{aligned} \tag{IV.4}$$

as well as the gradient of $\mathfrak{L}$ with respect to the initial perturbation, which has to be nullified in order to maximize the given $\mathfrak{L}$. Following previous chapters focusing on nonlinear optimal perturbations of laminar base flows (see also Pringle et al. (2012), Cherubini et al. (2010a), Duguet et al. (2013), Rabin et al. (2012), Cherubini and De Palma (2013), Cherubini et al. (2015)), the optimisation problem is solved by direct-adjoint iterations coupled with a gradient rotation algorithm (Farano et al., 2016; Foures et al., 2013). Computations are performed using the spectral-element code NEK5000 (Fischer et al., 2008), with Legendre polynomial reconstruction of degree 7 and second-order accurate Runge-Kutta time integration (Deville et al., 2002). The iterative procedure is stopped when the relative variation between two successive direct-adjoint loops, $e = (G^n - G^{n-1})/G^n$ is smaller than 10^{-7}, n being the iteration number. Depending on the selected target time, 40 to 80 direct-adjoint iterations are needed for reaching convergence for one set of parameters, each optimization needing 100.000 to 800.000 CPU hours on an IBM cluster Intel ES 4650.

The flow parameters are chosen according to the DNS of turbulent channel flow performed by Kim et al. (1987) for $Re_\tau = 180$. The computational domain is discretized by 24, 20, and 20 elements in the x, y, and z spatial directions, respectively, obtaining a total number of grid points equal to $192 \times 160 \times 160$. For this setting we obtain approximately the values of $\Delta x^+ \approx 12$, $\Delta z^+ \approx 7$, $\Delta y^+_{max} \approx 4.4$ and $\Delta y^+_{min} \approx 0.05$, similar to those used by Kim et al. (1987). DNS has been run for about 13 inner time units (tu_τ/h) in order to evaluate the mean flow and the Reynolds stress tensor. The fully turbulent flow obtained by DNS has been validated by comparing the mean flow and the Reynolds shear stress with the results of Kim et al. (1987), finding a very good agreement (see the Appendix for details). Furthermore, the direct-adjoint routine has been validated by computing linear optimal perturbations following the approach by Pujals et al. (2009), who performed a local stability analysis by considering a monochromatic sinusoidal coherent perturbation in x and z. Although we perform a global analysis, where $\tilde{\mathbf{u}}$ depends on the three spatial coordinates without any constraint, in the linear limit we have been able to reproduce the maximum energy amplification, the associated time, as well as the shape of the optimal perturbations with their wavelength, found by a local linear optimization using the approach of Pujals et al. (2009). This result validates our direct-adjoint procedure at least in the linear limit. Finally, the nonlinear optimization approach has been validated in the laminar case with the results of Farano et al. (2015).

IV.3 Results

IV.3.1 Optimal perturbations

Nonlinear optimal coherent structures have been computed for $Re_\tau = 180$ and for different target times, T, which is a crucial independent parameter for the optimization procedure. For such a moderate value of the Reynolds number, there is not a clear spatial scale separation among the flow structures. However, structures with different scales and dynamics may be found in the inner and outer region (Chen et al., 2014). The lifetime of coherent structures populating the flow can be employed as the target time to select the scale of the structures to be optimized. Butler and Farrell (1993) have chosen as representative of the time scale of coherent structures the eddy turnover time defined as the ratio between the turbulent kinetic energy and the dissipation rate, k/ϵ. In particular,

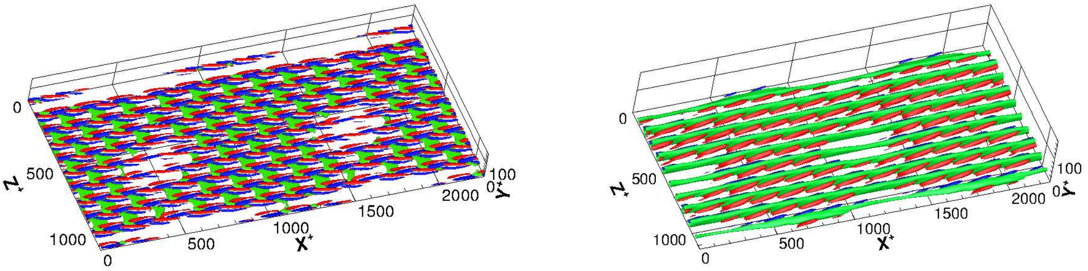
0
Z+
500
1000
0
500
1000
X+
1500
2000
100
0
Y+

(a) $t^+ = 0$ (b) $t^+ = T^+_{in}$

Figure IV.1: Shape of the optimal perturbation for $T^+_{in} = 80$ and $E_0 = 10^{-2}$ at (a) $t^+ = 0$ and (b) $t^+ = T^+_{in}$: isosurface of negative streamwise velocity (green, (a) $\tilde{u} = -0.025$, (b) $\tilde{u} = -0.18$) and Q-criterion ((a) $Q = 10^{-6}$, (b) (a) $Q = 2 \times 10^{-6}$) coloured by the value of the streamwise vorticity (positive blue, negative red).

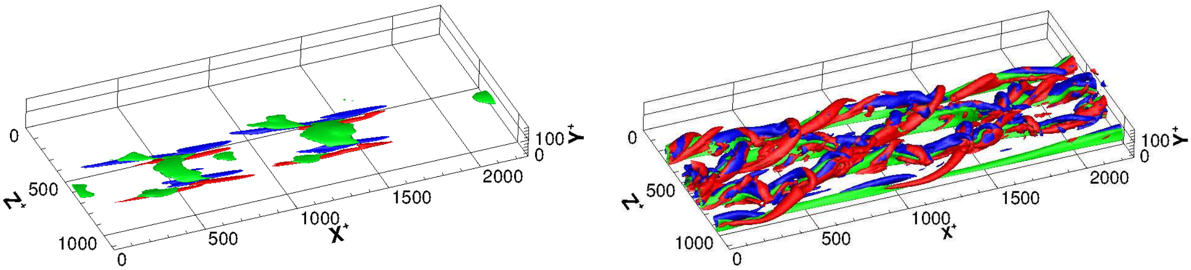
0
Z+
500
1000
0
500
1000
X+
1500
2000
100
0
Y+

(a) $t^+ = 0$ (b) $t^+ = T^+_{out}$

Figure IV.2: Shape of the optimal perturbation for $T^+_{out} = 305$ and $E_0 = 10^{-2}$ at (a) $t^+ = 0$ and (b) $t^+ = T^+_{out}$: isosurface of negative streamwise velocity (green, (a) $\tilde{u} = -0.016$, (b) $\tilde{u} = -0.3$) and Q-criterion ((a) $Q = 0.045$, (b) (a) $Q = 0.15$) coloured by the value of the streamwise vorticity (positive blue, negative red).

they consider the value of the eddy turnover time at $y^+ \approx 20$ (resulting in $T^+ = 80$ for $Re_\tau = 180$), finding optimal small-amplitude disturbances having the shape of low- and high-speed streaks with the inner typical spanwise spacing $\lambda_z^+ = 110$. Here, we employ the same criterion, choosing the inner optimization time $T_{in}^+ = 80$, ($T_{in} = 8.16$) roughly corresponding to one eddy turnover time evaluated in the buffer layer at $y^+ = 19$ (Butler and Farrell, 1993); and the outer optimization time $T_{out}^+ = 305$ ($T_{out} = 31.12$), corresponding approximately to one eddy turnover time at the centerline of the channel, consistent with that used by Pujals et al. (2009) for higher Reynolds numbers.

IV.3.1.1 Optimal perturbations at the inner time scale

The resulting nonlinear optimal finite-amplitude disturbance obtained for T_{in}^+ and $E_0 = 10^{-2}$ is shown in figure IV.1 at $t^+ = 0$ (a) and $t^+ = T_{in}^+$ (b). The initial optimal perturbation consists of alternated inclined streamwise vortices (red and blue), flanking localized regions of streamwise-velocity strong defects (green). In contrast, at T_{in}^+, the optimal disturbance consists of highly modulated streaks having a typical spanwise spacing of $\lambda_z^+ \approx 113$, surrounded by positive and negative streamwise vortices, with a spanwise spacing of $\lambda_z^+ \approx 56$; this is a typical value recovered for vortex spacing in turbulent channel flow (Panton, 2001). These nonlinear optimal streaks and vortices appear much more similar to the oscillating coherent streaky structures observed in turbulent flows than the idealized linear optimal perturbations presenting a perfect streamwise alignement (Butler and Farrell, 1993; Pujals et al., 2009). Moreover, they are localized in space in a spot-like fashion, instead of occupying homogeneously the whole computational domain like the linear optimal ones. These nonlinear optimal structures represent well the self-sustained turbulence wall cycle: linearly growing streaks saturate and oscillate due to secondary instability, regenerating new localized quasi-streamwise vortices by nonlinear coupling. Linear optimizations are able to describe only the first step of this cycle, whereas a nonlinear approach can capture all of the elements of the cycle. Notice that a very similar optimal structure has been recovered for smaller target times, made by oscillating coherent streaks and vortices at the walls, having smaller wavelength (for instance, $\lambda_z^+ \approx 65$ for $T^+ = 21.94$) but a very similar spot-like spatial localization. However, as already known (Jiménez and Moin, 1991), these streaks are not self-sustained. In fact, we have verified that the time evolution of these optimal small structures beyond the target time leads to their decay. Concerning the influence of E_0, we have observed that the optimal disturbances keep a similar structure as long as the initial energy is sufficiently high to trigger nonlinear effects.

The results obtained for the inner time scale are in good agreement with the well assessed streaky structures observed near the wall by several authors by experimental and numerical techniques (Kline et al., 1967; Panton, 2001); therefore, such results can be considered a successful validation of the proposed approach.

IV.3.1.2 Optimal perturbations at the outer time scale

Increasing the target time to the outer timescale T_{out}^+, the optimization algorithm provides a different flow structure, as shown in figure IV.2, at $t^+ = 0$ (a) and $t^+ = T_{out}^+$ (b). The

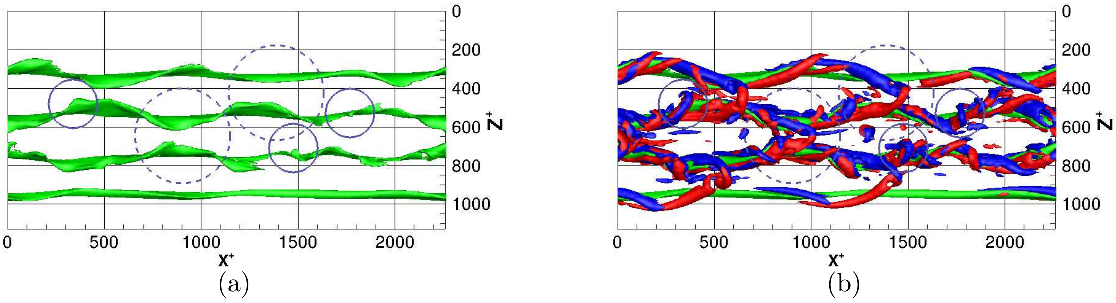
0
200
400
600
800
1000
Z⁺
0
500
1000
1500
2000
X⁺

(a) (b)

Figure IV.3: Shape of the optimal perturbation for $T^+_{out} = 305$ and $E_0 = 10^{-2}$ at $t^+ = T^+_{out}$: isosurface of negative streamwise velocity (green) (a,b); isosurface of Q-criterion coloured by contours of streamwise vorticity (positive blue, negative red) (b). The isosurface values are the same as in figure IV.2 (b). Small solid circles indicate small hairpin vortices, big dashed circles indicate big hairpin vortices.

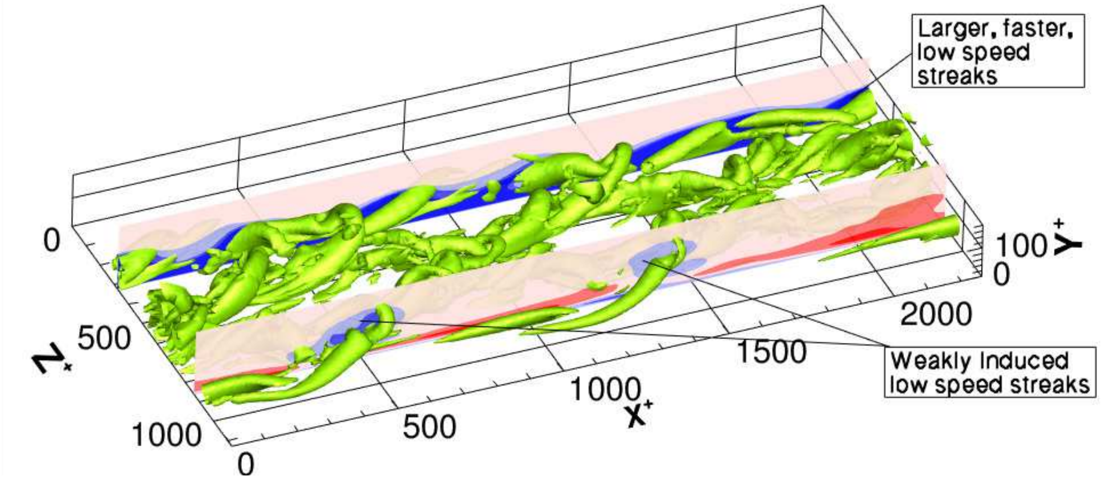
Larger, faster, low speed streaks
Weakly induced low speed streaks
0
500
1000
Z⁺
100
0
Y⁺
0
500
1000
1500
2000
X⁺

Figure IV.4: Outer optimal perturbation obtained for $T^+_{out} = 305$ and $E_0 = 10^{-2}$: isosurfaces of the Q-criterion (green) and isocontours of streamwise velocity (blue negative, red positive) on the planes $z^+ = 860$ and $z^+ = 320$. The isosurfaces values are the same as in figure IV.2 (b).

initial optimal perturbation is strongly localized in space and is characterized by alternated streamwise vortices (red and blue) near the wall and localized patches of streamwise velocity perturbations in the outer region. At $t^+ = T^+_{out}$ this initial perturbation turns into a much more complex structure, mostly composed of packets of hairpin vortices on top of highly oscillating streamwise streaks. In particular, strong vortical structures are observed at two different scales. The small-scale structures are not symmetric and have spanwise length $\lambda_z^+ \approx 100$ (consistent with the observations of Zhou et al. (1999)). They are placed on top of the low-speed streaks, apparently as a result of their sinuous instability, as shown in the solid circles in figure IV.3. On the other hand, the largest vortical structures in the dashed circles have a clear symmetric hairpin shape, with typical wavelengths $\lambda_z \approx 2h$ and $\lambda_x \approx 2.5h$, consistent with the observations of turbulent bulges and packets of hairpin of length $\approx 2h$ (Adrian, 2007) and with the dimensions of the largest attached eddy computed using large-eddy simulation by Hwang and Bengana (2016). As one can observe in figure IV.3, these hairpin vortices originate from the merging of the streamwise vortical structures flanking two distinct low-speed streaks (Adrian, 2007), which are modulated quasi-symmetrically with respect to a streamwise axis passing between them. Large-scale low-speed streaks, with $\lambda_z \approx 2.2h$ and $\lambda_x \approx 5h$ are also induced between the legs of these large hairpin structures; these streaks can be observed in figure IV.4 in a $z-$constant plane passing through the head of two large hairpin vortices (blue contours in the plane at $z^+ = 860$ for low-speed large-scale streaks). However, the streaks with higher intensity are those close to the wall, as shown by the blue contours in the $z^+ = 320$ plane. These features recall those found for packets of hairpin vortices described by Adrian (2007), who observed that the larger the packets, the weaker the backward-induced flow, due to the larger distance of the side vortices from the center of the hairpin loop. The same author also conjectured that the passage of hairpin packets can explain the occurrence of multiple second- and fourth-quadrant events typical of turbulent bursts.

IV.3.1.3 Probability density function analysis

We wonder whether this optimal perturbation characterized by a very complex shape, optimizing the energy at the outer spatial scale, might be a possible candidate for explaning the onset of transient recurrent bursts on top of the long-living oscillating streaks. To investigate whether ejections and sweeps could characterize the dynamics of the nonlinear optimal structure, indicating a strong correlation with bursting events, we have computed the probability density function (PDF) of the streamwise and wall-normal velocity disturbance at different wall-normal positions for the optimal perturbation at $t^+ = T^+_{out}$. Figure IV.5 shows, for $y^+ = 10,\ 50,\ 100$ (from top to bottom, left column), that the PDF is concentrated in the Q2 and Q4 quadrants of the $\tilde{u}-\tilde{v}$ plane, indicating the prevalence of ejection and sweep events, exactly as in a strong bursting event. Going from the buffer to the outer region, the strongest contribution to the Reynolds stress slightly moves towards the sweeps region, suggesting a mechanism of energy redistribution from the outer to the wall region by means of sweep events (Jiménez, 1999). This PDF has been compared with that extracted from the DNS of the turbulent flow, shown in the right column of figure IV.5 for corresponding wall-normal positions. The two set of PDF distributions are very similar, although the data in the left column are obtained by using only the perturbation at a given time, whereas the results in the right column are computed from the statistics of the DNS. On the other hand, the PDF of the inner optimal perturbation (not shown) is quite similar to that extracted from the DNS only at $y^+ = 10$, $\tilde{u}$ and $\tilde{v}$ rapidly fading away towards the center of the channel. This indicates that, while the inner optimal disturbance is representative of the self-sustained wall cycle, the outer nonlinear optimal disturbance is representative of bursting events populating the fully turbulent channel flow.

IV.3.1.4 Topology analysis

The outer optimal disturbance has been found to show the same typical features of a bursting event. However, one may wonder whether its complex structure is well representative of the vortical disturbances observed in fully turbulent conditions. In order to answer to this question, we have compared the main vorticity features of the optimal structures with those of the fully turbulent flow (Blackburn et al., 1996). Chong et al. (1990) proposed a topological analysis of vortical flow structures based on the first three invariants of the velocity gradient tensor $A = \nabla \mathbf{u}$, here referred to as $P = -tr(A)$, $Q = 0.5(P^2 - tr(A^2))$, and $R = -det(A)$, respectively. Incompressible flows being restrained to the $P = 0$ space, the flow topologies that can be found in the channel flow considered here can be classified depending on the values of Q and R: flow structures which fall in the upper region of the $Q - R$ plane are called stable (left) or unstable (right) focus, representing a vortex stretching or compression, respectively; whereas, in the lower region of the plane, stable (left) and unstable (right) nodes/saddle/saddle are found. The shapes of the local flow field corresponding to these topologies are sketched in figure IV.6. As described by Blackburn et al. (1996), for a turbulent channel flow, moving from the wall to the centerline of the channel, the PDF of Q and R will vary, indicating the different structures found at different wall-normal positions in the flow. Figure IV.7 provides the PDF of Q and R for the outer optimal disturbance (left column) and for the DNS of the corresponding turbulent flow (right column) at $y^+ = 10, 50, 100$. One can notice that in both cases, close to the wall, the PDFs are rather uniformly distributed among all quadrants of the $Q - R$ plane. On the other hand, towards the centerline of the channel, the dominant structures are tube-like shaped as those sketched in figure IV.6 above the line $D = 0$. Moreover, the PDFs spread mostly in the second and fourth quadrants, indicating a predominance of stable focus/stretching and unstable node/saddle/saddle topologies. As discussed by Blackburn et al. (1996) for the case of turbulent channel flow, stable focus/stretching topologies appear to provide a link between the inner and outer regions of the flow, with structures originating in the viscous sublayer and extending towards the outer region, mostly associated with hairpin or horseshoe shapes. The presence of hairpin vortices in the outer optimal disturbance and the fact that its Q-R topology distribution reproduces well that of the corresponding fully turbulent flow may indicate the presence of those structures in fully turbulent conditions, at least for the moderate value of the Reynolds number used here. On the other hand, the inner optimal disturbance, which does not show hairpin vortices, is characterized by a different topology distribution, without any clear preference for the stable focus/stretching and the unstable node/saddle/saddle topologies, with the vortices rapidly fading away far from the wall (not shown). Therefore, the similarity of the outer optimal flow topology with that of the fully turbulent flow suggests that these structures are well representative of the vortical dynamics of a turbulent channel

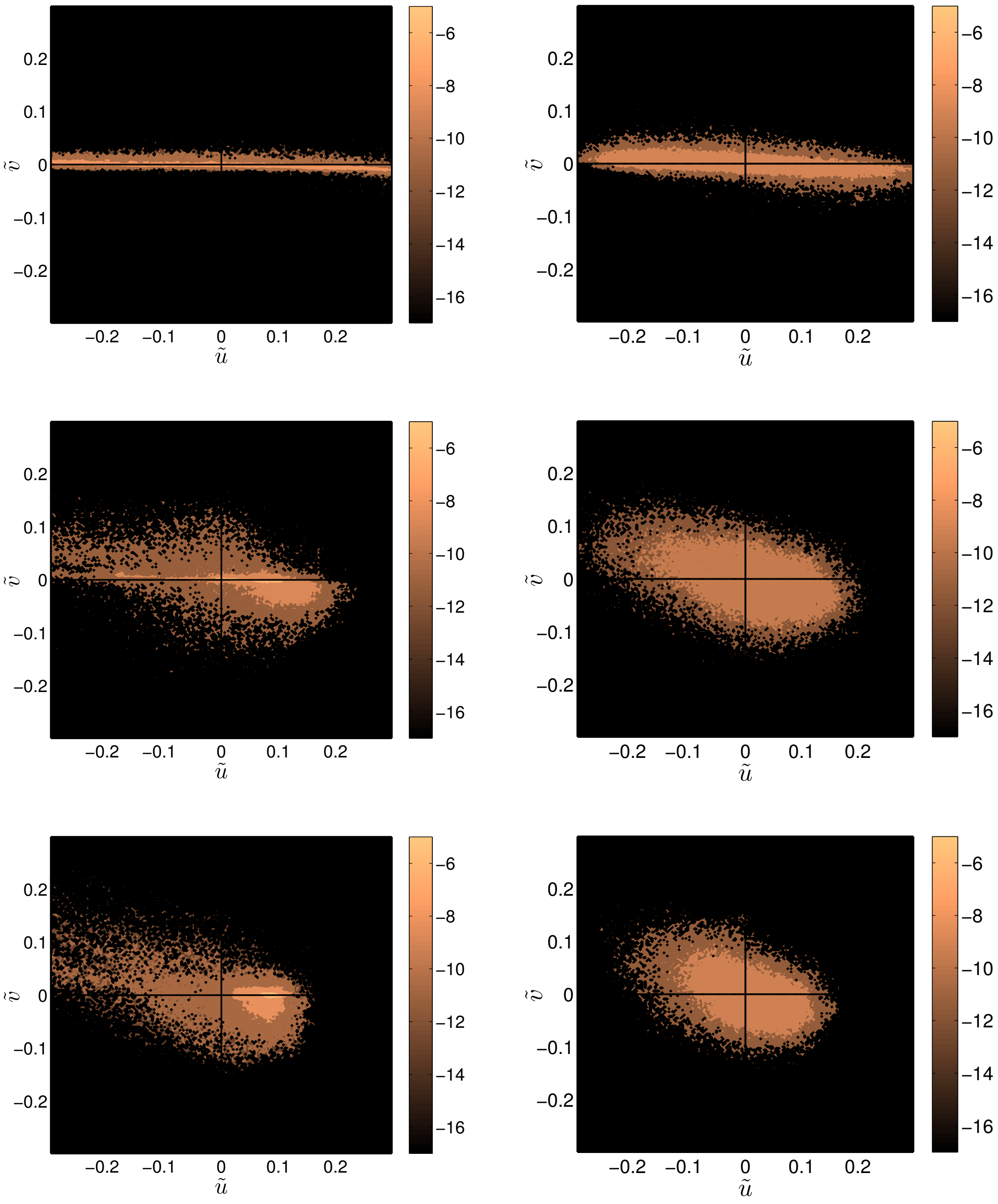

Figure IV.5: Logarithm of the PDF of the streamwise and wall normal velocity for the outer optimal structures at $t = T_{out}$ (left) and for the fully turbulent flow (right) at different constant y^+-planes: $y^+ = 10$, $y^+ = 50$, $y^+ = 100$, from top to bottom.

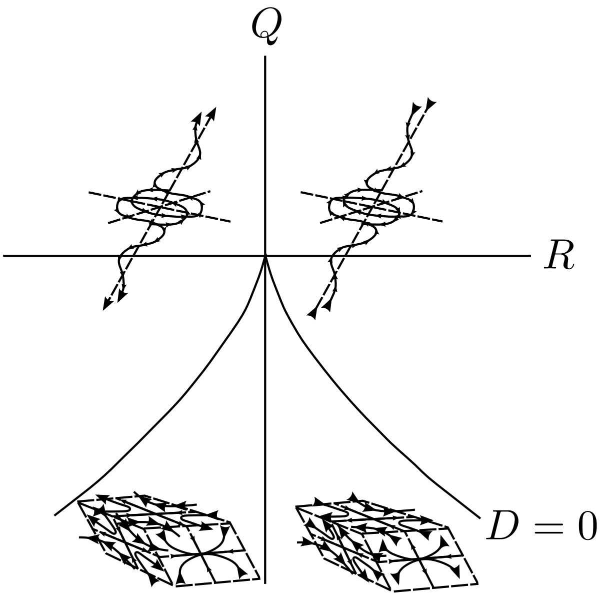

Figure IV.6: Sketch of the flow topologies associated with different regions of the $Q-R$ plane, Q and R being the second and third invariant of the velocity gradient tensor, and $D=(27/4)R^2+Q^3$ (Blackburn et al., 1996).

flow from the wall towards the centerline of the channel.

IV.3.1.5 Spectra analysis

We have found that the outer optimal disturbance reproduces well the vortical topology of the corresponding turbulent channel flow; now, we want to investigate whether the size of these vortices and their dominant wavelengths is representative of the broadband spectrum of wavelengths typical of turbulent flows. At this purpose, we have extracted the streamwise and spanwise premultiplied energy density spectra from the nonlinear optimal disturbances at T^+_{in} and T^+_{out}, and compared them with the same spectra extracted from the DNS of the corresponding fully developed turbulent flow. Figure IV.8 provides the premultiplied spectrum distributions along the wall-normal direction obtained from the DNS (shaded contours) and from the optimal disturbances at T^+_{in} (light blue isolines) and at T^+_{out} (black isolines). The spanwise (left column) and streamwise (right column) spectra have been obtained for energy densities computed on the basis of the streamwise (top), wall-normal (middle), and spanwise (bottom) components of velocity, $\hat{E}_{uu}$, $\hat{E}_{vv}$, and $\hat{E}_{ww}$, respectively. The X and the O symbols mark the peak value of the energy density spectrum for the inner and the outer optimal structures, respectively. Such peak values are also provided in table IV.1. For the inner optimal structure, the energy peak is found for $\lambda^+_z = 113.8$, rather close to the wall (y^+ ranging from 10 to 29 depending on the considered energy density), providing the typical spanwise spacing of streaks (Kline et al., 1967). Concerning the streamwise wavelength, the energy peak is at $\lambda^+_x = 189.4$, corresponding to the wavelength of the strong wiggling of the streaks due to the presence of streamwise vortices flanking them. However, looking at all of the streamwise spectra (right column), one can notice a secondary peak at $k^+_x \approx 0.0058$, corresponding to a secondary wavelength, $\lambda^+_x \approx 1082.7$, close to the typical streamwise wavelength of streaks in fully

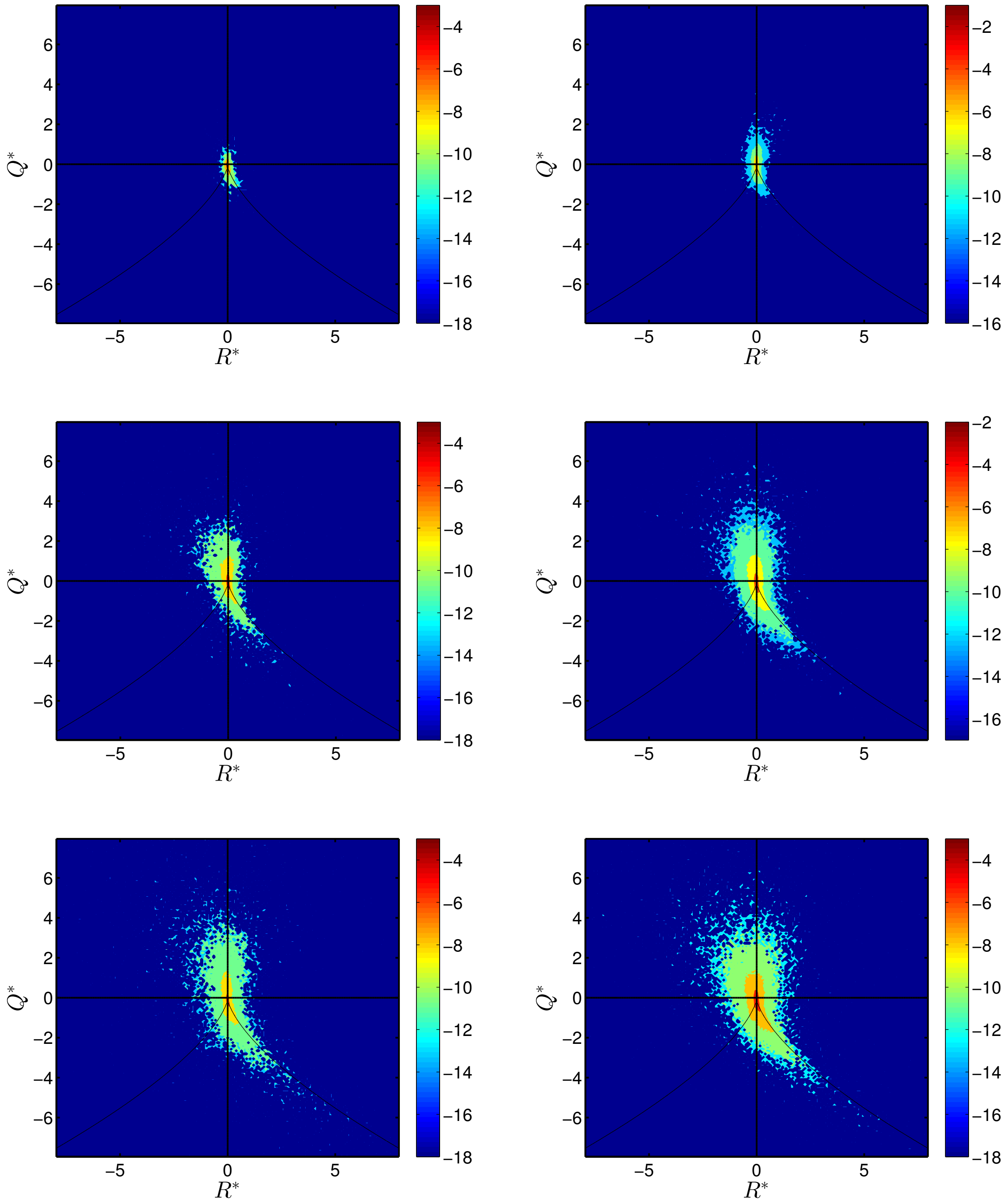

Figure IV.7: Logarithm of the PDF of the nondimensional second (Q^*) and third (R^*) invariant of the velocity gradient tensor, for the outer optimal structures at $t = T_{out}$ (left) and for the fully turbulent flow (right) at different constant $y^+ - plane$ (from top to bottom: $y^+ = 10, 50, 100$). Notice that $Q^* = Q/Q_w$ and $R^* = R/Q_w^{3/2}$, Q_w being the second invariant of the antisymmetric part of the tensor A, averaged on each y^+- constant plane.

	λ_z^+	y^+	λ_x^+	y^+
$t^+ = T_{in}^+$				
$\hat{E}_{uu}$	113.8	13.6	189.4	9.21
$\hat{E}_{vv}$	113.8	29.1	189.4	16.5
$\hat{E}_{ww}$	113.8	10.2	189.4	13.6
$t^+ = T_{out}^+$				
$\hat{E}_{uu}$	189.6	14.9	757.5	74.2
$\hat{E}_{vv}$	142.2	67.6	757.5	81.5
$\hat{E}_{ww}$	227.5	81.5	757.5	74.2

Table IV.1: Wave length and corresponding wall normal position of the peaks of the premultiplied energy density spectrum shown in figure IV.8.

turbulent conditions (Kline et al., 1967), and roughly corresponding to the wavelength of the spot-like localization of the optimal structures characterizing the inner optimal perturbation. Nevertheless, for this inner optimal structure, both streamwise and spanwise spectra appear very narrow, including only a small portion of the broadband range of wavenumbers found by the DNS (compare the light blue isolines with the shaded isocontours). On the other hand, the spectra computed for the outer optimal have energy peaks at larger wavelengths in x and z, with $\lambda_x^+ = 757.5$ well reproducing the peak value found by DNS in the $\hat{E}_{uu}$ spectrum, probably corresponding to the streak streamwise spacing found in the outer optimal disturbance. Moreover, the outer optimal-perturbation spectra almost overlap those extracted from the DNS (compare the black isolines with the shaded contours), indicating that the optimal structure computed for T_{out}^+ is well representative of the turbulent motion in the same flow condition.

Concerning the typical wavelength of the coherent structures in fully turbulent flow, the *attached eddy theory* of Townsend (1980) suggests that the size of the typical eddies in a turbulent shear flow scales with the wall normal direction, the smallest eddy dimension scaling with inner units (δ_ν), and the largest eddy dimension scaling with outer units, in both streamwise and spanwise directions. In order to verify whether this hypothesis is valid also for the optimal structures found here, we have considered the energy peaks of the premultiplied energy spectra, marked in figure IV.8 by X and O for the inner and outer optimal disturbance, respectively. Tracing a straight line between these two peaks (green dashed line), we can infer a scaling of the form $y^+ \propto \lambda_{x,z}^+$ ($y^+ \propto ({k^+}_{x,z})^{-1}$), as conjectured by Townsend (1980). Concerning the scaling coefficients, provided in the caption of figure IV.8, we have obtained values very close to those available in the literature for all components of the energy (Hoyas and Jiménez, 2006; Hwang, 2015). Thus, the scaling laws extracted on the basis of the inner and outer energy peaks reproduce well the scalings found in fully turbulent flows. However, we must remark that at the considered moderate Reynolds number a well distinct scale separation in the streamwise direction is not established yet, data at higher Reynolds numbers being needed for confirming the results (del Álamo and Jiménez, 2003).

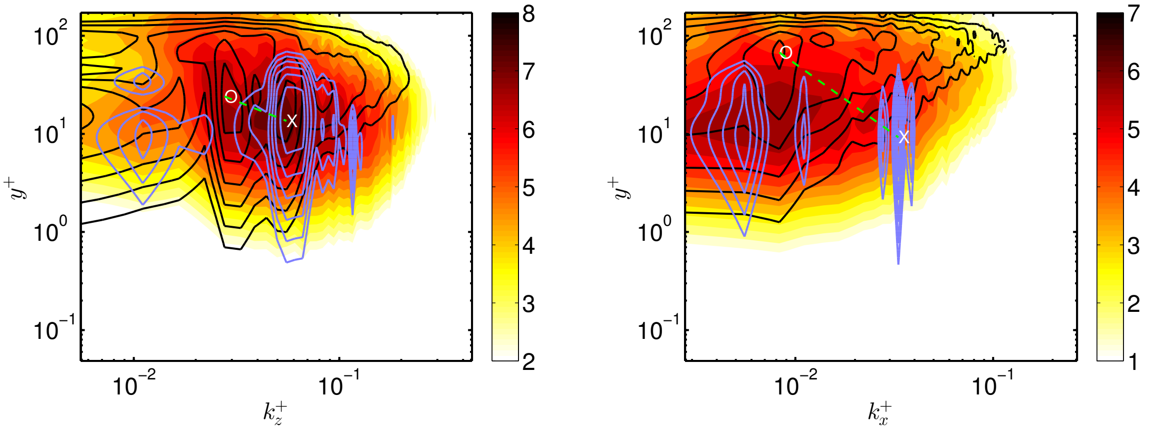

(a) $k_z^+ \hat{E}_{uu}^+(k_z^+)$ (b) $k_x^+ \hat{E}_{uu}^+(k_x^+)$

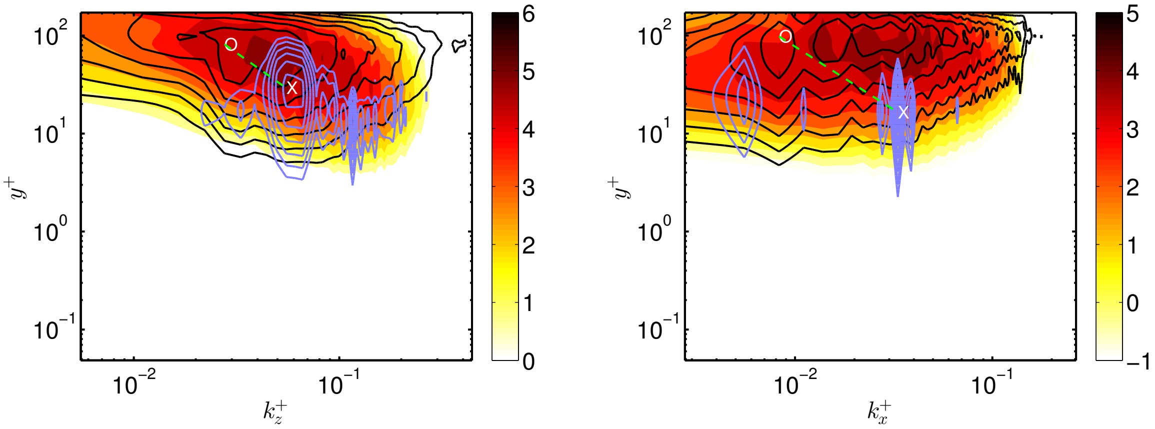

(c) $k_z^+ \hat{E}_{vv}^+(k_z^+)$ (d) $k_x^+ \hat{E}_{vv}^+(k_x^+)$

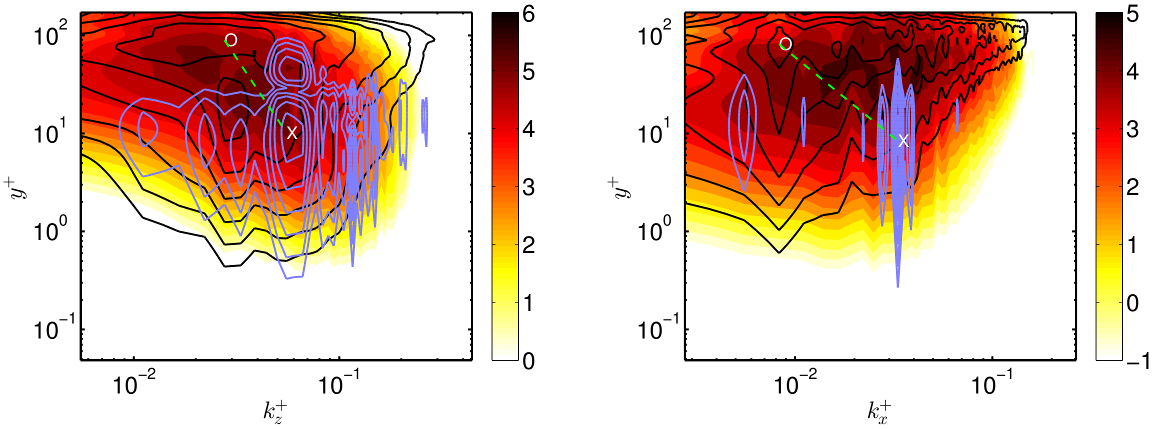

(e) $k_z^+ \hat{E}_{ww}^+(k_z^+)$ (f) $k_x^+ \hat{E}_{ww}^+(k_x^+)$

Figure IV.8: Logarithm of the premultiplied power spectrum versus the wall normal distance y^+ for the DNS (shaded contours), inner optimal solution (blue isolines) and outer optimal solution (black isolines) at target time. The symbols X and O indicate the maximum value for the inner and outer peak, respectively. The green dotted line joining the inner and outer energy peak provides the scaling laws $y^+ = c(k_{x,z}^+)^{-1}$, with slopes (a) $c = 0.0921$, (b) $c = 0.4608$, (c) $c = 0.6970$, (d) $c = 0.1028$, (e) $c = 0.1439$, (f) $c = 0.1287$.

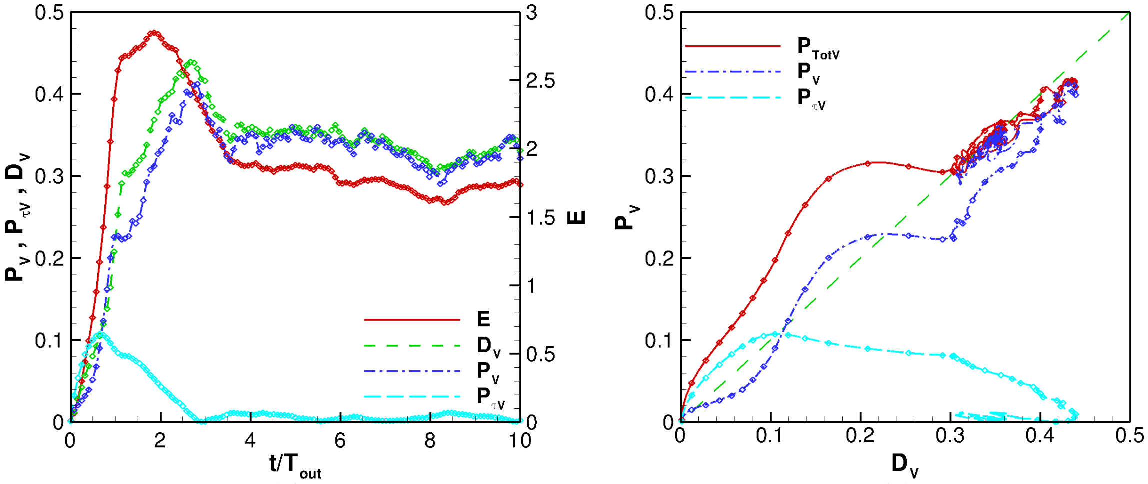

(a) (b)

Figure IV.9: (a) Time evolution of the energy E (red), production P_V (blue), Reynolds stress production $P_{\tau V}$ (cyan), and dissipation D_V (green). (b) Trajectories in the plane $D_V - P_V$ of the production P_V, Reynolds stress production $P_{\tau V}$, and total production $P_{TotV} = P_V + P_{\tau V}$. The time interval between symbols is equal to $\Delta t^+ = 24.5$.

IV.3.2 Time evolution of the outer optimal perturbation

IV.3.2.1 Production and dissipation analysis

The optimal structure arising at the outer time scale is structurally rather complex and the mechanisms leading to a strong energy growth cannot be simply related to a large-scale cycle similar to that characterizing the inner scale (Hwang and Cossu, 2010b). Insight into the energy growth mechanisms can be gained by considering the time evolution of the energy density of the structures. Scalar multiplication of equation (IV.1) by $\tilde{\mathbf{u}}$ provides the following Reynolds-Orr equation (Schmid and Henningson, 2012) for the disturbance:

$$\frac{1}{2}\frac{\partial E}{\partial t} = \int_V \underbrace{-\tilde{\mathbf{u}}\cdot(\tilde{\mathbf{u}}\cdot\nabla\mathbf{U})}_{P}\,dV - \int_V \underbrace{\frac{1}{Re}\nabla\tilde{\mathbf{u}}:\nabla\tilde{\mathbf{u}}}_{D}\,dV + \int_V \underbrace{\tilde{\mathbf{u}}\cdot\nabla\cdot\overbrace{(\overline{\tilde{\mathbf{u}}\tilde{\mathbf{u}}})}^{\tau}}_{P_\tau}\,dV, \tag{IV.5}$$

where $P(x, y, z, t)$ is the energy production, $D(x, y, z, t)$ is the energy dissipation, and $P_\tau(x, y, z, t)$ is the contribution of the Reynolds stress to the production. Figure IV.9 (a) shows the time evolution of these three terms integrated over the whole computational domain, denoted hereafter as P_V, D_V, and $P_{\tau V}$. First of all, the strong energy peak, followed by an increase of the dissipation D_V, confirms that the transient evolution of this optimal structure can be interpreted as a strong energy burst, which is then dissipated in time reaching a dissipation peak at $t^+ \approx 3T^+_{out}$. Such a time interval is in agreement with the large-scale temporal oscillation observed by Hwang and Bengana (2016) for the largest attached eddy and recognized as a bursting event by Flores and Jimenez (2010). One can notice the non-negligible contribution of the term $P_{\tau V}$ in the early time evolution of the perturbation, except at very small times ($t^+ \approx 25$), when the main production mechanism

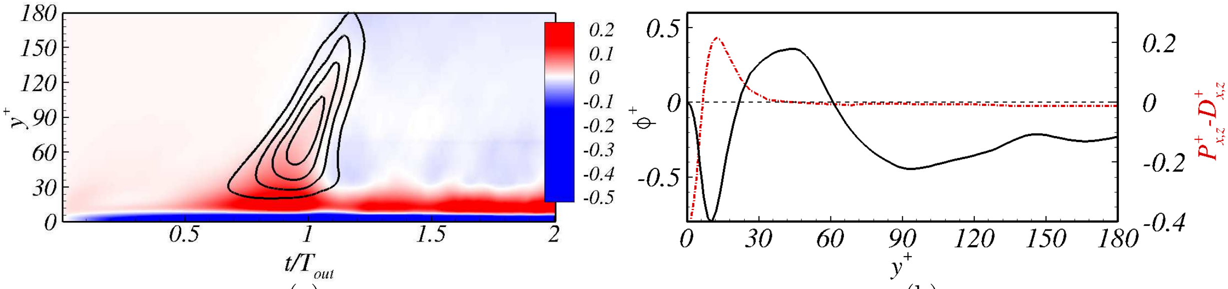

(a) (b)

Figure IV.10: (a) Time evolution of the net local energy production, given by the difference between the production and dissipation at each y^+ (shaded contours), and of the wall-normal energy flux (isolines for $\Phi^+ = 1, 2, 3, 4$, from the outermost to the innermost contour) for the outer optimal structure. (b) Net local energy production (red dashed line) and wall-normal flux (black solid line) versus y^+, extracted at $t^+ = 2T^+_{out}$, showing a production peak in the inner zone ($y^+ \approx 20$), whereas the outer region is characterized by a weak dissipation.

is the Orr mechanism (Orr, 1907), as inferred from analysing the time evolution of the optimal structures provided in subsection IV.3.2.2. This points out the important role of the Reynolds stress in the dynamics of the perturbation. It is noteworthy that this result is in agreement with the analysis of Jiménez (2015) who estimates that the effect of the linear energy growth due to the Orr mechanism is dominant for $\bar{t} = t^+/Re_\tau < 0.15$. In our case, $\bar{t}_{Orr} \approx 0.136$ and $\overline{T}_{out} = T^+_{out}/Re_\tau = 1.694$, therefore, the linear limit is less than one tenth of the target time. Figure IV.9 (a) shows that in the first part of the bursting event a strong linear growth can be observed followed by a larger nonlinear growth till $t^+ = 2T^+_{out}$. In particular, the contribution of the Reynolds stresses increases till $t^+ \approx T^+_{out}$ and becomes negligible for $t^+ > 2T^+_{out}$. In fact, the term $P_{\tau V}$ reaches its maximum approximately at the target time, when the generation of the largest hairpin vortices is completed, and then it decays in time, leading to the establishment of featureless turbulence. This behaviour can be better observed in figure IV.9 (b) providing the projection of the time evolution of the perturbation onto a production-dissipation plane. Starting close to the origin, the trajectory reaches the peak of the total production $P_V + P_{\tau V}$ due to the successive increase of $P_{\tau V}$ and P_V, before starting to oscillate around the point $P_V \approx D_V \approx 0.35$, representing the turbulent self-sustained state.

In order to analyse the energy production and dissipation mechanisms, we evaluate the energy exchange in the wall-normal direction by expressing the Reynolds-Orr equation using the Cartesian notation (Jiménez, 1999):

$$\left(\partial_t + U_j\partial_j - \frac{1}{Re}\nabla^2\right)\frac{\tilde{u}_i\tilde{u}_i}{2} + \partial_j\left(\tilde{u}_j\left(\tilde{p} + \frac{\tilde{u}_i\tilde{u}_i}{2}\right)\right) = -\tilde{u}_i\tilde{u}_j\partial_j U_i - \frac{1}{Re}(\partial_j\tilde{u}_i)^2 + \tilde{u}_i\partial_j\tau_{ij}. \tag{IV.6}$$

Integrating this equation in the streamwise and spanwise direction, we obtain an equation for the the wall-normal transport of energy,

$$\left(\partial_t - \frac{1}{Re}\nabla^2\right)E + \partial_2\Phi = P_{x,z} - D_{x,z} + \tilde{u}_i\partial_2\tau_{i2}, \tag{IV.7}$$

allowing one to identify the last term on the left hand side as the wall-normal energy flux, $\Phi = \tilde{v}[\tilde{p} + (\tilde{u}^2 + \tilde{v}^2 + \tilde{w}^2)/2]$, and the first two terms on the right hand side as the production and dissipation terms (whose integral counterparts are denoted as $P_{x,z}$ and $D_{x,z}$, respectively). The net energy production at a given y^+-constant plane, provided by the difference $P_{x,z} - D_{x,z}$, is plotted versus time in figure IV.10 (a) (shaded contours). As found for fully developed turbulent flows at comparable values of Re_τ (Jiménez, 1999), the net production of turbulent energy (red contours) is well localized at the inner scale ($y^+ \approx 20$) and extends to the outer layer for times smaller than the target time indicating that both inner and outer structures contribute to the perturbation energy increase. The isolines for positive wall-normal energy flux ($\Phi^+ = 1, 2, 3, 4$) are provided in figure IV.10 (a), clearly indicating an outward flux of energy towards the center of the channel for $t^+ \approx T^+_{out}$, corresponding to the formation of the hairpin vortex. Whereas, at the center of the channel, dissipation is found to exceed production, and the flux continuously decreases becoming slightly negative, as one can observe in figure IV.10 (b), showing the excess of local energy production and the wall-normal flux extracted at $t^+ = 2T^+_{out}$. This indicates the presence of a coherent inverse-cascade process (Jiménez, 1999) typical of moderate values of Re_τ, in which energy is transferred from the inner scales at the wall, i.e., the streaks, to large-scale dissipating structures in the outer layer, i.e., the hairpin vortices. Notice that at the considered value of Re_τ, when fully turbulent flow is achieved, no energy production is observed far from the wall, whereas at larger values of Re_τ a (weaker) production peak is observed also at the outer scale (see Lee and Moser (2015)). The large-scale dissipating hairpin structures will eventually breakdown, transferring the energy to incoherent small-scale fluctuations, closing the loop. This wall-normal energy transfer occurring in a short time is thus linked to the occurrence of a transient energy peak which appears in the form of a rapid ejection (positive wall-normal velocity $\tilde{v}$) followed by a longer sweep (negative $\tilde{v}$), similar to a typical bursting event.

IV.3.2.2 Analysis of the flow structures

To further characterize the dynamics of the outer nonlinear optimal perturbation, we analyze its time evolution. Figure IV.11 provides 10 snapshots of the perturbation (Q-criterion isosurfaces, coloured by the wall-normal distance), from $t^+ = 0$ to $t^+ = 431$. The initial perturbation is localized in the three space directions and is composed of two packets of thin counter rotating vortices showing a spanwise symmetry, placed at $y^+ \approx 20$ (as indicated by the colours in figure IV.11 (a)). Even if the optimization is based on the outer time scale, the core of the vortical structures at initial time appears to be in the inner region (see figure IV.11 (a)), the main part of the energy of the spanwise and wall-normal velocity being located at $y^+ \approx 10-40$ (whereas at $t^+ = T^+_{out}$ the energy peak is at $y^+ > 36$ or $y > 0.2$, as provided in table IV.1). Whereas, the streamwise velocity perturbation is located "far" away from the wall at $y^+ \approx 60$ (at $t^+ = 0$) (see figure IV.2 (a)). In figure IV.11 (b) one can observe the typical downstream tilting due to the Orr mechanism (Orr, 1907). This initial phase of the energy growth agrees with the linear analysis of Jiménez (2015) who demonstrates that for very short times ($\bar{t} = t^+/Re_\tau < 0.15$) the energy growth due to the Orr mechanism is dominant. Following the evolution of the perturbation, we can notice that the vortices tend to be lifted up from the wall towards the center of the channel, developing structures of increasing size in an inverse cascade from small to large scales (Jiménez, 1999). Concerning the vortical dynamics, one can observe the formation of new vortices aligned with the initial ones along modulated steamwise streaks (see figure IV.11 (c,d)). These vortices are lifted in the wall-normal direction, creating symmetric or non-symmetric arches on top of the negative streaks at the wall (Wang et al., 2015), as one can observe in figure IV.11 (d,e). Once the small-scale hairpin and *cane* vortices have been created, some of them further grow and lift in the outer region, merging with the nearest vortices in large-scale symmetric hairpin vortices whose heads are located between two streamwise streaks at the wall (Adrian et al., 2001), as shown in figure IV.11 (f,g), generating a new weaker large-scale negative streak between the hairpin legs. Once the structures have reached their maximum spatial growth, corresponding approximately to the energy peak in figure IV.9 (a), the structures begin to break down, starting an energy cascade from the large scales towards the small ones (figures IV.11 (h,i,j)).

Figure IV.12 summarizes the main steps of the time evolution of the outer optimal perturbation: we conjecture it is representative of a bursting event which transfers the energy from small to large scale structures, and then back towards small-scale perturbations. The left frame provides a sketch of the main steps of the evolution shown by seven successive snapshots on the right frame, for $t^+ = 49, 123, 147.5, 172, 196.5, 221, 294$, respectively. An initial perturbation leading to a bursting event is originated by two flanking pairs of small counter rotating vortices (red and blue isosurfaces at the bottom left angle of both frames), which are the first elements of the wall self-sustained cycle (Waleffe, 1997). These vortices initially increase their energy by the Orr mechanism and then generate low speed streaks by the lift-up mechanism (Landahl, 1980) (green isosurfaces, step (b)). These streaks increase their amplitude, and exhibit secondary sinuous or varicose instability (Andersson et al., 2001). As a result, the initial streamwise vortices bend over the streak at the point where the instability is triggered, forming arch-shaped structures (Schoppa and Hussain, 2002; Wang et al., 2015) (step c). Being very close to each other and continuously lifting in the wall-normal direction, two of these non-symmetric arch-shaped vortical structures merge together, generating a large symmetric hairpin structure (blue and red isosurfaces, step d). This large-scale hairpin vortex increases in size up to the centerline of the channel and then begins to break down dissipating the energy; instead, the non-symmetric small-scale vortices on top of the streaks might induce inflectional instabilities on the instantaneous velocity profile. In particular, strong low-speed streaks may induce an inflection point in the $x-y$ plane, triggering a Kelvin-Helmholtz type instability producing spanwise vorticity, such as the arch of the hairpin vortices, but also inflection points in the $x-z$ plane, producing wall-normal vorticity (Heist et al., 2000). The tilting of the wall-normal vorticity by the mean velocity profile induces streamwise vortices of opposite sign with respect to the initial one (step e), as discussed by Heist et al. (2000). This new counter-rotating vortex flanks the initial one, being able to create a new low-speed streak by the lift-up mechanism (step f), and the loop can restart again from the small-scale structures towards the large-scale ones. Concerning the time scales typical of this loop, the complete formation of the small arch vortices participating to the self-sustained cycle takes about $\Delta t^+ \approx 150$ time units (see figure IV.11 (c) to (i)) as in Wang et al. (2015), whereas the complete formation of the train of large-scale hairpin vortices takes about $\Delta t^+ \approx 300$ time units, which corresponds approximately to the target time T^+, similarly to the observations of Zhou et al. (1999) where the hairpin packets have spacing about equal to $\lambda_x^+ \approx 450$ (see figure IV.3). Notice that the self-sustained

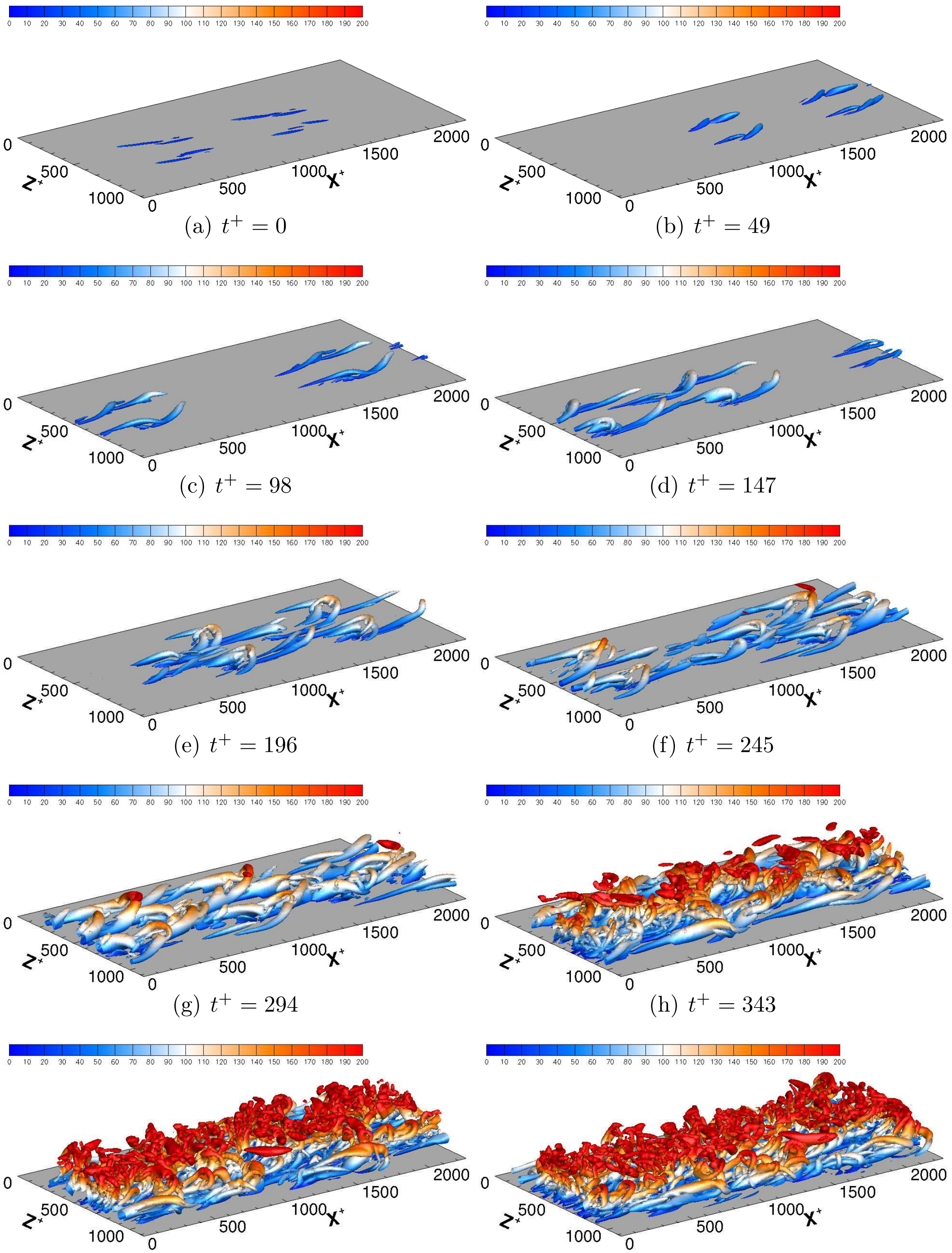
0 10 20 30 40 50 60 70 80 90 100 110 120 130 140 150 160 170 180 190 200
0
Z+
500
1000
0
500
1000
1500
2000
X+

(a) $t^+ = 0$ (b) $t^+ = 49$ (c) $t^+ = 98$ (d) $t^+ = 147$ (e) $t^+ = 196$ (f) $t^+ = 245$ (g) $t^+ = 294$ (h) $t^+ = 343$ (i) $t^+ = 392$ (j) $t^+ = 431$

Figure IV.11: Snapshots of the time evolution of the outer optimal structures: isosurfaces of Q-criterion coloured by the wall normal distance y^+.

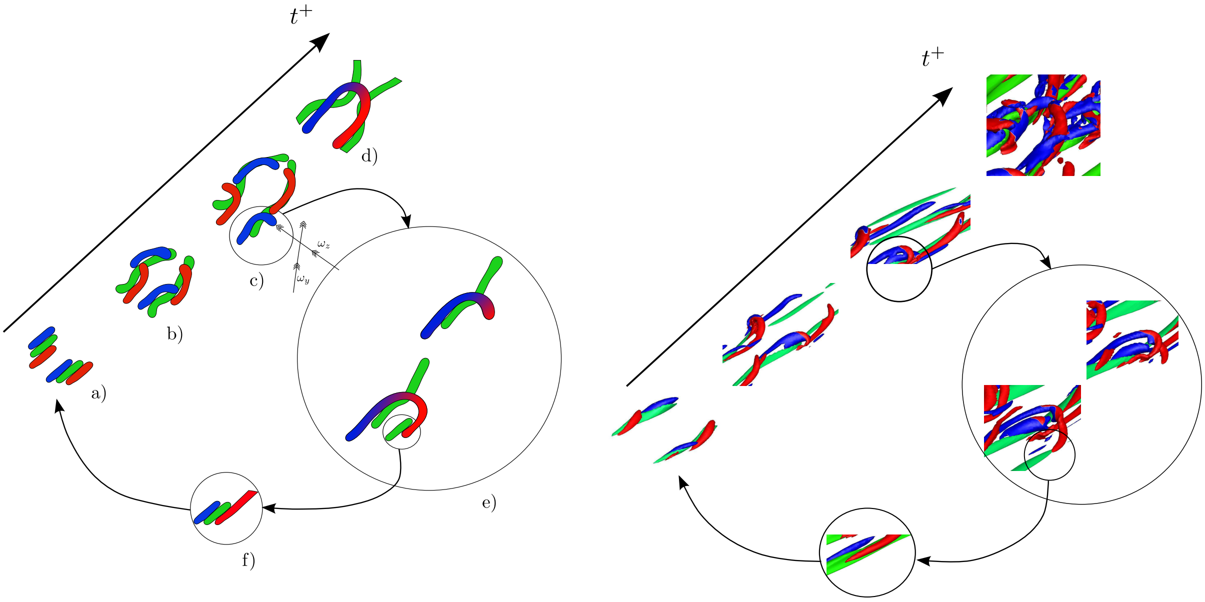

Figure IV.12: (Left) Sketch of the main steps of the dynamics of the outer optimal perturbation based on the snapshots (right) extracted at (a) $t^+ = 49$, (b) $t^+ = 123$, (c) $t^+ = 147.5$, (d) $t^+ = 294$, (e) $t^+ = 172, 196.5$, (f) $t^+ = 221$. Isosurfaces of negative streamwise velocity (green) and Q-criterion coloured by the values of streamwise vorticity (blue for positive, red for negative).

cycle mainly involves streaks and vortices close to the wall, but it transiently induces large-scale hairpin vortices as a by-product of ther evolution. These large vortical structures MF{are responsible of realizing an inverse energy cascade reaching the outer scale and dissipating the stored energy towards smaller scales, allowing a new wall cycle to be established. It appears thus that the large-scale hairpin vortices observed in the nonlinear optimal disturbance do not directly participate into the self-sustained cycle, but they are transient dynamical features which ensure the occurrence of energy peaks and subsequent dissipation typical of bursting events.

IV.4 Conclusion

It is known that, behind its chaotic dynamics, turbulent flow is populated by coherent structures, i.e., flow motions highly correlated over both space and time, carrying a large part of the flow momentum. In the present study, for the first time, a recently developed nonlinear optimization technique based on Lagrange multipliers is employed to unravel the dynamics of such structures.

In particular, a nonlinear transient growth analysis has been performed to study which kind of coherent structures are able to trigger rapid events with a strong energy growth, similar to bursting events, in a canonic wall-bounded turbulent flow such as the channel flow. The optimization procedure, focusing on the dynamics of finite-amplitude disturbances to the mean flow, provides different nonlinear optimal structures depending on the chosen time scale for the energy growth.

For an *inner* time-scale, corresponding about to one eddy turnover time evaluated in the buffer layer at $y^+ = 19$ (the superscript $^+$ indicating variables expressed in inner units), nonlinear optimal structures consist of highly modulated streaks having a typical spanwise spacing $\lambda_z^+ \approx 113$, surrounded by positive and negative streamwise vortices, with a spanwise spacing $\lambda_z^+ \approx 56$. These nonlinear optimal structures, localized in space in a spot-like fashion, well represent the self-sustained cycle of turbulence at the wall: linearly growing streaks saturate and oscillate due to secondary instability, regenerating new localized quasi-streamwise vortices by nonlinear coupling.
For the *outer* time scale, corresponding about to one eddy turnover time at the centerline of the channel, a much more complex optimal structure is observed, mostly composed of packets of hairpin vortices on top of highly oscillating streamwise streaks. In particular, strong vortical and streaky structures are observed at different spatial scales, ranging from the wall to the outer layer. The probability density function (PDF) of the velocity disturbance characterizing such an *outer optimal* is concentrated in the second and fourth quadrants of the streamwise versus wall-normal velocity plane. This indicates the prevalence of ejection and sweep events, as it happens in a strong bursting event. Moreover, we show that the outer most energetic structure well describes the wavenumber spectrum, the vortical topology, and the production-dissipation wall-normal distribution typical of turbulent flows at moderate Reynolds numbers. Whereas, the inner optimal structure includes only a small portion of the broadband range of wavenumbers and vortical topologies found at different wall-normal positions by a direct numerical simulations of the fully turbulent flow. The analysis of the distribution of the most energetic wavelengths in the wall-normal direction for the inner and outer optimal disturbances shows that the optimal structures computed here scale in size accordingly to the attached eddy theory of Townsend (1980). In particular, the spatial scaling laws extracted on the basis of the inner and outer energy peaks reproduce well the scalings found in fully turbulent flows.

Finally, a careful analysis of the time evolution of the optimal flow structures has been performed, providing the dynamics of the initial perturbations leading to a bursting event. An optimal bursting event is originated by two flanking pairs of small counter rotating vortices at the wall, the basic elements of the wall self-sustained cycle; due to the Orr and lift-up mechanisms, these vortices are able to generate strong low-speed streaks, which exhibit secondary sinuous or varicose instability; as a result, the initial streamwise vortices bend over the streak at the point where the instability is triggered, forming arch-shaped structures which lift in the wall-normal direction and merge together, generating large symmetric hairpin structures; the large-scale hairpin vortices increase in size up to the centerline of the channel and then breakdown dissipating the energy; in turn, the small-scale vortices on top of the wall streaks are bent and tilted by the mean flow, leading back to the creation of a pair of streamwise vortices, restarting the cycle. Thus, the self-sustained cycle at the wall appears to be the main source of energy of the bursting event, which transiently induces large-scale hairpin vortices as a by-product; these large vortical structures have the role of realizing an inverse energy cascade reaching the outer scale and eventually dissipating the stored energy towards smaller scales, allowing a new wall cycle to develop. This implies that hairpin vortices, even if inherently transient coherent structures (see Eitel-Amor et al. (2015)), are robust features of turbulent channel flows, at least at moderate friction Reynolds numbers, arising as a result of a strong nonlinear instability that repeats in time as a by-product of the self-sustained wall cycle.

These results show that, despite the main source of turbulent energy being located close to the wall and sustained by the wall cycle (Waleffe, 1997), for moderate values of Re_τ the turbulent motion is characterized by a complex energy transfer which involves inner and outer scales.

In conclusion, this study provides an explanation for the recurrence of energy *bursts* revealing that they correspond to optimal-energy flow structures embedded in the fully-turbulent flow. These optimal structures reproduce well the spatial spectra as well as the probability density function of the velocity typically measured in turbulent flows, recovering the mechanism of direct-inverse energy cascade. These results represent an important step towards understanding the dynamics of turbulence and paves the way to new non-linear techniques to manipulate and control the self-sustained turbulence dynamics. A further challenge will be to extend this analysis to larger values of Re_τ, for which a clear scale separation is observed in the spatial spectra and a second peak of energy production exists at the outer scale. This will allow to model the inner-outer interaction under different operating conditions, aiming at understanding the universal mechanisms underlying the turbulent coherent motion. An extension to higher turbulent Reynolds number is provided in the next chapter, where optimal structures for different Re_τ are compared. Important differences between low and high Reynolds number turbulent channel flows are discussed and a physical explanation is given for them.

IV.5 Appendix

In order to derive the equations governing the dynamics of perturbations of the mean turbulent velocity profile in a plane channel flow, we employ a Reynolds decomposition approach similar to that used by Eitel-Amor et al. (2015). The instantaneous flow vector $\mathbf{q} = [\mathbf{u}, p]^T$, where $\mathbf{u}$ is the velocity vector and p is the pressure, is decomposed into a mean flow component $\mathbf{Q} = [U, 0, 0, P]^T$ and a disturbance $\tilde{\mathbf{q}} = [\tilde{u}, \tilde{v}, \tilde{w}, \tilde{p}]^T$:

$$\mathbf{q}(x, y, z, t) = \mathbf{Q}(y) + \tilde{\mathbf{q}}(x, y, z, t), \tag{IV.8}$$

Injecting this decomposition in the Navier-Stokes (NS) equations and averaging over a long time, the following Reynolds-averaged-NS equations are obtained:

$$\mathbf{U} \cdot \nabla \mathbf{U} = -\nabla \mathrm{P} + \frac{1}{Re} \Delta \mathbf{U} - \nabla \cdot \overline{\tilde{\mathbf{u}}\tilde{\mathbf{u}}}, \tag{IV.9}$$

$\overline{\bullet}$ denoting long-time averaging. Subtracting the time-averaged equations (IV.9) from the NS equations provides the following final formulation for the dynamics of the disturbances:

$$\begin{aligned} \frac{\partial \tilde{\mathbf{u}}}{\partial t} + \tilde{\mathbf{u}} \cdot \nabla \tilde{\mathbf{u}} + \mathbf{U} \cdot \nabla \tilde{\mathbf{u}} + \tilde{\mathbf{u}} \cdot \nabla \mathbf{U} &= -\nabla \tilde{\mathrm{p}} + \frac{1}{Re} \Delta \tilde{\mathbf{u}} + \nabla \cdot \overline{\tilde{\mathbf{u}}\tilde{\mathbf{u}}}, \\ \nabla \cdot \tilde{\mathbf{u}} &= 0, \end{aligned}$$

where $Re = U_c h / \nu$, U_c indicating the steady centerline velocity magnitude in the plane channel. The last term of the momentum equation is the divergence of the Reynolds stress tensor $\tau = \overline{\tilde{\mathbf{u}}\tilde{\mathbf{u}}}$ forcing the mean turbulent velocity profile (see equation IV.9).

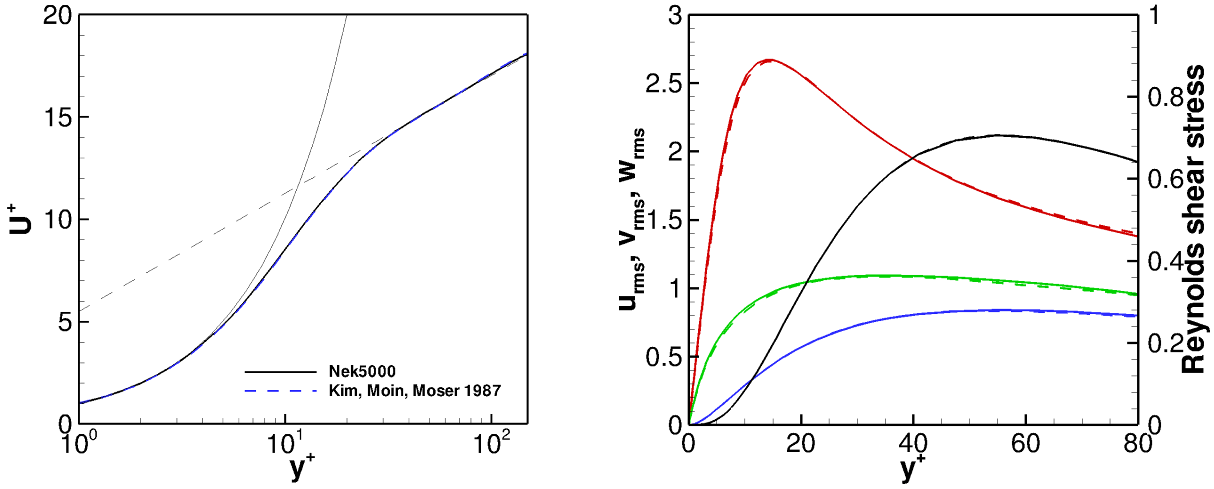

Figure IV.13: Left frame: mean velocity profile U^+ versus the wall-normal coordinate y^+ (blue thick lines) obtained by the present DNS (solid) compared with the results of Kim et al. (1987) (dashed). The black thin lines are the linear (solid) and logarithmic (dashed) profiles. Right frame: root mean square of $\tilde{u}$ (red), $\tilde{v}$ (blue), $\tilde{w}$ (green), and Reynolds shear stress $\overline{\tilde{u}\tilde{v}}$ (black) normalized by the wall shear velocity, versus y^+ obtained by the present DNS (solid) compared with the results of Kim et al. (1987) (dashed).

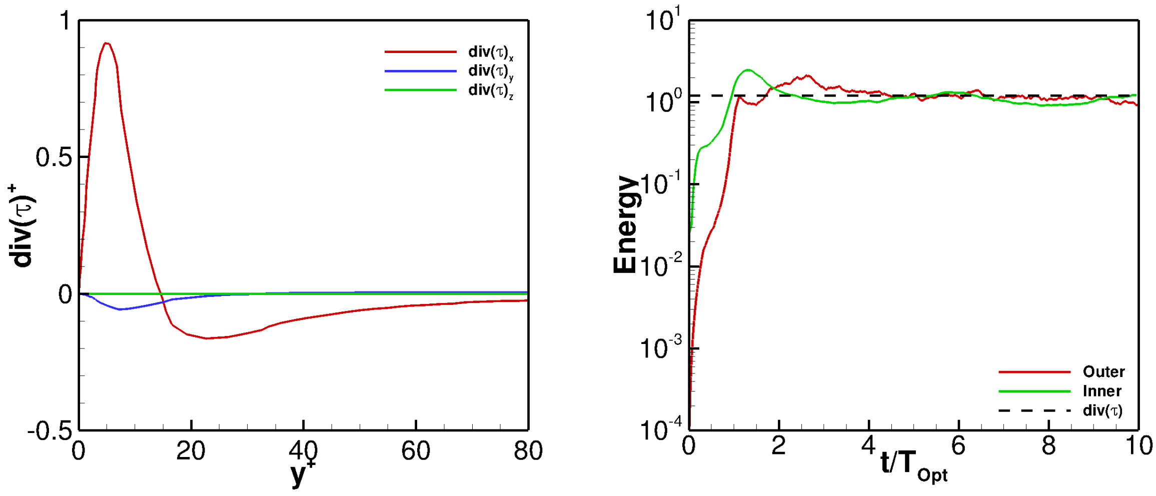

Figure IV.14: Left frame: streamwise (red), wall-normal (blue) and spanwise (green) components of the divergence of the Reynolds stress tensor τ versus y^+ obtained by the present DNS. Right frame: energy of $\nabla \cdot [\tilde{\mathbf{u}}\tilde{\mathbf{u}}]$ (where $[\bullet]$ denotes the spatial average in the $y = const$ planes) for the outer (red line) and inner (green line) optimal perturbations versus time; the dashed line indicates the energy of $\nabla \cdot \tau$.

This term appears when the perturbative formulation employs a base flow $\mathbf{U}$ which is not a solution of the steady Navier–Stokes equations. Reynolds stresses need to be known or modeled for closing the governing equations: in this work we compute them a-priori by a direct numerical simulation (DNS) of the fully-developed turbulent flow. At this purpose, firstly, the mean flow velocity $\mathbf{U}$ is computed by DNS averaging the instantaneous velocity over a long time interval and over the two homogeneous directions, obtaining the velocity profile shown in the left frame of figure IV.13 (solid thick line), which is compared to the mean flow computed by Kim et al. (1987) (dashed thick line). Then, subtracting the computed mean flow from the instantaneous velocity field, we obtain the perturbation $\tilde{\mathbf{u}}$, which contains both coherent and fluctuating parts of the disturbances. The product $\tilde{\mathbf{u}}\tilde{\mathbf{u}}$ is averaged in time and over the two homogeneous directions. The right frame of figure IV.13 provides the root-mean-square of $\tilde{u}$, $\tilde{v}$, $\tilde{w}$, as well as the Reynolds shear stress $\overline{\tilde{u}\tilde{v}}$ (solid lines) exctracted from the DNS, showing an excellent agreement with the same quantities computed by Kim et al. (1987) (dashed line). Based on these data, we achieve a direct evaluation of the Reynolds stress tensor $\tau = \overline{\tilde{\mathbf{u}}\tilde{\mathbf{u}}}$, whose divergence is shown in the left frame of figure IV.14 (the three solid lines showing the x, y, and z components of $\nabla \cdot \tau$ versus the wall-normal coordinate y^+). The computed Reynolds stress tensor is employed as a forcing term in equations (IV.1) for the optimization process, providing the inner and outer optimal perturbations. As a consistency check, it is also worth to verify that the computed optimal perturbations satisfy the long-time constraint implicitely imposed by forcing the NS equations with the Reynolds stress tensor. In the right frame of figure IV.14 one can observe the time evolution of the energy of $\nabla \cdot [\tilde{\mathbf{u}}\tilde{\mathbf{u}}]$, $\tilde{\mathbf{u}}$ being the inner (green line) or the outer (red line) optimal perturbation, and $[\bullet]$ denoting the spatial average in the $y - const$ planes. It appears that, after a short transient, the energy of this term oscillates around the energy of $\nabla \cdot \tau$, confirming the consistency of the proposed approach.

It is noteworthy that these equations are not suitable for a linear stability analysis; in fact, $\tilde{\mathbf{u}}$ cannot be considered infinitesimal, since it contains both the coherent $(\hat{\mathbf{u}})$ and fluctuating $(\mathbf{u}')$ part of the disturbances, the latter being non zero in a turbulent flow. Whereas, previous linear instability approaches such as those used by Pujals et al. (2009), Cossu et al. (2009) and Hwang and Cossu (2010a) used a triple decomposition approach (see Reynolds and Hussain (1972)) where $\mathbf{u} = \mathbf{U} + \hat{\mathbf{u}} + \mathbf{u}'$, optimising only the coherent part of the perturbation. However, the model used in these works cannot be easily extended to a nonlinear framework, since it neglects the long-time average of the nonlinear coherent perturbation term $\overline{\hat{\mathbf{u}}\hat{\mathbf{u}}}$, an hypothesis that cannot be extended to the case of finite-amplitude perturbations, where this term should be large (see also Viola et al. (2014)).

Finally, it is worth to point out that, using a triple decomposition approach, an equation formally equivalent to equation (IV.10) for the coherent part of the perturbation can be derived under the assumption that the variance of the probability distribution of the fluctuating part of the perturbation is small with respect to the Reynolds stress tensor τ, so that the phase average of the fluctuating nonlinear term $< \mathbf{u}'\mathbf{u}' >$ can be neglected.

Chapter V

Nonlinear large-scale optimal structures in turbulent channel flow

Contents

V.1 Introduction **73**

V.2 Numerical methods **74**

V.2.1 Nonlinear optimization 74

V.3 Results **75**

V.3.1 Nonlinear optimal structures 75

V.4 Conclusions **85**

V.1 Introduction

Coherent structures in turbulent shear flows usually take the form of packets of hairpin vortices reaching the outer region of the boundary layer along with streaks of different size, going from the near-wall to the outer region. The latter can be explained by the linear transient growth of the perturbations to the mean turbulent profile. Whereas, the former are found to be optimally-growing only in the presence of nonlinear effects, as ascertained for a turbulent channel flow at a low friction Reynolds number. In this chapter we extend the analysis performed in the previous one: we aim at investigating how the shape of nonlinearly optimally-growing perturbations changes with the Reynolds number in a turbulent channel flow. Increasing the friction Reynolds number from 180 up to 590, the nonlinear optimal perturbation tends towards more robust large-scale streaks and less coherent vortical structures. These streaks are generated by a large-scale lift-up mechanism, acting as a source term in the energy balance, inducing a positive turbulent kinetic energy production at the outer scale. This indicates that the outer energy production peak characterizing turbulent flows at high Reynolds numbers can be associated with the growth of optimal large-scale streaks which represent a robust feature of turbulent channel flows.

V.2 Numerical methods

We consider the turbulent flow in a channel at moderate Reynolds number $Re = U_c h/\nu$, h being the half distance between the plates and U_c the centerline velocity of the mean velocity profile. When considering a turbulent flow, variables can be normalized using the half height h and the velocity U_c (referred to as 'outer' units), or using the friction velocity $u_\tau = (\mu \mathrm{d}U/\mathrm{d}y)_w^{\frac{1}{2}}$ and the viscous length scale ν/u_τ (referred to as 'inner' units). Hereafter, variables expressed in inner units will be labeled with the superscript $^+$, otherwise any other variable is normalized with respect to outer units. The friction velocity is used to define the friction Reynolds number $Re_\tau = u_\tau h/\nu$, which here is set to the values $Re_\tau =$ 180 and 590. Computations are performed using the spectral-element code NEK5000 (Fischer et al., 2008), with Legendre polynomial reconstruction of degree seven and second-order accurate Runge-Kutta time integration (Deville et al., 2002). Dirichlet boundary conditions for the three velocity components are imposed at the wall, whereas periodicity is prescribed in the streamwise and spanwise directions (denoted with x and z, respectively, whereas y denotes the wall-normal direction). Details about the computational domain, as well as the number of grid points and the length of the cells are provided in table V.1.

	Re_τ	Re	Δx^+	Δz^+	Δy^+_{max}	Δy^+_{min}	L_x	L_z	$Nx \times Ny \times Nz$
C180	180	3300	12	7	4.4	0.05	4π	2π	$192 \times 160 \times 160$
C590	590	12450	9.7	4.8	7.2	0.05	2π	π	$384 \times 256 \times 384$

Table V.1: Simulation parameters for the two cases considered in the present work.

V.2.1 Nonlinear optimization

The aim is to compute optimal perturbations capable of inducing a peak of kinetic energy in a finite time T when evolving nonlinearly over the mean flow. To describe the nonlinear evolution of perturbations of the mean turbulent velocity profile we use the following system of equations ($\widetilde{NS}$):

$$\begin{aligned} \frac{\partial \tilde{\mathbf{u}}}{\partial t} &= -\tilde{\mathbf{u}} \cdot \nabla \tilde{\mathbf{u}} - \tilde{\mathbf{u}} \cdot \nabla \mathbf{U} - \mathbf{U} \cdot \nabla \tilde{\mathbf{u}} - \nabla \tilde{\mathrm{p}} + \frac{1}{Re} \nabla^2 \tilde{\mathbf{u}} + \nabla \cdot \tau, \\ \nabla \cdot \tilde{\mathbf{u}} &= 0, \end{aligned} \tag{V.1}$$

where $\tilde{\mathbf{u}} = (\widetilde{u}, \widetilde{v}, \widetilde{w})^T$ and $\tilde{\mathrm{p}}$ represent the velocity and pressure perturbations of the mean turbulent velocity profile $\mathbf{U}(y)$, and τ is the Reynolds stress tensor forcing the mean turbulent velocity profile, defined as the Reynolds average of $\tilde{\mathbf{u}}\tilde{\mathbf{u}}$. A DNS of the fully turbulent flow is used to compute the mean velocity profile as well as the Reynolds stress tensor averaged in time (although they could be extracted from an existing database). Details of the derivation of equations (V.1) are provided in the Appendix of the previous chapter (Farano et al., 2017).

In this work, we aim at maximizing the kinetic energy growth of perturbations $\tilde{\mathbf{u}}$ at a time T, the energy being defined as

$$E(t) = \{\tilde{\mathbf{u}}(t), \tilde{\mathbf{u}}(t)\} = \int_V \left(\widetilde{u}^2 + \widetilde{v}^2 + \widetilde{w}^2\right)(t) dV, \tag{V.2}$$

V being the volume of the computational domain. The energy gain $G(T) = E(T)/E(0)$ is maximized using a Lagrange multiplier approach where the initial energy E_0, along with the $\widetilde{NS}$ equations (V.1), are imposed as constraints using the Lagrange multipliers or adjoint variables $(\tilde{\mathbf{u}}^\dagger, \mathrm{p}^\dagger, \lambda)$. Following previous works focusing on nonlinear optimal perturbations of laminar base flows (see Pringle et al. (2012), Cherubini and De Palma (2013), Duguet et al. (2013)) and turbulent mean ones (Farano et al., 2017), the optimisation problem is solved by direct-adjoint iterations coupled with a gradient rotation algorithm (Farano et al., 2016; Foures et al., 2013). The iterative procedure is stopped when the relative variation between two successive direct-adjoint loops, $e = (G^n - G^{n-1})/G^n$ is smaller than 10^{-7}, n being the iteration number. Depending on the selected target time, 40 to 80 direct-adjoint iterations are needed for achieving convergence for one set of parameters, each optimization needing 800.000 to 2.000.000 CPU hours on an IBM cluster Intel ES 4650 depending on the value of the Reynolds number.

V.3 Results

Firstly, DNSs of turbulent channel flow at $Re_\tau = 180$ (C180) and $Re_\tau = 590$ (C590) have been performed. The mean velocity profile as well as the root mean square (r.m.s.) of the velocity field are coincident (within plotting accuracy) with those reported in Kim et al. (1987) and Moser et al. (1999). A visualisation of the flow structures is provided in figure V.1, showing the vortical structures identified by the second invariant of the velocity gradient tensor (known as Q-criterion, see Hunt et al. (1988)). For C180 (left), several hairpin-like vortical structures can be observed (Wu and Moin, 2009b). On the other hand, one can notice the loss of coherence of the vortical structures when increasing the Reynolds number (C180 left, C590 right). In both cases, looking at the instantaneous vortical structures, no clear evidence of LSM can be observed, as also remarked in Hwang and Cossu (2010b).

To show the presence of a streaky LSM, one can average the perturbation flow field in the streamwise direction. The result is shown in figure V.2 for C180 (left) and C590 (right). Top frames are scaled in inner units, showing a close-up of the wall region ($y^+ \leq 50$), whereas the bottom ones extend up to the center of the channel, with axes scaled in outer units. As one can notice from the top frames, the near-wall dynamics is characterised by an alternation of low- and high-velocity streaks spaced in the spanwise direction of about $\lambda_z^+ \approx 100$, as already reported in the literature (Moser et al., 1999). Whereas, the bottom frames show the presence of similar structures whose size grows moving from the wall to the centreline of the channel, reaching an average spacing of $O(h)$. It must be pointed out that this scale separation appears to exist at both considered Reynolds numbers (compare left with right frames), since in both cases the logarithmic law is well established (Chen et al., 2014; Farano et al., 2017), but it is much clearer at higher Re_τ.

V.3.1 Nonlinear optimal structures

Nonlinear optimizations are performed with target time $T = 31.12$ (corresponding to $T^+ \approx 305$ for C180 and $T^+ \approx 874$ for C590, respectively). This target time is approximately equal to the eddy turnover time at the center of the channel; therefore, we antic-

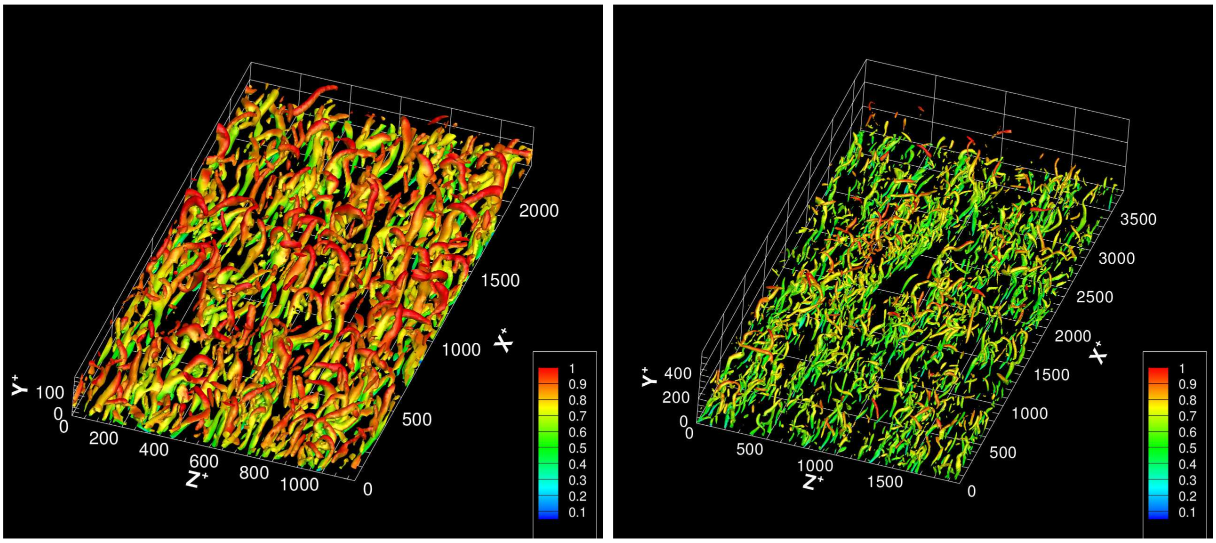

Figure V.1: Instantaneous isosurfaces of the second invariant of the velocity gradient tensor, Q-criterion ($Q/Q_{max} = 0.025$), coloured by the streamwise velocity: left, C180; right, C590

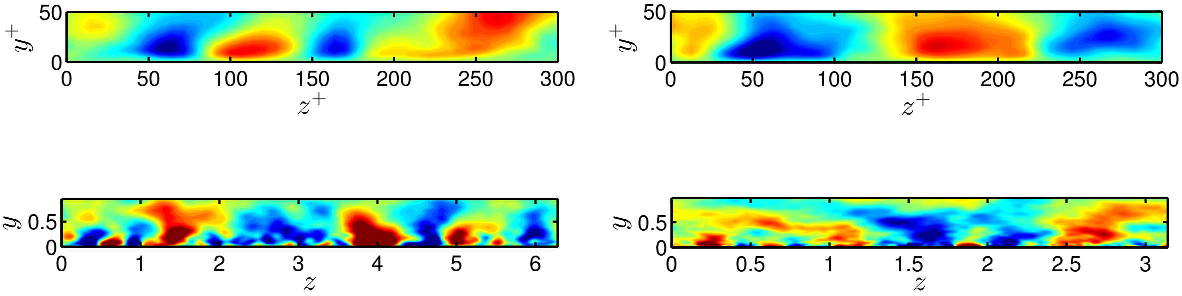

Figure V.2: Streamwise-averaged perturbation of the mean flow for C180 (left) and C590 (right), on a $y - z$ plane scaled in outer units (bottom) and a close-up where the lengths are scaled in inner units (top). Blue (red) contours indicate negative (positive) values of the streamwise velocity perturbations.

ipate that optimal structures maximizing the growth at the outer scale will be obtained (see Butler and Farrell (1993) and Farano et al. (2017)). Figure V.3 provides the optimal perturbations at the target time, computed for C180 ($E_0 = 10^{-2}$, left frame) and C590 ($E_0 = 7.5 \times 10^{-4}$, right frame). In both cases the initial energy has been chosen as the smallest energy providing a well converged finite amplitude solution (see the discussion in the Appendix of chapter IV (Farano et al., 2017)). It is noteworthy that slightly increasing E_0, does not change the behaviour of the resulting optimal perturbations. Both frames show that the optimals at target time are composed of elongated negative streaks (green) with spanwise spacing $\approx h$ along with a family of localized vortical structures (white), among which hairpin-like vortices can be recognized. These vortical structures are often observed as coherent structures populating the log layer and characterizing the outer motion of wall bounded turbulent flows (Adrian, 2007; Hwang, 2015; Hwang and Bengana, 2016; Hwang and Cossu, 2010b, 2011; Rawat et al., 2015). However, one may notice some

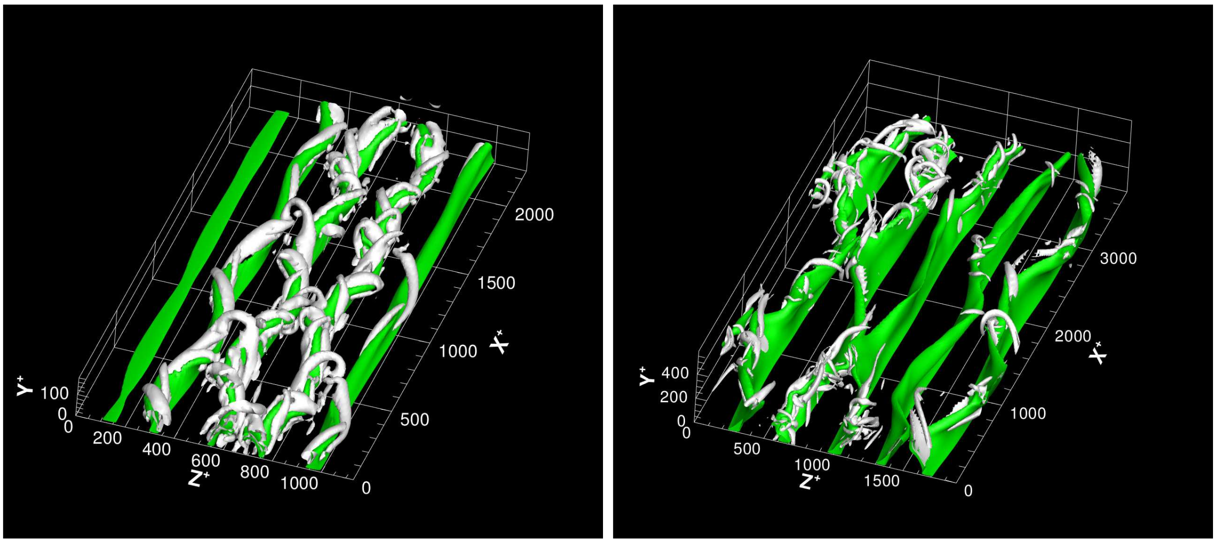

Figure V.3: Shape of the optimal perturbations at $t = T$: isosurfaces of negative streamwise velocity perturbation ($\tilde{u}/\tilde{u}_{max} = 0.45$, green) and of the second invariant of the velocity gradient tensor, Q-criterion ($Q/Q_{max} = 0.025$, grey). C180, $E_0 = 10^{-2}$ (left) and C590, $E_0 = 7.5 \times 10^{-4}$ (right).

differences between the optimal flow structures at the two considered Reynolds numbers. In particular, for the largest value of the Reynolds number, the streaks appear more visible at the outer scale, extending towards the center of the channel, whereas the vortical structures appear to lose coherence and decrease their size, in agreement with what has been observed in the DNS snapshots shown in figure V.1.

The dominating wavelengths constituting these nonlinear optimal disturbances, at $t = T^+$, can be analysed by inspecting their premultiplied spatial energy density spectra versus y^+, shown in figure V.4 (respectively, V.5) for the streamwise (spanwise) direction, k_x^+ (k_z^+) being the associated wavenumber expressed in inner units. Such figures also provide the premultiplied density energy spectra obtained by the DNS results (solid lines), for comparison. The spectra corresponding to $Re_\tau = 180$ and $Re_\tau = 590$ are shown on the left and right column, respectively; the top, middle, and bottom rows providing the streamwise (E_{uu}), wall-normal (E_{vv}), and spanwise (E_{ww}) energy densities. One can observe that, increasing Re_τ, all the DNS spectra extend to higher values of y^+ and lower values of $k_{x,z}^+$, suggesting the presence of LSM (Smits et al., 2011). However, comparing the optimal spectra with the DNS ones, it can be noticed that the former are localized mostly in the outer region, whereas the latter extend down towards the wall. This feature is due to the fact that the optimization is performed for a target time typical of the eddy turnover time at the center of the channel, selecting optimal structures able to reach the outer scale. This is confirmed by the green crosses in figure V.5, showing that all the optimal perturbation spectra peak at values of $\lambda_z = 2\pi/k_z$ of $O(h)$. Thus, the nonlinear optimal perturbations represent well the outer scale turbulent dynamics at different Re_τ. In order to investigate how the dominant streamwise wavelengths of the optimal pertur-

bations change when increasing Re_τ, we compare the corresponding streamwise energy density spectra (shaded contours, top frames of figures V.4). Increasing Re_τ, not only the spectrum moves to higher values of y^+, but also appears to stretch in the wall-normal direction, showing large values for a wider range of wall-normal positions. This means that high-amplitude streamwise disturbances can be recovered not only close to the wall (where the spectrum peak is located) but also in the outer region, indicating that streaky structures are indeed recovered at larger scales. Whereas, for $Re_\tau = 180$, the high-amplitude zone of the spectrum is confined close to the peak value, meaning that high-amplitude streaky structures are observed mainly at a precise near-wall position. It is also worth noticing that, while for the streamwise energy spectrum the peak remains close to the wall even at $Re_\tau = 590$, for the spanwise and wall-normal spectra the peak moves into the outer region, where most of the vortical structures are indeed located.
Moreover, in order to analyse the streamwise coherence of the optimal perturbations and to identify the main features of streaky structures, one may investigate whether the peaks of these spectra move towards larger or smaller values of k_x^+ when the Reynolds number changes. Figure V.4 shows that the streamwise energy density peak moves to much smaller wavenumbers (larger wavelengths) for increasing Re_τ, whereas the peak of the spanwise and wall-normal energy spectra show but a slight decrease of k_x^+ (the peak values, indicated by the green crosses in figures V.4 are provided in table V.2 for the ease of the reader). In particular, considering the streamwise energy spectra, the ratio between the two streamwise most energetic wavelengths at the two considered Reynolds numbers is close to the ratio of the two considered Re_τ themselves, $\lambda^+_{x\,590}/\lambda^+_{x\,180} \approx Re_{\tau 590}/Re_{\tau 180}$. Thus, the main streamwise wavelength of the streamwise disturbances scales in outer units. Whereas, for the wall-normal and spanwise energy spectra, the dominating λ_x^+ slightly changes with Re_τ , meaning that the size of the wall-normal and spanwise perturbations, representative of the vortical structures, scales with the inner units. These results indicate that for increasing Reynolds number the optimal perturbation is characterized by more robust streamwise-elongated streaks with increasing size reaching the outer scale, as well as vortical structures of smaller size.

In order to analyse the dynamics at the outer scale for the two considered Reynolds numbers, we analyse the two-point space correlation of the flow structures extracted from the DNS of turbulent channel flow as well as from the optimal perturbations at target time. This technique is often used in turbulent flows to characterise the behaviour of the coherent motion, i.e. the shape and size of coherent structures. Different kinds of correlation might be used, i.e., velocity-velocity, velocity-vorticity, or conditioned correlation, as discussed in Chen et al. (2014), Sillero et al. (2014) and Hwang et al. (2016a). Here, we employ a velocity-vorticity correlation (Chen et al., 2014) to link the dynamics of the

	Re_τ	E_{uu}	E_{vv}	E_{ww}
λ_x^+	180 (C180)	757.5	757.5	757.5
λ_x^+	590 (C590)	1857	928.7	619.1
y^+	180 (C180)	67.60	98.18	81.48
y^+	590 (C590)	47.80	229.0	209.6

Table V.2: Wavelength and corresponding wall-normal position of the peaks of the premultiplied energy density spectra shown in figure V.4.

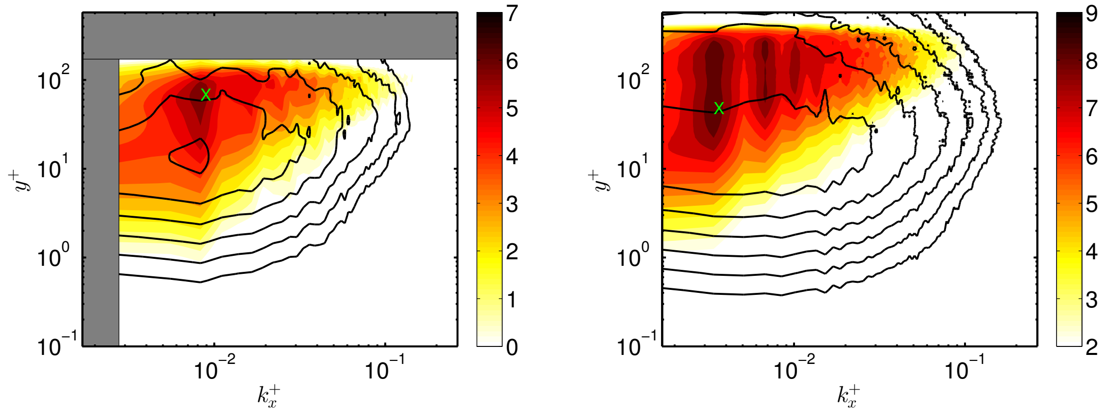

(a) Contours of $k_x^+ E_{uu}(k_x^+)$, C180 (b) Contours of $k_x^+ E_{uu}(k_x^+)$, C590

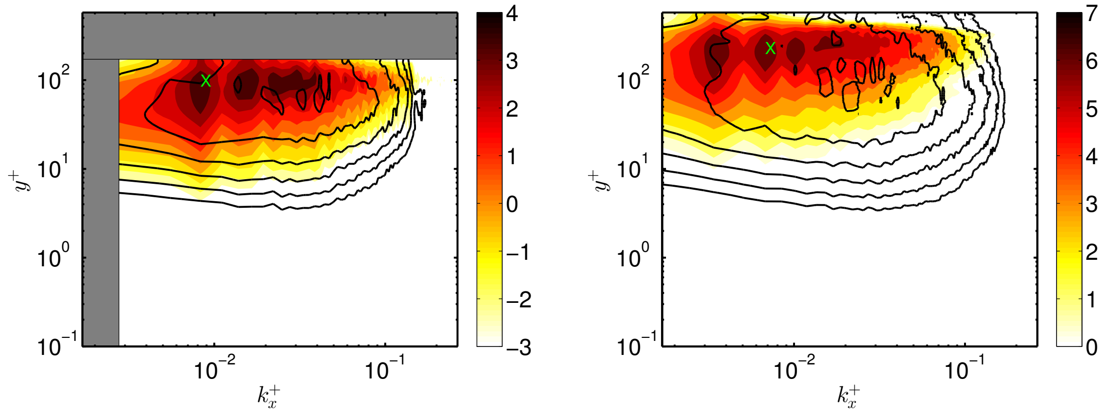

(c) Contours of $k_x^+ E_{vv}(k_x^+)$, C180 (d) Contours of $k_x^+ E_{vv}(k_x^+)$, C590

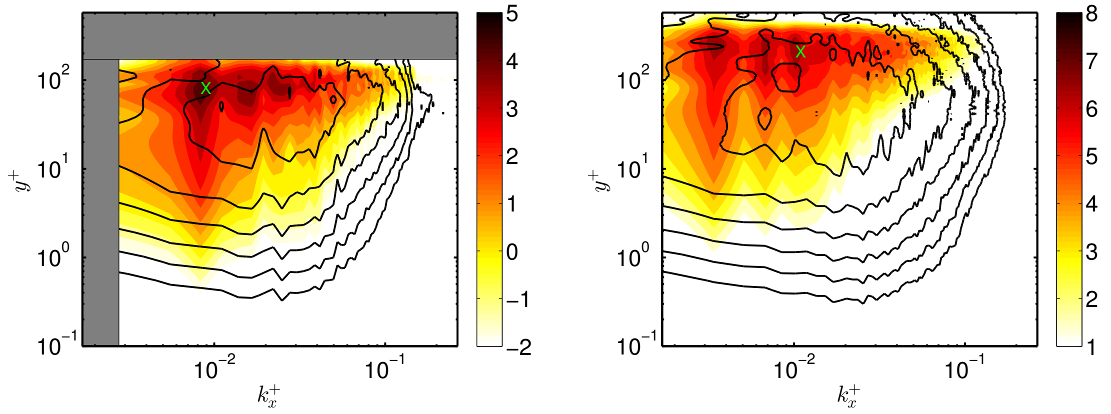

(e) Contours of $k_x^+ E_{ww}(k_x^+)$, C180 (f) Contours of $k_x^+ E_{ww}(k_x^+)$, C590

Figure V.4: Contours of the logarithm of the premultiplied energy density spectra in the $k_x^+ - y^+$ plane for the optimal solutions at target time (shaded contours) and the DNS (solid lines) for C180 (left) and C590 (right). The symbols X indicate the peak values of the optimal spectra. The gray zones for C180 indicate the cut off values of y^+ and k_x^+ corresponding to the half height and streamwise length of the channel.

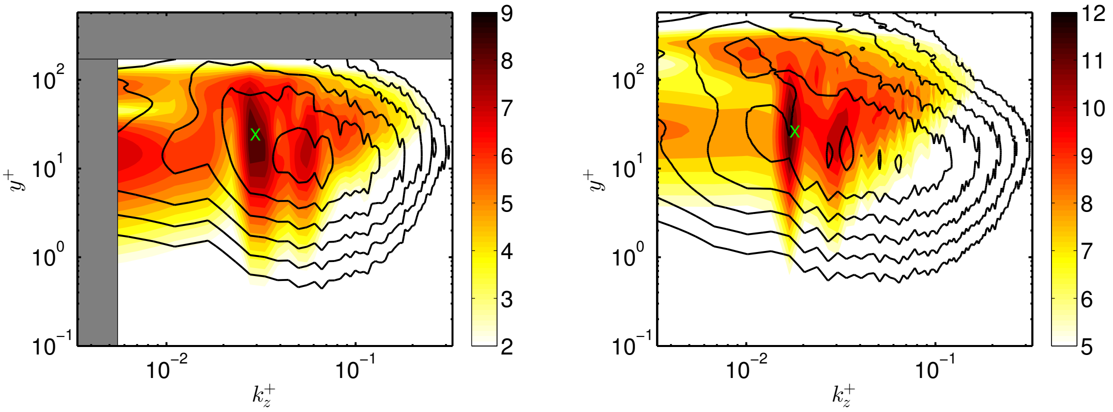

(a) Contours of $k_z^+ E_{uu}(k_z^+)$, C180 (b) Contours of $k_z^+ E_{uu}(k_z^+)$, C590

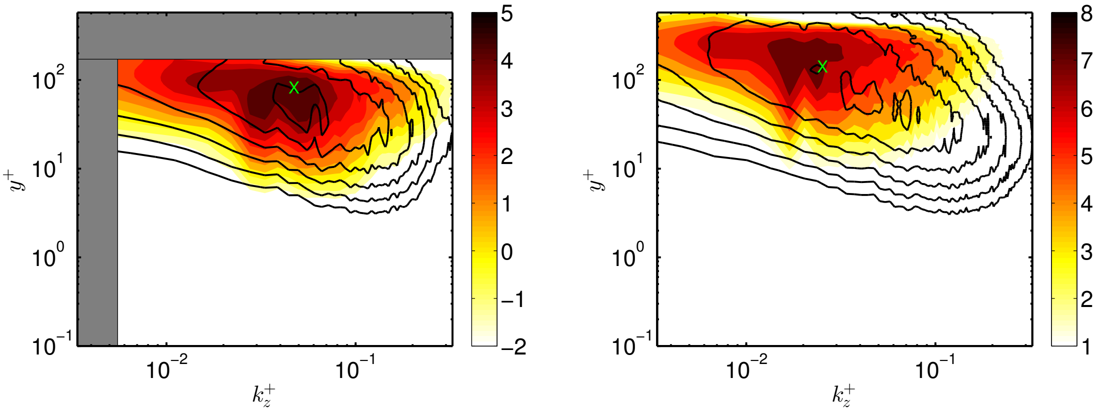

(c) Contours of $k_z^+ E_{vv}(k_z^+)$, C180 (d) Contours of $k_z^+ E_{vv}(k_z^+)$, C590

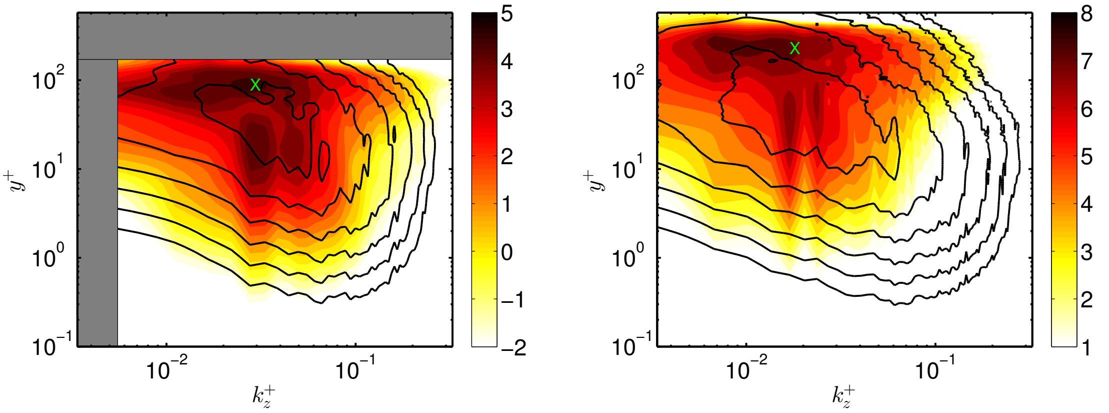

(e) Contours of $k_z^+ E_{ww}(k_z^+)$, C180 (f) Contours of $k_z^+ E_{ww}(k_z^+)$, C590

Figure V.5: Contours of the logarithm of the premultiplied energy density spectra in the $k_z^+ - y^+$ plane for the optimal solutions at target time (shaded contours) and the DNS (solid lines) for C180 (left) and C590 (right). The symbols X indicate the peak values of the optimal spectra. The gray zones for C180 indicate the cut off values of y^+ and k_z^+ corresponding to the half height and spanwise length of the channel.

vortical structures (such as streamwise vortices) to the (streaky) velocity components. Following Chen et al. (2014) and Hwang et al. (2016a), the velocity-vorticity correlation is used, defined as:

$$R_{ij}(y_r, r_x, y, r_z) = \frac{< \tilde{u}_i(x, y_r, z)\tilde{\omega}_j(x + r_x, y, z + r_z) >}{\tilde{u}_{i,rms}\tilde{\omega}_{j,rms}} \tag{V.3}$$

where $\tilde{\omega}$ is the vorticity perturbation; $i, j = 1, 2, 3$ denote respectively the streamwise, wall normal and spanwise components; y_r is a reference wall-normal distance; r_x, r_z are the correlation lengths in the streamwise and spanwise directions and $< \bullet >$ represents the corresponding spatial average operator. In particular, the first component of this tensor, R_{11}, provides the correlation between streamwise vortices and streaks, helping at identifying whether the lift-up mechanism (Landahl, 1980) is indeed active. For the DNS at $Re_\tau = 180$, as discussed also in Chen et al. (2014), increasing the value of y_r from the buffer layer to the logarithmic one, the shape of the highly-correlated structures changes, as one can observe in figure V.6 (left) providing the three dimensional two-point correlation R_{11} for the instantaneous turbulent field at three values of $y_r^+ = 10, 50, 100$.

In particular, close to the wall, a *quadrupole* configuration (called in Chen et al. (2014) a "*four cigar structure*") characterised by elongated streaky structures is observed, indicating a strong correlation between the reference wall-normal point and the near-wall region. This correlation between streamwise velocity and vorticity is associated with the lift-up mechanism, as confirmed by the presence of near wall streaks and steamwise counter-rotating vortices. Increasing y_r, the correlation becomes much weaker close to the wall, taking a *dipole* shape (called in Chen et al. (2014) a "*two blob structure*"), which suggests the presence of *bulge* structures linked to the head of hairpin vortices (Zhou et al., 1999), frequently observed at the outer scale. The optimal perturbation (right column of figure V.6), is characterized a very similar correlation, showing: i) an elongated *quadrupole cigar structure* near the wall associated to the presence of the streaks; ii) the disappearance of these elongated streaks when moving the reference point y_r far from the wall; iii) the onset of a *bulge* at $y_r^+ = 100$ indicating the presence of hairpin vortices heads lifted up from the wall. One can also notice that, in the optimal perturbation at $Re_\tau = 180$, the near-wall region remains correlated with the outer one (see the two near-wall structures in the bottom right frame of figure V.6 for $y_r^+ = 100$). This feature is consistent with the fact that the hairpin vortices constituting the optimal perturbation provide a connection between the near-wall region and the outer one during the bursting process, as discussed in Farano et al. (2017).

For the case C590, a different structure hierarchy has been observed. Figure V.7 (left) provides the correlation structures extracted from the DNS for $y_r = 10, 50, 100, 180$. For all of the considered values of y_r^+, the *quadrupole structure*, indicating the presence of the lift-up mechanism, is preserved, resulting in the generation of streaky coherent structures at the wall and in the outer region. In particular, in the linear and buffer region, the structures have the same size of those observed for C180, preserving the near-wall spacing of about 100 viscous length units. Whereas, increasing y_r, the correlation structures begin to drift in the spanwise directions (Hwang et al., 2016a), increasing their spanwise size. This larger spacing for $y_r^+ = 100, 180$ is present also close to the wall (see the bottom left frame of figure V.7), indicating that the counter-rotating streamwise vortices producing the streaks extend themselves from the wall to the outer region, creating large-scale streaks

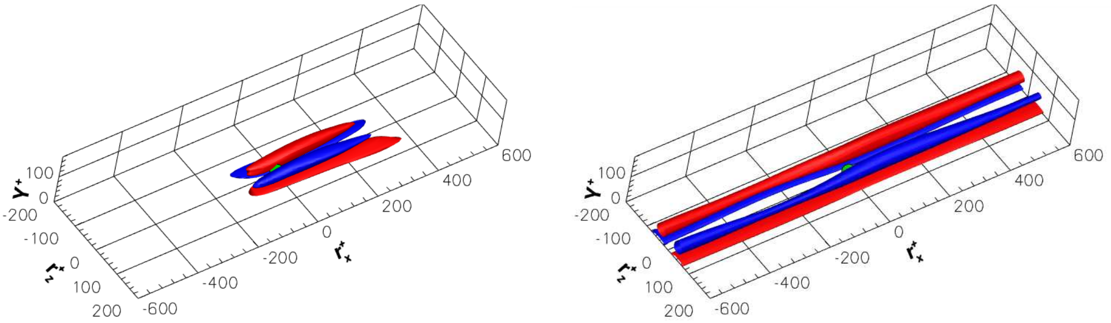

(a) C180, DNS, $y_r^+ = 10$ (b) C180, OPT, $y_r^+ = 10$

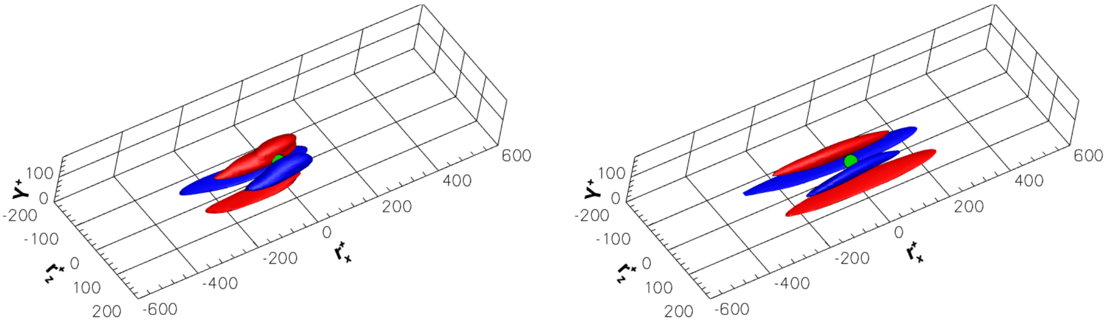

(c) C180, DNS, $y_r^+ = 50$ (d) C180, OPT, $y_r^+ = 50$

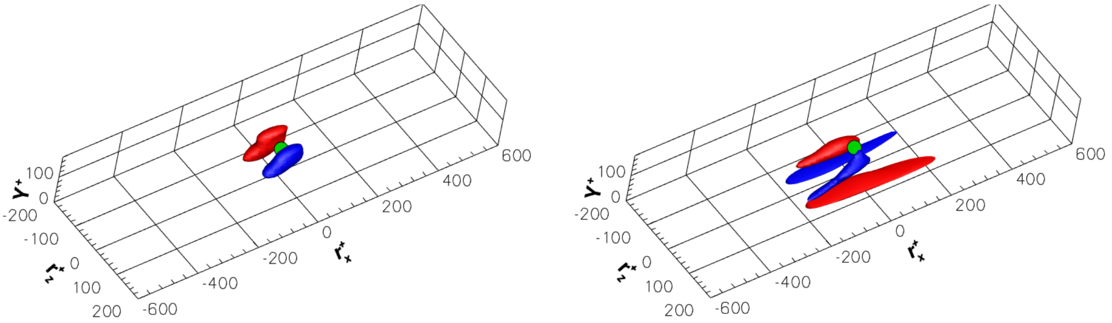

(e) C180, DNS, $y_r^+ = 100$ (f) C180, OPT, $y_r^+ = 100$

Figure V.6: Isosurfaces of the two-point cross-correlation coefficient R_{11} for the DNS (left) and the optimal perturbation at target time (right) for C180. Red (blue) surfaces represent positive (negative) values. The green circles represent the reference points y_r, with values $y_r = 10, 50, 100$ (top to bottom).

(Hwang and Cossu, 2010a, 2011) of $O(h)$ size. The absence of blob-like structures even at $y_r^+ = 180$ suggests the weaker relevance of hairpin structures at this higher value of the Reynolds number, as it appears by inspecting figure V.3. Concerning the optimal perturbation, the right frames of figure V.7 provide again the *quadrupole structure* linked with the presence of the streaks at all values of y_r^+. However, the spanwise and streamwise size of the correlation structures remain large independently of y_r^+, being the perturbation optimized with reference to an outer time scale.

The correlation results further confirm that, for increasing Reynolds number, the optimal perturbation is mostly characterized by robust streaks reaching the outer scale, accompanied by less coherent hairpin vortices. This is consistent with the fact that, unlike the case C180 (Jiménez, 1999), for larger values of Re_τ a positive (although weak)

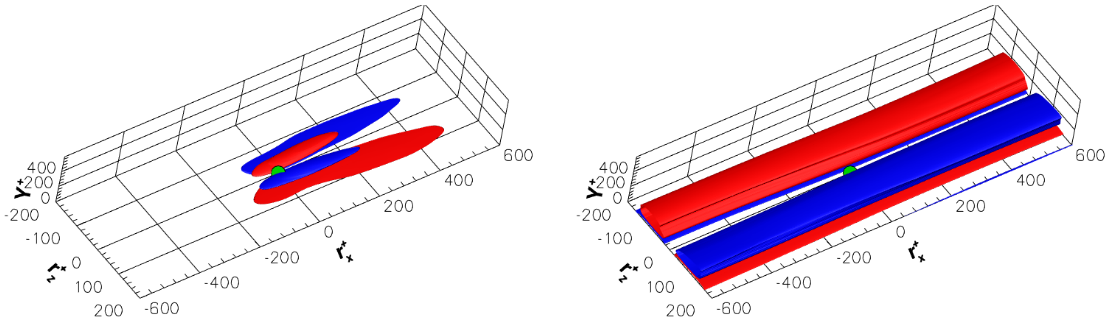

(a) C590, DNS, $y_r^+ = 10$ (b) C590, OPT, $y_r^+ = 10$

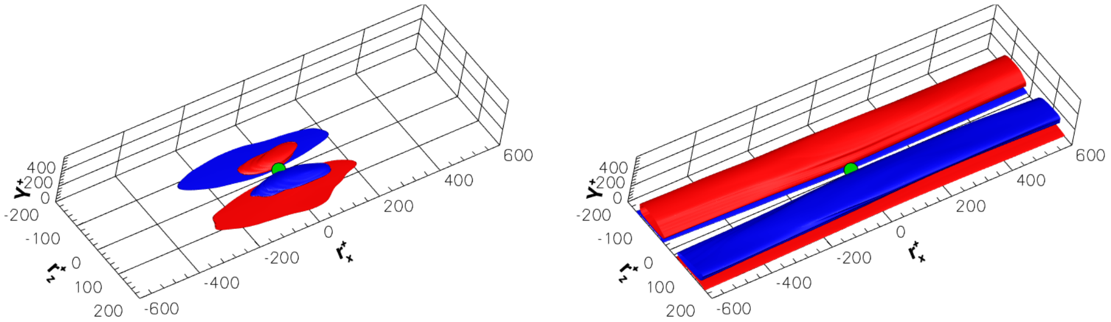

(c) C590, DNS, $y_r^+ = 50$ (d) C590, OPT, $y_r^+ = 50$

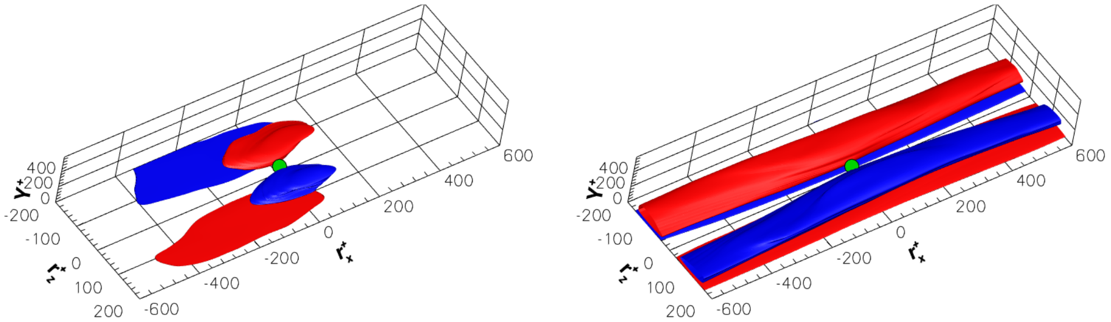

(e) C590, DNS, $y_r^+ = 100$ (f) C590, OPT, $y_r^+ = 100$

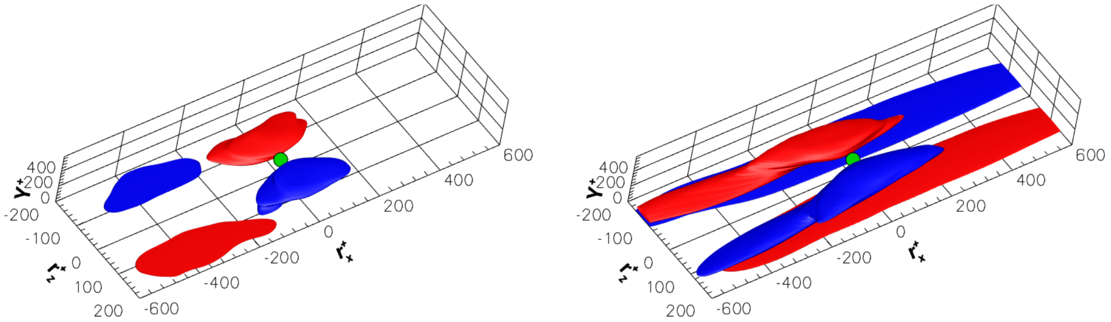

(g) C590, DNS, $y_r^+ = 180$ (h) C590, OPT, $y_r^+ = 180$

Figure V.7: Isosurfaces of the two-point cross-correlation coefficient R_{11} for the DNS (left) and the optimal perturbation at target time (right) for C590. Red (blue) surfaces represent positive (negative) values. The green circles represent the reference points y_r, with values $y_r = 10, 50, 100, 180$ (top to bottom).

production of turbulent kinetic energy is found outside the buffer zone (Moser et al., 1999). Such a net energy production might be associated with the lift-up mechanism, which is confined at the wall at small values of the Reynolds number and extends also at the outer scale for increasing values of Re_τ, sustaining the development of large-scale streaks. To ascertain the presence of kinetic energy production at the outer scale in the optimal perturbation, we have integrated in time the $\widetilde{NS}$ equations (V.1) initialised with the optimal solutions, measuring the difference between production and dissipation terms, $P(\mathbf{x}, t) = -\tilde{\mathbf{u}} \cdot (\tilde{\mathbf{u}} \cdot \nabla \mathbf{U})$ and $D(\mathbf{x}, t) = 1/Re \nabla \tilde{\mathbf{u}} : \nabla \tilde{\mathbf{u}}$, integrated along the homogeneous directions, referred to as $P_{x,z}(y, t)$ and $D_{x,z}(y, t)$, respectively. The results are shown in figure V.8, providing the net energy production $P_{x,z} - D_{x,z}$ in a y^+ versus time plane. In both cases, for $t < T$, a positive energy production (solid contours) extends from the inner to the outer region, associated to the energy growth of the optimal structures reaching the outer region (Farano et al., 2017). On the other hand, for $t > T$, the two flows have different behaviours. For C590, the net energy production in the outer zone is positive, which is likely due to the presence of a strong coherent lift-up mechanism acting at the outer region. Whereas, for C180 and $t > T$, (see figure V.8 (left)), the outer region is characterised by dissipation (dashed contours) associated with the breakdown of the hairpin vortices (Farano et al., 2017).

This suggests that, for low Reynolds number (C180), the energy production due to the lift-up mechanism is confined to the wall, whereas coherent hairpin vortices can reach the outer scale as a result of burst events dissipating the energy produced at the wall (Farano et al., 2017), explaining the observations of these structures at low values of Re_τ (Sayadi et al., 2013; Wu and Moin, 2009b). On the other hand, for C590, the outer scale coherent lift-up mechanism (Hwang and Cossu, 2011) generates large scale streaks, explaining the presence of the positive net energy production in the outer region. In order to confirm that this production peak is indeed linked to the presence of the lift-up mechanism, we have computed the spatial distribution of the production term $P_{lift-up}(\mathbf{x}) = -\tilde{u}\tilde{v}\partial U/\partial y$, which represents the production due to the wall-normal transport of the base flow shear. Figure V.9 shows the spatial distribution of $P_{lift-up}$ averaged in the streamwise direction for the optimal perturbations at $Re_\tau = 180$ (left) and 590 (right). One can observe that the lift-up mechanism is active mainly at $y^+ \leq 100$ for C180, whereas for C590 it extends up to $y^+ \approx 300$, corresponding to the wall-normal region at which an outer production energy peak is found in the DNS (see Moser et al. (1999)). Moreover, the lift-up mechanism appears to be active in correspondence with the large-scale streaks represented by the solid lines protruding into the outer region. This can be clearly seen at $Re_\tau = 590$, although a similar trend is also observed at $Re_\tau = 180$. This indicates that the kinetic energy production peak observed at the outer scale in several DNS for sufficiently large values of the Reynolds number is indeed due to the lift-up mechanism sustaining the large-scale streaks, which constitute (most part of) the optimal perturbation at these values of Re_τ. Whereas, for lower values of the friction Reynolds number, optimally-amplifying perturbations are found to be mostly composed of hairpin vortices, which are not able to produce kinetic energy. The reason for this structural change with Re_τ in the optimal coherent structures have yet to be investigated in detail. However, the results presented here indicate that the existence of an outer kinetic energy production peak at sufficiently large Reynolds numbers in turbulent channel flows is indeed due to the onset of optimally growing large-scale streaks which overtake the growth of the (dissipating) hairpin vortices able to maximise the energy growth at low values of Re_τ.

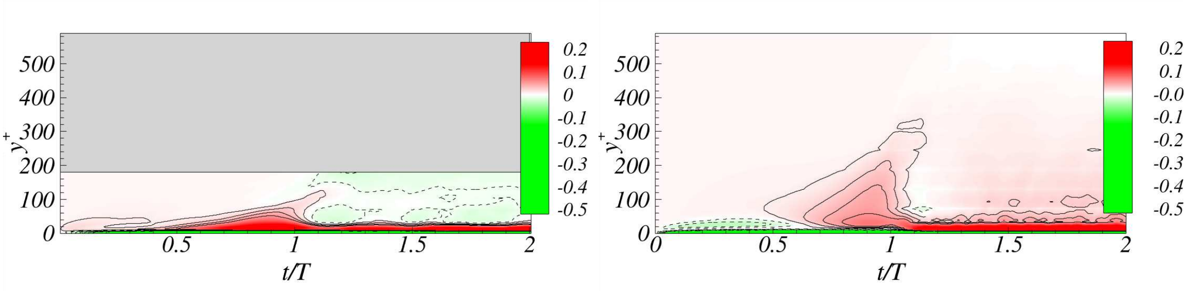

(a) (b)

Figure V.8: Time evolution of the net local energy production, given by the difference between the production and dissipation at each y^+ for the optimal disturbance for C180 (left) and C590 (right). Continuous and dashed lines represent respectively positive and negative values. The gray zones for C180 indicate the cut off values of y^+ corresponding to the half size of the channel.

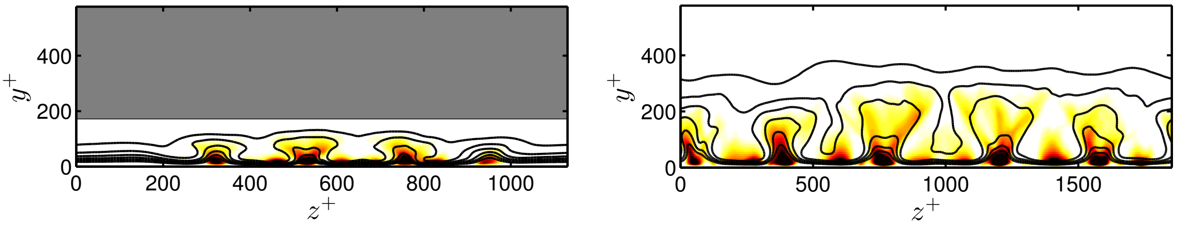

(a) (b)

Figure V.9: Lift-up production term averaged in the streamwise direction (shaded contours) and streamwise instantaneous velocity component (solid contours) in a $z^+ - y^+$ plane for the optimal perturbations in C180 (left) and C590 (right). The gray zones for C180 indicate the cut off values of y^+ corresponding to the half size of the channel.

V.4 Conclusions

Coherent structures are well organized motions of fluid flows with high spatial and temporal correlation. In simple turbulent shear flows they usually take the form of packets of hairpin vortices mostly placed in the outer region of the boundary layer along with streaks of different size, going from the near-wall to the outer region. Previous works, restrained to a linear approximation, have found that the latter are optimally-growing perturbations of the turbulent mean profile at different scales (see Pujals et al. (2009)). Whereas, when taking into account nonlinear effects, the optimal perturbations become mostly composed of hairpin vortices, at least at low friction Reynolds number such as $Re_\tau = 180$ (Farano et al., 2017). In this work we aim at investigating whether large-scale streaks can be considered optimally-growing perturbations of the mean velocity profile in a turbulent channel flow, also in the more general nonlinear framework. Towards this end, we compare nonlinear optimal perturbations of the mean flow at two friction Reynolds numbers, namely, $Re_\tau = 180$ and 590, for a target time typical of the motion at the outer scale. For the lower value of the Reynolds number the nonlinear optimal perturbation is represented by coherent hairpin vortices originated by the breakup of the near-wall streaks, dissipating in the outer region the energy produced at the wall. Whereas, at the higher Reynolds number, the nonlinear optimal perturbation is composed of more robust large-scale streaks and less coherent vortical structures. As confirmed by the turbulent kinetic energy balance, the large-scale streaks are generated by a coherent large-scale lift-up mechanism, which acts as a source term in the energy balance, inducing a positive turbulent kinetic energy production at the outer scale. The coherent structures induced by the lift-up mechanism as well as their dominating wavelengths are analysed by means of two-point correlations and premultiplied kinetic energy spectra. The results of such analyses suggest that optimal large-scale streaks are a robust feature of turbulent channel flows at a sufficiently high Reynolds number, being recovered by energy optimisation in both linear and nonlinear conditions. Moreover, the fact that for increasing Re_τ the optimally-growing perturbations are mostly characterized by large-scale streaks (instead of hairpin vortices) may be linked to the onset of a kinetic energy production peak at the outer scale at values of Re_τ between 180 and 590, as observed in the DNS by several authors (Moser et al., 1999). In fact, between these two Reynolds numbers, we observe that the outer lift-up mechanism becomes the optimal mechanism for energy growth, leaving a clear signature in the turbulent kinetic energy budget, namely, the outer production peak observed in the literature. Future work will aim at investigating the reason for this structural change in the optimal perturbation shape. Moreover, it can be interesting to determine whether the optimal coherent structures further change at higher values of the Reynolds number for which a more evident scale separation between the size of the coherent structures populating the inner and the outer regions exists (Smits et al., 2011). In particular, a crucial point will be to confirm (or, else, to confute) the fading of harpin vortices in the optimal solution at higher Reynolds numbers, further confirming, as postulated by many authors, that they are a robust coherent structure mostly for the transitional flow regime (Sayadi et al., 2013).

Chapter VI

How hairpin structures emerge from exact solutions of shear flows

Contents

VI.1 Introduction 87

VI.2 Problem formulation 88

VI.3 Results 89

VI.4 Conclusion 94

VI.1 Introduction

Despite its mostly chaotic dynamics, turbulence is characterized by the presence of motions highly correlated over both space and time, carrying a large amount of the flow momentum. These so-called *coherent structures* (Marusic et al., 2010; Sundkvist et al., 2005) have been observed in transitional and turbulent shear flows, taking the form of streaks (streamwise elongated regions of low and high momentum) and hairpin vortices (curved vortices having the shape of a hairpin (Adrian, 2007)). Among these recurrent flow structures, streaks have been computed as exact coherent states (ECS) populating the state space of the solutions of the Navier-Stokes equations, driving the turbulent and transitional dynamics. These ECS are exact, albeit unstable, solutions of the Navier-Stokes equations (Eckhardt et al., 2007b; Faisst and Eckhardt, 2003; Hof et al., 2004; Kreilos and Eckhardt, 2012; Nagata, 1997; Waleffe, 1998) such as equilibria, periodic orbits or even chaotic solution, mostly composed of streamwise vortices and streaks like the first ECS found by Nagata (Nagata, 1990). On the other hand, hairpin-like flow structures have not yet been given a precise place in this dynamical-system view of turbulence. Despite these structures seem to characterize the relative attractors on the laminar-turbulent boundary in the Blasius boundary-layer flow (see Cherubini et al. (2011a); Duguet et al. (2012)), they are not recovered in any of the exact coherent states computed up to now for simple parallel shear flows such as Couette or plane Poiseuille flow. This probably indicates that these recurrent vortices do not constitute an element of the self-sustained mechanism maintaining the ECS itself in a given region of the phase space, whereas they might be linked to the passage from one ECS to the other. Many numerical and experimental studies report strong energetic events, known as bursts (Adrian, 2007; Farano et al., 2017), associated with the onset of hairpin vortices. These observations lead to the idea that hairpin structures might be linked to a state space trajectory leaving an ECS in a direction of strong energetic growth, either being the unstable eigendirection of the chosen invariant solution or a direction in the stable manifold providing a large energy growth at short time. However, this possibility has not been investigated yet, leaving as an open question the representation of this relevant flow structure in the dynamical systems framework.

This chapter provides a dynamical system explanation for the recurrence of hairpin vortices in parallel shear flows. Focusing on the plane Poiseuille flow, we show that hairpin structures are triggered by an optimally growing finite-amplitude perturbation of a known exact traveling wave solution. This perturbation is not constituted of the unstable eigenmodes of the selected ECS, but of a combination of stable non-orthogonal eigenmodes, able to generate a strong energetic growth at a finite time concurrent to the generation of the hairpin vortices. This suggests that the stable manifold of the ECS may have a strong relevance in the dynamics of transitional and turbulent flows.

VI.2 Problem formulation

We consider the plane Poiseuille flow at $Re = 2300$ in a domain $l_x \times l_y \times l_z = 4\pi \times 2 \times 2\pi$, where y is the wall-normal direction, x and z are the streamwise and spanwise (periodic) directions, $Re = U_c h/\nu$, ν is the kinematic viscosity, U_c the centerline velocity and h the half gap between the walls of the channel. The travelling wave known as TW2 in Gibson and Brand (2014) is considered, which is a saddle solution with 27 unstable modes. The aim of the present work is to determine the initial perturbation of TW2, $\mathbf{u}'(0)$, constrained within an energy shell $E_0 = ||\mathbf{u}'(0)||_2^2 = \frac{1}{V}\int_V \mathbf{u}'(0)\cdot\mathbf{u}'(0)dV$ around TW2, which provides a maximal energy growth at a given target time T_{opt} while leaving TW2. We use an adjoint-based Lagrange multiplier technique to maximize the distance from TW2 expressed in the energy norm $E(T_{opt}) = ||\mathbf{u}'(T_{opt})||_2^2$ for different values of T_{opt} and E_0 (Cherubini et al., 2010a; Pringle and Kerswell, 2010). The objective function $E(T_{opt})$ is subject to partial differential constraints such as the perturbative incompressible NS equations and the initial energy shell, which are added to the objective function via scalar product with the Lagrange multipliers (or adjoint variables) $(\mathbf{u}^\dagger, p^\dagger, E^\dagger)$, yielding the *augmented functional*:

$$\mathcal{L} = E(T_{opt}) - \int_0^{T_{opt}} \left\langle \mathbf{u}^\dagger \cdot NS(\mathbf{u}', \mathbf{u}_{TW}, p') \right\rangle dt - \int_0^{T_{opt}} \left\langle p^\dagger \nabla \cdot \mathbf{u}' \right\rangle dt - E^\dagger \left(E(0) - E_0\right), \tag{VI.1}$$

where $\mathbf{u}_{TW}$ is the considered baseflow, $\langle \bullet \rangle$ indicates the scalar product $\frac{1}{V}\int_V (\mathbf{a}\cdot\mathbf{b})dV$, V being the volume of the considered computational domain, and $\mathbf{a}, \mathbf{b}$ two generic velocity fields in that domain. Integrating by parts and setting to zero the first variation of $\mathcal{L}$ with respect to $(\mathbf{u}'(t \in (0, T_{opt})), \mathbf{u}'(0), \mathbf{u}'(T_{opt}), p')$ yields the adjoint equations

$$\begin{aligned} \frac{\partial \mathbf{u}^\dagger}{\partial t} &= -(\mathbf{u}_{TW} + \mathbf{u}') \cdot \nabla \mathbf{u}^\dagger + \nabla(\mathbf{u}_{TW} + \mathbf{u}')^T \cdot \mathbf{u}^\dagger - \nabla p^\dagger - \frac{1}{Re}\nabla^2 \mathbf{u}^\dagger, \\ \nabla \cdot \mathbf{u}^\dagger &= 0, \end{aligned} \qquad \text{(VI.2)}$$

plus the compatibility conditions $2\mathbf{u}'(T_{opt}) - \mathbf{u}^\dagger(T_{opt}) = 0$ and the gradient $\dfrac{\partial \mathcal{L}}{\partial \mathbf{u}'(0)}$ which must be nullified to attain the maximum of the constrained objective function. This is accomplished by setting up an iterative procedure which, starting from an initial guess within a given energy shell from TW2, relies on the successive integration of the direct (from $t = 0$ to $t = T_{opt}$) and adjoint (from $t = T_{opt}$ to $t = 0$) NS equations (the latter being initialized via the compatibility condition and integrated backward in time due to the negative diffusion term), providing an update of the initial perturbation $\mathbf{u}'(0)$ using the direction of the gradient (see Foures et al. (2013) and Farano et al. (2015)). The procedure stops when the variation of $E(T)$ between two successive iterations is smaller than a chosen threshold $e = 10^{-6}$. The optimization method described here has been implemented in the spectral code `Channelflow` (Gibson, 2014). In the periodic directions, Fourier discretization is adopted, while in the wall normal direction, Chebyshev polynomials are used. The numerical grid consists of $N_x \times N_y \times N_z = 96 \times 97 \times 96$ points.

VI.3 Results

Figure VI.1 (a) shows TW2, which is localized towards one of the walls and characterized by modulated streaks flanked by streamwise-inclined vortices. The initial optimal perturbation lying in an energy shell $E_0 = 10^{-6}$ around TW2 and providing a maximum energy at $T_{opt} = 10$ is provided in figure VI.1 (b). This is characterized by streamwise-alternated positive/negative patches of velocity perturbation placed on top of the TW streaks. From the qualitative point of view, the computed optimal is characterized by a spatial support that differs from the elongated structure of the most unstable eigenmode of the linearized NS equations around TW2. The non-linear evolution of the previously shown optimal perturbation (figure VI.1 (b)) on top of TW2 is provided in figure VI.1 (c) and (d) at $t = 5$ and $t = T_{opt} = 10$, respectively. Already after 5 time units, the optimal perturbation evolves into a train of hairpin-like vortices (yellow surfaces), which are maintained and enhanced at target time. Similar results can be found for optimal perturbations initially constrained in different energy shells. The optimal perturbations obtained for $E_0 = 10^{-7}, 10^{-8}$ and $T_{opt} = 10$ are provided in figure VI.3 (a) and (c), respectively, whereas the corresponding time evolution of the energy is shown in figure VI.2 (solid lines). The spatial structure of the optimal perturbation barely changes for decreasing values of E_0, approaching that of the linear optimal. The energy curves are also comparable although the same energy levels are reached at different times. In particular, the inset of figure VI.2 shows that, for decreasing values of E_0, the square root of the energy gain $\sqrt{(}E(t)/E_0)$ approaches the linear one, represented by the black line. Moreover, extracting in the three considered cases the instantaneous flow structures at the times at which the same assigned energy value $E(t) = E(T_{opt})_{E_0=10^{-6}} \approx 2.3 \times 10^{-4}$ is reached (coloured dots in figure VI.2), very similar trains of hairpin-vortex like structures

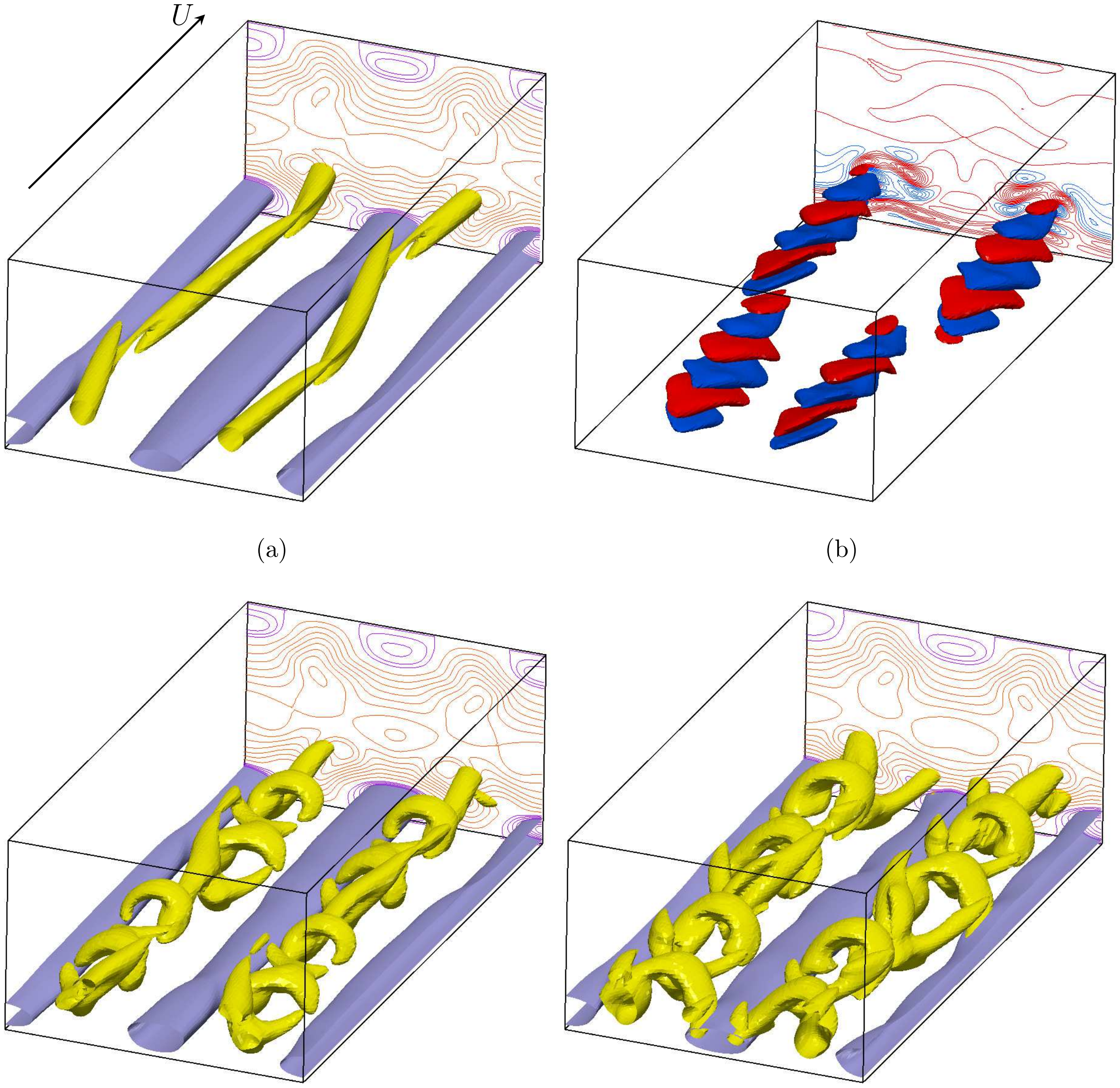

(a) (b)

(c) (d)

Figure VI.1: (a) Travelling wave $\mathbf{u}_{TW}$ and (b) associated optimal perturbation $\mathbf{u}'(0)$ lying at $t = 0$ in an energy shell $E_0 = 10^{-6}$ around TW2 providing a maximum energy amplifications at $T_{opt} = 10$. (c-d) Full velocity field $\mathbf{u}_{TW} + \mathbf{u}'(t)$ obtained by evolving the initial optimal perturbation on top of TW2: snapshots at $t = 5$, and $t = T_{opt} = 10$, respectively, both showing a train of hairpin vortices. (a,c,d) Isosurfaces of the Q criterion (yellow) of the full velocity field and of the positive streamwise velocity perturbation with respect to the laminar flow (violet). Isolines: streamwise velocity perturbation with respect to the laminar flow (orange for negative, violet for positive). (b) Isosurfaces of positive (red) and negative (blue) streamwise velocity perturbation $\mathbf{u}'(0)$. Isolines: streamwise velocity perturbation $\mathbf{u}'(0)$ (red for positive, blue for negative).

are found. The same can be said for variations of the target time up to $T_{opt} < 40$, whereas for larger target times the dynamics is driven by the asymptotic instability of the most unstable eigenmodes. Thus, the emergence of hairpin vortices on an *optimal* trajectory leaving the vicinity of TW2 appears as a robust phenomenon, occurring for different target times and initial energy shells. Moreover, the fact that the optimal perturbation as well as its evolution are only slightly dependent on the perturbation's initial amplitude indicates that such an optimal growth can be well approximated by a linear mechanism.

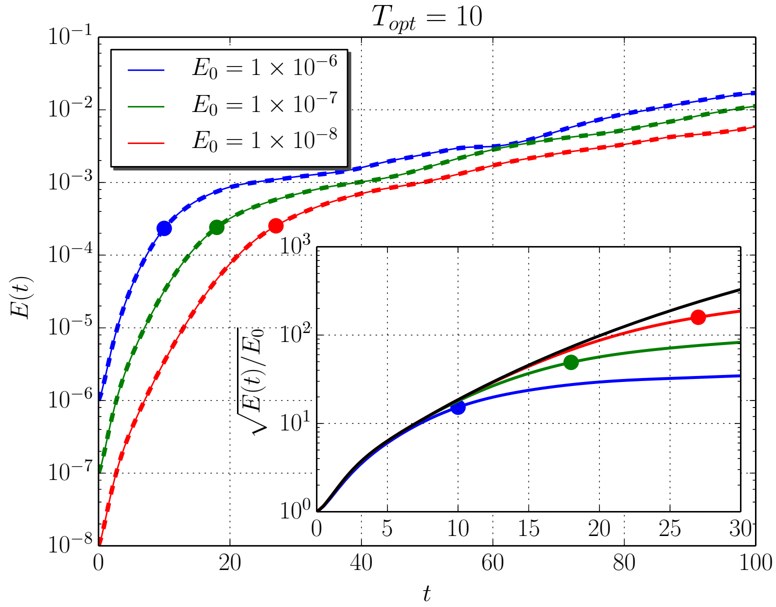

Figure VI.2: Evolution in time of the energy of three optimal perturbations (solid lines) with initial energy $E_0 = 10^{-6}$ (blue) 10^{-7} (green) 10^{-8} (red). Dashed lines represent the energy obtained for the same initial perturbations with the unstable directions of TW2 projected out. Inset: square root of the energy gain versus time. The black line is the energy gain obtained by a linear optimization. The dots indicate the times at which the flow fields in figure VI.1 (c) VI.3 (b,d) (from blue to red) have been extracted, which corresponds to the energy level $\approx 2.3 \times 10^{-4}$, at which the hairpin vortices are observed.

The most suited candidates for explaining this linear energy growth are the unstable eigenmodes of the linearised Navier-Stokes equation. To investigate whether this or other unstable eigenmodes have a role in the evolution of the optimal perturbation we project the latter onto the stable and unstable eigenmodes of TW2. The perturbation $\mathbf{u}'(0)$ is decomposed into an orthonormal basis $\widehat{\mathbf{u}}_i^{\perp}$ obtained using a Gram-Schmidt orthonormalisation of the eigenmode basis $\widehat{\mathbf{u}}_i$ (Alizard and Robinet, 2011), splitting the contribution of the unstable manifold $\mathbf{u}'_U$ and the stable one $\mathbf{u}'_S$ as follows:

$$\mathbf{u}'(0) \approx \sum_{i=1}^{N_U} k_i \widehat{\mathbf{u}}_i^{\perp} + \sum_{i=N_U+1}^{N_S+N_U} k_i \widehat{\mathbf{u}}_i^{\perp} = \mathbf{u}'_U + \mathbf{u}'_S \tag{VI.3}$$

where k_i is the expansion coefficient obtained by the Hermitian scalar product $k_i =< \mathbf{u}'(0), \widehat{\mathbf{u}}_i^{\perp} >$, and N_U and N_S are the number of the unstable and stable modes in the

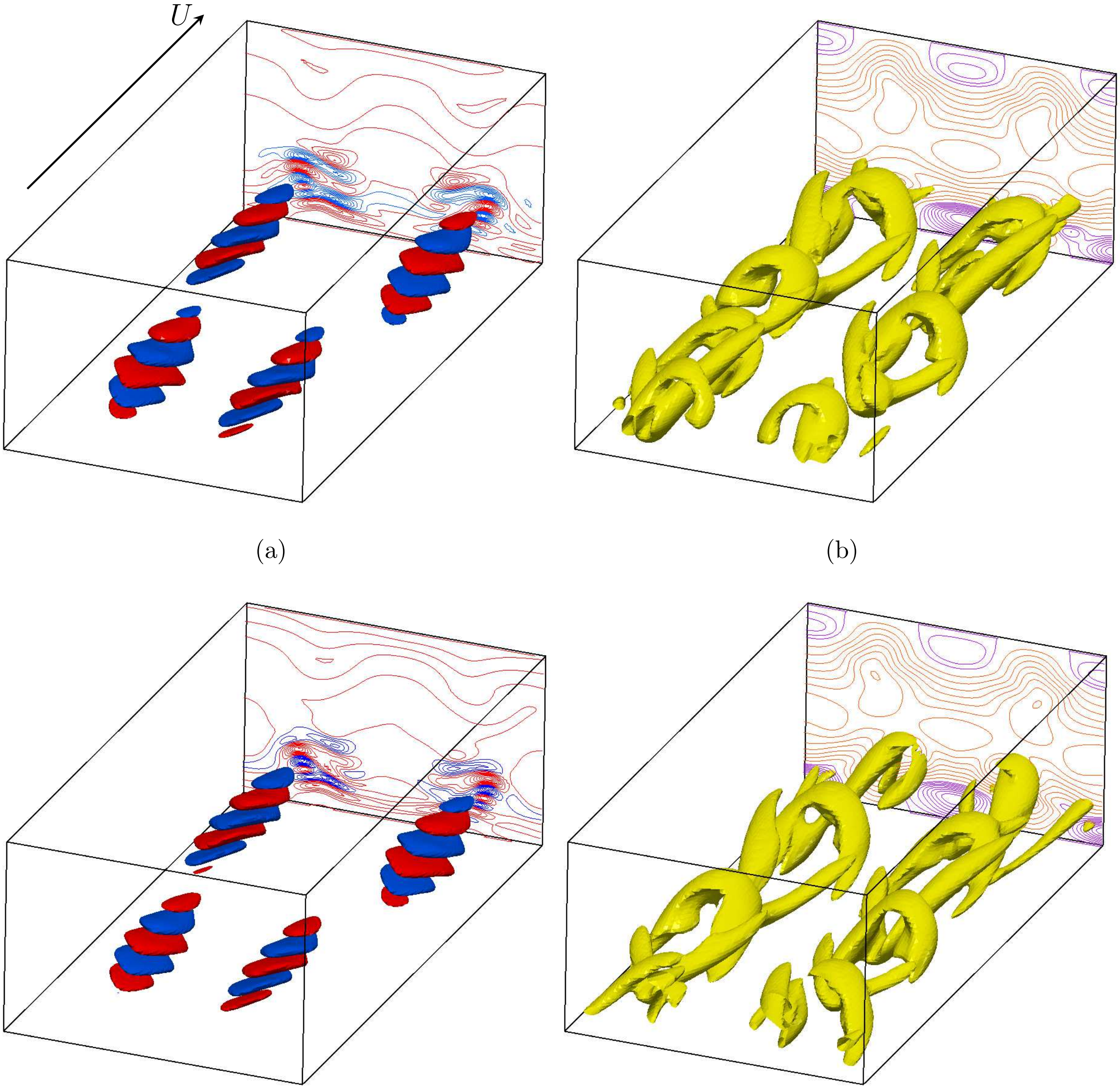

(a) (b) (c) (d)

Figure VI.3: Optimal perturbations $\mathbf{u}'(0)$ lying at $t = 0$ in an energy shell (a) $E_0 = 10^{-7}$, (c) $E_0 = 10^{-8}$ around TW2 providing the maximum energy amplification at $T_{opt} = 10$ (red, blue surfaces for positive, negative streamwise velocity perturbation, as well as for the isolines). Full velocity field $\mathbf{u}_{TW} + \mathbf{u}(t)$ obtained by evolving the two initial optimal perturbations on top of TW2: snapshots are extracted at $t = 18$ (b) and $t = 26.5$ (d), respectively, corresponding to the green and red dots in figure VI.2. Both snapshots show a train of hairpin vortices provided by the yellow surfaces representing the Q criterion of the full velocity field, whereas the isocontours represent the deviation from the laminar profile of the streamwise instantaneous velocity (violet for positive, orange for negative).

spectrum, respectively. Since we have used an orthonormal basis, the square of the module of each k_i represents the contribution of each eigenmode $\widehat{\mathbf{u}}_i^{\perp}$ to the energy of the initial optimal disturbance. In particular, the contribution of the unstable modes is very small,

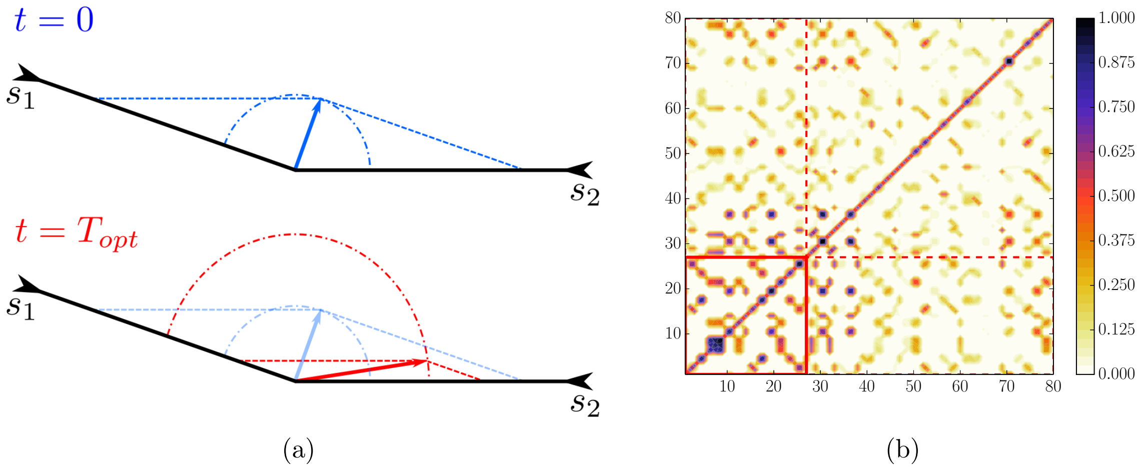

Figure VI.4: (a) Sketch illustrating the transient growth of a vector given by the sum of two time-decaying non-orthogonal eigenvectors, s_1 and s_2. While the amplitude of the two components of the vector along these eigendirections decreases in time (from top to bottom), the module of the resulting vector is transiently amplified (compare blue circle with red one). (b) Overlap matrix with entries given by the scalar product between the eigenvectors of the NS equations linearised around TW2, $\widehat{\mathbf{u}}_i, \widehat{\mathbf{u}}_j$. The darker the entry, the larger the overlap, with values between 0 and 1. For mutually orthogonal eigenvectors (as would be the case for a normal matrix) the scalar product would be non zero only on the matrix diagonal.

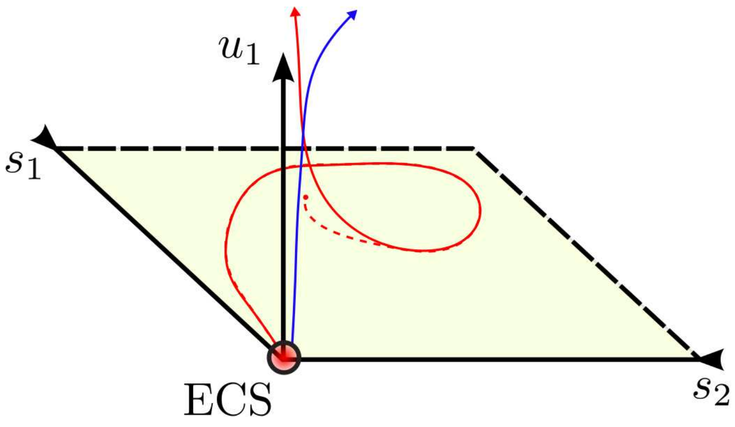

Figure VI.5: Sketch of the trajectory of the optimal perturbation initially lying on the neighbourhood of the ECS on a projection of the phase space given by the projection of the perturbation on the unstable direction u_1, and the stable ones s_1, s_2. The red line shows a trajectory associated to a rapid energy amplification (measured as the square of the distance from the ECS) in the stable subspace (yellow plane) with respect to the more classical scenario where the slower amplification follows the unstable one (blue line). The red and blue solid lines represent the trajectory in the full 3D space u_1, s_1, s_2, whereas the red dashed line is the projection of the trajectory in the 2D space s_1, s_2.

representing respectively 0.00901% and 0.4389% of E_0 for the cases at smaller and larger initial energy. Removing the contribution of the unstable modes from $\mathbf{u}'(t=0)$ and using the projection of the perturbation on the stable manifold ($\mathbf{u}'_S(0) = \mathbf{u}'(0) - \mathbf{u}'_U$) as initial condition for a direct numerical simulation, the same energy growth (dashed lines in figure VI.2) and flow structures are observed, featuring the formation of hairpin vortices at the selected target time. Notice that the we have projected on the stable subspace, which describes the dynamics of the linearised evolution, whereas the nonlinear flow follows curved invariant manifolds. However, we have previously shown that the optimal initial perturbation can be well approximated by a suitably scaled linear optimal solution, validating our approach. These results suggest that the recurrence of hairpin vortices in shear flows might be due to the existence of a preferred highly energetic path leaving the ECS along its stable manifold, thus bypassing the flow dynamics along the unstable manifold. Since this optimal mechanism is well approximated by a linear energy growth mechanism, it might be driven by the non-normality of the NS operator linearised around TW2. In fact, the (stable and unstable) eigenvectors of the linearized NS operator is non-orthogonal, leading to a strong transient energy increase that dominates the slow growth of the unstable modes, as sketched in figure VI.4 (a). Figure VI.4 (b) provides the absolute value of the scalar product between the eigenvectors of the linearized NS operator around TW2 $\widehat{\mathbf{u}}_i, \widehat{\mathbf{u}}_j$. Large values are found for many off-diagonal products indicating the non-normality of the NS operator linearized around TW2, whereas a normal operator would provide non-zero products only on the diagonal.

The non-normality of the NS operator linearized around this ECS has the potential for a large energy growth not along the most unstable direction but in a specific direction in the stable subspace (see Grossmann (2000); Waleffe (1995) for deep discussion), corresponding to the formation of highly energetic flow structures such as trains of hairpin vortices. This concept is schematically sketched in figure VI.5 where an optimally amplified trajectory leaves an ECS evolves mostly on the stable subspace (red lines) compared to the classical dynamics along the unstable manifold (blue one).

VI.4 Conclusion

Non-normality has been recognized as highly relevant for the transition from laminar to turbulent flow. The results shown here indicate that it is also fundamental for the dynamics within the turbulence-supporting network of exact invariant solutions. After having reached the vicinity of one ECS, trajectories should leave it and approach another invariant state within a finite time. Within this short time scale, the ECS's stable manifold (although exponentially contracting for an infinite time) can have a strong significance, since transient energy growth along it bears the potential for high amplitude excursions in the phase space, enabling the passage from the vicinity of one invariant solution to the other.

The scenario suggested by these results provides important hints in the understanding of orbits that connect the vicinities of two invariant states, challenging the simple picture of trajectories that wander in the phase space being attracted along the stable and ejected along the unstable manifold of invariant states, shadowing heteroclinic connections. In the next chapter we complete our analysis by proposing an algorithm that enables the identifications of heteroclinic connections; indeed these connections are relevant for the characterization of the transition and turbulence (Kawahara et al., 2012).

Chapter VII

CHELA: Computing HEteroclinic connections using a Lagrange multiplier Algorithm

Contents

VII.1 Introduction 97

VII.2 Problem formulation 98

VII.3 Results 101

VII.4 Conclusions and outlooks 103

VII.1 Introduction

Transition to turbulence can be studied in the framework of dynamical systems theory, the simple invariant solutions of the Navier-Stokes equation, such as equilibria, periodic and relative periodic solutions, playing a fundamental role in this approach. Although connections among them give a global picture of the whole dynamics that cannot be inferred from invariant solutions alone, there is not a general and robust algorithm to compute such connections. In this chapter a new algorithm for computing heteroclinic connections is provided and applied to the case of the plane Couette flow at $Re = 400$. The algorithm is based on nonlinear minimization using Lagrange multiplier methods. A direct-adjoint loop is implemented and used to compute six new connections. Thus, this work largely extends the existing one by Halcrow et al. (2009), which has been used for validation purposes. In the present work only fixed points are considered which, are considered a good starting point to show the effectiveness of the presented methodology. A description of the computed heteroclinic connections in the physical space and in a suitable projected state space is provided.

VII.2 Problem formulation

We consider plane Couette flow at Reynolds number $Re = 400$, where nondimensional variables are chosen such that half of the distance between the plates is $h = 1$ and half of the difference between the velocity of the two plates is 1. The incompressible flow is governed by the Navier-Stokes (NS) equations. Dirichlet boundary conditions for the three velocity components are imposed at the upper and lower wall ($U_{wall} = \pm 1$), whereas periodicity is prescribed in the streamwise and spanwise directions. Numerical simulations are performed in a computational domain of streamwise and spanwise size $L_x = 2\pi/1.14$ and $L_z = 2\pi/2.5$ respectively (Waleffe, 2003). x, y, z represent the streamwise, wall-normal and spanwise coordinates, respectively; likewise, u, v, w are the three Cartesian components of the velocity vector, $\mathbf{u}$. All the computations are performed using the code `Channelflow` (Gibson, 2014) based on a spectral discretization. The computational box is discretized by 32 Fourier points in the x direction, 35 Chebyshev points in the y direction and 32 Fourier points in the z direction.

We adapted a nonlinear optimization based on the Lagrange multiplier technique coupled with a direct-adjoint iterative procedure (Cherubini et al., 2010a; Monokrousos et al., 2011; Pringle and Kerswell, 2010), using a gradient-based method (Farano et al., 2015; Foures et al., 2013), to find heteroclinic connections between exact coherent states (ECS) of the NS equations. In particular, only fixed points are considered in the present work. In a heteroclinic connection, the velocity field varies over an infinite time interval leaving and approaching equilibria as time goes from $-\infty$ to $+\infty$, respectively. Those are the initial (ECS_{out}) and final equilibrium (ECS_{in}) of the heteroclinic connection. Since it is impossible to integrate over an infinite time interval, our computed heteroclinic connections start in a neighbourhood of the initial equilibrium and reach a neighbourhood of the final one, after a finite interval of time (T_{opt}). Therefore, we aim at finding the initial perturbation $\mathbf{u}'(0)$, constrained in the energy shell $E_{0_{out}}$ around the initial equilibrium, that minimizes, within a give threshold $E_{0_{in}}$, the distance to the final ECS at time $t = T_{opt}$. Such a distance is measured with the following metric, $E(T_{opt}) = ||\mathbf{u}'(T_{opt}) + \mathbf{u}_{ECS_{out}} - \mathbf{u}_{ECS_{in}}||_2^2$, where $|| \bullet || = 1/V \int_V \bullet^2 dV$, where V is the volume of the computational domain. Notice that the perturbation $\mathbf{u}'$ is defined with respect to the initial ECS and not to the laminar state. Thus the *augmented functional* of the Lagrangian optimization reads as follow:

$$\mathcal{L}\left(\mathbf{u}', p', \mathbf{u}^\dagger, p^\dagger, \mathbf{u}'(T_{opt}), \mathbf{u}'(0), \lambda\right) = ||\mathbf{u}'(T_{opt}) + \mathbf{u}_{ECS_{out}} - \mathbf{u}_{ECS_{in}}||_2^2 + \\ - \int_0^{T_{opt}} \left\langle \mathbf{u}^\dagger, NS(\mathbf{u}', \mathbf{u}_{ECS_{out}}, p')\right\rangle dt - \int_0^{T_{opt}} \left\langle p^\dagger, \nabla \cdot \mathbf{u}'\right\rangle dt - \lambda\left(||\mathbf{u}'(0)||_2^2 - E_0\right), \tag{VII.1}$$

where $\langle \mathbf{a}, \mathbf{b}\rangle$ indicates the scalar product $1/V \int_V (\mathbf{a} \cdot \mathbf{b}) dV$. Zeroing the derivatives of the functional $\mathcal{L}$ with respect to the variables $\mathbf{u}', p'$, one obtains the adjoint equations ($NS^\dagger$) as derived in the appendix of chapter II, where adjoint variables are indicated with the subscript †. Moreover, nullifying the gradient with respect to $\mathbf{u}'(T_{opt})$ one obtains the compatibility conditions at $t = T_{opt}$, namely, $\mathbf{u}^\dagger(T_{opt}) = \mathbf{u}'(T_{opt}) + \mathbf{u}_{ECS_{out}} - \mathbf{u}_{ECS_{in}}$. The initial energy constraint is guaranteed by using the gradient-rotation (Farano et al., 2015; Foures et al., 2013). The gradient of the functional with respect to the initial condition $\mathbf{u}'(0)$ is given by $\mathbf{u}(0)^\dagger$. Choosing a sufficiently long time horizon should guarantee that the heteroclinic connection is found (if it exists), in the limit of the approximation of the energy shells around the initial and final ECSs. The main obstacle is the chaotic behaviour of the flow subject to the NS equations, which, for increasing optimization time, may hinder the convergence of the algorithm. To avoid this problem, we perform a sequence of optimizations, slowly increasing the target time until final convergence is achieved, proceding as follows. For a given value of the target time, the direct-adjoint iteration is performed until the residual $\epsilon = ((E(T_{opt})^{n+1} - E(T_{opt})^{n})/E(T_{opt})^{n}$ becomes smaller than a given value ϵ_{cr}, as sketched in figure VII.1. At the end of these direct-adjoints iterations, for the current value of the target time, the perturbation gets close to the final ECS, but not close enough to reach the desired energy threshold E_{0out}. Thus T_{opt} is increased and a new iteration cycle is started. The algorithm stops when the initial condition develops in time to reach a distance from the final ECS smaller than the chosen threshold $E_{0_{out}}$. The complete direct-adjoint algorithm is summarized in Algorithm 1.

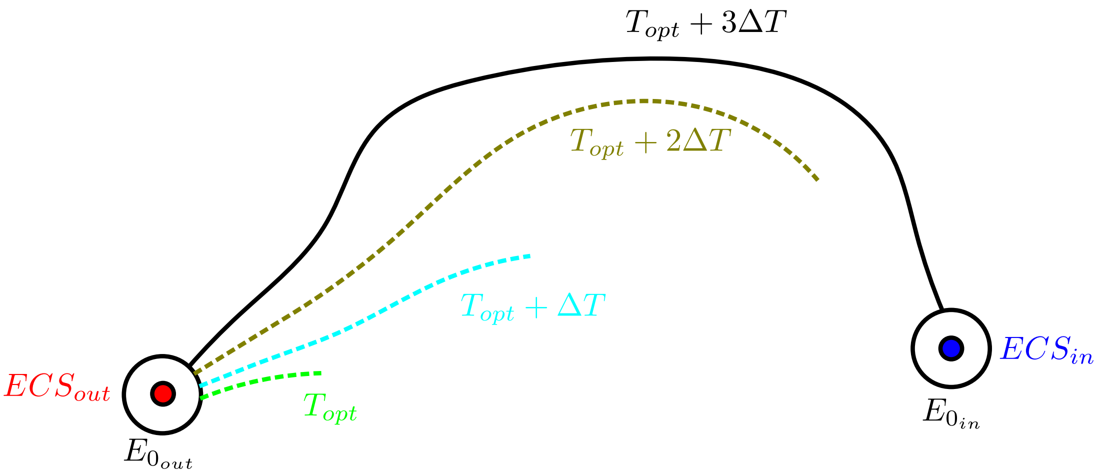

Figure VII.1: Schematic sketch describing the algorithm for computing heteroclinic connections using nonlinear optimization method based on Lagrange multipliers. The sketch shows how the initial condition, and the related trajectory towards the final ECS, changes after updating the optimization time T_{opt} (dashed lines). The algorithm stops when the integration time is sufficiently large to allow the flow field to be sufficiently close to the final stage (solid line).

It is noteworthy that the proposed algorithm contains several improvements with respect to that employed by Halcrow et al. (2009), which is a shooting method. The latter employs a perturbation of the initial equilibrium obtained as a linear combination of only two unstable eigenvectors of the base flow and aims at optimizing the coefficients of such a linear combination in order to approach the final state. To ensure the validity of this linear approximation, this algorithm requires the perturbation to be in a very small neighbourhood of the initial equilibrium. This increases the physical time associated to each connection as well as the required computational time to obtain them. It also renders more difficult to search for possible connections because of the chaotic behaviour of the NS equations over a long time interval, as explained before. Moreover, the method becomes less accurate when the dimension of the unstable subspace of the initial equilibrium is greater than two, since it restricts the initial conditions to be a linear combination of only two unstable eigenvectors, losing information about many possible unstable directions which the connections might follow when leaving the initial state. This is evident

```
Data: $E_{0_{out}}$, $E_{0_{in}}$, $\epsilon_{cr}$, $\Delta T$
Input: $\mathbf{u}'(0)$, $T_{opt}$ ;                                /* Initial guess */
begin
    while $E(T_{opt}) > E_{0_{in}}$ do
        $T_{opt} \longleftarrow T_{opt} + \Delta T$ ;                /* Increment $T_{opt}$ */
        while $\epsilon > \epsilon_{cr}$ do
            $\mathbf{u}'(T_{opt}) \longleftarrow NS\,(\mathbf{u}'(0))$;
            Evaluate $E(T_{opt})$ and $\epsilon$;
            if $\epsilon > \epsilon_{cr}$ then
                $\mathbf{u}^\dagger(T_{opt}) = \mathbf{u}'(T_{opt}) + \mathbf{u}_{ECS_{out}} - \mathbf{u}_{ECS_{in}}$ ;   /* Compatibility
                conditions */
                $\mathbf{u}^\dagger(0) \longleftarrow NS^\dagger\left(\mathbf{u}^\dagger(T_{opt})\right)$;
                Update $\mathbf{u}'(0)$ ;     /* Gradient rotation to enforce $E_{0_{out}}$ */
            end
        end
    end
    return $\mathbf{u}'(0)$, $T_{opt}$ ;        /* $\mathbf{u}'(0 \to T_{opt})$ provides the heteroclinic
    connection */
end
```

Algorithm 1: Schematic synthesis of the algorithm for searching heteroclinic connections.

by looking at the convergence plot in figure 1 of Halcrow et al. (2009).

On the other hand, the present algorithm does not constrain the initial perturbation to a subspace of unstable eigenvectors of the initial equilibrium. In fact, any perturbation in the neighbourhood of the initial ECS can be considered, without any constraint except the initial energy shell. This also allows the perturbation not to be in a very close neighbourhood of the ECS, taking into account the curvature of the unstable manifold while leaving the equilibrium. In this way we can increase the size of the initial energy shell remaining reasonably close to the initial state. We consider a value of $E_{0_{out}} = 10^{-6}$. Note that the energy shell around the initial state is of the same order of magnitude of that around the final state, which is sufficiently small to consider the heteroclinic connection well converged (Halcrow et al., 2009).

We also speculate that this method is more efficient than the previous one since it has been able to compute better converged connections with respect to the existing ones. Moreover, some of the computed heteroclinic connections end up on a final state with more than one unstable direction, whereas (Halcrow et al., 2009) succeded only at computing connections reaching the edge state. This is due to the fact that a closer approach to a slightly unstable equilibrium, such as the edge state, is easier and more likely than a connection to a highly unstable one. This indicates that our approach might be more robust than the previous one.

VII.3 Results

We considered the invariant solutions found by Gibson et al. (2009) and available in the database (Gibson, 2014). We have validated the algorithm computing three of the existing heteroclinic connections for plane Couette flow at $Re = 400$ (Halcrow et al., 2009). Moreover, we have found six previously unknown heteroclinic connections. Information about the heteroclinic connections are given in table VII.1.

Heteroclinic connections	Symmetry	$d(W^u(EQ_{out}))$	$d(W^u_s(EQ_{out}))$	$d(W^u_s(EQ_{in}))$	T_{opt}
$EQ5 \to EQ1$	(s_1, s_2, s_3)	11	4	1	250
$EQ4 \to EQ1$	(s_1, s_2, s_3)	6	3	1	230
$EQ3 \to EQ1$	(s_1, s_2, s_3)	4	2	1	273
$EQ4 \to EQ3$	(s_1, s_2, s_3)	6	3	2	322
$EQ9 \to EQ3$	(s_3)	5	3	2	284
$EQ4 \to EQ9$	(s_3)	6	4	3	228
$EQ10 \to EQ1$	(s_3)	10	7	1	216
$EQ9 \to EQ1$	(s_3)	5	3	1	550
$EQ11 \to EQ1$	(s_3)	15	10	1	500

Table VII.1: Computed heteroclinic connections for $Re = 400$ and corresponding symmetry subspace. The dimension of the unstable manifold of the starting equilibrium (ECS_{out}) is $d(W^u)$, while $d(W^u_S)$ is the dimension of the intersection of the unstable manifold with the symmetry invariant subspace reported here for the initial and final equilibrium (ECS_{in}).

The symmetry subspace considered here is named $S = \{1, s_1, s_2, s_3\}$ and it is defined in Gibson et al. (2008), where s_1 and s_2 are the "shift-reflect" and "shift-rotate" symmetry respectively, and $s_3 = s_1 s_2$. Details about the convergence of the computed heteroclinic connections are provided in figure VII.2 (left).

It is noteworthy that the computed heteroclinic connections fulfill the condition that two submanifolds in general position are likely to intersect if the sum of their dimensions is higher than or equal to the dimension of the state space (Halcrow et al., 2009). This means that the codimension of the stable manifold in the S-invariant space $d(W^u_s(EQ_{in}))$ of the final state (EQ_{in}) should be lower-equal than the dimension of the unstable manifold of the initial state $d(W^u_s(EQ_{out}))$ (see table VII.1). This should be sufficient to guarantee that the unstable manifold of the initial state and the stable one of the final state intersect in a stable way.

The dynamics of the computed heteroclinic connection can be analysed by looking at the trajectories in the plane $I - D$ (energy input-dissipation rate) (Kawahara and Kida, 2001) provided in figure VII.2 (right). Most of the trajectories are located in the lower-left part of the graph. This means that those connections might be relevant for the transition or relaminarization process and not for turbulent statistics as previously discussed in Gibson et al. (2009), since the connected exact coherent states are far from the turbulent chaotic saddle which is located slightly above the value $D = I \approx 2.5$ (Cherubini and De Palma, 2014). In particular, except the trajectories connecting $EQ3$ and $EQ9$ with $EQ1$, all the other connections go from high value of the friction Reynolds number (Re_τ)

to lower one. Moreover, all the connections join upper with lower branch solutions which are typically associated to the transitional dynamics (Wang et al., 2007).

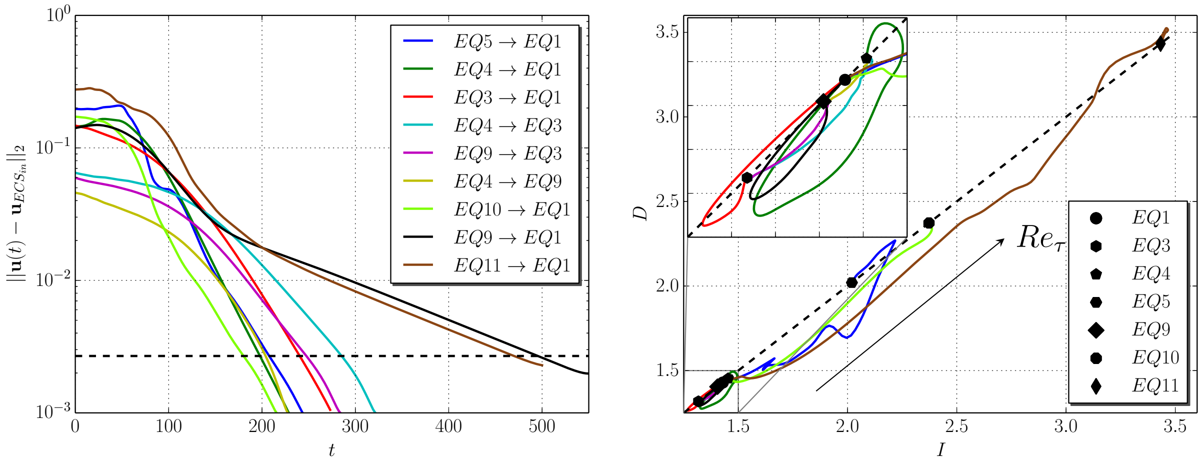

Figure VII.2: Left: Plots of distances of the velocity field $\mathbf{u}(t)$ to the target equilibrium $\mathbf{u}_{ECS_{in}}$ along the computed heteroclinic connections versus time. The dashed line represents the highest residual value for the heteroclinic connections computed in Halcrow et al. (2009). Right: Projection of the orbits onto the energy input rate, I, and the dissipation rate, D, normalized by their value in laminar flow.

A description of the new connections is provided in the following.
EQ4 → EQ3. Those two equilibria are upper and lower branch, respectively, emerging from a saddle node bifurcation and are very similar to each other in terms of vortical structure. The trajectory connects the upper with the lower solution: figure VII.3 shows how $EQ4$ slightly changes in the evolution towards $EQ3$.
EQ4 → EQ9. It is known that $EQ9$ is produced by a pitchfork bifurcation off $EQ4$ at $Re \approx 370$ (Gibson et al., 2009) This connection describes how EQ9 is thus related to EQ4 after the bifurcation point. The change in symmetry during the trajectory along the s_3 symmetric and s_1,s_2 antisymmetric subspaces leads to a heteroclinic connection between these two states (see figure VII.4).
EQ9 → EQ3. The trajectory connecting EQ9 to EQ3 shown in figure VII.5 restores the symmetry subspace of EQ4 and EQ3. This confirms how those three equilibria are dynamically related.
All the remaining trajectories connect the starting equilibrium with the edge state (EQ1) as those found in (Halcrow et al., 2009) ($EQ5 \to EQ1$, $EQ4 \to EQ1$, $EQ3 \to EQ1$).
EQ9 → EQ1. EQ9 is connected to the edge state via a heteroclinic connection following a dynamics symilar to that connecting EQ4 and EQ3 to EQ1, as shown in figure VII.6.
EQ10 → EQ1, **EQ11 → EQ1**. EQ10 and EQ11 are s_3 invariant and are generated by a saddle node bifurcation. Among all the equilibria and the related connections found here, those two states are the closest to the "turbulent attractor" (see figure VII.2 (right)), and both these connections towards the edge state describe the streaks oscillations typically observed in the turbulent dynamics. The associated time evolutions are reported in figures VII.7 and VII.8 showing the connections from EQ10 and EQ11 to EQ1 respectively.

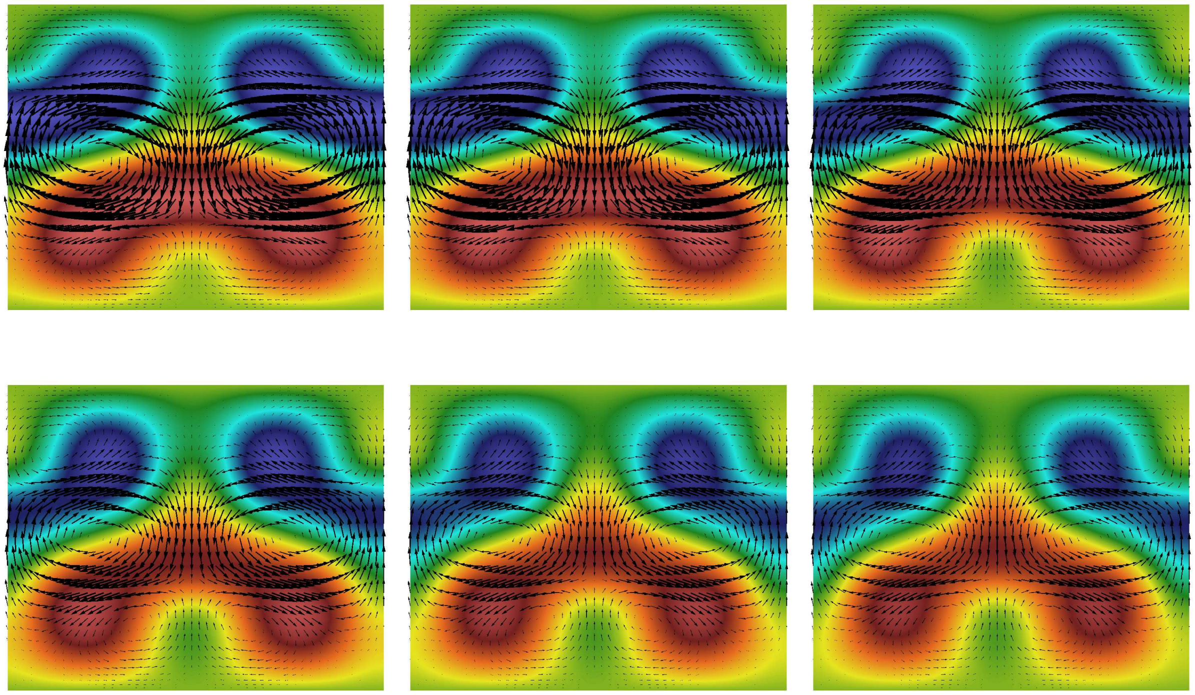

Figure VII.3: Streamwise averaged velocity field (with the laminar flow subtracted) at $t = 0$, $t = 43$, $t = 100$, $t = 157$, $t = 214$, $t = T_{opt}$, respectively (from top left to bottom right) of the computed heteroclinic connection from $EQ4$ to $EQ3$. Shaded contours represent the streamwise velocity (blue negative, red positive). The quiver plot shows the wall normal and spanwise component. Scales are set to the maximum (minimum) value of the quantities of the initial ECS.

To better visualize how the ECS are mutually connected via heteroclinic orbits, a low-order state space projection is necessary, to reduce the degree of the state space which counts more than (10^4) variables. A suitable projection of the state space is proposed by Gibson et al. (2008) and also used in Halcrow et al. (2009) to show the existing connections. Here, the new computed trajectories are plotted on the same projection of the state space, for comparison.

In particular, we projected the velocity field evolving along the computed heteroclinic trajectory $\mathbf{u}(t)$ onto a 3D orthonormal basis $(\mathbf{e}_1, \mathbf{e}_2, \mathbf{e}_3)$, defined in (Gibson et al., 2008), based on EQ_2 and its half-cell translated siblings. Time series of the coefficients $(a_1(t), a_2(t), a_3(t))$ are obtained using the inner product $a_i(t) =< \mathbf{u}(t), \mathbf{e}_i >$ defined above, where $i = 1, 2, 3$. The resulting trajectories projected onto this reduced basis are reported in figure VII.9.

VII.4 Conclusions and outlooks

Recent dynamical system approach to turbulence has shown the importance of invariant solutions of the NS equations, such as equilibria, travelling waves, periodic orbits and chaotic attractors. With the improvement of the computational resources and numerical

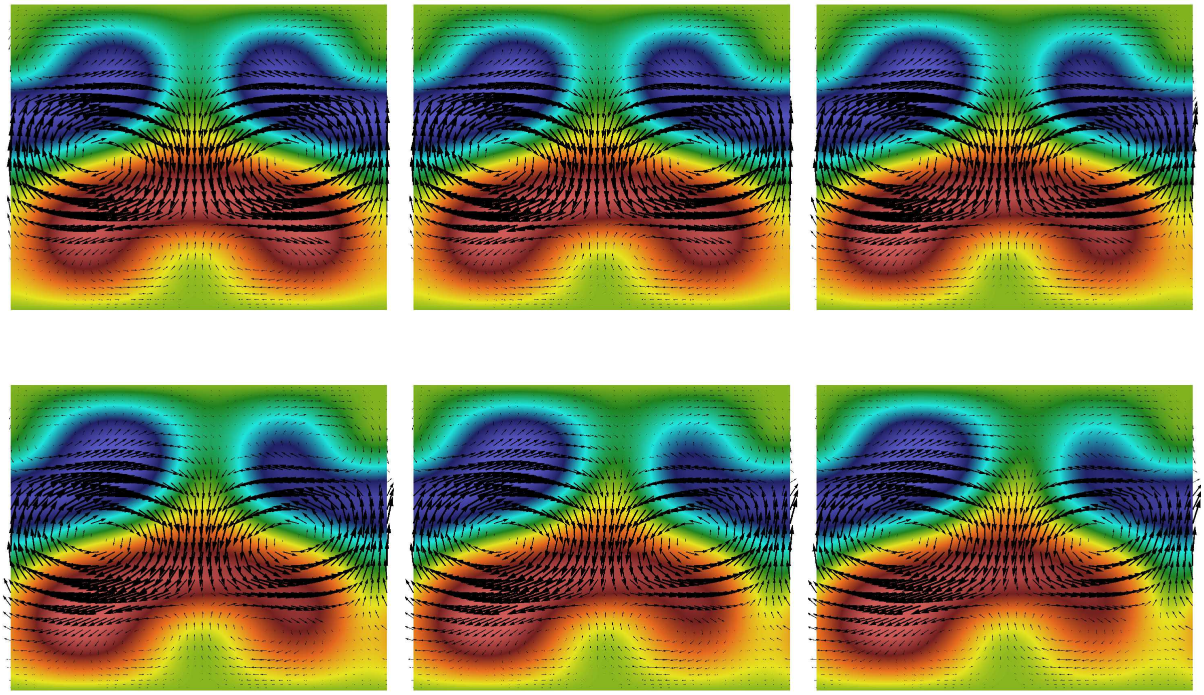

Figure VII.4: Streamwise averaged velocity field (with the laminar flow subtracted) at $t = 0$, $t = 26$, $t = 82$, $t = 123$, $t = 164$, $t = T_{opt}$, respectively (from top left to bottom right) of the computed heteroclinic connection from $EQ4$ to $EQ9$. Shaded contours represent the streamwise velocity (blue negative, red positive). The quiver plot shows the wall normal and spanwise component. Scales are set to the maximum (minimum) value of the quantities of the initial ECS.

algorithms, it has been possible to compute an increasing number of these nonlinear invariant solutions, which support the dynamics in the transitional and turbulent regimes. However, only a small number of homoclinic/heteroclinic connections among them have been found, mainly because of the lack of a good algorithm to detect them.

In this work we developed a new method based on a nonlinear optimization technique able to compute heteroclinic connections in plane Couette flow. We provided a detailed explanation of the algorithm and we showed the six new trajectories. Time series extracted during the evolution are also shown to visualize the change in the velocity field and vortical structures. Finally, we provide a visualization of the trajectories on a suitable projection of the state space.

This method represents a powerful tool to gain understanding about the dynamics of transitional and turbulent flows. In particular an extension of this algorithm might be used to find more complicated objects such as connections among periodic orbits and chaotic attractors. With the discovery of new invariant solutions, this method can be used to find more trajectories linking them. Extension of the application to other flow configurations is a straightforward step. Further investigation of the behaviour of the computed connections when parameters, e.g. Reynolds number are varied, is required to understand how those connections emerge or disappear in the bifurcation process.

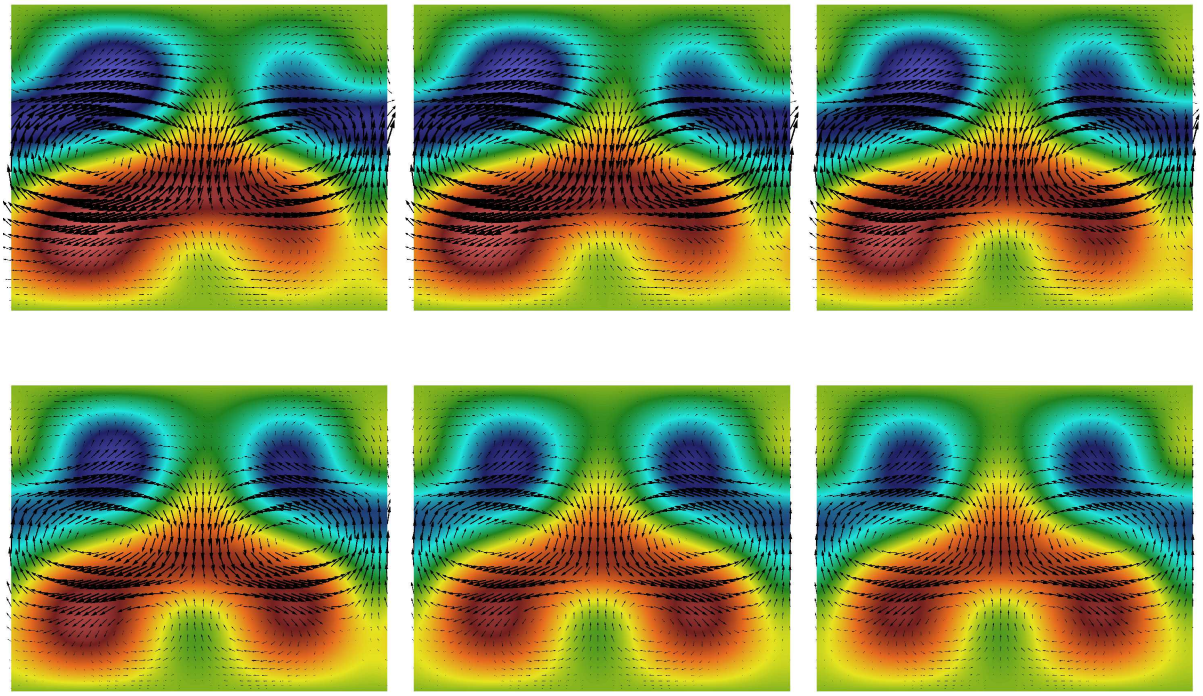

Figure VII.5: Streamwise averaged velocity field (with the laminar flow subtracted) at $t = 0$, $t = 26$, $t = 78$, $t = 130$, $t = 183$, $t = T_{opt}$, respectively (from top left to bottom right) of the computed heteroclinic connection from $EQ9$ to $EQ3$. Shaded contours represent the streamwise velocity (blue negative, red positive). The quiver plot shows the wall normal and spanwise component. Scales are set to the maximum (minimum) value of the quantities of the initial ECS.

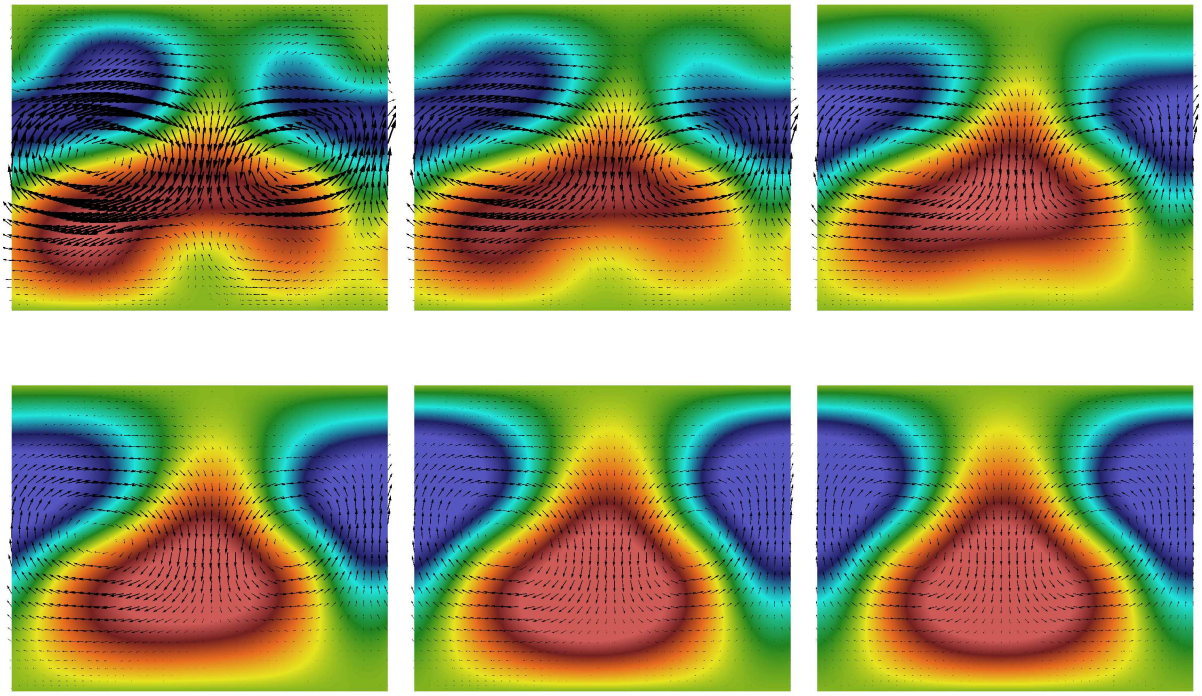

Figure VII.6: Streamwise averaged velocity field (with the laminar flow subtracted) at $t = 0$, $t = 60$, $t = 90$, $t = 120$, $t = 200$, $t = T_{opt}$, respectively (from top left to bottom right) of the computed heteroclinic connection from $EQ9$ to $EQ1$. Shaded contours represent the streamwise velocity (blue negative, red positive). The quiver plot shows the wall normal and spanwise component. Scales are set to the maximum (minimum) value of the quantities of the initial ECS.

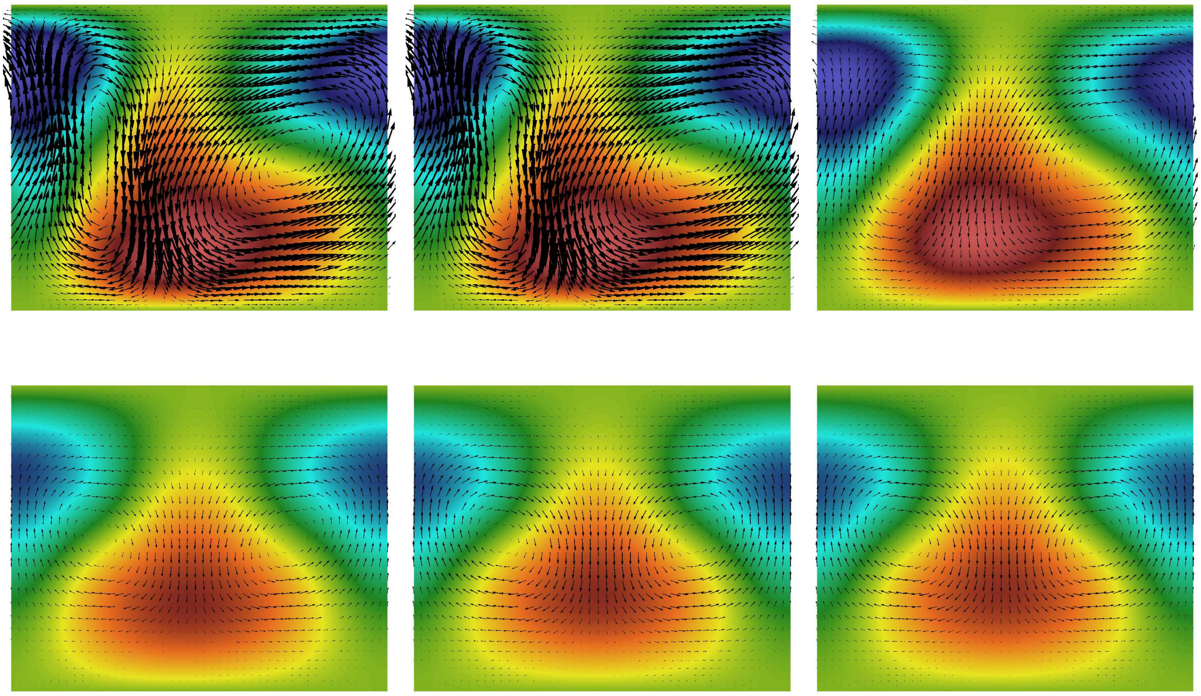

Figure VII.7: Streamwise averaged velocity field (with the laminar flow subtracted) at $t = 0$, $t = 9$, $t = 48$, $t = 87$, $t = 127$, $t = T_{opt}$, respectively (from top left to bottom right) of the computed heteroclinic connection from $EQ10$ to $EQ1$. Shaded contours represent the streamwise velocity (blue negative, red positive). The quiver plot shows the wall normal and spanwise component. Scales are set to the maximum (minimum) value of the quantities of the initial ECS.

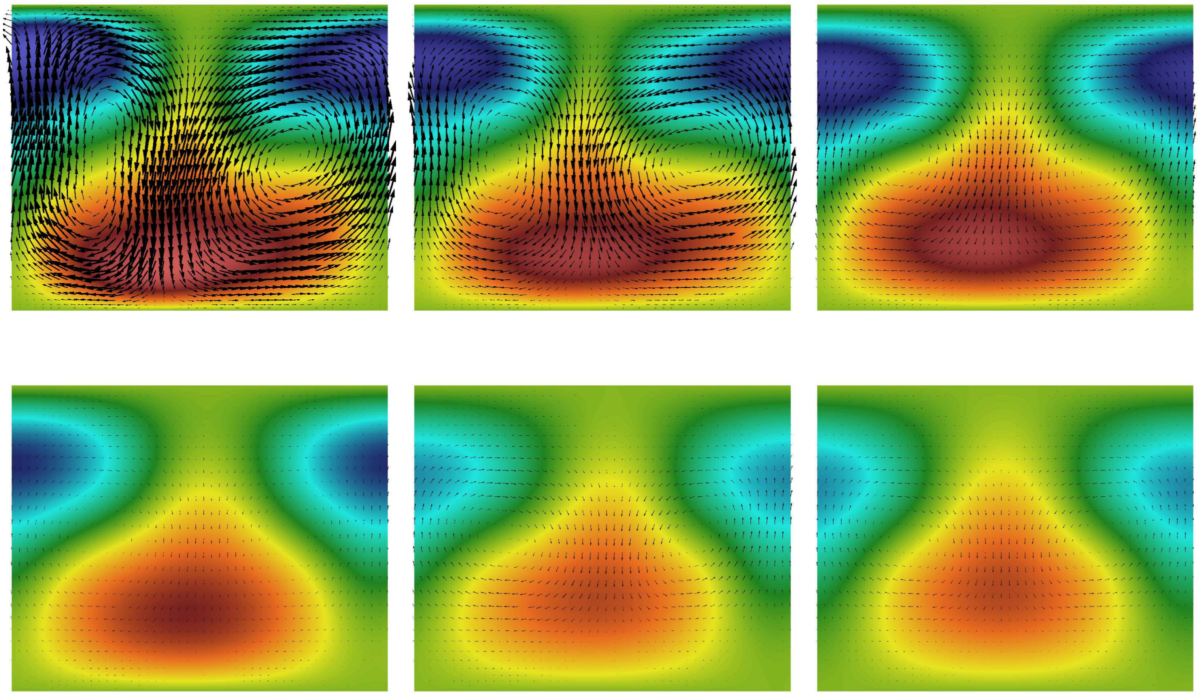

Figure VII.8: Streamwise averaged velocity field (with the laminar flow subtracted) at $t = 0$, $t = 50$, $t = 80$, $t = 110$, $t = 150$, $t = T_{opt}$, respectively (from top left to bottom right) of the computed heteroclinic connection from $EQ11$ to $EQ1$. Shaded contours represent the streamwise velocity (blue negative, red positive). The quiver plot show the wall normal and spanwise component. Scales are set to the maximum (minimum) value of the quantities of the initial ECS.

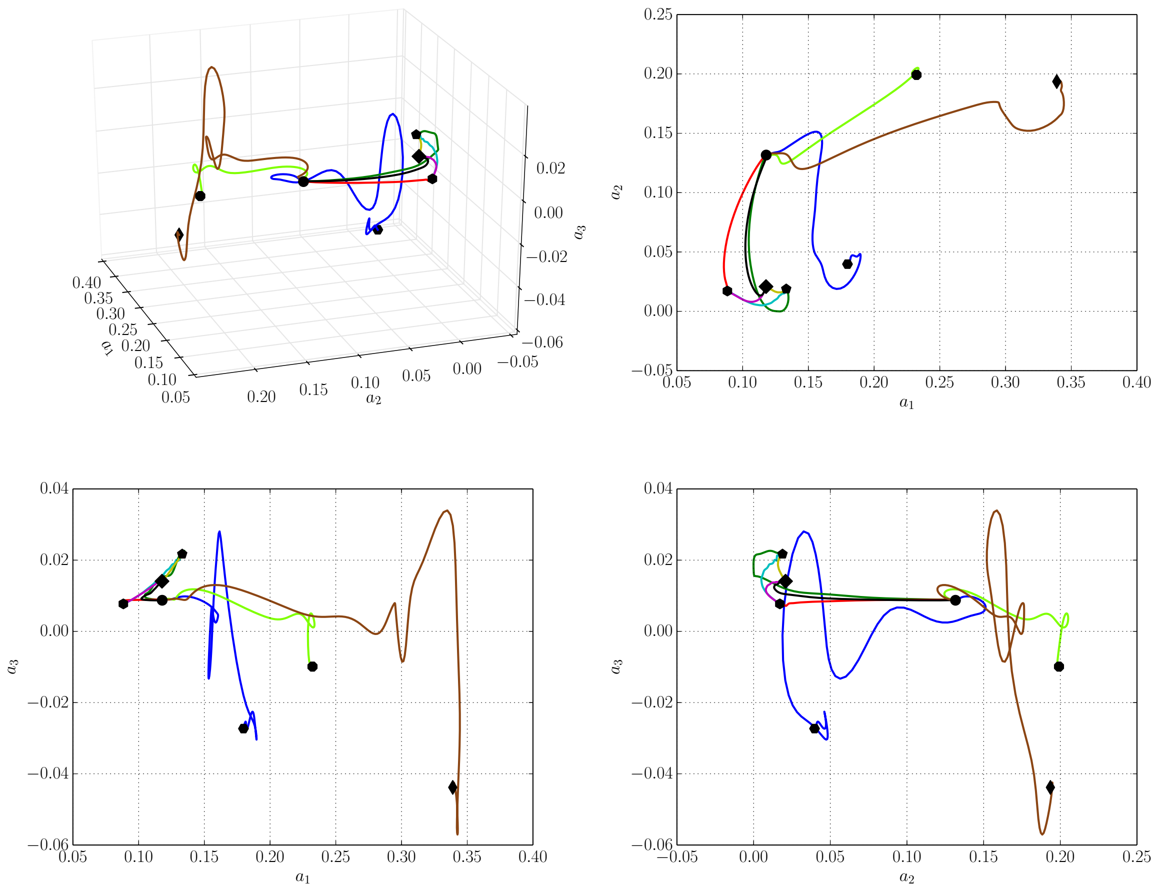

Figure VII.9: A state-space projection of the computed heteroclinic connections at $Re = 400$. Symbols and colours are the same as in figure VII.2.

Chapter VIII

Overall conclusions

VIII.1 Conclusions

In this thesis, a nonlinear optimization technique has been employed to investigate the behaviour of transitional and turbulent shear flows. The well known direct-adjoint optimization loop has been adapted for different applications with different purposes.

In chapters II and III, linear and nonlinear optimal perturbations have been computed for plane Poiseuille flow configuration in subcritical regime, where instabilities are induced by finite amplitude perturbation which grows due to the non-normality of the Navier-Stokes operator. Different kinds of optimal initial conditions able to trigger turbulence efficiently have been computed, showing different dynamics and flow structures. Varying the initial energy disturbance, the target time, and the objective function (only for linear cases), five initial optimal perturbations can be recognized:

1. linear optimal perturbation for low initial energy: streamwise independent rolls;
2. weakly nonlinear optimal perturbation for initial energy on the edge of chaos (minimal seed): streamwise and spanwise wavy rolls;
3. highly nonlinear optimal perturbation for finite high energy amplitude and “long” optimization time: localized spanwise-antisymmetric disturbance;
4. hairpin-like nonlinear optimal perturbation for finite high energy amplitude and “short” optimization time: localized spanwise-symmetric disturbance;
5. p-norm linear optimal perturbation: spanwise localized straight streamwise rolls.

The properties of the optimal perturbations have been analyzed, with particular attention to their localization in space and their efficiency in triggering transition to turbulence. At this purpose, the results obtained using high-norm objective function with a linear approach have been compared with those obtained by a fully nonlinear approach. The capability of localized optimal perturbations to induce transition has been investigated by means of direct numerical simulations. For a given initial energy, it was observed that enhancing localization in the linear optimization doesn’t provide always the most efficient disturbances compared to the nonlinear optimal even when the latter is not localized. It was also assessed that the spanwise and streamwise modulation of the vortical structures of the perturbation and the nonlinear interactions are often the main mechanisms responsible of the energy growth.

Moreover, it was shown for the first time that *hairpin vortices*, commonly observed in experiments and numerical simulations of transitional flows, represent an optimal solution of the Navier-Stokes equations, as well as a structure naturally selected by the flow, once perturbed with high energy disturbances. For this high energy route to turbulence, a new transition scenario has been observed, for which elongated streaky structures, their growth and breakdown are bypassed by the sudden formation of train of hairpin vortices.

In chapters IV and V the optimization technique has been employed in a turbulent framework in order to investigate the turbulent kinetic energy production mechanisms and to identify the coherent structures responsible of such an energy growth.

In particular for low values of friction Reynolds number ($Re_\tau \approx 180$) we found two different optimal structures as main sources of energy growth. The first one is associated to the presence of near wall self sustained streaks, which contribute to the positive average energy production in the inner region; the second one is associated to the presence of isolated burst events characterised by the presence of transient large scale motion with the shape of hairpin vortices, and not relevant for average quantities.

On the other hand, for sufficiently high value of Re_τ, namely 590, a positive energy production contribution due to large scale motion is found in the average kinetic energy balance, generating a footprint of the so called *outer peak* in the kinetic energy spectra. The optimal structure associated to this outer peak has the shape of large scale elongated streaks, and the production mechanism is the outer coherent lift-up, similar to the near wall one.

The last part of this manuscript is focused on the dynamical system approach to the study of transition and turbulence. The Navier-Stokes equations are considered as a time dependent dynamical system with its own equilibrium states. Those states appear to be relevant in the dynamics of transient turbulence, but to the author's knowledge a study of the geometry of the phase space in the neighbourhood of those equilibria has never been performed.

In chapter VI the dynamics in the neighbourhood of a particular travelling wave has been investigated for plane Poiseuille flow while leaving such a state. A possible dynamics in the stable manifold of the equilibrium has been observed, which is based on the non-orthogonality of the eighenmodes of the linearised Navier-Stokes operator. Relevant vortical structures, such as train of hairpin vortices, can be recovered by following a high energetic path laying in the stable manifold of the invariant solution. In particular we challenged the common simple scenario where an invariant state is approached along its stable manifold, and is left along its unstable one. After having reached the vicinity of one exact coherent state, trajectories should leave it and approach another invariant state within a finite time. Within this short time scale it is shown that because of the non-normality, a large excursion in the stable manifold can be followed while leaving the coherent state, bypassing the asymptotic time exponential growth given by the unstable modes.

Nevertheless, unstable manifolds remains relevant objects in the dynamical system framework. It can be the starting point for a possible existing heteroclinic connection between two exact coherent states. In chapter VII, a new algorithm for computing such an object has been developed based on a nonlinear minimization approach. With this method new heteroclinic connections have been computed in plane Couette flow. Increasing the knowledge of invariant solutions, as well as the connections among them, one can gain significant understanding of transient turbulence since those objects represent the “backbone” of its dynamics.

VIII.2 Perspectives

The PhD work presented in this manuscript has aimed at studying the role of coherent structures in transitional and turbulent flows from a numerical and theoretical point of view.

Concerning the stability of laminar shear flows, several fully nonlinear routes to turbulence involving energy growth have been deeply investigated in plane Poiseuille flow. Nevertheless, for experimental and practical purposes, the use of small computational domain with periodic boundary conditions in streamwise and spanwise directions represents a limit that should be overcame using larger box sizes. In this case, a more complex spatio-temporal dynamics exists, and coexistence of laminar and turbulent region is observed. Thus, to further investigate the presence and formation mechanisms of localized spot, patterns and stripes, perturbations optimally inducing those states could be computed using nonlinear optimization methods presented here. Moreover by computing energy threshold for turbulent transition in these configurations, a precise value of the Reynolds number at which turbulent is triggered can be theoretically determined.

Concerning fully developed turbulent flow, a clear extension of this work is to increase the friction Reynolds number in order to further investigate how large scale coherent structures change in shape and moreover how very large scale motions are originated and organized. Those structures appear when the Reynolds number is high enough to provide enough spatial scale separation between the inner and the outer region. Researchers have started to study these structures with the increase of computational power which has allowed one to perform simulations at higher and higher value of Reynolds. It is still not clear whether those structure are made by agglomerations of smaller scale structures, i.e. train of hairpin vortices on top of negative streaks, or are individual structures. What seems to be clear is that those structures carry a great part of the turbulent kinetic energy in the outer region. For this reason, energy growth can be investigated by using energy optimization even for those high Reynolds numbers in order to unravel the mechanisms behind the production of large scale structures. Extension to non-parallel turbulent flows, e. g. boundary layer flows, is another interesting topic.

A completely new perspective in the same context could be to use the mean flow equations considered here, to compute invariant solutions and apply the dynamical system pictures to fully developed turbulent flows. This would allow one to characterize relevant coherent structures populating turbulent flow with the use of an exact set of equations, in contrast to the recent (under-resolved) LES model aiming at the same purpose. In the present work it has been shown how this set of equations is suitable for a fully nonlinear analysis of turbulent mean flows, more accurate than other models used in previous works for linear analysis.

Concerning the dynamical system approach to turbulent transition, this work gives the initial input to investigate the non-normality of the Navier-Stokes operator in the turbulent chaotic saddle. Non-orthogonality has been deeply studied for the laminar base state, but none has ever investigated this behaviour for the nonlinear equilibria, i.e. exact coherent states. The importance of unstable direction has been questioned by the fact that a relevant dynamic in the stable manifold has been found. This results paves the way for a new perspective where the linear stability of exact coherent states may be not enough to characterize the turbulent dynamics.

In the same context, a solid mathematical method for computing heteroclinic connections among stationary equilibrium is provided here. A further challenge would be to extend this methodology to generalized invariant states, namely travelling waves and periodic orbits.

Depending on one's sensibility, numerous other prospectives could be added to this non-exhaustive list. However, the present list clearly summarises the author's thoughts about the most challenging way to continue this work.

Scientific production

List of all the conferences attended during the PhD thesis as well as of all the papers accepted, submitted or currently in preparation.

National conferences

- M. Farano, S. Cherubini, J.C. Robinet, P. De Palma
  Short-time nonlinear optimal perturbation in plane Poiseuille flow
  AIMETA 2015

International conferences

- M. Farano, S. Cherubini, J.C. Robinet, P. De Palma
  P-norm optimal 3D perturbations in the Poiseuille flow
  86th *Annual Meeting of the International Association of Applied Mathematics and Mechanics, 2015*

- M. Farano, S. Cherubini, J.C. Robinet, P. De Palma
  Localized optimal perturbations in plane Poiseuille flow
  11th *ERCOFTAC SIG 33 Workshop, Progress in Transition Modelling and Control, 2015*

- M. Farano, S. Cherubini, J.C. Robinet, P. De Palma
  A hairpin-shaped optimal perturbation in a plane Poiseuille flow
  6th *International symposium on Bifurcation and Instabilities in Fluid Dynamics, 2015*

- M. Farano, S. Cherubini, J.C. Robinet, P. De Palma
  Nonlinear optimal coherent structures in turbulent channel flow
  24th *International congress of theoretical and applied mechanics, 2016*

- M. Farano, S. Cherubini, J.C. Robinet, P. De Palma
  Optimal perturbations in transitional and turbulent flows at moderate Reynolds numbers
  12th *European Conference on Turbomachinery Fluid Dynamics and Thermodynamics, ETC 2017*

- M. Farano, P. De Palma, J.C. Robinet, S. Cherubini, T. M. Schneider
  The emergence of hairpin vortices from exact coherent state in plane Poiseuille flow
  7th International symposium on Bifurcation and Instabilities in Fluid Dynamics, 2017
- C. Mancini, M. Farano, J.C. Robinet, P. De Palma, S. Cherubini
  Global stability analysis of three-dimensional round jet diffusion flames
  7th International symposium on Bifurcation and Instabilities in Fluid Dynamics, 2017
- M. Farano, P. De Palma, J.C. Robinet, S. Cherubini, T. M. Schneider
  Connecting exact coherent states in plane Couette flow
  591 EUROMECH, Three-dimensional instability mechanisms in transitional and turbulent flows, 2017

Papers

- M. Farano, S. Cherubini, J.C. Robinet, P. De Palma
  Hairpin-like optimal perturbations in plane Poiseuille flow
  Journal of Fluid Mechanics, 775, R2 (2015)
- M. Farano, S. Cherubini, J.C. Robinet, P. De Palma
  Subcritical transition scenarios via linear and nonlinear localized optimal perturbations in plane Poiseuille flow
  Fluid Dynamics Research, 48, 061409 (2016)
- M. Farano, S. Cherubini, J.C. Robinet, P. De Palma
  Optimal bursts in turbulent channel flow
  Journal of Fluid Mechanics, 817, pp. 35-60 (2017)
- M. Farano, S. Cherubini, J.C. Robinet, P. De Palma
  Nonlinear large-scale optimal structures in turbulent channel flow
  Submitted
- M. Farano, P. De Palma, J.C. Robinet, S. Cherubini, T. M. Schneider
  How hairpin structures emerge from exact solutions of shear flows
  In Preparation
- M. Farano, P. De Palma, J.C. Robinet, S. Cherubini, T. M. Schneider
  Computing heteroclinic connections in shear flows
  In Preparation

In addition the author has contributed to the following articles that are not integrated into this cumulative thesis.

- C. Mancini, M. Farano, P. De Palma, J.C. Robinet, S. Cherubini
  Global stability analysis of lifted diffusion flames
  Energy Procedia, 126, pp. 867-874 (2017)

- M. Farano, C. Mancini, P. De Palma, J.C. Robinet, S. Cherubini
  3D global hydrodynamic stability analysis of a diffusion flame
  Submitted

Bibliography

Acarlar, M. S. and Smith, C. R. (1987). A study of hairpin vortices in a laminar boundary layer Part 2 Hairpin vortices generated by fluid injection . *J. Fluid Mech.*, 175:43–48.

Adrian, R. J. (2007). Hairpin vortex organization in wall turbulence). *Physics of Fluids (1994-present)*, 19(4):041301.

Adrian, R. J., Balachandar, S., and Lin, Z. (2001). Spanwise growth of vortex structure in wall turbulence. *KSME international journal*, 15(12):1741–1749.

Alizard, F. and Robinet, J.-C. (2011). Modeling of optimal perturbations in flat plate boundary layer using global modes: benefits and limits. *Theoretical and Computational Fluid Dynamics*, 25(1):147–165.

Andersson, P., Brandt, L., Bottaro, A., and Henningson, D. S. (2001). On the breakdown of boundary layer streaks. *Journal of Fluid Mechanics*, 428:29–60.

Avila, K., Moxey, D., de Lozar, A., Avila, M., Barkley, D., and Hof, B. (2011). The onset of turbulence in pipe flow. *Science*, 333(6039):192–196.

Barkley, D., Song, B., Mukund, V., Lemoult, G., Avila, M., and Hof, B. (2015). The rise of fully turbulent flow . *Nature*, 526:550–553.

Barkley, D. and Tuckerman, L. S. (2007). Mean flow of turbulent–laminar patterns in plane couette flow. *Journal of Fluid Mechanics*, 576:109–137.

Blackburn, H. M., Mansour, N. N., and Cantwell, B. J. (1996). Topology of fine-scale motions in turbulent channel flow. *Journal of Fluid Mechanics*, 310:269–292.

Bogard, D. G. and Tiederman, W. G. (1986). Burst detection with single-point velocity measurements. *Journal of Fluid Mechanics*, 162:389–413.

Bottin, S. and Chaté, H. (1998). Statistical analysis of the transition to turbulence in plane couette flow. *The European Physical Journal B-Condensed Matter and Complex Systems*, 6(1):143–155.

Brandt, L., Andersson, P., and Henningson, D. (2000). Secondary instability of streaks in boundary layers. *Advances in Turbulence VIII*, pages 141–144.

Brandt, L., Schlatter, P., and Henningson, D. S. (2004). Transition in boundary layers subject to free-stream turbulence. *Journal of Fluid Mechanics*, 517:167–198.

Butler, K. M. and Farrell, B. F. (1992). Three-dimensional optimal perturbations in viscous shear flow. *Physics of Fluids A: Fluid Dynamics (1989-1993)*, 4(8):1637–1650.

Butler, K. M. and Farrell, B. F. (1993). Optimal perturbations and streak spacing in wall-bounded turbulent shear flow. *Physics of Fluids A: Fluid Dynamics*, 5(3):774–777.

Chantry, M., Tuckerman, L. S., and Barkley, D. (2017). Universal continuous transition to turbulence in a planar shear flow. *J. Fluid Mech.*, 824:R2.

Chen, J., Hussain, F., Pei, J., and She, Z.-S. (2014). Velocity–vorticity correlation structure in turbulent channel flow. *Journal of Fluid Mechanics*, 742:291–307.

Cherubini, S. and De Palma, P. (2013). Nonlinear optimal perturbations in a couette flow: bursting and transition. *Journal of Fluid Mechanics*, 716:251–279.

Cherubini, S. and De Palma, P. (2014). Minimal perturbations approaching the edge of chaos in a couette flow. *Fluid Dynamics Research*, 46(4):041403.

Cherubini, S., De Palma, P., Robinet, J., and Bottaro, A. (2011a). Edge states in a boundary layer . *Phys. Fluids*, 23:051705.

Cherubini, S., De Palma, P., and Robinet, J.-C. (2015). Nonlinear optimals in the asymptotic suction boundary layer: Transition thresholds and symmetry breaking. *Physics of Fluids (1994-present)*, 27(3):034108.

Cherubini, S., De Palma, P., Robinet, J.-C., and Bottaro, A. (2010a). Rapid path to transition via nonlinear localized optimal perturbations in a boundary-layer flow. *Physical Review E*, 82(6):066302.

Cherubini, S., De Palma, P., Robinet, J.-C., and Bottaro, A. (2011b). The minimal seed of turbulent transition in the boundary layer. *J. Fluid Mech.*, 689:221–253.

Cherubini, S., Robinet, J.-C., Bottaro, A., and De Palma, P. (2010b). Optimal wave packets in a boundary layer and initial phases of a turbulent spot . *J. Fluid Mech.*, 656:231–259.

Cherubini, S., Robinet, J.-C., and De Palma, P. (2013). Nonlinear control of unsteady finite-amplitude perturbations in the Blasius boundary-layer flow . *J. Fluid Mech.*, 737:440–465.

Chong, M., Perry, A. E., and Cantwell, B. (1990). A general classification of three-dimensional flow fields. *Physics of Fluids A: Fluid Dynamics (1989-1993)*, 2(5):765–777.

Cohen, J., Karp, M., and Mehta, V. (2014). A minimal flow-elements model for the generation of packets of hairpin vortices in shear flows. *Journal of Fluid Mechanics*, 747:30–43.

Cohen, J., Philip, J., and Ben-Dov, G. (2009). Aspects of linear and nonlinear instabilities leading to transition in pipe and channel flows. *Phil. Trans. R. Soc. A*, 367(1888):509–527.

Cossu, C. (2005). An optimality condition on the minimum energy threshold in subcritical instabilities. *Comptes Rendus Mécanique*, 333(4):331–336.

Cossu, C., Brandt, L., Bagheri, S., and Henningson, D. S. (2011). Secondary threshold amplitudes for sinuous streak breakdown. *Physics of Fluids (1994-present)*, 23:074103.

Cossu, C., Pujals, G., and Depardon, S. (2009). Optimal transient growth and very large–scale structures in turbulent boundary layers. *Journal of Fluid Mechanics*, 619:79–94.

Darbyshire, A. and Mullin, T. (1995). Transition to turbulence in constant-mass-flux pipe flow. *Journal of Fluid Mechanics*, 289:83–114.

Dauchot, O. and Daviaud, F. (1995). Finite amplitude perturbation and spots growth mechanism in plane couette flow. *Physics of Fluids (1994-present)*, 7(2):335–343.

del Álamo, J. C. and Jiménez, J. (2003). Spectra of the very large anisotropic scales in turbulent channels. *Physics of Fluids*, 15(6):L41.

Deville, M. O., Fischer, P. F., and Mund, E. H. (2002). *High-order methods for incompressible fluid flow*, volume 9. Cambridge University Press.

Duguet, Y., Brandt, L., and Larsson, B. R. J. (2010). Towards minimal perturbations in transitional plane couette flow. *Physical Review E*, 82(2):026316.

Duguet, Y., Monokrousos, A., Brandt, L., and Henningson, D. S. (2013). Minimal transition thresholds in plane couette flow. *Physics of Fluids (1994-present)*, 25(8):084103.

Duguet, Y., Pringle, C. C., and Kerswell, R. R. (2008a). Relative periodic orbits in transitional pipe flow. *Physics of fluids*, 20(11):114102.

Duguet, Y., Schlatter, P., Henningson, D., and Eckhardt, B. (2012). Self-sustained localized structures in a boundary-layer flow . *Phys. Rev. Lett.*, 108:044501.

Duguet, Y., Willis, A. P., and Kerswell, R. R. (2008b). Transition in pipe flow: the saddle structure on the boundary of turbulence. *Journal of Fluid Mechanics*, 613:255–274.

Eckhardt, B., Faisst, H., Schmiegel, A., and Schneider, T. M. (2008). Dynamical systems and the transition to turbulence in linearly stable shear flows. *Philosophical Transactions of the Royal Society of London A: Mathematical, Physical and Engineering Sciences*, 366(1868):1297–1315.

Eckhardt, B., Schneider, T. M., Hof, B., and Westerweel, J. (2007a). Turbulence transition in pipe flow. *Annu. Rev. Fluid Mech.*, 39:447–468.

Eckhardt, B., Schneider, T. M., Hof, B., and Westerweel, J. (2007b). Turbulence transition of pipe flow . *Annu. Rev. Fluid Mech.*, 39:447–468.

Eitel-Amor, G., Örlü, R., Schlatter, P., and Flores, O. (2015). Hairpin vortices in turbulent boundary layers. *Physics of Fluids (1994-present)*, 27(2):025108.

Faisst, H. and Eckhardt, B. (2003). Travelling waves in pipe flow . *Phys. Rev. Lett.*, 91:224502.

Farano, M., Cherubini, S., Robinet, J.-C., and De Palma, P. (2015). Hairpin-like optimal perturbations in plane poiseuille flow. *Journal of Fluid Mechanics*, 775.

Farano, M., Cherubini, S., Robinet, J.-C., and De Palma, P. (2016). Subcritical transition scenarios via linear and nonlinear localized optimal perturbations in plane poiseuille flow. *Fluid Dynamics Research*, 48:061409.

Farano, M., Cherubini, S., Robinet, J.-C., and De Palma, P. (2017). Optimal bursts in turbulent channel flow. *Journal of Fluid Mechanics*, 817:35–60.

Farrell, B. F. (1988). Optimal excitation of perturbations in viscous shear flow. *Physics of Fluids*, 31(8):2093.

Fischer, P., Lottes, J., and Kerkemeir, S. (2008). nek5000 Web pages. http://nek5000.mcs.anl.gov.

Flores, O. and Jimenez, J. (2010). Hierarchy of minimal flow units in the logarithmic layer. *Physics of Fluids*, 22:071704.

Foures, D., Caulfield, C., and Schmid, P. (2013). Localization of flow structures using ∞-norm optimization. *Journal of Fluid Mechanics*, 729:672–701.

Foures, D. P. G., Caulfield, C. P., and Schmid, P. J. (2012). Variational framework for flow optimization using seminorm constraints. *Physica Review E*, 86:026306.

Gibson, J. and Brand, E. (2014). Spanwise-localized solutions of planar shear flows. *Journal of Fluid Mechanics*, 745:25–61.

Gibson, J. F. (2014). Channelflow: A spectral Navier-Stokes simulator in C++. Technical report, U. New Hampshire. `Channelflow.org`.

Gibson, J. F., Halcrow, J., and Cvitanović, P. (2008). Visualizing the geometry of state space in plane couette flow. *Journal of Fluid Mechanics*, 611:107–130.

Gibson, J. F., Halcrow, J., and Cvitanović, P. (2009). Equilibrium and traveling-wave solutions of plane Couette flow . *J. Fluid Mech.*, 638:243.

Grossmann, S. (2000). The onset of shear flow turbulence. *Reviews of modern physics*, 72(2):603.

Halcrow, J., Gibson, J. F., Cvitanović, P., and Viswanath, D. (2009). Heteroclinic connections in plane couette flow. *Journal of Fluid Mechanics*, 621:365–376.

Hamilton, J. M., Kim, J., and Waleffe, F. (1995). Regeneration mechanisms of near-wall turbulence structures. *Journal of Fluid Mechanics*, 287:317–348.

Heist, D., Hanratty, T., and Na, Y. (2000). Observations of the formation of streamwise vortices by rotation of arch vortices. *Physics of Fluids (1994-present)*, 12(11):2965–2975.

Henningson, D. S., Lundbladh, A., and Johansson, A. V. (1993). A mechanism for bypass transition from localized disturbances in wall-bounded shear flows. *Journal of Fluid Mechanics*, 250:169–207.

Hof, B. and Budanur, N. B. (2017). Heteroclinic path to spatially localized chaos in pipe flow. *Journal of Fluid Mechanics*, 827.

Hof, B., van Doorne, C., Westerweel, J., Nieuwstadt, F., Faisst, H., Eckhardt, B., Wedin, H., Kerswell, R., and Waleffe, F. (2004). Experimental Observation of Nonlinear Traveling Waves in Turbulent Pipe Flow . *Science*, 305:1594–1598.

Hof, B., van Doorne, C. W., Westerweel, J., and Nieuwstadt, F. T. (2005). Turbulence regeneration in pipe flow at moderate reynolds numbers. *Physical review letters*, 95(21):214502.

Hoyas, S. and Jiménez, J. (2006). Scaling of the velocity fluctuations in turbulent channels up to re_τ= 2003. *Physics of Fluids (1994-present)*, 18(1):011702.

Hunt, J. C. R., Wray, A., and Moin, P. (1988). Eddies, stream, and convergence zones in turbulent flows. *Center for Turbulence Research Report*, CTR-S88.

Hwang, J., Lee, J., Sung, H. J., and Zaki, T. A. (2016a). Inner–outer interactions of large-scale structures in turbulent channel flow. *Journal of Fluid Mechanics*, 790:128–157.

Hwang, Y. (2015). Statistical structure of self-sustaining attached eddies in turbulent channel flow. *Journal of Fluid Mechanics*, 767:254–289.

Hwang, Y. and Bengana, Y. (2016). Self-sustaining process of minimal attached eddies in turbulent channel flow. *Journal of Fluid Mechanics*, 795:708–738.

Hwang, Y. and Cossu, C. (2010a). Amplification of coherent streaks in the turbulent couette flow: an input–output analysis at low reynolds number. *Journal of Fluid Mechanics*, 643:333–348.

Hwang, Y. and Cossu, C. (2010b). Self-sustained process at large scales in turbulent channel flow. *Physical Review Letters*, 105(4):044505.

Hwang, Y. and Cossu, C. (2011). Self-sustained processes in the logarithmic layer of turbulent channel flows. *Physics of Fluids (1994-present)*, 23(6):061702.

Hwang, Y., Willis, A. P., and Cossu, C. (2016b). Invariant solutions of minimal large-scale structures in turbulent channel flow for re_τ up to 1000. *Journal of Fluid Mechanics*, 802.

Jiménez, J. (1999). The physics of wall turbulence. *Physica A: Statistical Mechanics and its Applications*, 263(1):252–262.

Jiménez, J. (2013). How linear is wall-bounded turbulence? *Physics of Fluids*, 25:110814.

Jiménez, J. (2015). Direct detection of linearized bursts in turbulence. *Physics of Fluids*, 27:065102.

Jiménez, J. and Moin, P. (1991). The minimal flow unit in near-wall turbulence. *Journal of Fluid Mechanics*, 225:213–240.

Jiménez, J. J., Kawahara, G., Simens, M. P., N., N., and Shiba, M. (2005). Characterization of near-wall turbulence in terms of equilibrium and 'bursting' solutions. *Physics of Fluids*, 17:015105.

Jiménez, J. J. and Pinelli, A. (1999). The autonomous cycle of near-wall turbulence. *Journal of Fluid Mechanics*, 389:335–359.

Karp, M. and Cohen, J. (2014). Tracking stages of transition in couette flow analytically. *J. Fluid Mech.*, 748:896–931.

Kawahara, G. and Kida, S. (2001). Periodic motion embedded in plane couette turbulence: regeneration cycle and burst. *Journal of Fluid Mechanics*, 449:291–300.

Kawahara, G., Uhlmann, M., and Van Veen, L. (2012). The significance of simple invariant solutions in turbulent flows. *Annual Review of Fluid Mechanics*, 44:203–225.

Kerswell, R. (2005). Recent progress in understanding the transition to turbulence in a pipe. *Nonlinearity*, 18(6):R17.

Kim, J., Moin, P., and Moser, R. (1987). Turbulence statistics in fully developed channel flow at low reynolds number. *Journal of fluid mechanics*, 177:133–166.

Kline, S. J., Reynold, W. C., Schraub, F., and Rundstander, P. (1967). The structure of turbulent boundary layer flows. *J. Fluid Mech.*, 30:741–773.

Kreilos, T. and Eckhardt, B. (2012). Periodic orbits near onset of chaos in plane couette flow. *Chaos: An Interdisciplinary Journal of Nonlinear Science*, 22(4):047505.

Kreilos, T., Veble, G., Schneider, T. M., and Eckhardt, B. (2013). Edge states for the turbulence transition in the asymptotic suction boundary layer. *Journal of Fluid Mechanics*, 726:100–122.

Kreiss, G., Lundbladh, A., and Henningson, D. S. (1994). Bounds for threshold amplitudes in subcritical shear flows. *Journal of Fluid Mechanics*, 270:175–198.

Landahl, M. (1980). A note on an algebraic instability of inviscid parallel shear flows. *Journal of Fluid Mechanics*, 98(02):243–251.

Lee, M. and Moser, R. D. (2015). Direct numerical simulation of turbulent channel flow up to $re_\tau \approx 5200$. *Journal of Fluid Mechanics*, 774:395–415.

Lemoult, G., Shi, L., Avila, K., Jalikop, S. V., Avila, M., and Hof, B. (2016). Directed percolation phase transition to sustained turbulence in Couette flow . *Nature Physics*, 12:254–258.

Levin, O. and Henningson, D. S. (2007). Turbulent spots in the asymptotic suction boundary layer. *Journal of Fluid Mechanics*, 584:397–413.

Luchini, P. (2000). Reynolds-number-independent instability of the boundary layer over a flat surface: optimal perturbations. *Journal of Fluid Mechanics*, 404:289–309.

Marusic, I., Mathis, R., and Hutchins, N. (2010). Predictive model for wall-bounded turbulent flow. *Science*, 329:193—196.

Matsubara, M. and Alfredsson, P. H. (2001). Disturbance growth in boundary layers subjected to free-stream turbulence. *J. Fluid Mech.*, 430:149–168.

Mellibovsky, F. and Meseguer, A. (2007). Pipe flow transition threshold following localized impulsive perturbations. *Physics of Fluids (1994-present)*, 19(4):044102.

Moin, P. and Kim, J. (1985). The structure of the vorticity field in turbulent channel flow. part 1: Analysis of instantaneous fields and statistical correlations. *Journal of Fluid Mechanics*, 155:441–464.

Monokrousos, A., Åkervik, E., Brandt, L., and Henningson, D. S. (2010). Global three-dimensional optimal disturbances in the blasius boundary-layer flow using time-steppers. *Journal of Fluid Mechanics*, 650:181–214.

Monokrousos, A., Bottaro, A., Brandt, L., Di Vita, A., and Henningson, D. S. (2011). Nonequilibrium thermodynamics and the optimal path to turbulence in shear flows. *Phys. Rev. Lett.*, 106(13):134502.

Moser, R. D., Kim, J., and Mansour, N. N. (1999). Direct numerical simulation of turbulent channel flow up to $re_\tau = 590$. *Phys. Fluids*, 11(4):943–945.

Mösta, P., Ott, C. D., Radice, D., Roberts, L. F., Schnetter, E., and Haas, R. (2015). A large-scale dynamo and magnetoturbulence in rapidly rotating core-collapse supernovae. *Nature*, 528:376–379.

Moum, J. N., Perlin, A., Nash, J. D., and McPhaden, M. J. (2013). Seasonal sea surface cooling in the equatorial pacific cold tongue controlled by ocean mixing. *Nature*, 500:64–67.

Nagata, M. (1990). Three-dimensional finite-amplitude solutions in plane couette flow: bifurcation from infinity. *Journal of Fluid Mechanics*, 217:519–527.

Nagata, M. (1997). Three-dimensional traveling-wave solutions in plane Couette flow . *Phys. Rev. E*, 55:2023.

Orr, W. M. (1907). The stability or instability of the steady motions of a perfect liquid and of a viscous liquid. part ii: A viscous liquid. In *Proceedings of the Royal Irish Academy. Section A: Mathematical and Physical Sciences*, pages 69–138. JSTOR.

Panton, R. L. (2001). Overview of the self-sustaining mechanisms of wall turbulence. *Progress in Aerospace Sciences*, 37(4):341–383.

Park, J. S. and Graham, M. D. (2015). Exact coherent states and connections to turbulent dynamics in minimal channel flow. *Journal of Fluid Mechanics*, 782:430–454.

Patel, V. and Head, M. (1969). Some observations on skin friction and velocity profiles in fully developed pipe and channel flows. *Journal of Fluid Mechanics*, 38(01):181–201.

Perry, A., Lim, T., and Teh, E. (1981). A visual study of turbulent spots. *Journal of Fluid Mechanics*, 104:387–405.

Pinnau, R. and Ulbrich, M. (2008). *Optimization with PDE constraints*, volume 23. Springer.

Pope, S. B. (2001). Turbulent flows.

Pringle, C. C., Willis, A. P., and Kerswell, R. R. (2012). Minimal seeds for shear flow turbulence: using nonlinear transient growth to touch the edge of chaos. *Journal of Fluid Mechanics*, 702:415–443.

Pringle, C. C. T. and Kerswell, R. (2010). Using nonlinear transient growth to construct the minimal seed for shear flow turbulence. *Phys. Rev. Lett.*, 105:154502.

Pujals, G., García-Villalba, M., Cossu, C., and Depardon, S. (2009). A note on optimal transient growth in turbulent channel flows. *Physics of Fluids (1994-present)*, 21(1):015109.

Rabin, S., Caulfield, C., and Kerswell, R. (2012). Triggering turbulence efficiently in plane couette flow. *Journal of Fluid Mechanics*, 712:244–272.

Rawat, S., Cossu, C., Hwang, Y., and Rincon, F. (2015). On the self-sustained nature of large-scale motions in turbulent couette flow. *Journal of Fluid Mechanics*, 782:515–540.

Rawat, S., Cossu, C., and Rincon, F. (2016). Travelling-wave solutions bifurcating from relative periodic orbits in plane poiseuille flow. *Comptes Rendus Mécanique*, 344(6):448–455.

Reddy, S. C., Schmid, P. J., Baggett, J. S., and Henningson, D. S. (1998). On stability of streamwise streaks and transition thresholds in plane channel flows. *Journal of Fluid Mechanics*, 365:269–303.

Reynolds, O. (1883). An experimental investigation of the circumstances which determine whether the motion of water shall be direct or sinuous, and of the law of resistance in parallel channels. *Proceedings of the royal society of London*, 35(224-226):84–99.

Reynolds, W. and Hussain, A. (1972). The mechanics of an organized wave in turbulent shear flow. part 3. theoretical models and comparisons with experiments. *Journal of Fluid Mechanics*, 54(02):263–288.

Robinson, S. K. (1991). Coherent motions in the turbulent boundary layer. *Annual Review of Fluid Mechanics*, 23(1):601–639.

Sano, M. and Tamai, K. (2016). A universal transition to turbulence in channel flow. *Nature Physics*, 12:249–253.

Sasaki, E., Kawahara, G., Sekimoto, A., and Jiménez, J. (2016). Unstable periodic orbits in plane couette flow with the smagorinsky model. In *Journal of Physics: Conference Series*, volume 708. IOP Publishing.

Sayadi, T., Hamman, C. W., and Moin, P. (2013). Direct numerical simulation of complete h-type and k-type transitions with implications for the dynamics of turbulent boundary layers. *Journal of Fluid Mechanics*, 724:480–509.

Schlichting, H. and Gersten, K. (2000). *Boundary-layer theory.* Springer.

Schmid, P. J. and Henningson, D. S. (2012). *Stability and transition in shear flows*, volume 142. Springer Science & Business Media.

Schoppa, W. and Hussain, F. (2002). Coherent structure generation in near-wall turbulence. *Journal of fluid Mechanics*, 453:57–108.

Sillero, J. A., Jiménez, J., and Moser, R. D. (2014). Two-point statistics for turbulent boundary layers and channels at reynolds numbers up to $\delta^+ \approx 2000$. *Physics of Fluids (1994-present)*, 26(10):105109.

Singer, B. A. (1996). Characteristics of a young turbulent spot. *Phys. Fluids*, 8(2):509–521.

Singer, B. A. and Joslin, R. D. (1994). Metamorphosis of a hairpin vortex into a young turbulent spot. *Phys. Fluids*, 6(11):3724–3736.

Smits, A. J., McKeon, B. J., and Marusic, I. (2011). High-reynolds number wall turbulence. *Annual Review of Fluid Mechanics*, 43:353–375.

Sundkvist, D. Krasnoselskikh, V., Shukla, P. K., Vaivads, A., AndrÃľ, M., Buchert, S., and RÃĺme, H. (2005). In situ multi-satellite detection of coherent vortices as a manifestation of alfvÃľnic turbulence. *Nature*, 436:825–828.

Suponitsky, V., Cohen, J., and Bar-Yoseph, P. Z. (2005). The generation of streaks and hairpin vortices from a localized vortex disturbance embedded in unbounded uniform shear flow. *Journal of Fluid Mechanics*, 535:65–100.

Toh, S. and Itano, T. (2003). A periodic-like solution in channel flow. *Journal of Fluid Mechanics*, 481:67–76.

Tomkins, C. D. and Adrian, R. J. (2003). Spanwise structure and scale growth in turbulent boundary layers. *Journal of Fluid Mechanics*, 490:37–74.

Townsend, A. A. (1980). *The structure of turbulent shear flow.* Cambridge university press.

Trefethen, L., Trefethen, A., Reddy, S., Driscoll, T., et al. (1993). Hydrodynamic stability without eigenvalues. *Science*, 261(5121):578–584.

Tuckerman, L. S., Kreilos, T., Schrobsdorff, H., Schneider, T. M., and Gibson, J. F. (2014). Turbulent-laminar patterns in plane poiseuille flow. *Physics of Fluids*, 26(11):114103.

van Veen, L. and Kawahara, G. (2011). Homoclinic tangle on the edge of shear turbulence. *Physical review letters*, 107(11):114501.

Verzicco, R. and Orlandi, P. (1996). A finite-difference scheme for three-dimensional incompressible flows in cylindrical coordinates. *J. Comput. Phys.*, 123(2):402–414.

Viola, F., Iungo, G. V., Camarri, S., Portè-Agel, F., and Gallaire, F. (2014). Prediction of the hub vortex instability in a wind turbine wake: stability analysis with eddy-viscosity models calibrated on wind tunnel data. *Journal of Fluid Mechanics*, 750:R1.

Waleffe, F. (1995). Transition in shear flows. nonlinear normality versus non-normal linearity. *Phys. Fluids*, 7(12):3060–3066.

Waleffe, F. (1997). On a self-sustaining process in shear flows. *Physics of Fluids*, 9(4):883–900.

Waleffe, F. (1998). Three-dimensional coherent states in plane shear flow . *Phys. Rev. Lett.*, 81:4140–4143.

Waleffe, F. (2002). Exact coherent structures and their instabilities: Toward a dynamical-system theory of shear turbulence. In *Proceedings of the International Symposium on Dynamics and Statistics of Coherent Structures in Turbulence: Roles of Elementary Vortices*, pages 115–128.

Waleffe, F. (2003). Homotopy of exact coherent structures in plane shear flows. *Physics of Fluids*, 15(6):1517–1534.

Wang, J., Gibson, J., and Waleffe, F. (2007). Lower branch coherent states in shear flows: transition and control. *Physical Review Letters*, 98(20):204501.

Wang, Y., Huang, W., and Xu, C. (2015). On hairpin vortex generation from near-wall streamwise vortices. *Acta Mechanica Sinica*, 31(2):139–152.

Wu, X. and Moin, P. (2009a). Direct numerical simulation of turbulence in a nominally zero-pressure-gradient flat-plate boundary layer. *Journal of Fluid Mechanics*, 630:5–41.

Wu, X. and Moin, P. (2009b). Forest of hairpins in a low-reynolds-number zero-pressure-gradient flat-plate boundary layer. *Physics of Fluids (1994-present)*, 21(9):091106.

Wygnanski, I. and Champagne, F. (1973). On transition in a pipe. part 1: The origin of puffs and slugs and the flow in a turbulent slug. *Journal of Fluid Mechanics*, 59(02):281–335.

Wygnanski, I., Sokolov, M., and Friedman, D. (1976). On a turbulent “spot” in a laminar boundary layer. *Journal of Fluid Mechanics*, 78(04):785–819.

Yasuda, T., Goto, S., and Kawahara, G. (2014). Quasi-cyclic evolution of turbulence driven by a steady force in a periodic cube. *Fluid Dynamics Research*, 46(6):061413.

Zhou, J., Adrian, R. J., Balachandar, S., and Kendall, T. (1999). Mechanisms for generating coherent packets of hairpin vortices in channel flow. *Journal of Fluid Mechanics*, 387:353–396.

Zuccher, S., Luchini, P., and Bottaro, A. (2004). Algebraic growth in a blasius boundary layer: optimal and robust control by mean suction in the nonlinear regime. *Journal of Fluid Mechanics*, 513:135–160.

Utilisation d’une optimisation non-linéaire pour comprendre les structures cohérentes dans la turbulence et la transition

RESUME : Cette thèse vise à démêler les principaux mécanismes impliqués dans les écoulements transitoires et turbulents. L’idée centrale est d'utiliser une technique d’optimisation non linéaire pour étudier l’origine et le rôle des structures cohérentes habituellement observées dans ces écoulements. Cette méthode a été utilisée dans trois contextes différents. Tout d’abord, un écoulement laminaire linéairement stable a été considéré et l'optimisation a été utilisée pour calculer les perturbations les plus amplifiées parmi toutes les perturbations capables de déclencher une transition vers la turbulence. Une fois que la turbulence est bien établie, une optimisation non linéaire entièrement 3D maximisant l'énergie cinétique turbulente est utilisée pour étudier les structures cohérentes qui peuplent l’écoulement turbulent et les mécanismes responsables de la croissance et de l’échange d’énergie (optimale) sont étudiés. Ensuite, une approche de type système dynamique est appliquée aux équations du mouvement. La géométrie de l’espace des phases est étudiée en utilisant la théorie de la croissance transitoire pour évaluer l’importance des variétés stable et instable dans la dynamique. Dans le même cadre, un algorithme de minimisation non linéaire est utilisé pour calculer les connexions hétérocliniques parmi les solutions invariantes des équations de Navier-Stokes.

Mots clés : Transition vers la turbulence, instabilités non-linéaires, optimisation non-linéaire, écoulement turbulent, structures cohérentes, système dynamique.

Using nonlinear optimization to understand coherent structures in turbulence and transition

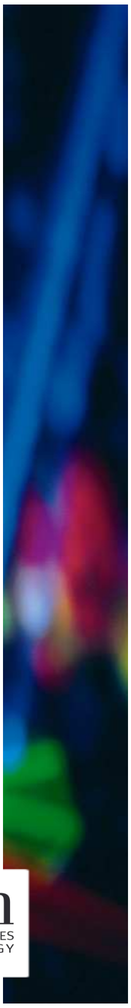

ABSTRACT : This thesis aims at unraveling the main mechanisms involved in transitional and turbulent flows. The central idea is that of using a nonlinear optimization technique to investigate the origin and role of coherent structures usually observed in these flows. This method has been used in three different contexts. First, a linearly stable laminar flow has been considered and the optimization has been used to compute the most amplified perturbations among all disturbances able to trigger transition to turbulence. Once turbulence is well established, a fully 3D nonlinear optimization maximizing the turbulent kinetic energy is used to study coherent structures populating turbulent shear flow as well as investigate the mechanisms responsible for the energy (optimally) growth and exchange. Then, a dynamical system approach is applied to fluid flow equations. The geometry of the state space is investigated by using transient growth theory to reveal the importance of the stable and unstable manifold. In the same framework, a nonlinear minimization algorithm is used to compute heteroclinic connections among invariant solutions of the Navier-Stokes equations.

Keywords : Transition to turbulence, nonlinear instability, nonlinear optimization, turbulent flows, coherent structures, dynamical system

ARTS ET MÉTIERS ParisTech

ParisTech
INSTITUT DES SCIENCES ET TECHNOLOGIES
PARIS INSTITUTE OF TECHNOLOGY